Maneuverability, Load Alleviation, and Ride Qualities of Transonic High-Aspect-Ratio-Wing Aircraft

by

Divya Sanghi

A dissertation submitted in partial fulfillment
of the requirements for the degree of
Doctor of Philosophy
(Aerospace Engineering)
in the University of Michigan
2022

Doctoral Committee:

Professor Carlos E. S. Cesnik, Chair
Professor Bogdan I. Epureanu
Professor Ilya V. Kolmanovsky
Professor Cristina Riso
Dr. Fabio Vetrano

Divya Sanghi
dsanghi@umich.edu
ORCID iD: 0000-0002-6083-6366

ACKNOWLEDGMENTS

This dissertation has been made possible due to the support of a lot of people. I would first like to thank my advisor Prof. Carlos E. S. Cesnik, for giving me the opportunity to work on this incredible project. Every interaction with him has been a learning experience, and I am very grateful to him for all his guidance and encouragement. The pandemic was a challenging period for my family, and I really appreciate his support during that time.

I am also grateful to Prof. Cristina Riso for being a mentor and, more importantly, a great friend. The project was extremely challenging, and working with her made it easier. I am also thankful to Dr. Fabio Vetrano for all his suggestions and for providing insights from an industry perspective. I would also like to thank my other committee members, Prof. Epureanu and Prof. Kolmanovsky, for all their suggestions to improve the dissertation.

Thanks to all my friends in the A^2SRL and the Aerospace Department: Bernardo, Bilal, Braden, Chris, Christina, Gary, Guillaume, Leandro, Mateus, Molong, Nan, Patricia, Patrizio, Pedro, Renato, Siddharth, Thiago, and Qingzhao. They have all helped me in one way or the other throughout my time in this program.

I am also very grateful to all the friends I made in Ann Arbor who have been like family to me in the last six years. I want to thank Tatyana and Arushi for being the best roommates and making living away from home easier. A special thanks to Nishtha, with whom I became friends in Ann Arbor by chance. I don't think I would have survived the past four years without her support. Thanks to Alg for always being there for me, especially during the last few months, without which finishing this work would have been impossible.

Thanks to my childhood friends, Aanchal and Palak, who can solve all my problems with just a phone call. Finally, I would like to thank my parents and brother for always supporting and encouraging me to achieve my goals even if that meant moving to a different country.

The material of this work is based upon work supported by Airbus in the frame of the Airbus-Michigan Center for Aero-Servo-Elasticity of Very Flexible Aircraft (CASE-VFA). I want to thank Airbus for providing the XRF1 test case as a mechanism for demonstrating the approaches presented in this work.

TABLE OF CONTENTS

LIST OF FIGURES

FIGURE

LIST OF TABLES

TABLE

LIST OF APPENDICES

LIST OF ACRONYMS

A^{2}SRL Active Aeroelasticity and Structures Research Laboratory

CASE-VFA Center for Aero-Servo-Elasticity of Very Flexible Aircraft

CFD computational fluid dynamics

CRM Common Research Model

DLM double lattice method

DOFs degrees of freedom

FA flexible aircraft

FAA Federal Aviation Administration

FEM finite element method

FFWT flared folding wingtip

GFEM global finite element model

GLA gust load alleviation

HALE high-altitude long-endurance

HARW high-aspect-ratio wing

ICAO International Civil Aviation Organization

ISO International Organization for Standardization

LE leading-edge

MLA maneuver load alleviation

PSD power spectral density

SAH semi-aeroelastic hinge

TE trailing-edge

UAV unmanned air vehicle

UM/EF2S University of Michigan's Enhanced FEM2Stick

UM/F2S University of Michigan's FEM2Stick

UM/NAST University of Michigan's Nonlinear Aeroelastic Simulation Toolbox

UVLM unsteady vortex-lattice method

VCCTEF variable camber continuous trailing-edge flaps

VFA very flexible aircraft

WRBM wing root bending moment

WRTM wing root torsion moment

XRF1 Airbus standard aircraft research test case

ABSTRACT

Reducing the environmental impact of aviation is driving civil transport aircraft designs toward longer, high-aspect-ratio wings with higher aerodynamic efficiency. However, high-aspect-ratio-wing configurations show increased structural flexibility compared to contemporary, stiffer and lower aspect-ratio-wing ones. This increased wing flexibility causes higher loads and degrades maneuverability. These issues require novel solutions to guarantee load alleviation and maneuverability while maintaining pilot and passenger ride comfort.

This work explores conventional and unconventional control effectors such as distributed trailing- and leading-edge control surfaces and flared folding wingtips for improving load alleviation and maneuverability of very flexible, transonic high-aspect-ratio-wing aircraft representative of a potential future civil transport configuration. The impact on aircraft ride qualities during gust encounters is also investigated. The studies utilize a coupled nonlinear aeroelastic-flight dynamics framework (UM/NAST) that can model different control effectors. It was enhanced in this work with the capability of modeling flared folding wingtips and evaluating an acceleration-based ride quality metric among other things.

A spanwise placement study of trailing- and leading-edge control surfaces showed that ailerons of high-aspect-ratio-wing aircraft should be placed at a more inboard location relative to the wing span than in aircraft with typical aspect ratios to provide adequate roll maneuverability. The study showed that the peak of control-surface effectiveness along with the wing span moves inboard (and decreases in value) for higher wing aspect ratios. The simulations showed that inboard leading-edge control surfaces are ineffective compared with trailing-edge control surfaces at the same spanwise locations; however, outboard leading-edge control surfaces provide higher load alleviation capability than their trailing-edge counterparts while avoiding control reversal. Releasing flared folding wingtips while deploying control surfaces alleviate loads with no significant impact on roll maneuverability at flight conditions where aeroelastic effects are moderate. However, it causes higher loads and degrades roll maneuverability in the presence of strong wash-out effects at higher dynamic pressure conditions or with increased wing flexibility. Increasing wing stiffness improves flared folding wingtips' load alleviation performance and their ability to enhance roll maneuverability. The results also showed that these devices degrade ride quality due to their flapping-induced vibrations. However, this negative impact is smaller than the ride quality enhancements

resulting from higher wing flexibility. Therefore, the ride qualities of high-aspect-ratio-wing aircraft with released flared folding wingtips remain higher than for stiffer configurations with a typical wing aspect ratio. Finally, these results demonstrated the importance of considering the impact of wing flexibility when exploring different control effectors for enhancing roll maneuverability and/or explore load alleviation.

CHAPTER 1

Introduction

This chapter begins by describing the motivation of the dissertation. A literature review in the area of maneuverability, load alleviation, and ride qualities of transonic high-aspect-ratio-wing aircraft is presented in Sec. 1.2. Based on the gaps identified in the literature, the dissertation's objectives are defined in Sec. 1.3, followed by an outline of the dissertation in Sec. 1.4.

1.1 Motivation

The civil transport aircraft has come a long way from the first jet-powered civil transport airliner, the de Havilland Comet that took flight in 1952 (Fig. 1.1a). Today's aircraft have much longer range, maximum speeds and capacity while being significantly safer and efficient. This progress has been made possible by decades of continuous research in the aerospace industry to meet the ever increasing demand of air transportation. As air transportation becomes more accessible, this demand is going to accelerate over the next few decades. Estimates show that there will be more than 10 billion passengers flying each year by 2050, compared to the 4.5 billion people flying annually in 2022 [1]. There has been an industry-wide push toward developing highly fuel efficient designs to cater to this growing demand.

Despite the improvement in the efficiency of the transport aircraft over the years, their environmental impact continue to increase. Sustainability and lower environmental impact are critical challenges for the future growth of the aviation industry. Although the contribution of civil aviation to global emissions remains less than 3%, the environmental impact is substantial due to the nature of emissions at higher altitudes. The contribution to global emissions is projected to increase rapidly by 2050 if disruptive changes in aircraft design and operations are not incorporated.

The highly ambitious goal of achieving sustainable civil aviation by 2050 has been put forward by different organizations including the Federal Aviation Administration (FAA) [6] and International Civil Aviation Organization (ICAO) [1]. Airbus is developing ZEROe [5] aircraft with hydrogen propulsion to help achieve their goal of flying a zero-emission civil transport

(a) de Havilland Comet: First jet powered civil transport aircraft [2]

(b) A380: Current civil transport aircraft [3]

(c) NASA Sugar: Future HARW civil transport aircraft concept [4]

(d) Airbus ZEROe: Future HARW civil transport aircraft concept [5]

Figure 1.1: Evolution of civil transport aircraft.

aircraft by 2035. Civil aviation could reduce its environmental impact by [6]:

- Shifting to a cleaner propulsion system with alternative fuels
- Shifting towards efficient aircraft designs

Innovations are required in every area to reduce the environmental impact of civil aviation. Improving the airframe efficiency or fuel burn requires the design of future civil transport aircraft to reduce the drag and weight of the airframe. This results in a high-aspect-ratio-wing (HARW) aircraft with lower induced drag and a very flexible aircraft (VFA) due to lower weight fraction. Therefore, there is a shift towards next-generation civil transport aircraft with very flexible HARWs (see Figs. 1.1c and 1.1d).

However, the shift to very flexible HARW aircraft brings new challenges in terms of their design, simulation, and control. As wings becomes longer and flexible, they exhibit larger aeroelastic deflections resulting in a geometrically nonlinear behaviors. They also exhibit low-frequency natural vibration modes, which result in the aircaft aeroelastic response being tightly coupled with flight dynamics and influenced by nonlinear effects [7]. This requires design tools that can capture the coupled nonlinear aeroelastic-flight dynamics behavior of very flexible HARW aircraft.

A longer wingspan will also have operational challenges due to current airport gate constraints and the required distance to be maintained during taxing. The A380 [3] with its 80 m wingspan, can operate out of limited airports around the world. Recently, B777 [8] with a wingspan of 72 m incorporated a folding wingtip to allow operating from all the major airports by reducing its wingspan by 6 m.

Additionally, the increased wing flexibility causes higher loads, degrades maneuverability, and impacts the ride and handling qualities. Future aircraft configurations with very flexible HARWs may use novel solutions based on unconventional control effectors, such as leading-edge control surfaces and folding wingtips to guarantee load alleviation and maneuverability.

This work focuses on analyzing the maneuverability, load alleviation, and ride qualities of very flexible HARW aircraft representing a potential future civil transport configuration. Computational investigations are conducted utilizing trailing- and leading-edge control surfaces and folding wingtips within a coupled nonlinear aeroelastic-flight dynamics framework.

1.2 Literature Review

This section summarizes previous work addressing some of the critical challenges in transonic HARW aircraft related to load alleviation (1.2.1), roll maneuverability(1.2.2), and ride qualities (1.2.3). While several potential solutions have been studied to address these issues in the literature,

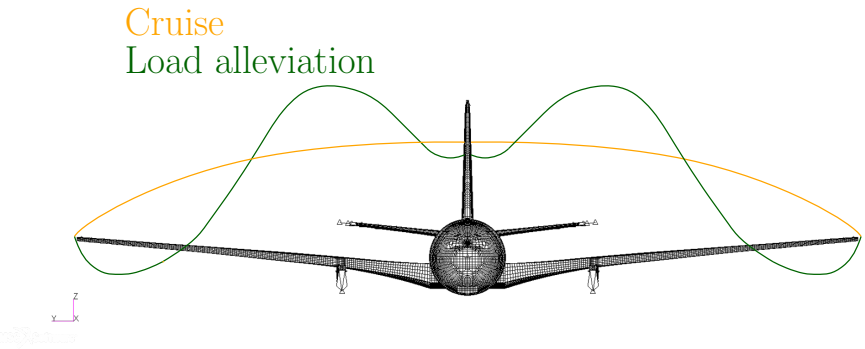

Figure 1.2: Redistribution of lift during load alleviation.

this section describes previous studies utilizing conventional control effectors like trailing-edge control surfaces and unconventional control effectors like leading-edge control surfaces and flared folding wingtips. Finally, Sec.1.3 summarizes the open questions in the literature, to introduce the research objectives of this work.

1.2.1 Load Alleviation

The structural sizing of an aircraft is based on the worst load case scenario resulting from its response during either a maneuver or a gust disturbance. Higher operating loads are expected with very flexible HARW configurations due to higher deflections. Reducing loads in very flexible HARW aircraft will enable weight savings with the ultimate consequence of lowering fuel consumption. Additionally, load alleviation also helps increase the life-cycle of an aircraft by mitigating structural fatigue. The basic idea of any load alleviation system is to change the shape of the wing to shift the loads inboard (see Fig. 1.2). A load alleviation system can be either active or passive. Passive load alleviation strategies are primarily based on aeroelastic tailoring, which helps change the wing's shape favorably under a given load. The review paper by Jutte and Stanford [9] provides a detailed overview of the investigations related to passive aeroelastic tailoring with an emphasis on civil transport aircraft.

Current civil transport aircraft typically use an active load alleviation system that involves deploying trailing-edge control surfaces for gust and maneuver load alleviation. The review paper by Regan and Jutte [10] provides a detailed summary of the active load alleviation systems in the current civil transport aircraft. Most load alleviation systems use existing control effectors such as ailerons, spoilers, and elevators. Such load alleviation systems offer advantages in terms of easier deployment without any changes to the structural design. However, with increasing wing flexibility, wash-out effects reduce the effectiveness of these devices and may even result in control reversal [11].

Therefore, future aircraft configurations with very flexible, HARWs may use novel load alleviation solutions based on unconventional control effectors. Several studies have investigated different control effectors such as distributed trailing-edge control surfaces, leading-edge control surfaces, and flared folding wingtips.

The loss of effectiveness and control reversal of trailing-edge control surfaces in flexible wings have motivated studies in the area of distributed trailing-edge or leading-edge control surfaces. Several optimization studies have investigated distributed trailing-edge control surfaces as load alleviation devices [12, 13, 14, 15, 16]. These studies consider a variable camber continuous trailing-edge flaps (VCCTEF) concept, which utilizes multiple control surfaces along the wingspan that can be deployed together to achieve load alleviation. The studies showed that the optimizer deflects different control surfaces for maneuver load alleviation (MLA) compared with gust load alleviation (GLA). The Common Research Model (CRM) was considered with an aspect ratio of nine under transonic aerodynamic loading. A series of studies [17, 18, 19] have also experimentally tested a scaled model of the CRM wing with a VCCTEF concept for GLA. The studies were limited to a flexible wing (the model's first bending frequency was 2.2 Hz). In a follow-up study, the high-aspect-ratio variant of the CRM was considered in the MLA and GLA investigations by Stanford [20]. However, all the numerical studies considered an isolated root-clamped wing analyzed by means of a linear structural solver.

Besides the studies involving VCCTEF or other similar concepts, Breuker et al. [21] investigated the trade-off between utilizing trailing-edge control surfaces for active gust load and varying bending-twist coupling for passive load alleviation. They considered a regular-aspect ratio wing test case simulated using a linear structural analysis. Their studies show that a higher load alleviation was achieved with the combination of both techniques since passive tailoring can help increase control effectiveness. Pusch et al. [22] optimized the aileron layout for alleviating gust loads of a flexible aircraft. Krupa et al. [23, 24] investigated the impact of combined deflections of distributed trailing-edge control surfaces and passive wingbox tailoring through optimization of a composite wing for reducing weight and maneuver load alleviation.

Several studies have also investigated leading-edge control surfaces as load alleviation devices. A few studies investigated their load alleviation performance experimentally [25, 26, 27, 28]. Woods et al. [25] demonstrated active maneuver load alleviation using a combination of leading- and trailing-edge control surfaces on a flexible wing wind-tunnel model. Oremland et al. [28] numerically investigated the benefits of deploying leading- and training-edge control surfaces for flutter suppression and gust load alleviation. However, most of these investigations were conducted at low speeds and did not consider a HARW. Following studies considered transonic aerodynamics in their analyses. Klug et al. [29] studied actuator concepts, including leading-edge control surfaces for gust load alleviation. Their results showed that leading-edge control surfaces help reduce

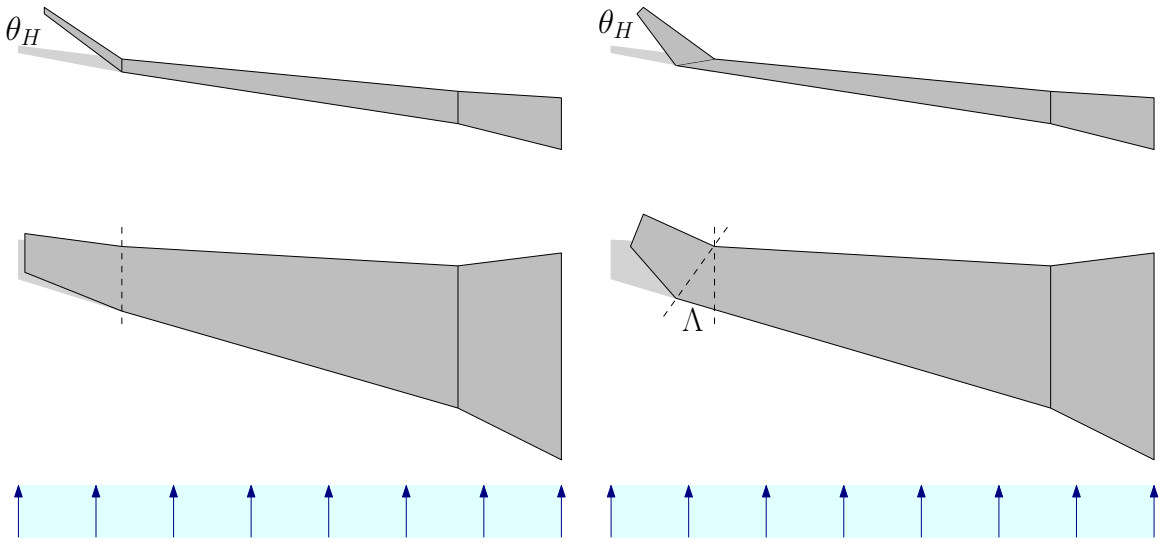

(a) $\Lambda = 0°$ (b) $\Lambda > 0°$

Figure 1.3: Folding wingtip with hinge flare angle Λ.

torsion moments. Recently, Ullah et al. [30, 31] demonstrated gust-induced wing root bending and torsion moment alleviation by actuating leading- and trailing-edge control surfaces. The trailing-edge control surfaces were deployed to reduce the bending moment, while the leading-edge control surfaces were deployed to reduce the torsion moment. They investigated the impact of both steady and dynamic flap deflections. While their simulations considered transonic flight conditions, the aircraft model and the flexibility levels were not representative of a very flexible transonic HARW aircraft. This allowed the deployment of outboard trailing- and leading-edge control surfaces for load alleviation without exhibiting loss of effectiveness or reversal.

Future civil transport aircraft with HARWs also drive new interest in folding wingtips. These devices enhance aerodynamic efficiency by increasing wing aspect ratio in flight while meeting airport constraints on the ground—a capability leveraged in novel designs such as the NASA Sugar concept [32] and the Boeing-777-X [8].

Several different types of folding wingtip devices have been studied in the past. Mastracci et al. [33] provide a detailed review of different wingtip devices in their study. One such folding wingtip device that has been studied for load alleviation is the flared folding wingtip (FFWT). Previous work [34, 35, 36, 37] studied the load alleviation benefits of FFWTs where the hinge line is not parallel to the oncoming flow (see Fig. 1.3). The angle between the hinge line and the incoming flow is the flare angle denoted by Λ as shown in Fig. 1.3. For a hinge rotated outboard of the incoming flow, a reduction in the local angle of attack outboard of the hinge is introduced for an upward rotation of the wingtip (see θ_H in Fig. 1.3). This effect reduces the bending moment by

unloading the wingtip. For a hinge with zero stiffness, no bending loads are transmitted through the hinge, which helps in alleviating loads at the wing root. The load alleviation mechanism of FFWTs can also be explained by the following equation [34]:

$$\Delta\alpha = -\arctan(\sin\Lambda \tan\theta_H), \tag{1.1}$$

where $\Delta\alpha$ is the change in the local angle of attack, a positive value of flare angle Λ signifies the rotation of the hinge line outboard. A positive value of hinge rotation θ_H represents an upwards rotation of the wingtip.

FFWTs are passive load alleviation devices since their motion is not controlled by an actuator but by a balance of loads. These devices can be locked during the cruise and released through a dedicated mechanism during a gust or maneuver. Once released, FFWTs are free to rotate about the hinge, and their rotation is determined by the balance of loads acting outboard of the hinge. These devices are also called semi-aeroelastic hinge (SAH) [38].

Castrichini et al. [34, 35, 36] conducted parametric studies for different wingtip parameters through static and dynamic analysis in a test case representative of a flexible civil transport aircraft. The studies showed that these devices could enable an increase in wingspan without any significant increase in load. Later, Castrichini et al. [39] studied gust load alleviation using FFWTs with nonlinear hinge springs. They observed that delaying the release of the FFWTs can significantly impact their load alleviation performance. However, these studies did not consider geometric nonlinearities and were also limited to a flexible wing.

These devices have also been evaluated through flight and wind tunnel tests. Wilson et al. [40, 41, 42] evaluated these devices experimentally in the AlbatrossONE Semi Aeroelastic Hinge (SAH) small-scale demonstrator. Flight tests confirmed the load alleviation induced by the folding wingtips and verified their stability in flight. Cheung et al. [43, 44] conducted several wind-tunnel tests on a straight HARW with a FFWT, showing a 6–11% reduction in wing root bending moment. They evaluated the impact of different flare angles and compared the experimental results against numerical simulations. Their static wind tunnel tests showed that the free hinge reduced the rolling moment due to the reduction in bending moment. Later, they also investigated the impact of a trailing-edge control surface on the wingtip that can be actuated to control the behavior of the FFWTs [45, 46].

Gu et al. [47] implemented a preliminary sizing framework for aircraft with FFWTs. They considered a beam model with the double lattice method (DLM). They conducted the sizing process for several models with varying aspect ratios and wingtip lengths. A 40% reduction in aircraft weight was observed due to the load alleviation benefits of the FFWTs.

Some previous studies [48, 49] also investigated these devices through high-fidelity static

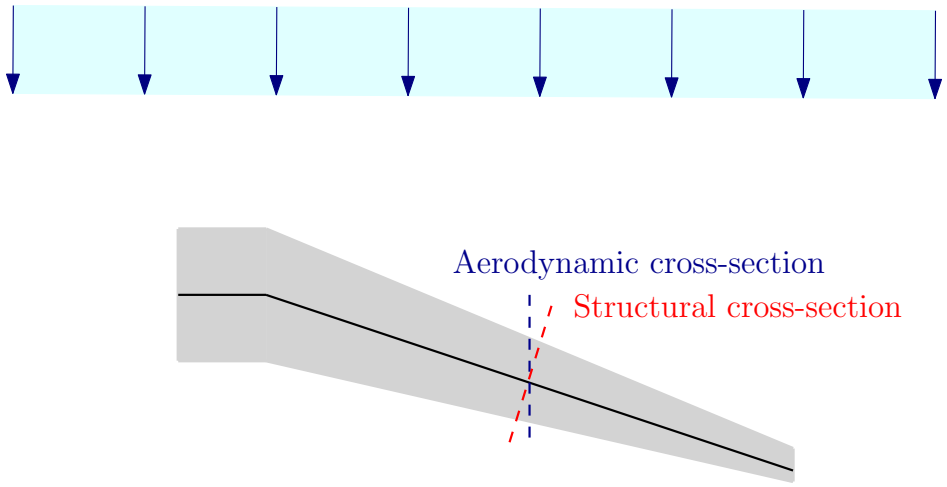

Figure 1.4: Washout effects in aft-swept wings.

aerostructural solutions. Delavenne et al. [49] investigated the effect of wingtip hinge line spanwise location and flare angle on drag and wing root bending moment of a HARW. However, most studies have utilized a beam model in their investigations.

While those studies highlighted the potential load alleviation advantages of FFWTs, they considered a linear aeroelastic model in their investigations. Recently Conti et al. [50], and Mastracci et al. [33] presented a nonlinear dynamic multibody formulation to incorporate the nonlinear effects due to large rotations of the wingtip. The aerodynamic forces were modeled as follower forces in their formulation. Their model consists of a rigid wingtip connected to the flexible main airframe. However, the main frame was modeled as a linear structure. Healey et al. [51] also implemented a formulation to capture the geometrically nonlinear effects due to the wingtip rotation, which was verified through numerical and wind tunnel experiments. Their numerical studies considered a linearized model about the deformed state of the wing deployed with a FFWT.

1.2.2 Roll Maneuverability

Loss of control-surface effectiveness and reversal are well known aeroelastic phenomena affecting flexible aircraft wings [11, 52]. Additionally, civil transport aircraft have significant afterward wing sweep angles because of their transonic cruise conditions. This causes strong wash-out effects where wing aerodynamic cross-sections twist down (up) in the presence of upward (downward) out-of-plane bending displacements (see Fig. 1.4). Wash-out effects contrast the change in lift commended by aileron inputs, so reducing control effectiveness and causing slower roll maneuvers [11, 52]. While these issues are well known, they will be exacerbated in future HARW configurations due to their higher flexibility and larger aeroelastic deflections, making it challenging to meet roll capability certification requirements [53, 54]. Therefore, it is critical to investigate

the impact of HARWs on aircraft roll maneuverability.

Several different strategies have been studied for improving roll maneuverability. Passive and active aeroelastic tailoring can improve aircraft roll maneuverability by alleviating wash-out effects. However, most previous studies investigated the impact of aeroelastic tailoring on load alleviation or stability [55, 56, 57, 58, 59, 60]. Among the previous work in the area of active aeroelastic tailoring for roll maneuverability, Chen et al. [61] studied the roll maneuverability benefits of an adaptive variable-stiffness spar. Cesnik et al. [62] investigated piezoelectric actuation embedded in high-aspect-ratio composite wings. Khot et al. [63] designed a flexible wing structure with enhanced roll performance using an internal actuation system. The design utilized wing flexibility for performing roll maneuvers without using ailerons.

Previous work also investigated passive aeroelastic tailoring strategies to improve roll maneuverability. Most of these studies showed improvement in roll maneuverability by considering an optimized composite wingbox. Gibson et al. [64] maximized the aileron control reversal speed of a wingbox by reinforcing its upper skin using topology optimization. Kitson et al. [65] studied the roll maneuverability of an optimized CRM [66] configuration with an aspect ratio of 13.5 [67]. They observed higher roll maneuverability when considering a tow-steered composite wingbox in place of a more flexible metallic wingbox with the same aspect ratio

Few studies investigated the impact of aileron placement considering roll maneuverability. Weisshaar et al. [11] studied the impact of aileron placement and sizing on lateral control. Anderson et al. [68] investigated the effect of combining trailing- and leading-edge control surfaces on a flexible rectangular wing test case. The results showed higher roll control authority by combining the control surfaces. Cook et al. [69] compared the roll control effectiveness of ailerons on a high-altitude long-endurance (HALE) unmanned air vehicle (UAV) with rectangular, very flexible wings. Their results showed that ailerons were in reversal at cruise, while spoilers had higher maneuverability.

Maraniello and Palacios [70] provided insights regarding the impact of bending and torsional flexibility on the roll maneuverability of very flexible wings through static and dynamic analyses. Their results showed a 50% decrease in damping due to roll rate with increasing flexibility. However, they considered a rectangular straight beam model and a single aileron layout.

The VCCTEF concept for load alleviation has also been investigated for improving roll maneuverability. Ting et al. [13] analyzed the VCCTEF control effectors for an aircraft with varying wing flexibility. Through static aeroelastic analysis, they evaluated rolling moment derivatives and hinge moments of the VCCTEF control effectors. Their studies showed that the hinge loads increased with increasing wing flexibility. Dowell et al. [71] explored deploying leading- and training-edge control surfaces for improving roll control effectiveness. They showed that deploying a leading-edge control surface along with a trailing-edge control surface can help eliminate control reversal.

Recently, FFWTs have also been investigated for improving roll maneuverability in HARW aircraft by deploying them with ailerons. Dussart et al. [72] investigated the impact of FFWTs on the roll response of a flexible aircraft. They evaluated both aileron effectiveness and roll damping derivatives for a flexible and rigid swept wing. Castrichini et al. [73] evaluated the roll maneuverability of aircraft equipped with these devices. They found that releasing FFWTs during maneuvers enhances roll maneuverability due to a reduction in roll damping. Healy et al. [41] explored the advantage of FFWTs for improving the roll maneuverability of a straight rectangular wing. Their wind-tunnel experiments showed an improvement in the steady roll rate for the wing with FFWT compared with a wing with the same span. William et al. [74] investigated the impact of a trailing-edge control surface on FFWTs for improving roll maneuverability. They showed that higher roll maneuverability could be achieved by deflecting the trailing-edge control surfaces on the wingtip. However, since they considered a straight rectangular wing, the impact of washout effects remains to be investigated for an outboard placed trailing-edge tab on a FFWT.

1.2.3 Ride Quality

Ride qualities measure passenger and pilot comfort while aircraft experience vibrations and accelerations during flight. Assessing ride qualities is critical to ensure aircraft meet operational requirements. Ensuring passenger comfort is also a requirement for load alleviation technology as defined by the European Union Safety Agency [54]. It states that even though the priority of a gust load alleviation system is to ensure structural integrity, the comfort of the passengers should not be compromised.

Ride quality metrics are typically acceleration-based, and it is essential to consider both vertical and lateral accelerations. There are limited studies in the literature dedicated to measuring the ride qualities of civil transport aircraft because it is usually a proprietary information of an aircraft manufacturer [10]. However, these metrics are primarily based on accelerations at different points of the fuselage corresponding to passenger and pilot positions.

In the 1970's, NASA [75, 76, 77] developed ride quality metrics to quantify passenger comfort. Leatherwood et al. [78] introduced a metric for evaluating passenger comfort as a function of the fuselage's vertical and lateral acceleration in the frequency domain. Since gust load alleviation and ride qualities are closely related, most of the studies in literature investigated the combined impact of these two parameters in their work. Konig et al. [79] introduced a load alleviation and ride quality smoothing system using an open-loop controller. Regan and Jutte [10] have provided a review of the various gust load alleviation technologies and ride quality metric evaluation studies in the literature. The International Organization for Standardization (ISO) provides the standard ISO 2631-1 [80] to quantify human comfort levels exposed to vehicle vibrations. The

MIL-STD-1472G [81], a military aircraft ride quality standard, is also based on the ISO-2631-1. The ride quality metric based on ISO-2631-1 was used by Bizinos [82] and Okolo [83] to assess passenger ride qualities due to wake surfing. Wang [84] proposed a control law for improving ride comfort and alleviating loads during gust encounters using a ride quality metric introduced by Jacobson [85]. This metric was based on vertical and lateral accelerations but considered a quasi-rigid aircraft in their simulations. Khalil [86] studied the lateral ride qualities of sailplanes by comparing the lateral acceleration's power spectral density (PSD) for different modal damping values. They found that increasing modal damping reduces the maximum lateral acceleration at the pilot location. Hanson et al. [87] experimentally measured passenger comfort in a business jet using the metric developed by Leatherwood [78]. This metric was used by Nguyen et al. [17] and Hartwell et al. [88] to explore acceleration control to improve ride qualities in flexible aircraft. Nguyen et al. [17] considered the NASA Generic Transport Model, a flexible wing transport aircraft, to assess the impact of different flight controllers on improving ride quality. They measured ride qualities for a single location inside the fuselage. Hartwell [88] analyzed the gust load alleviation and ride qualities for a HARW CRM model at two locations on the fuselage. They investigated the impact of a multi-objective flight controller. They found that it successfully alleviated loads and improved ride comfort at the aircraft's center of gravity location but increased discomfort at the pilot's location.

Recently, Krishnamurthy and Handajo [89] introduced a passenger ride quality metric based on the vertical, lateral, angular roll, and angular pitch acceleration. They found that vertical acceleration contributes the most to ride discomfort. The aircraft model considered had an aspect ratio of 9.

1.3 Dissertation Objectives

This section describes the objectives of this dissertation which will contribute to addressing some of the open questions in the literature related to maneuverability, load alleviation, and ride qualities in very flexible, transonic HARW aircraft.

Section 1.2.2 provided an overview of the literature addressing the roll maneuverability of very flexible, transonic HARW aircraft through trailing- and leading-edge control surfaces, aeroelastic tailoring, and FFWTs. The impact of deploying trailing-edge control surfaces and aeroelastic tailoring in a very flexible HARW has been investigated mostly through high-fidelity aeroelastic optimization of clamped wingbox models. Most of these studies considered the distributed trailing-edge or VCCTEF concept and focused on load alleviation. A better understanding of the impact of the spanwise placement of control surfaces on roll maneuverability can provide valuable guidelines for optimization studies. Some studies investigated the dynamic roll response of a HARW aircraft with trailing- and leading-edge control surfaces. However, they considered a straight rectangular wing or a single control surface layout. Finally, some recent studies have also explored FFWTs for improving roll maneuverability in HARW aircraft. These studies provided insights regarding the roll response of FFWTs but considered moderate aspect ratios and flexibility levels that may not represent a very flexible, transonic HARW aircraft. Also, they did not consider fully coupled nonlinear aeroelastic-flight dynamic analyses. These analyses are necessary for capturing the behavior of very flexible HARW aircraft [7]. This limitation comes from the lack of computational frameworks to account for coupling effects among nonlinear structural dynamics, rigid-body dynamics, and aerodynamics while considering FFWTs. These open questions motivate the first research objective of this dissertation:

- Investigate questions regarding roll maneuverability in transonic HARW aircraft
  - What is the impact of aileron placement on the static and dynamic roll response?
  - What are the benefits and limitations of varying aileron placement versus tailoring the wingbox for improving roll maneuverability?
  - Can unconventional control effectors like leading-edge control surfaces and FFWTs improve roll maneuverability?
    - What is the best spanwise placement of a leading-edge control surface?
    - What is the impact of deploying FFWTs with the different spanwise placement of trailing- and leading-edge control surfaces?

The second research objective will address questions regarding maneuver and gust load alleviation. Section 1.2.1 presented a summary of literature utilizing either trailing- and leading-edge

control surfaces or FFWTs for load alleviation. Similar to roll maneuverability studies, most past investigations were limited to optimization of a clamped HARW or moderate flexibility and regular aspect-ratio wings. Regarding FFWTs, several investigations have studied their load alleviation benefits. However, the load alleviation performance of FFWTs has not been investigated for a very flexible transonic HARW aircraft, especially at higher dynamic pressure conditions where the impact of aeroelastic effects is stronger. Few recent studies have incorporated the geometric nonlinearities due to the wingtip rotation but considered a linear model for the main airframe. Based on the above gaps in the literature, the second objective of the dissertation is to:

- Investigate questions regarding load alleviation in transonic HARW aircraft
  - Can unconventional control effectors like leading-edge control surfaces and FFWTs improve load alleviation?
  - What is the impact of the wing flexibility on the maneuver and gust load alleviation performance of FFWTs?
  - What is the impact of considering different flight conditions on the load alleviation performance of FFWTs?

The third research objective will focus on analyzing the ride qualities of transonic HARW aircraft during a gust disturbance. Based on the literature review in Sec. 1.2.3, to the author's best knowledge, there is no previous work that has investigated the impact of ride qualities in a HARW civil transport aircraft compared to the current regular aspect-ratio aircraft. As aircraft designs move to higher-aspect-ratio and lower structural weight wings, resulting in very flexible structures, assessing ride qualities earlier in the design process becomes critical. It is also essential to investigate the impact of the novel gust load alleviation devices that are being considered in such aircraft. The effect of FFWTs on ride qualities has not been studied. This motivates the third objective of the dissertation:

- Investigate questions regarding ride qualities of transonic HARW aircraft
  - How does wing flexibility impact ride qualities?
  - How do FFWTs impact ride qualities?

The three objectives of the dissertation will be addressed by roll and gust response analyses. Since the studies focus on capturing the behavior of a very flexible HARW aircraft, this work will also highlight the impact of geometrically nonlinear effects on the roll and gust response. This includes isolating the impact of linear vs. nonlinear kinematics and the impact of modeling aerodynamic loads as follower or non-follower forces. The shortening effects are not captured by

linear kinematics while the non-follower forces do not consider the change in the orientation of the aerodynamic loads as the wing deflects.

To investigate the objectives of this dissertation, this work considers:

Computational framework with the ability to model and simulate flexible and very flexible aircraft in free flight considering coupled nonlinear aeroelasticity and flight dynamics. As part of this work, the framework is enhanced with the capability to model FFWTs and evaluate ride qualities. Section 2.1 provides additional details about the framework.

Aircraft test cases with structural properties representative of a next-generation very flexible civil transport HARW aircraft. The studies also consider a flexible test case with a regular aspect ratio to highlight the impact of higher wing flexibility and aspect ratio. Details about the models and level of flexibility are highlighted in Sec. 3.2 by their natural frequencies and tip vertical displacements at trim conditions. The aerodynamic models were developed in Ref. [90] using the method of segments [91], to capture the quasi-steady transonic effects. Section 3.3 provides details about the low-order aerodynamic model of the aircraft test cases.

1.4 Dissertation Outline

This section provides an overview of the dissertation. Based on the dissertation objectives, the dissertation is organized as follows:

Chapter 2 presents the computational framework that will be utilized to fulfill the dissertation objectives. The key features of the computational framework are described, followed by the theoretical and computational enhancements implemented as part of this work which enabled the investigations presented in subsequent chapters. Parts of this chapter were published previously in [92, 93, 94].

Chapter 3 describes the aircraft models utilized to fulfill the dissertation objectives. The aircraft models are representative of a contemporary civil transport aircraft and a future civil transport aircraft with HARW. The structural models are derived from an industry-standard multidisciplinary test case, Airbus XRF1. Parts of this chapter were published previously in [90, 93].

Chapter 4 presents the results considering roll maneuverability and MLA in transonic HARW aircraft. First, the feasibility of deploying trailing-edge control surfaces to provide adequate roll maneuverability in a HARW is investigated through a placement study. Second, the impact of wingbox passive aeroelastic tailoring is examined. Third, the benefits and limitations of deploying leading-edge control surfaces and FFWTs are investigated. Finally, the impact of geometrically nonlinear effects on roll maneuverability is also discussed. The studies in this chapter address the dissertation's first and second research objectives (except GLA, which is addressed in the next chapter). Parts of this chapter were published previously in [90, 95, 93].

Chapter 5 presents the results discussing gust load alleviation and ride qualities in transonic HARW aircraft. First, the impact of geometrically nonlinear effects on capturing the response of HARW aircraft to gust disturbances is assessed. This is followed by the results highlighting the benefits and limitations of deploying FFWTs on gust load alleviation. The impact of wing flexibility is also discussed. Next, the effect of wing flexibility and deploying FFWTs for gust load alleviation on ride qualities of transonic HARW aircraft is investigated. The studies in this chapter address the remaining questions under this dissertation's second and third research objectives. Parts of this chapter were published previously in [94].

Chapter 6 provides a summary of the results, highlighting the key contributions of the dissertation. Finally, some recommendation for future work are discussed.

CHAPTER 2

Computational Developments

This chapter presents the computational framework used in this work to investigate the key objectives of the thesis. Sec. 1.3 details the computational framework requirements for analyzing very flexible HARW aircraft. Based on those requirements, this work leverages the University of Michigan's Nonlinear Aeroelastic Simulation Toolbox (UM/NAST) [96], a low-order multidisciplinary framework for modeling, analyzing, and simulating (very) flexible aircraft in free flight considering coupled nonlinear structural and rigid-body dynamics, aerodynamics, and controls.

The baseline UM/NAST framework allows modeling of aerodynamic effects of leading- and trailing-edge control surfaces. However, additional capabilities were required to address the thesis objectives, such as the ability to model FFWTs and evaluate ride qualities. Therefore, various theoretical and computational enhancements were developed as part of this work. This chapter first describes the formulation of the baseline computational framework in Sec. 2.1. This introduces the quantities required to describe the key theoretical and computational enhancements in Sec. 2.2.1-2.2.3.

2.1 Computational Framework

UM/NAST represents aircraft as sets of beam-type members associated with different components (wing, fuselage, etc.) that undergo arbitrary structural deflections. The framework describes structural deflections using a strain-based, geometrically exact beam formulation [96, 97] that assumes elemental strains (axial extension, bending and torsion curvatures) as the independent structural degrees of freedom (DOFs) and recovers the deformed shape by marching nonlinear kinematic relations in space.

To model aircraft in free flight, UM/NAST augments the structural DOFs with rigid-body DOFs associated with the position, attitude, and linear/angular velocity of the body-fixed frame in the inertial frame. To model unsteady wake effects, the framework adds a set of additional DOFs which can come from inflow theory of Peters et al. [98], unsteady vortex-lattice method (UVLM),

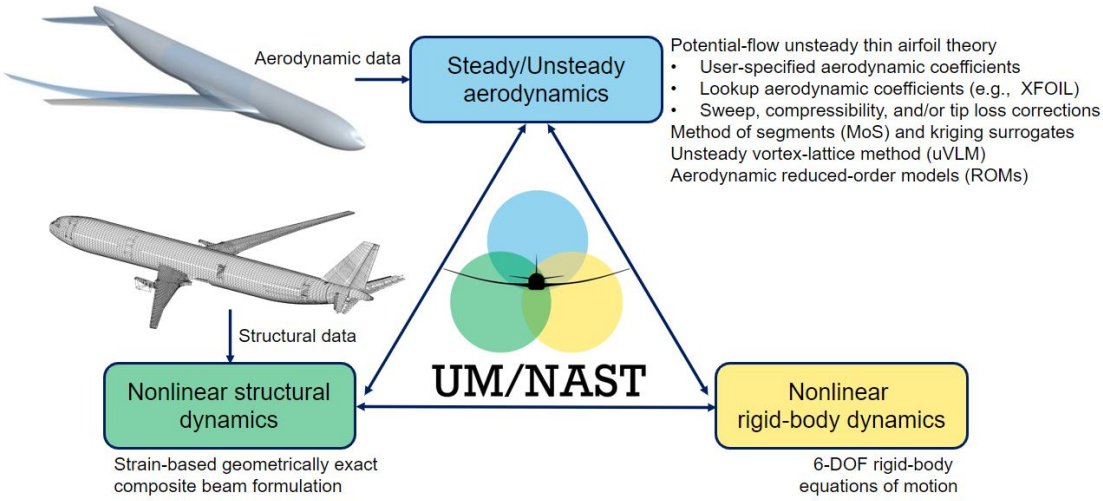

Figure 2.1: UM/NAST simulation framework.

or reduced-order models.

UM/NAST can handle different load types such as gravity, point or distributed forces and moments, and aerodynamic loads, which are computed using a spectrum of aerodynamic models (see Fig. 2.1). The models presented in this work use the method of segments [91], a quasi-steady surrogate aerodynamic modeling technique based on high-fidelity computational fluid dynamics (CFD) data. The method of segments builds on strip-theory assumptions: the aerodynamic coefficients at the cross sections of the UM/NAST structural nodes are assumed to depend only on the local flow and control parameters (effective angle of attack, Mach number, flap deflections, etc.). The coefficient values at each cross section are predicted by a kriging surrogate model that fits a coefficient database obtained by "slicing" the full-vehicle, steady-state CFD solutions for various parameter combinations. The method of segments is chosen here due to its ability to capture transonic effects with computational effort suited for design exploration studies in this work.

2.1.1 Reference Frames and State Variables

UM/NAST describes the motion of an aircraft in free flight in terms of the rigid-body motion of a body-fixed frame B relative to the inertial frame G as shown in Fig. 2.2. The B frame origins at an arbitrary aircraft point and is such that the unit vector B_x points downstream, B_y toward the right wingtip, and $B_z = B_x \times B_y$ completes the right-hand triad. The motion of the B frame within the

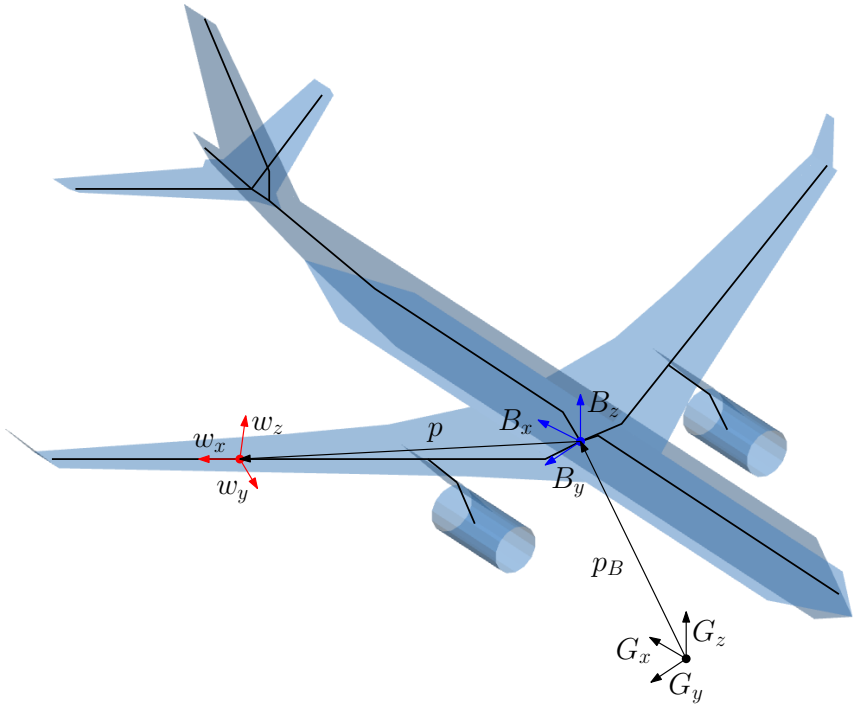

Figure 2.2: Reference frames used for describing aircraft motion.

G frame is described by the column vectors:

$$b = \begin{Bmatrix} p_B \\ \theta_B \end{Bmatrix}, \quad \beta = \begin{Bmatrix} v_B \\ \omega_B \end{Bmatrix}, \quad \dot{\beta} = \begin{Bmatrix} \dot{v}_B \\ \dot{\omega}_B \end{Bmatrix}. \tag{2.1}$$

The quantities p_B and θ_B in Eq. (2.1) are the position and orientation of the B frame relative to the G frame; v_B and ω_B are the B-frame linear and angular velocities; and $\dot{v}_B$ and $\dot{\omega}_B$ are the B-frame linear and angular accelerations respectively. The column vectors in Eq. (2.1) are all resolved in the B frame.

Elastic displacements relative to the B frame are described by modeling the aircraft as a set of geometrically nonlinear beams discretized as three-noded finite elements [96, 97]. The position and orientation at a generic point of the reference axis along a beam member is described by the 12-component column vector with components in the B frame:

$$h(s)^T = \left\{ p(s)^T, w_x(s)^T, w_y(s)^T, w_z(s)^T \right\}. \tag{2.2}$$

The quantity s in Eq. (2.2) is the local curvilinear abscissa along the beam reference axis; p is the origin of a local structural frame w that evolves along the beam reference axis with respect to the

B frame; and the unit vectors w_x, w_y, and w_z define the local frame w fixed at the location s. The w frame origins at the point p and is oriented such that w_x is along the beam reference axis, w_y points toward the leading edge, and $w_z = w_x \times w_y$.

While displacement-based formulations assume nodal displacements as the flexible (elastic) DOFs, UM/NAST uses element strains [97]. A strain-based beam finite element is described by the 4-component strain vector:

$$\varepsilon_e^T = \left\{\epsilon_x, \kappa_x, \kappa_y, \kappa_z\right\}. \tag{2.3}$$

The quantity ϵ_x in Eq. (2.3) is the beam reference axis axial extension and κ_x, κ_y, and κ_z are the twist, out-of-plane, and in-plane bending curvatures. The following quantities dependent on the strain vector (2.3) are introduced for the element:

$$h_e^T = \left\{h_{e1}^T, h_{e2}^T, h_{e3}^T\right\}, \quad \theta_e^T = \left\{\theta_{e1}^T, \theta_{e2}^T, \theta_{e3}^T\right\}. \tag{2.4}$$

The column vectors h_{e1}, h_{e2}, and h_{e3} in Eq. (2.4) are the h vectors evaluated at the three element nodes; the column vectors θ_{e1}, θ_{e2}, and θ_{e3} list the nodal rotations about the beam reference axis at those nodes. Assuming N finite elements, the independent and dependent global column vectors for the entire model are given by

$$\varepsilon^T = \left\{\varepsilon_1^T, \ldots, \varepsilon_N^T\right\}, \quad h^T = \left\{h_1^T, \ldots, h_N^T\right\}, \quad \theta^T = \left\{\theta_1^T, \ldots, \theta_N^T\right\}. \tag{2.5}$$

2.1.2 Governing Equations

The governing equations are derived using the principle of virtual work:

$$\delta W = \int_V \delta u^T f \, dV = 0. \tag{2.6}$$

The quantity V in Eq. (2.6) is the material volume, δu the local virtual displacement, and f the corresponding local load vector. Because the aircraft is described as a set of beam members with known cross-sectional stiffness and mass distributions, Eq. (2.6) reduces to a one-dimensional integration along the beam reference axis of each member that can be conducted based on the assumed discretization.

The virtual work of the internal loads on a beam element is given by [96, 97]:

$$\delta W_e^{int} = -\delta h_e^T M_e \ddot{h}_e - \delta \varepsilon_e^T C_e \dot{\varepsilon}_e - \delta \varepsilon_e^T K_e (\varepsilon_e - \varepsilon_e^0). \tag{2.7}$$

These terms account for the inertial, damping, and elastic loads. The quantity M_e in Eq. (2.7) is a 36×36 cross-sectional mass matrix, C_e is the 4×4 element stiffness-proportional damping matrix,

ε_e^0 is the initial strain vector, and

$$K_e = \begin{bmatrix} K_{11} & K_{12} & K_{13} & K_{14} \\ K_{12} & K_{22} & K_{23} & K_{24} \\ K_{13} & K_{23} & K_{33} & K_{34} \\ K_{14} & K_{24} & K_{34} & K_{44} \end{bmatrix} \tag{2.8}$$

is the 4×4 element stiffness matrix of the generally non-isotropic beam constitutive relation of the strain-based formulation of Su and Cesnik [97]. The diagonal terms K_{11}, K_{22}, K_{33}, and K_{44} are the beam axial, torsion, out-of-plane bending, and in-plane bending stiffness constants; the off-diagonal terms K_{ij} are generally non-zero and describe coupling terms between strain measures.

The virtual work due to the (external) applied loads on a beam element is [96, 97]:

$$\delta W_e^{ext} = \delta p_e^T (B_e^F F_e^{distr} + F_e^{pt}) + \delta\theta_e^T (B_e^M M_e^{distr} + M_e^{pt}) - \delta h_e^T N_e \, g \tag{2.9}$$

and includes the effects of distributed/concentrated forces and moments along with the effect of the self-weight due to the gravity acceleration vector g. The 9-component column vector p_e in Eq. (2.9) lists the p vectors evaluated at the element nodes; the influence matrices B_e^F, B_e^M, and N_e result from the integration of distributed forces and moments along the element beam reference axis [96, 97]; and the B-frame components of distributed/concentrated forces and distributed/concentrated moments applied at the element nodes are listed in the 9-component column vectors:

$$F_e^{distr} = \left\{ \begin{array}{c} F_{e1}^{distr} \\ F_{e2}^{distr} \\ F_{e3}^{distr} \end{array} \right\}, \quad F_e^{pt} = \left\{ \begin{array}{c} F_{e1}^{pt} \\ F_{e2}^{pt} \\ F_{e3}^{pt} \end{array} \right\}, \quad M_e^{distr} = \left\{ \begin{array}{c} M_{e1}^{distr} \\ M_{e2}^{distr} \\ M_{e3}^{distr} \end{array} \right\}, \quad M_e^{pt} = \left\{ \begin{array}{c} M_{e1}^{pt} \\ M_{e2}^{pt} \\ M_{e3}^{pt} \end{array} \right\}. \tag{2.10}$$

The total virtual work is the sum of the contributions from the N elements:

$$\begin{aligned} \delta W &= \delta W^{int} + \delta W^{ext}, \\ \delta W^{int} &= \delta h^T M \ddot{h} + \delta\varepsilon^T C \dot{\varepsilon} + \delta\varepsilon^T K(\varepsilon - \varepsilon^0), \\ \delta W^{ext} &= \delta p^T (B^F F^{distr} + F^{pt}) + \delta\theta^T (B^M M^{distr} + M^{pt}) - \delta h^T N \, . \end{aligned} \tag{2.11}$$

The terms in Eq. (2.11) are obtained by assembling the elemental contributions [97]. Next, the

variations and time derivatives in the dependent DOFs are written as:

$$\begin{aligned}
\delta h &= J_{h\varepsilon}\delta\varepsilon + J_{hb}\delta b, & \delta\theta &= J_{\theta\varepsilon}\delta\varepsilon + J_{\theta b}\delta b,\\
dh &= J_{h\varepsilon}d\varepsilon + J_{hb}db, & d\theta &= J_{\theta\varepsilon}d\varepsilon + J_{\theta b}db,\\
\dot{h} &= J_{h\varepsilon}\dot{\varepsilon} + J_{hb}\beta, & \dot{\theta} &= J_{\theta\varepsilon}\dot{\varepsilon} + J_{\theta b}\beta,\\
\ddot{h} &= J_{h\varepsilon}\ddot{\varepsilon} + \dot{J}_{h\varepsilon}\dot{\varepsilon} + J_{hb}\dot{\beta} + \dot{J}_{hb}\beta, & \ddot{\theta} &= J_{\theta\varepsilon}\ddot{\varepsilon} + \dot{J}_{\theta\varepsilon}\dot{\varepsilon} + J_{\theta b}\dot{\beta} + \dot{J}_{\theta b}\beta.
\end{aligned} \tag{2.12}$$

The Jacobians in Eq. (2.12) are obtained from the strain-based kinematics [97]:

$$J_{h\varepsilon} = \frac{dh}{d\varepsilon}\,, \quad J_{hb} = \frac{dh}{db}\,, \quad J_{\theta\varepsilon} = \frac{d\theta}{d\varepsilon}\,, \quad J_{\theta b} = \frac{d\theta}{db}. \tag{2.13}$$

Substituting Eq. (2.12) into Eq. (2.11) gives the following equations in the flexible (strain) and rigid-body DOFs:

$$\begin{aligned}
&\begin{bmatrix} M_{FF}(\varepsilon) & M_{FB}(\varepsilon) \\ M_{BF}(\varepsilon) & M_{BB}(\varepsilon) \end{bmatrix} \begin{Bmatrix} \ddot{\varepsilon} \\ \dot{\beta} \end{Bmatrix} + \begin{bmatrix} C_{FF}(\varepsilon,\dot{\varepsilon},\beta) & C_{FB}(\varepsilon,\dot{\varepsilon},\beta) \\ C_{BF}(\varepsilon,\dot{\varepsilon},\beta) & C_{BB}(\varepsilon,\dot{\varepsilon},\beta) \end{bmatrix} \begin{Bmatrix} \dot{\varepsilon} \\ \beta \end{Bmatrix} \\
&\qquad + \begin{bmatrix} K_{FF} & 0 \\ 0 & 0 \end{bmatrix} \begin{Bmatrix} \varepsilon \\ b \end{Bmatrix} = \begin{Bmatrix} R_F(\ddot{\varepsilon},\dot{\varepsilon},\varepsilon,\dot{\beta},\beta,\zeta,\lambda) \\ R_B(\ddot{\varepsilon},\dot{\varepsilon},\varepsilon,\dot{\beta},\beta,\zeta,\lambda) \end{Bmatrix},
\end{aligned} \tag{2.14}$$

where the independent DOFs and their time derivatives are listed in the column vectors:

$$q = \begin{Bmatrix} \varepsilon \\ b \end{Bmatrix} = \begin{Bmatrix} \varepsilon \\ p_B \\ \theta_B \end{Bmatrix}, \quad \dot{q} = \begin{Bmatrix} \dot{\varepsilon} \\ \beta \end{Bmatrix} = \begin{Bmatrix} \dot{\varepsilon} \\ v_B \\ \omega_B \end{Bmatrix}, \quad \ddot{q} = \begin{Bmatrix} \ddot{\varepsilon} \\ \dot{\beta} \end{Bmatrix} = \begin{Bmatrix} \ddot{\varepsilon} \\ \dot{v}_B \\ \dot{\omega}_B \end{Bmatrix}. \tag{2.15}$$

In Eqs. (2.14) and (2.15), ε is the model strain vector, v_B and ω_B are the linear and angular velocities, respectively, of the B frame with respect to the G frame and the vector b consists of their time integrals. The generalized mass and damping submatrix blocks are given by:

$$\begin{aligned}
M_{FF}(\varepsilon) &= J_{h\varepsilon}^T M J_{h\varepsilon}, & M_{FB}(\varepsilon) &= J_{h\varepsilon}^T M J_{hb},\\
M_{BF}(\varepsilon) &= J_{hb}^T M J_{h\varepsilon}, & M_{BB}(\varepsilon) &= J_{hb}^T M J_{hb},\\
C_{FF}(\varepsilon,\dot{\varepsilon},\beta) &= J_{h\varepsilon}^T M \dot{J}_{h\varepsilon} + C, & C_{FB}(\varepsilon,\dot{\varepsilon},\beta) &= J_{h\varepsilon}^T M H_{hb} + 2J_{h\varepsilon}^T M \dot{J}_{hb},\\
C_{BF}(\varepsilon,\dot{\varepsilon},\beta) &= J_{hb}^T M \dot{J}_{h\varepsilon}, & C_{BB}(\varepsilon,\dot{\varepsilon},\beta) &= J_{hb}^T M H_{hb} + 2J_{hb}^T M \dot{J}_{hb},
\end{aligned} \tag{2.16}$$

with

$$H_{hb} = \begin{bmatrix} \tilde{\omega}_B & \dots & 0 \\ \vdots & \ddots & \vdots \\ 0 & \dots & \tilde{\omega}_B \end{bmatrix} J_{hb}. \tag{2.17}$$

Here, $\tilde{\omega}_B$ is the 3×3 skew-symmetric matrix representing the cross-product by ω_B. The only non-zero block in the generalized stiffness matrix is $K_{FF} = K$. Assuming linear stress-strain constitutive relations, this matrix is constant with respect to the flexible DOFs in the strain-based formulation [97]. The generalized load vectors in Eq. (2.14) are given by:

$$\begin{aligned} R_F(\ddot{\varepsilon}, \dot{\varepsilon}, \varepsilon, \dot{\beta}, \beta, \zeta, \lambda) &= J_{p\varepsilon}^T (B_F F^{distr} + F^{pt}) + J_{\theta\varepsilon}^T (B_M M^{distr} + M^{pt}) - J_{h\varepsilon}^T N g + K_{FF}\, \varepsilon^0, \\ R_B(\ddot{\varepsilon}, \dot{\varepsilon}, \varepsilon, \dot{\beta}, \beta, \zeta, \lambda) &= J_{pb}^T (B_F F^{distr} + F^{pt}) + J_{\theta b}^T (B_M M^{distr} + M^{pt}) - J_{hb}^T N g. \end{aligned} \tag{2.18}$$

Aerodynamics loads are included in Eq. (2.18) as distributed loads [96]. The quantity ζ in Eq. (2.18) is the quaternion vector and λ is a vector of inflow states that may be included to describe unsteady aerodynamic effects (e.g., according to the theory of Peters et al. [98]). For free flight conditions, Eq. (2.14) is augmented with the B-frame propagation equations [96]:

$$\dot{\zeta} = -\frac{1}{2}\Omega_\zeta(\beta)\zeta, \qquad \dot{P}_B = \begin{bmatrix} C^{GB}(\zeta) & 0 \end{bmatrix} \beta. \tag{2.19}$$

The quantity C^{GB} in Eq. (2.19) is a rotation matrix from the B to the G frame and P_B denotes the position of the origin of the B frame resolved in the G frame. The problem is completed by evolution equations for the unsteady aerodynamic states in the vector λ that can be cast in the form:

$$\dot{\lambda} = F_1(\varepsilon) \begin{Bmatrix} \ddot{\varepsilon} \\ \dot{\beta} \end{Bmatrix} + F_2(\varepsilon) \begin{Bmatrix} \dot{\varepsilon} \\ \beta \end{Bmatrix} + F_3 \lambda. \tag{2.20}$$

The coefficient matrices F_1, F_2, and F_3 in Eq. (2.20) depend on the finite-state unsteady aerodynamic model employed. The detailed derivation of Eqs. (2.14) and (2.15) is reported in Ref. [96]. Building on this fundamental description, additional modifications are implemented in the framework as detailed in the following Section 2.2.

2.1.3 Kinematics

UM/NAST solves for element strains as the independent flexible DOFs and recovers nodal displacements by integrating the kinematic relations. The h vector and the ε vector at a generic beam

reference axis point are related by:

$$\frac{\partial h(s)}{\partial s} = \mathbb{K}(s)h(s) = \begin{bmatrix} 0 & 1+\epsilon_x(s) & 0 & 0 \\ 0 & 0 & \kappa_z(s) & -\kappa_y(s) \\ 0 & -\kappa_z(s) & 0 & \kappa_x(s) \\ 0 & \kappa_y(s) & -\kappa_x(s) & 0 \end{bmatrix} h(s), \tag{2.21}$$

where each block in $\mathbb{K}(s)$ is a 3×3 diagonal matrix. Assuming constant strain along each element, Eq. (2.21) gives:

$$h(s) = e^{\mathbb{K}(s-s_0)} h_0 = e^{G(s)} h_0. \tag{2.22}$$

The quantity h_0 in Eq. (2.22) is the known solution at the element starting point s_0. The discrete form of Eq. (2.22) for the nth element is:

$$h_{n1} = D_{nm} h_{m3}, \quad h_{n2} = e^{G_n} h_{n1}, \quad h_{n3} = e^{G_n} h_{n2}. \tag{2.23}$$

The quantity h_{m3} in Eq. (2.23) is the h vector at the last node of the mth element that coincides with the first node of the nth element; D_{nm} is a 12×12 transformation matrix that accounts for geometrical discontinuities in the beam reference axis due to changes in twist, dihedral angle, or sweep between the mth and nth elements. $G_n = \mathbb{K}_n \Delta s_n / 2$, where $\mathbb{K}_n$ is the matrix in Eq. (2.21) evaluated for the nth element of length Δs_n. Once the strain vector ε is known at a solution step, the deformed configuration is obtained by writing Eq. (2.23) for all the elements of a member (or group of members) and by solving the resulting system of algebraic equations [97].

2.2 Computational Framework Enhancements

This section describes the key enhancements to the UM/NAST framework to support the thesis objectives. Following enhancements were developed as part of this work:

- Modeling of FFWTs
- Ride quality metric evaluation
- Linearized kinematics
- Fuselage aerodynamics
- Modeling of flexible control surfaces

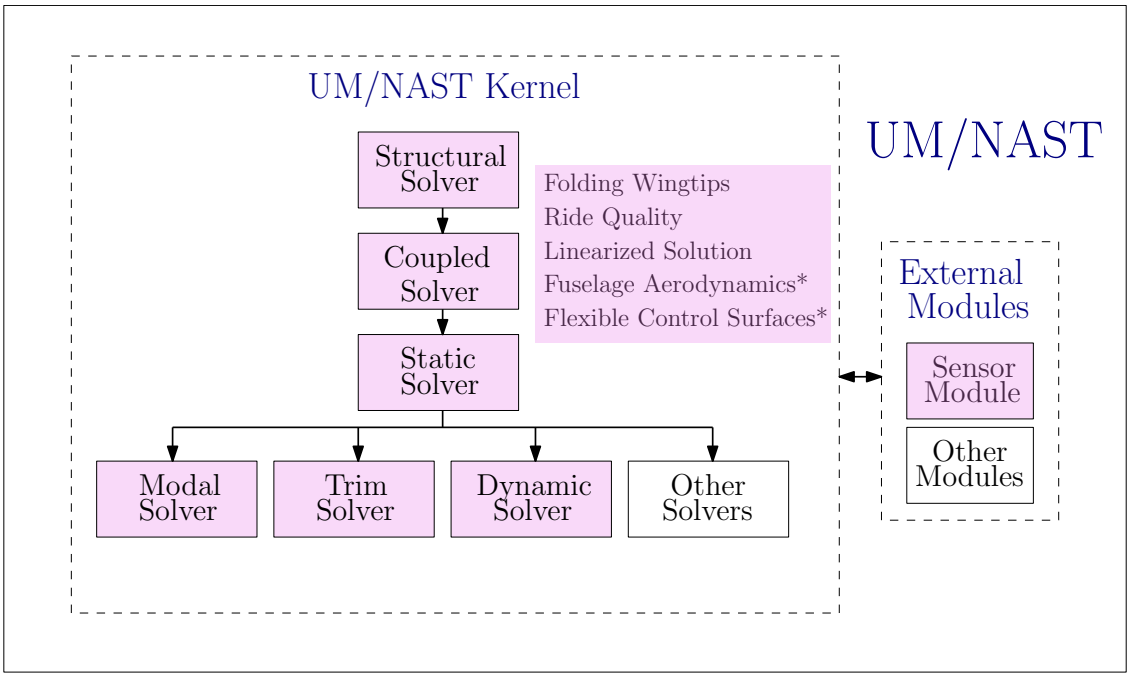

Figure 2.3: UM/NAST framework enhancements.

Figure 2.3 shows the various components of the baseline UM/NAST framework that were modified for the above listed developments.

The numerical investigations in this dissertation use the first three features. Other features were developed to capture additional aerostructural effects of different aircraft components. However, they were not considered in the studies since they require additional supporting data (fuselage aerodynamics) and enhancements (time integration scheme improvement for flexible control surfaces). The details for these two features are described in Appendix A and B respectively.

2.2.1 Flared Folding Wingtips

This work extended UM/NAST with the ability to model FFWTs (leading- and trailing-edge control surfaces modeling was available in the baseline framework). This enables investigating their impact on maneuverability, load alleviation, and ride qualities within a coupled nonlinear aeroelastic-flight dynamics framework. The theoretical developments are described in Sec. 2.2.1.1 followed by the implementation details in Sec. 2.2.1.2.

2.2.1.1 Theoretical Development

FFWTs are modeled as beam members able to rotate about a user-specified hinge line passing through their first node, coincident with the end node of the fixed parent member. The relative

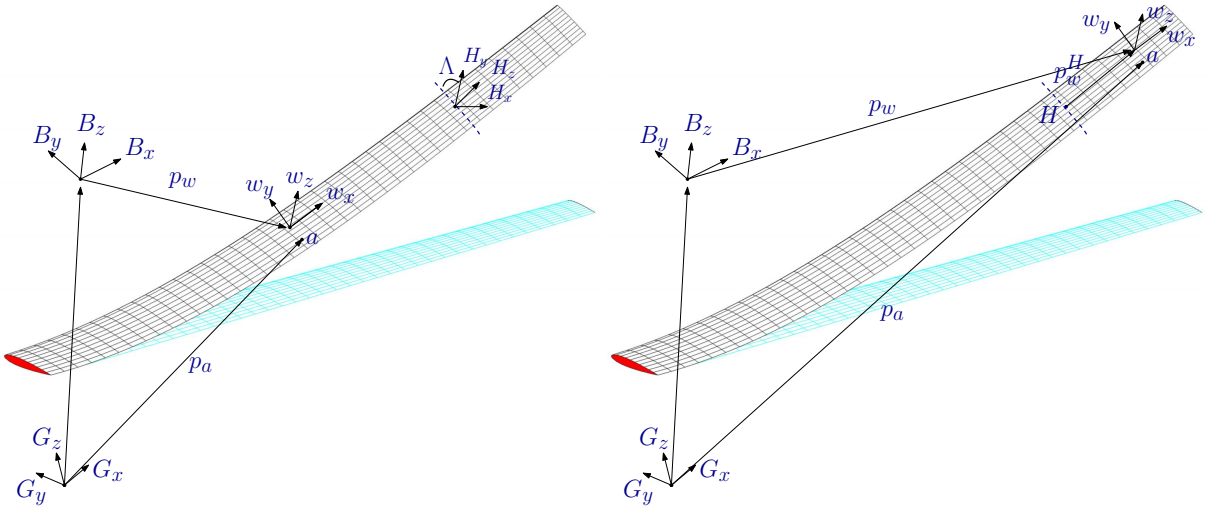

(a) Generic point in a wing member

(b) Generic point in a wingtip member

Figure 2.4: Reference frames for FFWT.

rotations between the FFWT and the parent wing are determined by the moment equilibrium about the hinge. These rotations are modeled by defining a local frame H at the starting node of each flexible FFWT that has the H_y axis aligned with the hinge line (see Fig. 2.4). The rotation angles and angular velocity components of the H frame relative to the B frame are listed in the 3×1 column vectors θ_H and ω_H, respectively:

$$\theta_H = \{\theta_{H_x}, \theta_{H_y}, \theta_{H_z}\}^T, \quad \omega_H = \{\omega_{H_x}, \omega_{H_y}, \omega_{H_z}\}^T. \tag{2.24}$$

The quantity θ_H in Eq. (2.24) defines the orientation of the H frame with respect to the B frame; ω_H is the angular velocity; and $\dot{\omega}_H$ the angular acceleration. All these quantities are resolved in the B frame.

According to this description, each FFWT corresponds to three additional equations to be solved. However, the H frame orientation is described by a scalar equation in the H frame, as only rotations about the hinge line are of interest here. The additional equations in the framework are first derived in the body frame for easier extension and implementation of the formulation. They are then rewritten in the local H frame, to finally have one additional equation for each FFWT.

The governing equations are derived below considering an isolated wing composed of a fixed parent member and a FFWT member. The formulation can be generalized to aircraft where multiple wingtips are present. The internal virtual work (2.11) is derived for the fixed member first. The virtual work due to the inertia is derived starting from the position p_a (see Fig. 2.4), velocity

$\dot{p}_a$, and acceleration $\ddot{p}_a$ of a point a at an arbitrary cross section:

$$\begin{aligned}
p_a &= p_B + p + yw_y + zw_z, \\
\dot{p}_a &= \dot{p}_B + \dot{p} + y\dot{w}_y + z\dot{w}_z + \tilde{\omega}_B(p_B + p + yw_y + zw_z), \\
\ddot{p}_a &= \ddot{p}_B + \ddot{p} + y\ddot{w}_y + z\ddot{w}_z + \dot{\tilde{\omega}}_B(p_B + p + yw_y + zw_z) + 2\tilde{\omega}_B(\dot{p}_B + \dot{p} + y\dot{w}_y + z\dot{w}_z) \\
&\quad + \tilde{\omega}_B\tilde{\omega}_B(p + yw_y + zw_z).
\end{aligned} \tag{2.25}$$

The quantity p in Eq. (2.25) is the position of the beam reference axis point (origin of the local frame w) at the cross-section that contains a with respect to the origin of the B frame, which is part of the h vector (2.2). The infinitesimal virtual work on a unit volume is

$$\delta W^{int} = \delta p_a^T dF_a = \delta p_a^T (\rho \ddot{p}_a dA ds). \tag{2.26}$$

The virtual work due to the inertia at the curvilinear abscissa s of the current cross section is obtained by integrating Eq. (2.26) over the cross-sectional area:

$$\begin{aligned}
\delta W^{int}(s) \;= -\delta h^T(s) M(s) \Bigg(& \begin{Bmatrix} \ddot{p} \\ \ddot{w}_x \\ \ddot{w}_y \\ \ddot{w}_z \end{Bmatrix} + \begin{bmatrix} I_3 & \tilde{p}^T \\ 0_3 & \tilde{w}_x^T \\ 0_3 & \tilde{w}_y^T \\ 0_3 & \tilde{w}_z^T \end{bmatrix} \dot{\beta} + \begin{bmatrix} \tilde{\omega}_B & 0 & 0 & 0 \\ 0 & \tilde{\omega}_B & 0 & 0 \\ 0 & 0 & \tilde{\omega}_B & 0 \\ 0 & 0 & 0 & \tilde{\omega}_B \end{bmatrix} \begin{bmatrix} I_3 & \tilde{p}^T \\ 0_3 & \tilde{w}_x^T \\ 0_3 & \tilde{w}_y^T \\ 0_3 & \tilde{w}_z^T \end{bmatrix} \beta \\
& + 2 \begin{bmatrix} 0_3 & \dot{\tilde{p}}^T \\ 0_3 & \dot{\tilde{w}}_x^T \\ 0_3 & \dot{\tilde{w}}_y^T \\ 0_3 & \dot{\tilde{w}}_z^T \end{bmatrix} \beta \Bigg).
\end{aligned} \tag{2.27}$$

The quantity $M(s)$ in Eq. (2.27) is the cross-sectional inertia matrix:

$$M(s) = \begin{bmatrix} m & 0 & mr_y & mr_z \\ 0 & 0 & 0 & 0 \\ mr_y & 0 & I_{zz} & I_{yz} \\ mr_z & 0 & I_{zy} & I_{yy} \end{bmatrix}. \tag{2.28}$$

Each block in Eq. (2.28) is a 3×3 identity matrix. The quantity m is the mass per unit span at each cross section; (r_y, r_z) is the position of the cross-sectional mass center in the w frame; and I_{ij} are the cross-sectional mass moments of inertia about the local w_y and w_z axes.

Using the Jacobians in Eq. (2.12), Eq. (2.26) can be cast as:

$$\begin{aligned}\delta W^{int}(s) \quad &= -\{\delta\varepsilon^T(s)\ \ \delta b^T\}\left(\begin{bmatrix} J_{h\varepsilon}^T M(s) J_{h\varepsilon} & J_{h\varepsilon}^T M(s) J_{hb} \\ J_{hb}^T M(s) J_{h\varepsilon} & J_{hb}^T M(s) J_{hb}\end{bmatrix}\begin{Bmatrix}\ddot{\varepsilon}(s)\\ \dot{\beta}\end{Bmatrix}\right. \\ &\left. + \begin{bmatrix} J_{h\varepsilon}^T M(s) \dot{J}_{h\varepsilon} & J_{h\varepsilon}^T M(s) H_{hb} + 2 J_{h\varepsilon}^T M(s) \dot{J}_{hb} \\ J_{hb}^T M(s) \dot{J}_{h\varepsilon} & J_{hb}^T M(s) H_{hb} + 2 J_{hb}^T M(s) \dot{J}_{hb}\end{bmatrix}\begin{Bmatrix}\dot{\varepsilon}(s)\\ \beta\end{Bmatrix}\right).\end{aligned} \tag{2.29}$$

If the arbitrary point a lies on a folding wingtip, its position and orientation also depend on the relative rotations of the H frame. Hence, its velocity and acceleration are given by:

$$\begin{aligned}\dot{p}_a^{wt} &= \dot{p}_B + \dot{p} + y\dot{w}_y + z\dot{w}_z + \tilde{\omega}_B(p_B + p + yw_y + zw_z) + \tilde{\omega}_H(p^H + yw_y + zw_z) \\ &= \dot{p}_a + \tilde{\omega}_H(p^H + yw_y + zw_z), \\ \ddot{p}_a^{wt} &= \ddot{p}_a + \dot{\tilde{\omega}}_H(p^H + yw_y + zw_z) + \tilde{\omega}_H(\dot{p}^H + y\dot{w}_y + z\dot{w}_z) + \tilde{\omega}_H\tilde{\omega}_H(p^H + yw_y + zw_z).\end{aligned} \tag{2.30}$$

The contributions $\dot{p}_a$ and $\ddot{p}_a$ in Eq. (2.30) are given by Eq. (2.25) and the other terms are due to relative rotations about the hinge line. The quantity p^H is the position of the origin of the H frame with respect to the B, with components resolved in the B frame.

The above terms lead to the following additional virtual work contribution for the folding wingtip member:

$$\delta W_{wt}^{int}(s) = -\delta h^T(s) M(s)\left(\begin{bmatrix}\tilde{p}^T\\ \tilde{w}_x^T\\ \tilde{w}_y^T\\ \tilde{w}_z^T\end{bmatrix}\dot{\omega}_H + \begin{bmatrix}\tilde{\omega}_H & 0 & 0 & 0\\ 0 & \tilde{\omega}_H & 0 & 0\\ 0 & 0 & \tilde{\omega}_H & 0\\ 0 & 0 & 0 & \tilde{\omega}_H\end{bmatrix}\begin{bmatrix}\tilde{p}^T\\ \tilde{w}_x^T\\ \tilde{w}_y^T\\ \tilde{w}_z^T\end{bmatrix}\omega_H + \begin{bmatrix}\dot{\tilde{p}}^T\\ \dot{\tilde{w}}_x^T\\ \dot{\tilde{w}}_y^T\\ \dot{\tilde{w}}_z^T\end{bmatrix}\omega_H\right). \tag{2.31}$$

The additional DOFs introduced by the hinge also modify the Jacobians in Eq. (2.12) as:

$$\begin{aligned}\delta h &= J_{h\varepsilon}\delta\varepsilon + J_{hb}\delta b + J_{h\theta_H}\delta\theta_H, & \delta\theta &= J_{\theta\varepsilon}\delta\varepsilon + J_{\theta b}\delta b + J_{\theta\theta_H}\delta\theta_H, \\ dh &= J_{h\varepsilon}d\varepsilon + J_{hb}db + J_{h\theta_H}d\theta_H, & d\theta &= J_{\theta\varepsilon}d\varepsilon + J_{\theta b}db + J_{\theta\theta_H}d\theta_H, \\ \dot{h} &= J_{h\varepsilon}\dot{\varepsilon} + J_{hb}\beta + J_{h\theta_H}\dot{\theta}_H, & \dot{\theta} &= J_{\theta\varepsilon}\dot{\varepsilon} + J_{\theta b}\beta + J_{\theta\theta_H}\dot{\theta}_H, \\ \ddot{h} &= J_{h\varepsilon}\ddot{\varepsilon} + \dot{J}_{h\varepsilon}\dot{\varepsilon} + J_{hb}\dot{\beta} & \ddot{\theta} &= J_{\theta\varepsilon}\ddot{\varepsilon} + \dot{J}_{\theta\varepsilon}\dot{\varepsilon} + J_{\theta b}\dot{\beta} \\ &\quad + \dot{J}_{hb}\beta + J_{h\theta_H}\ddot{\theta}_H + \dot{J}_{h\theta_H}\dot{\theta}_H, & &\quad + \dot{J}_{\theta b}\beta + J_{\theta\theta_H}\ddot{\theta}_H + \dot{J}_{\theta\theta_H}\dot{\theta}_H.\end{aligned} \tag{2.32}$$

Substituting Eq. (2.32) into Eq. (2.31) and adding the resulting virtual work to Eq. (2.29) gives the total internal virtual work due to the inertia for a folding wingtip:

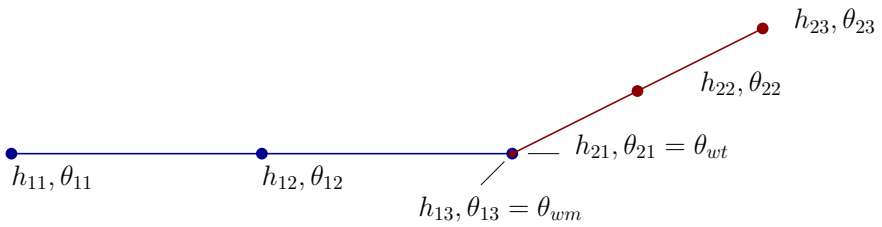

Figure 2.5: Wing and folding wingtip member discretized in one element each.

$$\delta W^{int}(s) = -\{\delta\varepsilon^T(s) \;\; \delta b^T \;\; \delta\theta_H^T\}\Bigg(\begin{bmatrix} J_{h\varepsilon}^T M(s) J_{h\varepsilon} & J_{h\varepsilon}^T M(s) J_{hb} & J_{h\varepsilon}^T M(s) J_{h\theta_H} \\ J_{hb}^T M(s) J_{h\varepsilon} & J_{hb}^T M(s) J_{hb} & J_{hb}^T M(s) J_{h\theta_H} \\ J_{h\theta_H}^T M(s) J_{h\varepsilon} & J_{h\theta_H}^T M(s) J_{hb} & J_{h\theta_H}^T M(s) J_{h\theta_H} \end{bmatrix} \begin{Bmatrix} \ddot{\varepsilon}(s) \\ \dot{\beta} \\ \dot{\omega}_H \end{Bmatrix} +$$
$$\Bigg(\begin{bmatrix} J_{h\varepsilon}^T M(s) \dot{J}_{h\varepsilon} & J_{h\varepsilon}^T M(s) H_{hb} & J_{h\varepsilon}^T M(s) H_{h\theta_H} \\ J_{hb}^T M(s) \dot{J}_{h\varepsilon} & J_{hb}^T M(s) H_{hb} & J_{hb}^T M(s) H_{h\theta_H} \\ J_{h\theta_H}^T M(s) \dot{J}_{h\varepsilon} & J_{h\theta_H}^T M(s) H_{hb} & J_{h\theta_H}^T M(s) H_{h\theta_H} \end{bmatrix} +$$
$$\begin{bmatrix} 0 & 2J_{h\varepsilon}^T M(s) \dot{J}_{hb} & J_{h\varepsilon}^T M(s) \dot{J}_{h\theta_H} \\ 0 & 2J_{hb}^T M(s) \dot{J}_{hb} & J_{hb}^T M(s) \dot{J}_{h\theta_H} \\ 0 & 2J_{h\theta_H}^T M(s) \dot{J}_{hb} & J_{h\theta_H}^T M(s) \dot{J}_{h\theta_H} \end{bmatrix} \begin{Bmatrix} \dot{\varepsilon}(s) \\ \beta \\ \omega_H \end{Bmatrix}\Bigg)\Bigg). \tag{2.33}$$

In addition to the inertial effects, elastic reactions and dissipation may also occur due to the relative rotations about the hinge. These effects are described by a concentrated spring-damper element that adds the potential energy contribution:

$$\Pi^{sd} = \frac{1}{2} K^{sd} \left(\theta_{wt} - \theta_{wm} - \Delta\theta_0\right)^2 + \frac{1}{2} C^{sd} \left(\dot{\theta}_{wt} - \dot{\theta}_{wm}\right)^2 = \frac{1}{2} K^{sd} \left(\theta_H - \Delta\theta_0\right)^2 + \frac{1}{2} C^{sd} \dot{\theta}_H. \tag{2.34}$$

The quantity $\theta_{wt} = \theta_{wm} + \theta_H$ in Eq. (2.34) is the rotation vector at the starting node of the wingtip member; θ_{wm} is the rotation vector at the (coincident) ending node of the fixed parent member; and $\Delta\theta_0$ is relative initial rotation vector. All the rotation vectors are resolved in the B frame. Finally, the quantities K^{sd} and C^{sd} are the 3×3 stiffness and damping matrices associated with the spring-damper element at the hinge. The potential energy variation associated with Eq. (2.34) is written as:

$$\delta\Pi^s = \delta\theta_H^T \left[K^{sd} \left(\theta_H - \Delta\theta_0\right) + C^{sd} \dot{\theta}_H\right] = \delta\theta_H^T K^{sd} \theta_H + \left(\delta\theta_H\right)^T C^{sd} \dot{\theta}_H - \left(\delta\theta_H\right)^T K^{sd} \Delta\theta_0. \tag{2.35}$$

The governing equations including the folding wingtip can be obtained by extending Eq. (2.14)

with the contribution from the integral of Eq. (2.33) along the reference axis and by adding the effect of the spring-damper element at the hinge:

$$\begin{bmatrix} M_{FF} & M_{FB} & M_{FH} \\ M_{BF} & M_{BB} & M_{BH} \\ M_{HF} & M_{HB} & M_{HH} \end{bmatrix} \begin{Bmatrix} \ddot{\varepsilon} \\ \dot{\beta} \\ \dot{\omega}_H \end{Bmatrix} + \begin{bmatrix} C_{FF} & C_{FB} & C_{FH} \\ C_{BF} & C_{BB} & C_{BH} \\ C_{HF} & C_{HB} & C_{HH} \end{bmatrix} \begin{Bmatrix} \dot{\varepsilon} \\ \beta \\ \omega_H \end{Bmatrix} + \begin{bmatrix} K_{FF} & 0 & 0 \\ 0 & 0 & 0 \\ 0 & 0 & K_{HH} \end{bmatrix} \begin{Bmatrix} \varepsilon \\ b \\ \theta_H \end{Bmatrix} = \begin{Bmatrix} R_F \\ R_B \\ R_H \end{Bmatrix}. \tag{2.36}$$

The additional mass, damping, and stiffness matrix blocks due to the wingtip are:

$$\begin{aligned} M_{FH} &= J_{h\varepsilon}^T M J_{h\theta_H}, \quad & C_{FH} &= J_{h\varepsilon}^T M H_{h\theta_H} + J_{h\varepsilon}^T M \dot{J}_{h\theta_H}, \\ M_{BH} &= J_{hb}^T M J_{h\theta_H}, \quad & C_{BH} &= J_{hb}^T M H_{h\theta_H} + J_{hb}^T M(s) \dot{J}_{h\theta_H}, \\ M_{HH} &= J_{h\theta_H}^T M J_{h\theta_H}, \quad & C_{HH} &= J_{h\theta_H}^T M H_{h\theta_H} + 2 J_{h\theta_H}^T M \dot{J}_{h\theta_H} + C^{sd}, \\ K_{HH} &= K^{sd}, & R_H &= K^{sd}\theta_0 + J_{p\theta_H}^T (B_F F^{distr} + F^{pt}) + \\ & & & J_{\theta\theta_H}^T (B_M M^{distr} + M^{pt}) - J_{h\theta_H}^T N g. \end{aligned} \tag{2.37}$$

While the stiffness and damping matrices K_{HH} and D_{HH} associated with spring-damper element are resolved in the B frame, the element properties are more conveniently given in the H frame. For a single spring-damper element, one has:

$$K_{HH} = \left(D^{HB}\right)^T \begin{bmatrix} k_x^H & 0 & 0 \\ 0 & k_y^H & 0 \\ 0 & 0 & k_z^H \end{bmatrix} D^{HB}. \tag{2.38}$$

The quantities k_i^H $(i = x, y, z)$ in Eq. (2.38) are the spring elastic constants and D^{HB} is the rotation matrix from the B frame to the H frame. A relation similar to Eq. (2.38) can be derived for D_{HH}.

Now, as discussed in the introduction of the formulation, the H frame orientation can be described using a scalar equation since only the rotation about the local H_y axis is of interest here. Therefore, the equations associated with the FFWT are rewritten in the local H frame using the following scalar independent variables:

$$\theta_H^H = D^{HB}\theta_H^B, \quad \omega_H^H = D^{HB}\omega_H^B, \tag{2.39}$$

where D^{HB} is the rotation matrix from the B frame to the H function of the flare angle Λ (see

Fig. 1.3):

$$D^{HB^T} = \begin{Bmatrix} \sin(\Lambda) \\ \cos(\Lambda) \\ 0 \end{Bmatrix}. \tag{2.40}$$

With the above relations, the extended governing equations become

$$\begin{bmatrix} M_{FF} & M_{FB} & M_{FH}D^{BH} \\ M_{BF} & M_{BB} & M_{BH}D^{BH} \\ D^{HB}M_{HF} & D^{HB}M_{HB} & D^{HB}M_{HH}D^{BH} \end{bmatrix} \begin{Bmatrix} \ddot{\varepsilon} \\ \dot{\beta} \\ \dot{\omega_H}^H \end{Bmatrix} +$$

$$\begin{bmatrix} C_{FF} & C_{FB} & C_{FH}D^{BH} \\ C_{BF} & C_{BB} & C_{BH}D^{BH} \\ D^{HB}C_{HF} & D^{HB}C_{HB} & D^{HB}C_{HH}D^{BH} + D^H_{HH} \end{bmatrix} \begin{Bmatrix} \dot{\varepsilon} \\ \beta \\ \omega_H{}^H \end{Bmatrix} + \tag{2.41}$$

$$\begin{bmatrix} K_{FF} & 0 & 0 \\ 0 & 0 & 0 \\ 0 & 0 & K^H_{HH} \end{bmatrix} \begin{Bmatrix} \varepsilon \\ b \\ \theta^H_H \end{Bmatrix} = \begin{Bmatrix} R_F \\ R_B \\ R^H_H \end{Bmatrix}.$$

The quantities $K^H_{HH} = k^H_y$ and $D^H_{HH} = d^H_y$ in Eq. (2.41) are the scalar spring stiffness and damping constants associated with the hinge line (about H_y), expressed in the H frame. The set of additional equations given by Eq. (2.41) provides the formulation used to simulate a flexible aircraft with FFWTs that can be released during flight. Each of these devices adds its own rotation angle θ^H_H and the corresponding equation.

2.2.1.2 Implementation

The equation of motions derived for the FFWTs are implemented for a modal, static, trim and, dynamic simulations. The key implementation details are described in this section. The static solver solves for the following equation:

$$\begin{bmatrix} K_{FF} & 0 \\ 0 & K^H_{HH} \end{bmatrix} \begin{Bmatrix} \varepsilon \\ \theta^H_H \end{Bmatrix} = \begin{Bmatrix} R_F \\ R^H_H \end{Bmatrix}. \tag{2.42}$$

However, the hinge stiffness (K^H_{HH}) of a FFWT can be zero. Note, that the load due to the hinge (R^H_H) is a function of hinge rotation (θ^H_H) since the local angle of attack varies with the wingtip rotation. For such a case, the hinge equation to be solved is given by:

$$0 = R^H_H. \tag{2.43}$$

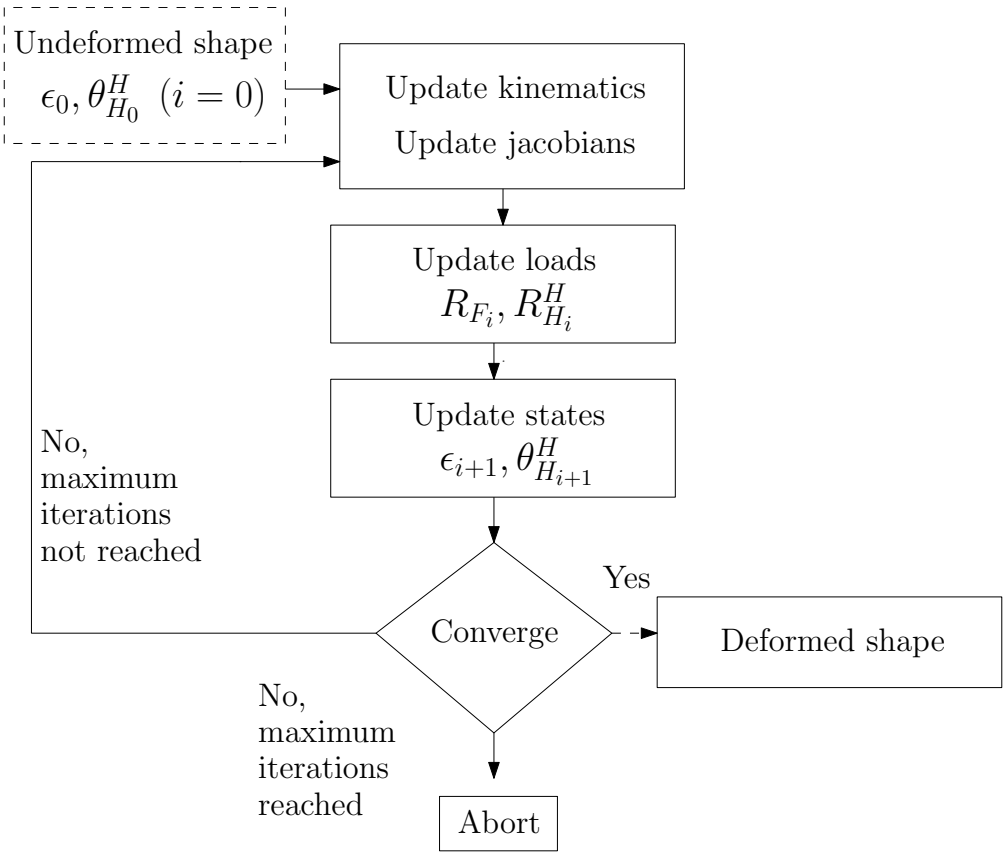

Figure 2.6: Modified iterative static solution for FFWTs.

Therefore, to solve for hinge rotation for the case of zero hinge stiffness, the implementation of the static equations is modified to:

$$\begin{bmatrix} K_{FF} & 0 \\ 0 & K^H_{HH} + K^* \end{bmatrix} \begin{Bmatrix} \varepsilon \\ \theta^H_H \end{Bmatrix} = \begin{Bmatrix} R_F \\ R^H_H + K^* \theta^H_H \end{Bmatrix}, \tag{2.44}$$

where K^* is the artificial stiffness term. This term is introduced to enable using the same solution architecture already built-in in UM/NAST even when the hinge stiffness is zero, i.e., $K^H_{HH} = 0$ N-m/rad.

Now, these two equations are solved in an iterative process as described in the Fig. 2.6. At every static iteration, the flexible and hinge states are updated as follows:

$$\epsilon_{i+1} = \alpha_F \epsilon_i + (1 - \alpha_F) K_F^{-1} R_{F_i}, \tag{2.45}$$

$$\theta^H_{H_{i+1}} = \alpha_H \theta^H_{H_i} + (1 - \alpha_H)(K^H_{HH} + K^*)^{-1}(R^H_{H_i} + K^* \theta^H_{H_i}), \tag{2.46}$$

where α_F and α_H are relaxation parameters for incremental loading for the flexible and hinge

states respectively. Note, that the equation for the hinge states is a scalar equation for every FFWT defined in the model.

An important step in calculating the deformed shape from the strains is to update the kinematics as explained in Sec. 2.1.3. With a FFWT, the process to update the kinematics is modified by including the effect of the relative rotation of the FFWT about the hinge.

Considering Fig. 2.5, if there was no hinge (fixed hinge) between the wing and the folding wingtip member, the kinematics would be update by (see Eq. (2.23)):

$$h_{wt} = D_{wm} h_{wm}, \tag{2.47}$$

where D_{wm} accounts for the geometrical discontinuities between the two members. However, when the FFWT is free to rotate about the hinge, there is an additional rotation between the two members that needs to be accounted. Therefore, the rotation of the first node of the wingtip member is updated by:

$$\theta_{wt} = \theta_{wm} + \theta_H. \tag{2.48}$$

Then, an additional transformation matrix D_{wt} which accounts for the θ_{wt} is calculated and the kinematics are updated as follows:

$$h_{wt} = D_{wm} D_{wt} h_{wm}. \tag{2.49}$$

Next, the implementation of the equation of motions for dynamic simulations with FFWTs is described. The dynamic solver solves for the baseline equations of motion by expressing them in first-order form as [99]:

$$Q_1 \dot{x} + Q_2 x = Q_3, \tag{2.50}$$

where

$$x = \begin{bmatrix} \epsilon & \dot{\epsilon} & \beta & \zeta & p_B \end{bmatrix}, \tag{2.51}$$

$$Q_1 = \begin{bmatrix} I & 0 & 0 & 0 & 0 \\ 0 & M_{FF} & M_{FB} & 0 & 0 \\ 0 & M_{BF} & M_{BB} & 0 & 0 \\ 0 & 0 & 0 & I & 0 \\ 0 & 0 & 0 & 0 & I \end{bmatrix}, \tag{2.52}$$

$$Q_2 = \begin{bmatrix} 0 & -I & 0 & 0 & 0 \\ K_{FF} & C_{FF} & C_{FB} & 0 & 0 \\ 0 & C_{BF} & C_{BB} & 0 & 0 \\ 0 & 0 & 0 & \frac{1}{2}\Omega_\zeta & 0 \\ 0 & 0 & C^{BG}(\zeta) & 0 & 0 \\ 0 & C^H_{HF} & C^H_{HB} & 0 & 0 \end{bmatrix}, \tag{2.53}$$

and

$$Q_3 = \begin{bmatrix} 0 & R_F & R_B & 0 & 0 \end{bmatrix}. \tag{2.54}$$

The above equations are modified to account for the FFWTs which gives us the following modified equations:

$$x = \begin{bmatrix} \epsilon & \dot{\epsilon} & \beta & \zeta & p_B & \omega^H_H & \theta^H_H \end{bmatrix}, \tag{2.55}$$

$$Q_1 = \begin{bmatrix} I & 0 & 0 & 0 & 0 & 0 & 0 \\ 0 & M_{FF} & M_{FB} & 0 & 0 & M^H_{FH} & 0 \\ 0 & M_{BF} & M_{BB} & 0 & 0 & M^H_{BH} & 0 \\ 0 & 0 & 0 & I & 0 & 0 & 0 \\ 0 & 0 & 0 & 0 & I & 0 & 0 \\ 0 & M^H_{HF} & M^H_{HB} & 0 & 0 & M^H_{HH} & 0 \\ 0 & 0 & 0 & 0 & 0 & 0 & I \end{bmatrix}, \tag{2.56}$$

$$Q_2 = \begin{bmatrix} 0 & -I & 0 & 0 & 0 & 0 & 0 \\ K_{FF} & C_{FF} & C_{FB} & 0 & 0 & C^H_{FH} & 0 \\ 0 & C_{BF} & C_{BB} & 0 & 0 & C^H_{BH} & 0 \\ 0 & 0 & 0 & \frac{1}{2}\Omega_\zeta & 0 & 0 & 0 \\ 0 & 0 & C^{BG}(\zeta) & 0 & 0 & 0 & 0 \\ 0 & C^H_{HF} & C^H_{HB} & 0 & 0 & C^H_{HH} & K^H_{HH} \\ 0 & 0 & 0 & 0 & 0 & -I & 0 \end{bmatrix}, \tag{2.57}$$

and

$$Q_3 = \begin{bmatrix} 0 & R_F & R_B & 0 & 0 & R^H_H & 0 \end{bmatrix}. \tag{2.58}$$

2.2.2 Linearized Mode

The UM/NAST formulation is based on a strain-based geometrically exact beam formulation. To access the impact of the geometric nonlinearities in the structural analysis, the formulation can also solve for linearized equations. This requires two changes in the formulation:

- Jacobians must remain constant about the undeformed shape throughout the solution.
- The nonlinear strain-displacement relationship in Eq. (2.22) should be switched to a linearized relationship when updating the kinematics.

Not updating the jacobians is trivial in the implementation and already existed as part of the framework. The implementation of the linear relationship and updating the linearized kinematics was implemented as part of this work. The implementation was verified against both the MSC Nastran's nonlinear solver SOL400 and the linear solver SOL101.

2.2.3 Ride Quality Metric

In this work, the UM/NAST formulation was extended with the ability to evaluate an acceleration-based ride quality metric during flight. The selected ride metric was studied by Puyou [100], and it is based on ISO 2631-1 [80] and BS 6841 [101].

The metric is calculated from the vertical and lateral accelerations at different points along the fuselage. The metric follows the scheme shown in Fig. 2.7 and uses information from the acceleration data in the frequency domain:

$$\text{Ride quality metric}(p) = \sqrt{\frac{1}{\pi}\int_0^\infty a_\omega^2(\omega, p)d\omega}\ , \tag{2.59}$$

where $a_\omega(\omega, p)$ is the magnitude of the acceleration in the frequency domain obtained via Fourier transform at a point p of the aircraft. The ISO standards define comfort level ranges for values of the ride quality metric: increasing values mean increasing discomfort. For new HARW aircraft, the values of the ride quality metric are not as important as their comparison with existing aircraft.

The acceleration data at any aircraft point are collected during flight (simulation) by means of accelerometer sensors. The resulting time histories are then used to evaluate Eq. (2.59). The acceleration outputs from the sensors are provided in the time domain. A Fast-Fourier Transform utility is used to obtain the acceleration data in the frequency domain. The ride quality metric (2.59) is then evaluated using the trapezoidal numerical integration scheme.

For a dynamic simulation in UM/NAST, the acceleration information at any point on the aircraft can be recovered by sensors defined through the sensor module [102]. The ride quality metric is evaluated using accelerometer outputs.

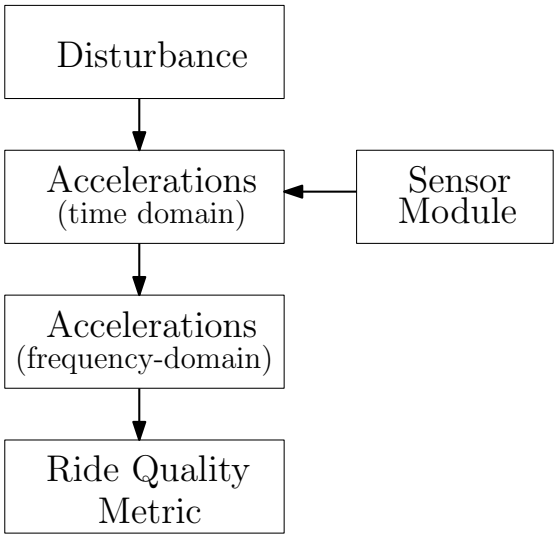

Figure 2.7: Schematic of the ride quality metric evaluation.

CHAPTER 3

Numerical Models

This chapter presents the aircraft models used in this work for investigating the key objectives of the thesis. These aircraft models are derived from the Airbus XRF1, an industry standard multidisciplinary research test case representing a contemporary configuration for a long-range, wide-body civil transport aircraft. This work utilizes both the baseline XRF1 and its HARW derivative, named XRF1-HARW [90]. The HARW aircraft model's aspect ratio and flexibility is representative of future civil transport aircraft. Low-order beam-type representations of the test cases were developed for investigating the research objectives in UM/NAST. The beam-type representations are verified by comparing natural frequencies and aeroelastic trim results from UM/NAST with reference solutions from MSC Nastran modal analyses and from coupled MSC Nastran/CFD aeroelastic trim analyses.

This chapter is organized as follows: Sec. 3.1 describes the high-order models. Sec. 3.2 and 3.3 describe the UM/NAST baseline and HARW aircraft models used in this work including their modal and static aeroelastic trim results.

3.1 High-Order Models

The global finite element model (GFEM) of the XRF1 is shown in Fig. 3.1a. The first XRF1 variant replaces the wingbox in Fig. 3.1b with the black wingbox in Fig. 3.1a with the same aspect ratio but simplified structural features; this variant is denoted as the flexible aircraft (FA) test case because it represents a conventional aircraft with moderate flexibility. The second XRF1 variant, named XRF1-HARW, considers the blue wingbox in Fig. 3.1b with a higher aspect ratio resulting from an aerostructural optimization [103] of the black wingbox; this variant is denoted as the very flexible aircraft (VFA) test case for its higher flexibility, as expected in future high-efficient aircraft. While not shown here, each test case comes with a CFD model for high-fidelity aerodynamic calculations [104]. The inertial properties and the first five in-vacuum free-free natural frequencies of the VFA and FA test cases are compared in Tables 3.2 and 3.3, respectively, for a typical half-

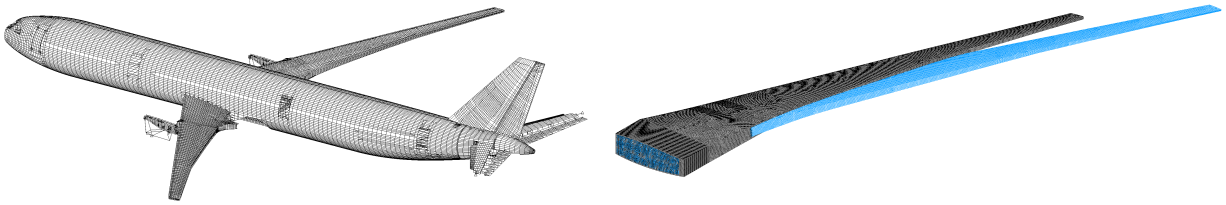

(a) Original full-vehicle model

(b) Wingbox model variants of the XRF1 (black) and XRF1-HARW (blue)

Figure 3.1: XRF1 global finite element model (GFEM).

Table 3.1: Properties of the FA and VFA test case.

Test case	FA	VFA
Aspect ratio	9.43	12.89
Half-span (m)	28.88	35.10
Mass (kg)	184968.51	185967.35

loaded mass case. The VFA MSC Nastran mode shapes for the full vehicle are shown in Fig. 3.2 for a previous version of the VFA model [90]. The VFA models used in this study differ from those versions only for small variations in the wing structural and aerodynamic properties.

The VFA test case has $+33\%$ and $+9\%$ larger roll and yaw moments of inertia, respectively, compared to the FA test case and significantly lower natural frequencies. Note that the first out-of-plane bending moment of the VFA test case is 43% smaller than the FA test case. The VFA test case is 22% longer compared to the FA test case (see Table 3.1).

Table 3.2: VFA vs. FA test case inertia property comparison (half-loaded mass case).

Property	Property variation (%)
Mass	0.54
Longitudinal center-of-mass position	7.31
Lateral center-of-mass position	-0.54
Vertical center-of-mass position	-0.36
Roll moment of inertia	32.98
Pitch moment of inertia	3.26
Yaw inertia moment of inertia	8.77

(a) Symmetric wing out-of-plane bending (mode #1)

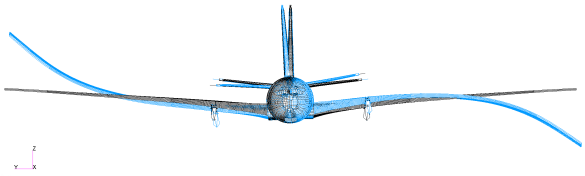

(b) Anti-symmetric wing out-of-plane bending (mode #2)

(c) Symmetric wing/pylon out-of-plane bending (mode #3)

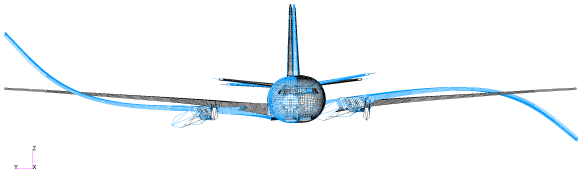

(d) Anti-symmetric wing/pylon out-of-plane bending (mode #4)

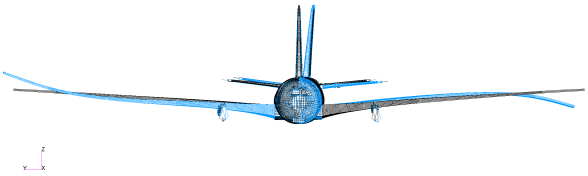

(e) Anti-symmetric wing in-plane bending (mode #5)

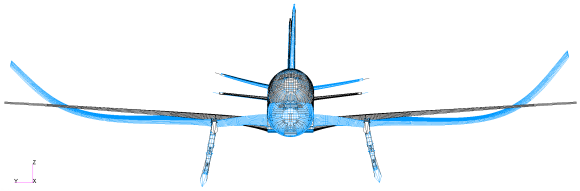

(f) Symmetric wing/pylon/fuselage out-of-plane bending (mode #6)

Figure 3.2: VFA test case in-vacuum free-free MSC Nastran mode shapes (half-loaded mass case).

Table 3.3: VFA vs. FA test case free-free natural frequency comparison (half-loaded mass case).

Mode #	Mode type	Frequency variation (%)
1	Wing out-of-plane bending (sym)	-43.15
2	Wing out-of-plane bending (asym)	-37.73
3	Wing/pylon out-of-plane bending (sym)	-25.36
4	Wing/pylon out-of-plane bending (asym)	-28.86
5	Wing in-plane bending (asym)	-27.54

Table 3.4: VFA vs. FA test case clamped natural frequency comparison (half-loaded mass case).

Mode #	Mode type	Frequency variation (%)
1	Wing out-of-plane bending	-43.83
2	Wing/pylon out-of-plane bending	-24.10
3	Wing/pylon out-of-plane bending	-36.45
4	Wing in-plane bending	-40.93
5	Wing/pylon/fuselage out-of-plane bending	-44.98

3.2 Low-Order Structural Models

To analyze the FA and VFA test cases, their GFEMs (Fig. 3.1) are reduced to low-order beam representations by computing equivalent inertia and stiffness distributions for each component (wing, tail, etc.) along a selected beam reference axis. These distributions are computed by enhancing the University of Michigan's FEM2Stick (UM/F2S) framework [105] to handle the detailed structural modeling features of the GFEMs in Fig. 3.1. The enhancements address two limitations of F2S: the equivalent inertia calculation based on analytical relations for specific finite element types; and the equivalent stiffness calculation that assumes zero axial extension and neglects coupling effects between axial and bending or torsion strains. The first enhancement consists of a new equivalent inertia calculation based on data from the GFEM mass matrix that is applicable to any finite element type; the second enhancement consists of a new equivalent stiffness calculation based on six static load cases to identify 6×6 cross-sectional stiffness matrices. Note that only the second implementation was done as part of this work. The resulting equivalent beam modeling framework, University of Michigan's Enhanced FEM2Stick (UM/EF2S) [90], is described in the Appendix C for readers interested in a systematic procedure to extract beam properties out of general GFEMs.

The FA test case is modeled as a set of equivalent beams by identifying the inertia and stiffness distributions of each GFEM component separately and by assembling their beam representations to form the full-vehicle model. The VFA test case beam model is the same as the FA model but for

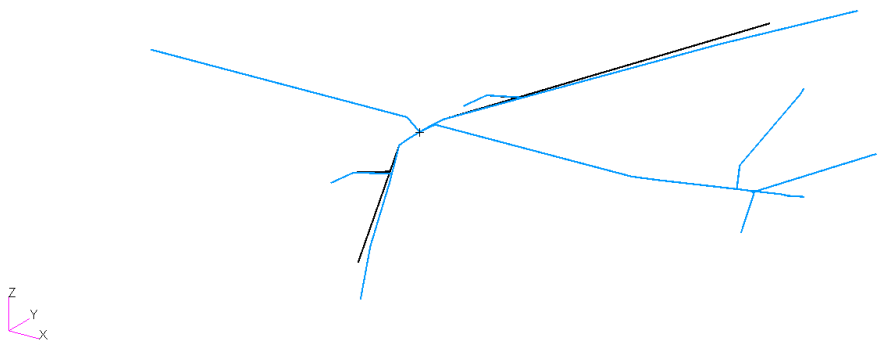

Figure 3.3: Beam-type representation of the FA (black) and VFA (blue) test cases.

a different wing beam representation obtained by extracting the inertia and stiffness distributions of the HARW wingbox in Fig. 3.1. The low-order beam representations of the FA and VFA test cases are verified in two ways. The inertia distributions are verified by checking that the total mass, center of mass position, and inertia tensor of the beam representation of each test case match the ones of their parent GFEM. The comparison is not shown because the equivalent inertia property extraction is numerically exact. The stiffness distributions are verified by comparing the natural frequencies of the beam representations of the FA and VFA wingboxes with the ones of their parent GFEMs in Fig. 3.1. Table 3.5 reports the results normalized by the first frequency of the FA wingbox GFEM. The frequency errors for the first five modes between the beam representation of each wingbox and their parent GFEMs range from 1% to 6%, demonstrating the accuracy of the equivalent beam models despite the much fewer DOFs compared with the GFEMs (Table 3.7).

3.3 Low-Order Aerodynamic Models

The beam structural models of Sec. 3.1 are coupled to quasi-steady aerodynamic models based on the method of segments [91]. The key steps in the aerodynamic modeling process are summarized below. The process starts with conducting steady rigid CFD calculations on the full-vehicle high-fidelity aerodynamic model in a typical flight shape for various combinations of the Mach number M and the body angle of attack α. In this work, the Mach number ranges from $M \in [0.5, 0.9]$ and the body angle of attack ranges from $\alpha \in [-8, +10]$ deg. The results from each CFD solution are used to compute the aerodynamic lift, drag, and quarter-chord pitching moment coefficient distributions along the wing and tail spans. The coefficient values from all CFD solutions for a given cross section corresponding to a beam structural node are used to build a surrogate kriging

Table 3.5: FA wingbox normalized natural frequencies (half-load case).

		Normalized frequency		
Mode #	Mode type	GFEM	Beam	Diff. (%)
1	Out-of-plane bending	1.00	0.98	−2.44
2	Out-of-plane bending	2.44	2.46	1.00
3	In-plane bending	2.76	2.76	−0.03
4	Out-of-plane bending	5.12	5.42	5.87
5	Torsion	6.38	6.48	1.50
6	In-plane bending	8.39	9.31	11.00
7	Out-of-plane bending	11.01	10.74	−2.44
8	Torsion	13.44	13.98	4.01
9	Out-of-plane bending	14.44	14.96	3.63
10	In-plane bending	16.33	17.36	6.28

Table 3.6: VFA wingbox normalized natural frequencies (half-load case).

		Normalized frequency		
Mode #	Mode type	GFEM	Beam	Diff. (%)
1	Out-of-plane bending	1.00	0.99	−1.10
2	Out-of-plane bending	2.47	2.50	1.03
3	In-plane bending	2.75	2.79	1.32
4	Out-of-plane bending	5.01	5.20	3.73
5	Torsion	6.60	6.75	2.35
6	In-plane bending	8.57	9.13	6.48
7	Out-of-plane bending	12.76	13.90	8.98
8	Torsion	14.34	14.79	3.14
9	Out-of-plane bending	15.96	16.15	1.20
10	In-plane bending	22.97	20.55	−10.55

Table 3.7: FA and VFA wingbox structural DOFs.

	Structural DOFs		
Test case	GFEM	Beam	Reduction factor
FA	514884	176	2925
VFA	514884	212	2429

Table 3.8: Flight conditions considered for numerical investigations.

Mach number	Altitude (m)	Dynamic pressure (Pa)
0.65	7000	11800
0.83	8484	16000

model. The inputs to the surrogate model are the Mach number and the local angle of attack at that cross section, the latter given by the sum of the body angle of attack, the jig shape twist, and the incremental twist due to the elastic deformation in the reference flight shape; the outputs are the lift, drag, and quarter-chord circulatory pitching moment coefficient at that cross section. Further details on the application of method of segments within UM/NAST is detailed in Refs. [65, 106]. Once a surrogate kriging model is developed for each cross section, it is used in flight simulations to compute the circulatory aerodynamic loads based on the Mach number and instantaneous local angle of attack based on the local velocity due to the vehicle's rigid-body and elastic motion. The non-circulatory aerodynamic loads are also summed to the circulatory values based on thin airfoil theory relations [98].

The aerodynamic models developed for the FA and VFA test cases are verified by removing the CFD solutions for some Mach number and body angle of attack combinations from the kriging surrogate creation. The verification consists of using the surrogate for predicting the steady lift, drag, and quarter-chord pitching moment coefficients distributions along the wing and tail for the flight conditions eliminated from the kriging modeling and the results are compared with the known CFD solutions [106]. The inflow states are not considered in this work since this aerodynamic modeling techniques does not capture the unsteady aerodynamic effects.

3.3.1 Static Aeroelastic Trim Solution

To further emphasize the level of flexibility of the VFA test case, Tables 3.9 compares the FA and VFA right wing tip vertical displacements for trim at varying load factor. Displacements are normalized by each wing's semispan. The deformed shape at trim for varying load factors is shown by Fig. 3.4 and 3.5. Table 3.8 summarizes the two flight conditions considered for the investigations and they will be referred by their Mach number from this point on. Results are obtained at $M_\infty = 0.65$ for an altitude of 7000 m (dynamic pressure $q_D = 11800$ Pa) and $M_\infty = 0.83$ for an altitude of 8484 m ($q_D = 16000$ Pa). These flight conditions represent a low dynamic pressure case and a typical cruise case for a long-range wide-body civil transport aircraft. These two flight conditions are considered to highlight the impact of aeroelastic effects, whose strength increases with dynamic pressure.

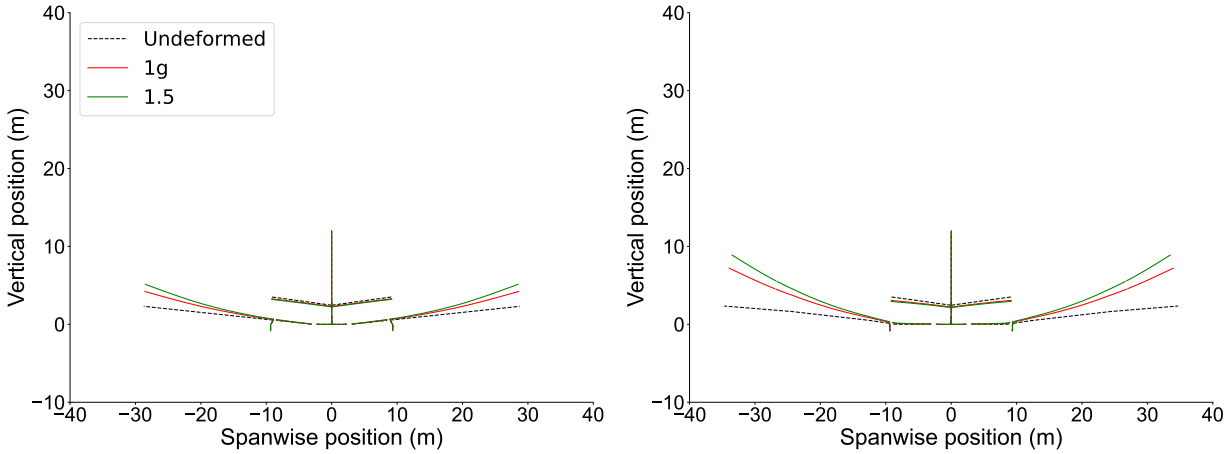

(a) FA

(b) VFA

Figure 3.4: Static aeroelastic trim shape, $M_\infty = 0.65$.

Table 3.9: FA and VFA right wing tip trim vertical displacements.

	Displ. (% semispan)			
	$M_\infty = 0.65$		$M_\infty = 0.83$	
Load factor (g)	FA	VFA	FA	VFA
1.0	6.6	14.2	5.6	11.2
1.5	9.8	19.1	8.3	14.8
2.0	-	-	11.4	18.5

At 1 g and $M_\infty = 0.65$, the VFA wing tip vertical displacement is 14.2% semispan, more than twice that of the FA wing tip. At 1.5 g, the VFA wing tip vertical displacement reaches 19.1% semispan compared with the 9.8% semispan displacement of the FA wing tip. Similarly, at 1 g and $M_\infty = 0.83$, the VFA wing tip vertical displacement is 11.2% semispan, twice that of the FA wing tip. At 2 g, the VFA wing tip vertical displacement reaches 18.5% semispan compared with the 11.4% semispan displacement of the FA wing tip[1].

3.3.2 VFA Test Case with Flared Folding Wingtips

The studies conducted for the VFA test with the FFWTs consider the wingtip spanning approximately 22% of the VFA's semispan. This corresponds to the hinge line in Fig. 3.6 located approximately at the wingtip of the FA test case. The flare angle Λ denotes the angle between the hinge

[1]Results at load factors higher than 1.5 g at $M_\infty = 0.65$ are not available due to a limitation with aerodynamic data at these flight conditions.

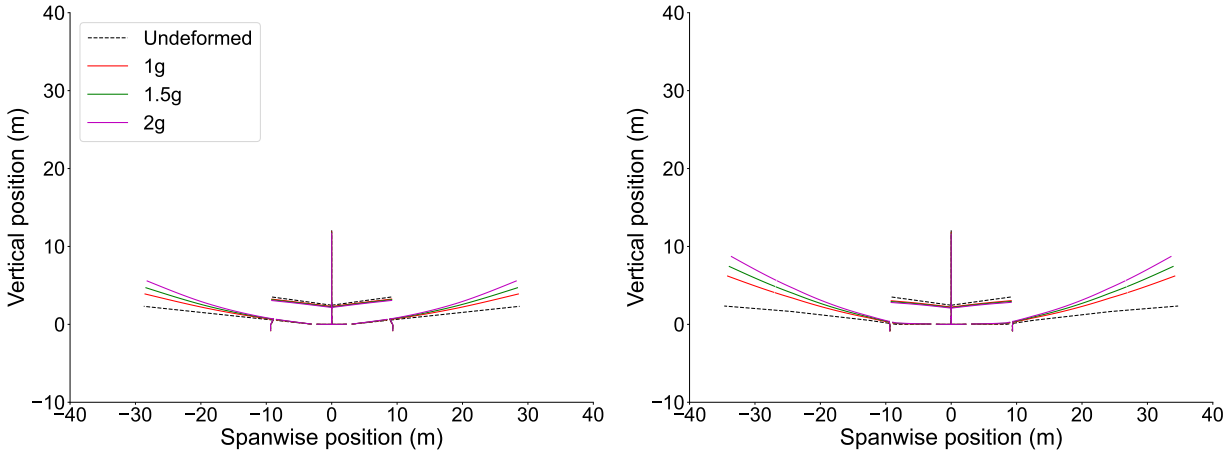

(a) FA (b) VFA

Figure 3.5: Static aeroelastic trim shape, $M_\infty = 0.83$.

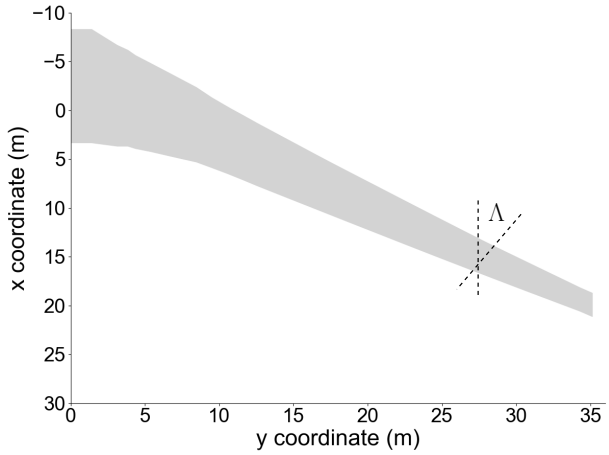

Figure 3.6: Position of the FFWT's hinge for the VFA test case.

line and the flow direction and is positive for an outward hinge line orientation.

First, Table 3.10 shows the impact of varying hinge stiffness on the natural frequencies for the clamped VFA wingbox. The impact of flare angle for these results are not considered. For a zero hinge stiffness, there is a rigid body mode for the folding wingtip. As the hinge stiffness is increased, the frequencies start converging to the fixed hinge case. Also, the impact of the hinge stiffness is observed mainly for the first few modes. The impact of flare angle on the structural frequencies is low as shown in Table 3.11.

The dynamic simulations considered in this work start from a nonlinear trimmed solution. Fig. 3.7 shows the static aeroelastic trim shape of the VFA test case with FFWTs with zero hinge stiffness for varying load factors. At $M_\infty = 0.65$, the FFWTs rotate more compared to $M_\infty = 0.83$.

Table 3.10: VFA wingbox normalized natural frequencies with FFWT for varying hinge stiffness and $\Lambda = 0$ deg (half-load case).

	Frequency (Hz)			
Mode #	k_y^H = 0 Nm/rad	k_y^H = 10^4 Nm/rad	k_y^H = 10^8 Nm/rad	Fixed hinge
1	0.00	0.02	1.00	1.00
2	1.35	1.35	2.70	2.71
3	2.81	2.81	2.84	2.84
4	4.59	4.59	5.68	5.70
5	7.34	7.34	7.34	7.34
6	9.31	9.31	9.73	9.73
7	9.74	9.74	9.98	9.98
8	11.41	11.41	13.97	14.03
9	15.22	15.22	15.58	15.60
10	16.02	16.02	16.04	16.04

Table 3.11: VFA wingbox normalized natural frequencies with FFWT for varying flare angle and k_y^H = 0 Nm/rad (half-load case).

	Frequency (Hz)		
Mode #	$\Lambda = 0$ deg	$\Lambda = 10$ deg	$\Lambda = 25$ deg
1	0.00	0.00	0.00
2	1.35	1.35	1.35
3	2.81	2.81	2.81
4	4.59	4.59	4.58
5	7.34	7.34	7.34
6	9.31	9.53	9.65
7	9.74	9.75	9.84
8	11.41	11.47	11.53
9	15.22	15.38	15.56
10	16.02	16.02	16.00

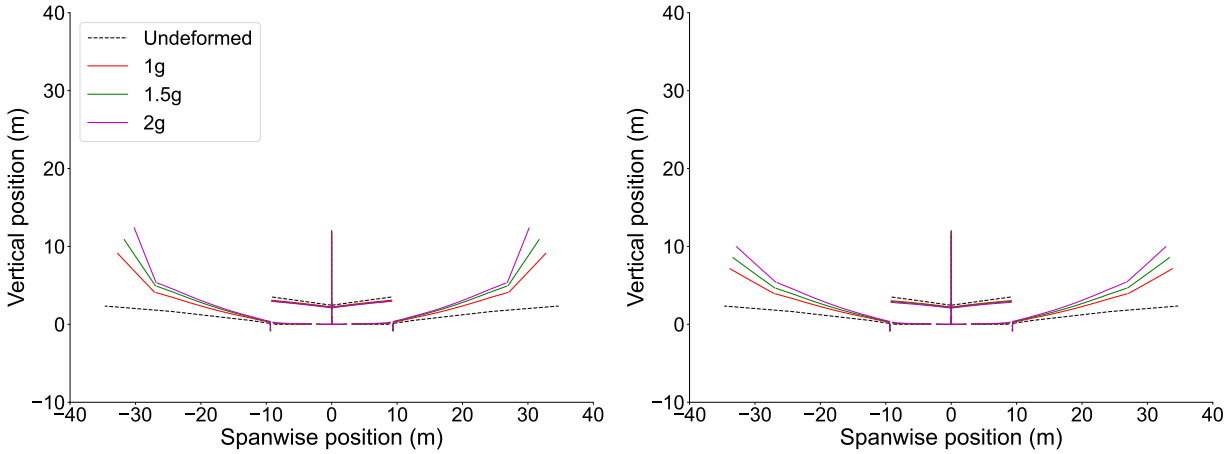

(a) $M_\infty = 0.65$ (b) $M_\infty = 0.83$

Figure 3.7: VFA static aeroelastic trim shape with FFWTs.

These results are further explored further in the subsequent chapters.

CHAPTER 4

Roll Maneuverability and Maneuver Load Alleviation

The studies in this chapter address the first and second research objective of the thesis by investigating roll maneuverability and load alleviation in transonic HARW aircraft. First, the chapter discusses the effectiveness of using traditional trailing-edge control surfaces for rolling these aircraft, considering varying spanwise placement. Second, the chapter explores the benefits and limitations of wingbox passive aeroelastic tailoring for improving roll maneuverability when commanding deflections of trailing-edge control surfaces. Third, the chapter explores the potential use of unconventional control effectors such as leading-edge control surfaces and FFWTs for performing roll maneuvers and alleviate the resulting loads. Finally, this chapter also investigates impact of geometrically nonlinear effects on the roll control effectiveness of transonic HARW aircraft.

4.1 Roll Maneuver for Certification

The FAA [53] roll maneuverability certification requirement for civil transport aircraft states:

> "With the airplane in trim, or as nearly as possible in trim, for straight flight, establish a steady 30-degree banked turn. Demonstrate that the airplane can be rolled to a 30-degree bank angle in the other direction in not more than 11 seconds. The rudder may be used to the extent necessary to minimize sideslip. Demonstrate this maneuver in the most adverse direction. The maneuver may be unchecked, that is, the pilot need not apply a control input to stop the roll until after the 30-degree bank angle is achieved. Care should be taken to prevent excessive sideslip and bank angle during the recovery."

To fulfill the above criterion, the aircraft must establish a roll rate in a given time. A simplified expression for the roll motion of a rigid aircraft is given by:

$$I_{xx}\dot{p} = L_{\delta}\delta + L_{p}p. \tag{4.1}$$

In this equation, p is the roll rate, $\dot{p}$ is its time derivative, I_{xx} is the roll moment of inertia, δ is the control-surface deflection, L_δ is the roll moment coefficient, and L_p is the roll rate damping coefficient. The roll rate of an aircraft for a given control-surface deflection depends on three main factors: control-surface effectiveness given by the L_δ term, roll damping given by the $L_p p$ term (which increases with the wing span), and the roll moment of inertia. Increasing the control-surface effectiveness and decreasing the roll damping and roll moment of inertia improve the aircraft's roll maneuverability. The impact of these factors on the roll maneuverability of a transonic HARW aircraft is studied through static and dynamic analyses. The static analyses highlight the impact of the control-surface effectiveness; the dynamic analyses, which consider a roll maneuver similar to the certification criterion, show the impact of the roll damping and roll moment of inertia.

This chapter starts with Sec. 4.2, which discusses the studies on the effectiveness of trailing-edge control surfaces at various spanwise positions. This is followed by Sec. 4.3, which compares the benefits and limitations of deploying leading-edge control surfaces compared with trailing-edge control surfaces. Section 4.4 investigates the roll maneuverability and maneuver load alleviation resulting from deploying trailing- and leading-edge control surfaces along with FFWTs. Finally, Sec. 4.5 summarizes the results.

4.2 Trailing-Edge Control Surfaces

This section investigates the impact of the spanwise placement of trailing-edge control surfaces on roll maneuverability of the VFA test case compared to the FA test case. The static and dynamic responses of the FA and VFA test cases for given control-surface deflections are compared in terms of control-surface effectiveness (static response) and of the roll angle developed during a bank-to-bank maneuver (dynamic response). Results for parametric variations in the wing stiffness properties, which mimic passive aeroelastic tailoring, are presented to discuss design guidelines for improving roll maneuverability. The impact of geometrically nonlinear effects is also discussed by comparing the aileron effectiveness. Section 4.2.1 describes the numerical studies and Secs. 4.2.3 and Sec. 4.2.4 discuss the static and dynamic results, respectively.

4.2.1 Analysis Setup

Roll maneuvers are simulated by time-marching the coupled nonlinear aeroelastic-flight dynamics equations of motion [Eqs. (2.14) and (2.15)] along with the associated kinematic equations, starting with the aircraft trimmed for 1-g level flight. The trim solution at each flight condition takes into account the aircraft statically deformed shape, which is determined by means of a nonlinear aeroelastic trim process (see Sec. 3.3.1).

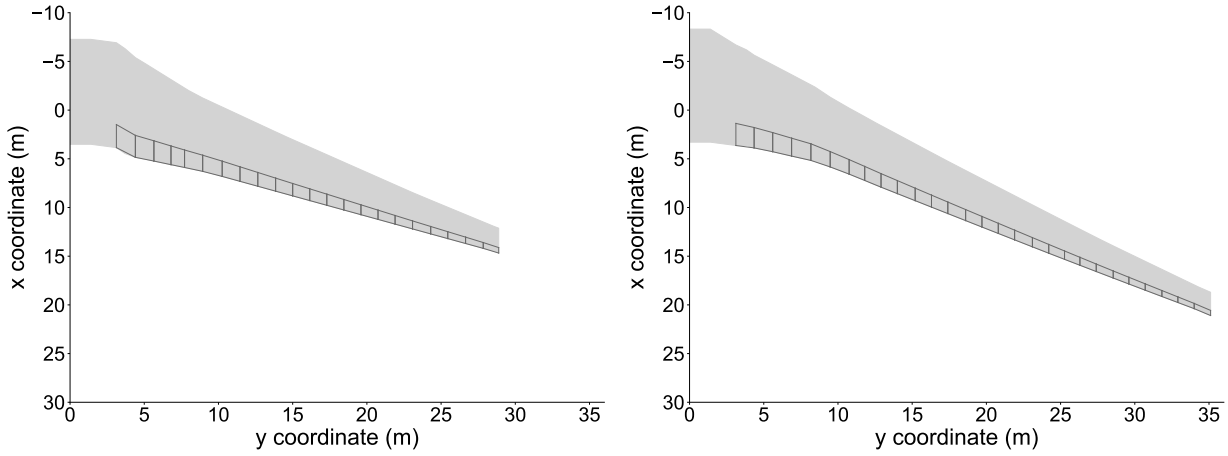

(a) FA (b) VFA

Figure 4.1: Location of trailing-edge control surfaces.

To study the impact of control-surface spanwise placement, the wings of the FA and VFA test cases are subdivided into multiple regions associated with control surfaces that can be deflected individually, as shown in Fig. 4.1. The regions are reported in Table 4.1 and are chosen to have control surfaces of approximately the same spanwise length. The trailing-edge control-surface hinge line considers a constant control-surface to wing chord fraction of 0.22, which is a representative value for a civil transport aircraft.

The control surfaces numbered from #1 to #4 span from the wing-fuselage interface to the pylon location (first group in Table 4.1). The pylon is placed at the same dimensional spanwise location in the FA and VFA test cases [90]. The segments from #6 to #22 span from the pylon to the FA wingtip (second group in Table 4.1). The VFA has more aileron segments associated with the longer wing span (third group in Table 4.1).

4.2.2 Control-Surface Aerodynamic Models

The trailing-edge control-surface derivatives for the lift and quarter-chord pitching moment coefficient at a given cross section are given by the analytical relations [17, 107]:

$$c_{l_\delta} = \frac{c_{l_\alpha}}{\pi}(\cos^{-1}c^* + \sqrt{1-c^{*^2}}), \quad c_{m_\delta} = -\frac{(1+c^*)\sqrt{1-c^{*^2}}}{2}\ . \tag{4.2}$$

The quantity $c^* = 1 - 2c_{\text{fr}}$ where c_{fr} is the control-surface to wing chord fraction (0.22 for the trailing-edge control surfaces in this study). For a constant value of this parameter, c_{m_δ} is constant along the span and c_{l_δ} varies with the local lift curve slope c_{l_α}. Figure 4.2 shows the variation of the c_{l_δ} along the VFA wing span for $M_\infty = 0.65, 0.83$ using the assumed parameters. The dependency

Table 4.1: FA and VFA control-surface segments.

	Spanwise location (m)			
	Start		End	
Segment #	FA	VFA	FA	VFA
1	3.12	3.12	4.40	4.35
2	4.40	4.35	5.65	5.60
3	5.65	5.60	6.80	6.88
4	6.80	6.88	7.71	8.18
5	7.71	8.18	8.94	9.48
6	8.94	9.48	10.25	10.75
7	10.25	10.75	11.45	11.80
8	11.45	11.80	12.65	12.90
9	12.65	12.90	13.85	14.00
10	13.85	14.00	15.00	15.20
11	15.00	15.20	16.15	16.30
12	16.15	16.30	17.30	17.40
13	17.30	17.40	18.45	18.60
14	18.45	18.60	19.60	19.70
15	19.60	19.70	20.75	20.80
16	20.75	20.80	21.90	21.90
17	21.90	21.90	23.08	23.10
18	23.08	23.10	24.30	24.20
19	24.30	24.20	25.45	25.27
20	25.45	25.27	26.65	26.30
21	26.65	26.30	27.84	27.40
22	27.84	27.40	28.88	28.55
23	–	28.55	–	29.60
24	–	29.60	–	30.70
25	–	30.70	–	31.83
26	–	31.83	–	32.90
27	–	32.90	–	34.00
28		34.00		35.11

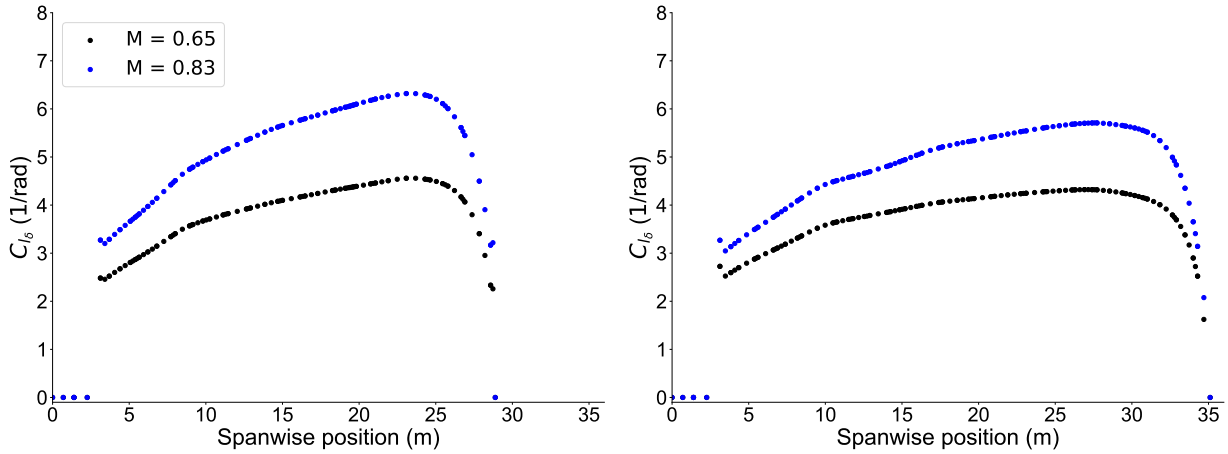

(a) FA

(b) VFA

Figure 4.2: Spanwise variation of c_{l_δ} for trailing-edge control surfaces.

of c_{l_δ} on the flight condition is through the local lift curve slope, which also varies along the span. The c_{m_δ} is constant with the flight condition and the spanwise location, equal to -0.646 rad^{-1} with the chosen control-surface to wing chord fraction. The c_{d_δ} is zero.

4.2.3 Static Analysis

The discussion of static results is as follows: Sec. 4.2.3.1 compares the control effectiveness of the FA and VFA test cases for different control-surface spanwise placement; Sec. 4.2.3.2 explores the impact of passive aeroelastic tailoring; and Sec. 4.2.3.3 investigates the relevance of geometrical nonlinearities associated with nonlinear kinematics and follower aerodynamic loads.

4.2.3.1 Control-Surface Effectiveness

This section begins by comparing the static roll response of the FA and VFA test cases to highlight the impact of moving from a regular-aspect-ratio wing to a HARW. The wings of the two test cases are considered as root-clamped, isolated components at a rigid (wing-root) angle of attack of 2 deg, which is representative of a typical trim value for a 1-g level flight cruise case. Figures 4.3 compares the roll aerodynamic moments of the VFA test case considering two different trailing-edge control-surface segments as the ailerons with the aerodynamic moments of the FA test case considering the trailing-edge control-surface segment that corresponds to the typical aileron position for a contemporary civil transport aircraft. While the aileron locations for current aircraft with regular-aspect-ratio wings are known, the best locations for these devices on future HARW versions is undefined. Thus, two choices are considered to investigate how spanwise placement

impacts roll control effectiveness.

For the FA test case, the inboard and outboard ailerons span the segments from #16 to #18 and from #19 to #21, respectively. For the VFA test case, two aileron layouts are considered. In configuration 1, the VFA inboard and outboard ailerons span the segments from #19 to #21 and from #22 to #24. These segments are chosen so the ailerons occupy the same normalized spanwise locations as the corresponding FA ailerons. With this choice, the VFA ailerons are placed at a larger dimensional distance from the wing root than in the FA test case, resulting in longer moment arms. Despite the longer aileron moment arms, the VFA wing develops smaller roll aerodynamic moment increments for given deflections than the FA wing. This is due to the stronger washout effects, which are exacerbated in the VFA test case with aileron configuration 1 due to the higher wing structural flexibility in the outer part of the wing. Additionally, the VFA aileron response in the case of configuration 1 shows nonlinear effects at $M_\infty = 0.83$ for both the inboard and outboard ailerons. This is also observed for the outboard ailerons at $M_\infty = 0.65$ (see Fig. 4.3b). The higher VFA wing flexibility causes control reversal in the outboard ailerons (see Figs. 4.3b and 4.3d).

In configuration 2, the VFA inboard and outboard ailerons are positioned at the same dimensional distance from the wing root as the FA ailerons. This results in higher aileron effectiveness due to the more inboard placement. Since the inboard wing region is stiffer, the inboard VFA aileron response is linear and qualitatively similar to the FA aileron response. The VFA test case develops larger roll moments (in magnitude) at $M_\infty = 0.83$ for the outboard ailerons.

Inboard ailerons are always more effective than the outboard ailerons for each test case, flight condition, and aileron configuration (for the VFA test case) despite the longer moment arm. This is motivated by lower wash-out effects due to the lower out-of-plane bending displacements more inboard. Additional studies analyze the impact of trailing-edge control-surface placement on roll maneuverability of the VFA test case. The static roll response is quantified in terms of control effectiveness η_δ as a function of control-surface spanwise placement y for selected deflections. Control effectiveness is computed as the roll aerodynamic moment increment ΔL per unit deflection δ and area S_δ:

$$\eta_\delta(y) = \frac{\Delta L(y)}{\delta} \frac{1}{S_\delta(y)} \, . \tag{4.3}$$

The area S_δ varies along the span because all control surfaces have approximately the same spanwise length but smaller chord values toward the tip due to the assumed uniform ratio of their chord compared with the local wing chord.

Figure 4.4 shows the variation in the control effectiveness with the spanwise placement of the deflected trailing-edge control surface considering the wing as rigid. Each horizontal bar denotes the level of control effectiveness for given control-surface spanwise location. For both flight con-

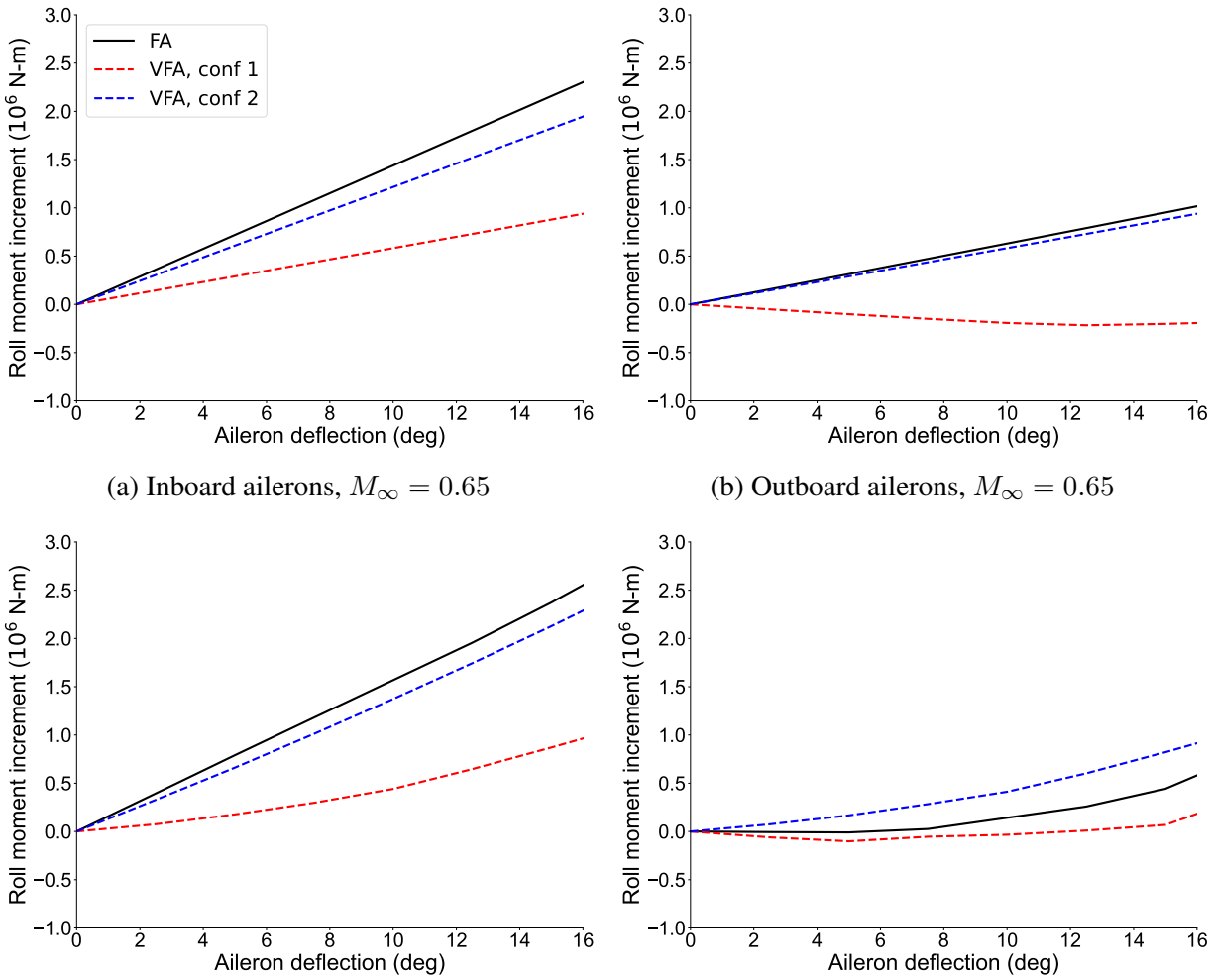

(a) Inboard ailerons, $M_\infty = 0.65$

(b) Outboard ailerons, $M_\infty = 0.65$

(c) Inboard ailerons, $M_\infty = 0.83$

(d) Outboard ailerons, $M_\infty = 0.83$

Figure 4.3: VFA vs. FA static roll moment comparison for given inboard/outboard aileron deflection.

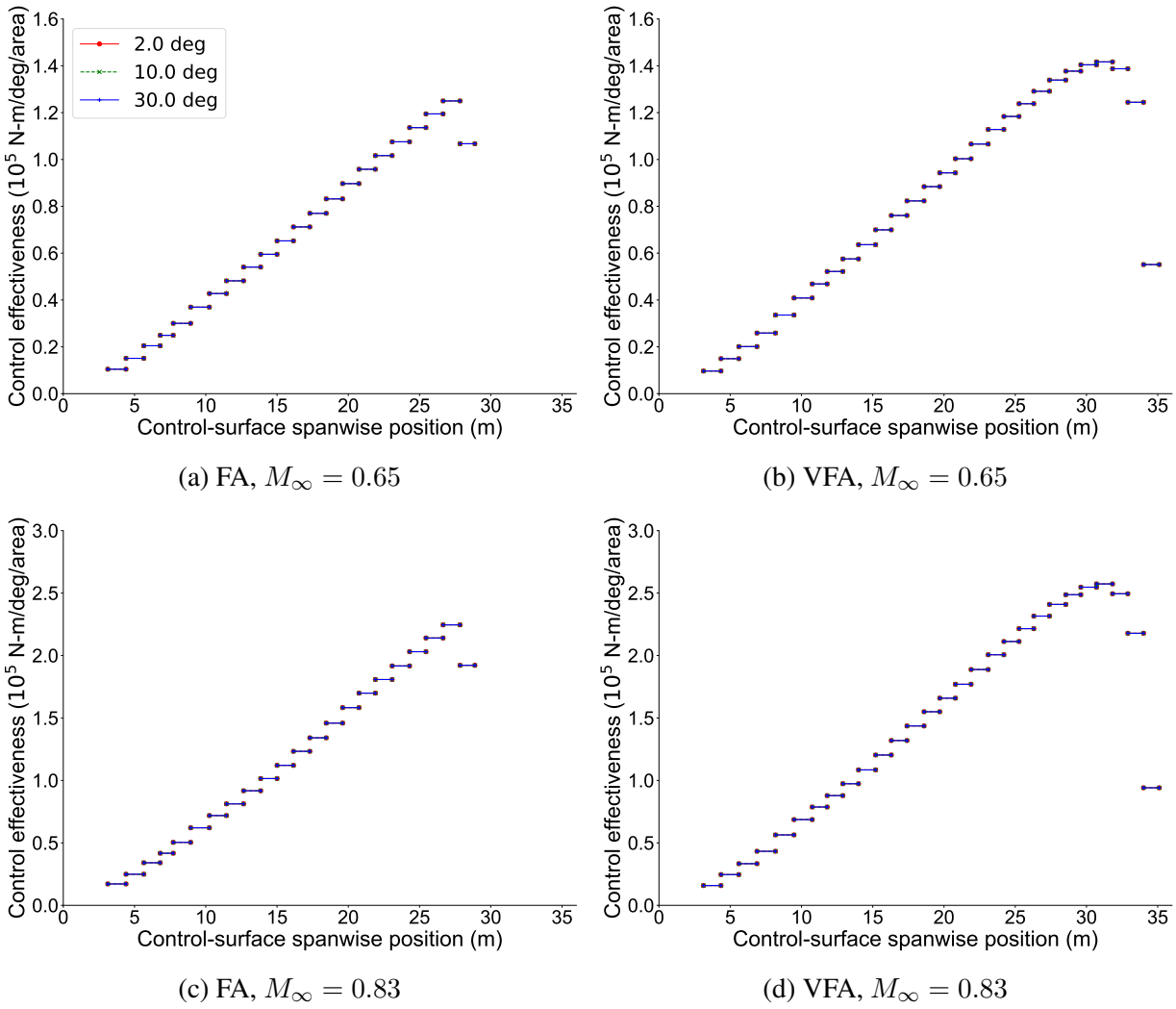

(a) FA, $M_\infty = 0.65$

(b) VFA, $M_\infty = 0.65$

(c) FA, $M_\infty = 0.83$

(d) VFA, $M_\infty = 0.83$

Figure 4.4: VFA vs. FA roll control effectiveness as a function of control-surface spanwise placement (rigid wing).

ditions, control effectiveness peaks when deflecting control surfaces at 85% of the semispan. This is a trade-off between the increase in moment arm and the drop in c_{l_δ} (see Fig. 4.2) toward the wingtip. The roll control effectiveness of VFA is higher than for the FA for each control surface in the absence of flexibility. Control effectiveness also increases with dynamic pressure because the rigid wing generates more lift for the same control-surface deflection.

Figure 4.5 shows the results for the case of flexible wings. For both flight conditions, each configuration shows similar qualitative spanwise trends. Control effectiveness increases when moving from the wing root to a spanwise location of approximately 17.5 m, then it decreases in the outer wing region. The spanwise location where control effectiveness peaks corresponds to 60% of the FA test case semispan and to 50% of the VFA test case semispan. The initial increase in control ef-

fectiveness when moving away from the wing root is due to the longer moment arm of the deflected control surfaces. This increase continues as long as the control surface remains in a wing region subject to moderate aeroelastic effects. The decrease in aileron effectiveness from the 17.5-meter spanwise location to the wingtip is motivated by the detrimental influence of aeroelastic deflections in the outer wing region. Control surfaces toward the wingtip not only have lower effectiveness, but also exhibit stronger nonlinear effects, particularly at $M_\infty = 0.83$ and for the VFA test case. This can be observed by the variation in aileron effectiveness with the commanded deflection angle. While they are exacerbated in the VFA test case, nonlinear effects and control reversal in the outboard ailerons are present even for the FA test case at $M_\infty = 0.83$. However, the VFA test case experiences control reversal for small values of the deflection angle at both flight conditions.

For a given aircraft, comparing results at $M_\infty = 0.65$ and $M_\infty = 0.83$ shows that outer aileron segments are less effective at $M_\infty = 0.83$. This is expected due to the larger aeroelastic deflections in the wing region toward the wingtip, resulting in stronger wash-out effects. However, inboard segments (for both FA and VFA) are more effective at $M_\infty = 0.83$ than at $M_\infty = 0.65$. This is because wing deflections at those spanwise locations remain modest, while the higher dynamic pressure at $M_\infty = 0.83$ results in larger roll moment increments for the same deflection angle. Comparing FA and VFA results at $M_\infty = 0.65$ shows that aileron segments at the same spanwise locations have comparable effectiveness, while the additional outboard segments placed in the VFA region beyond the FA wingtip are in reversal. Similar behavior is observed at $M_\infty = 0.83$, although at this flight condition the the response of the outboard segments highly depends on the deflection angle.

These results show that placing the VFA ailerons at the same dimensional spanwise locations as the FA ailerons results in comparable control effectiveness. In contrast, placing the VFA ailerons at the same normalized spanwise location results in a significant degradation of control effectiveness. For both test cases, an even higher aileron effectiveness and slighter nonlinear effects can be achieved by moving the ailerons closer to the spanwise location where control effectiveness peaks. This location moves from 60% of the semispan for the FA test case to the midspan for the VFA test case.

4.2.3.2 Impact of Wingbox Passive Aeroelastic Tailoring

Next, the influence of spanwise placement of trailing-edge control surfaces is studied in combination with wingbox passive aeroelastic tailoring for the VFA test case. The objective of these investigations is to understand how the wing stiffness impacts control effectiveness. For a swept wing, the roll response is affected by the kinematic coupling of out-of-plane bending and torsion due to the sweep angle. The effect of this coupling is exacerbated with higher flexibility in both out-of-plane bending and torsion stiffness. The out-of-plane bending and torsion stiffness coupling

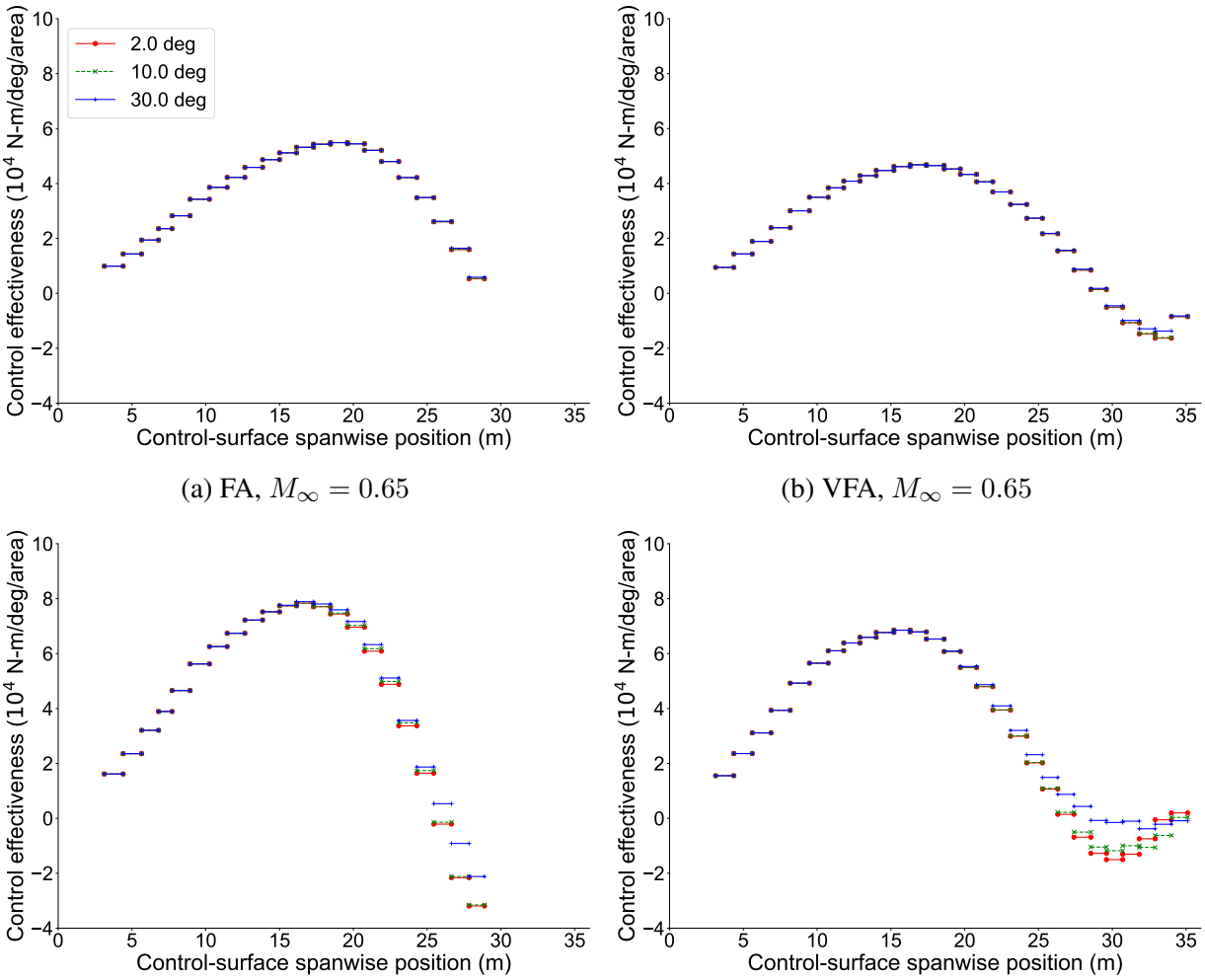

(a) FA, $M_\infty = 0.65$

(b) VFA, $M_\infty = 0.65$

(c) FA, $M_\infty = 0.83$

(d) VFA, $M_\infty = 0.83$

Figure 4.5: VFA vs. FA roll control effectiveness as a function of control-surface spanwise placement (flexible wing).

term of the wing is an additional factor. To isolate the effect of these different factors, the studies consider uniform variations in the VFA wing's out-of-plane bending and torsion stiffness spanwise distributions and in the coupling term between out-of-plane bending and torsion.

Figure 4.6 shows the results an aileron deflection of 2 deg with a 15% and a 100% increase in stiffness. A 15% increases in stiffness corresponds to a practical variation that can be considered for passive aeroelastic tailoring; a 100% increase corresponds brings the VFA test case flexibility to comparable with the FA test case. The results for varying coupling term consider the case of reversal in sign and of zero coupling. Figure 4.7 shows an additional limiting case for the out-of-plane bending and torsion stiffness with an infinite increase in the respective stiffness terms for varying deflection angles. Variations in the out-of-plane bending stiffness have a stronger impact on control effectiveness, which increases moving from the wing root to the wingtip. Figs. 4.6a and 4.6b show the outboard shift in the peak value of control effectiveness with increasing stiffness. A lower out-of-plane bending stiffness is the key factor in the reduced control effectiveness along the wingspan. In fact, the results in Figs. 4.7a and 4.7b where the VFA wing is rigid in out-of-plane bending but flexible in torsion show similar spanwise trends as observed for the rigid wing (see Fig. 4.4). Figures 4.6c and 4.6d show a less significant impact of varying the wing's torsion stiffness. However, if the spanwise placement study is repeated for a wing rigid in torsion but flexible in out-of-plane bending (see Fig. 4.7), the nonlinear effects for the outboard layout are reduced. At $M_\infty = 0.65$, the stiffened wing in torsion has the same control effectiveness for a given spanwise placement regardless of the deflection angle. These results show that torsion stiffness drives the nonlinearities in the control-surface effectiveness, while the global spanwise placement trends are influenced by the out-of-plane bending stiffness. The last two plots of Fig. 4.6 show the role of the coupling term between out-of-plane bending and torsion. Reversing the coupling term sign has a negligible impact, specially towards the wingtip. The results obtained for $M_\infty = 0.85$ show similar qualitative trends, but the impact of property variations increases due to stronger aeroelastic effects. These results highlight the benefits of increasing the wing out-of-plane bending stiffness for maximizing the effectiveness of a given aileron, compatibly with other constraints and penalties in performance. However, the influence of wingbox passive aeroelastic tailoring becomes slighter for more inboard ailerons and at lower dynamic pressure conditions, where aileron effectiveness is primarily dictated by the spanwise placement.

4.2.3.3 Impact of Geometrically Nonlinear Effects

To conclude the static studies, this section investigates the impact of geometrically nonlinear effects to understand whether they must be considered to capture roll control effectiveness of transonic HARW aircraft. The study considers the ailerons for the results in Fig. 4.3. Those results assumed nonlinear kinematics and follower aerodynamic loads as a default. In the case of linear kinematics,

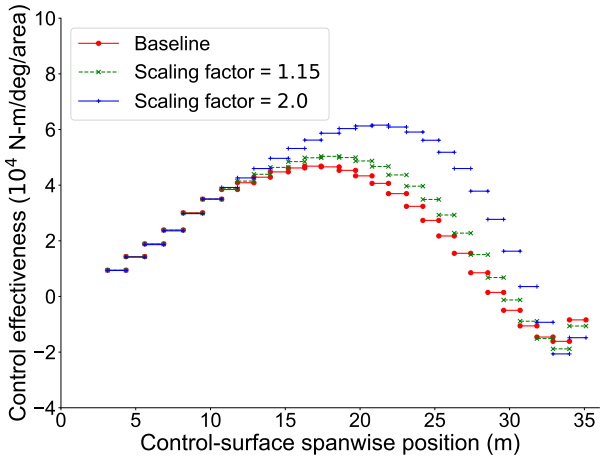

(a) Out-of-plane bending stiffness, $M_\infty = 0.65$

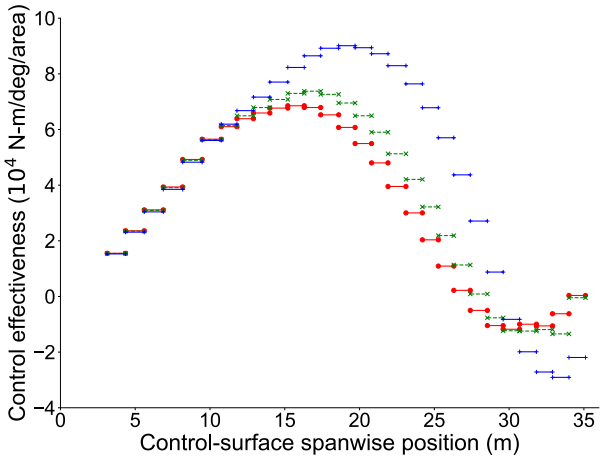

(b) Out-of-plane bending stiffness, $M_\infty = 0.83$

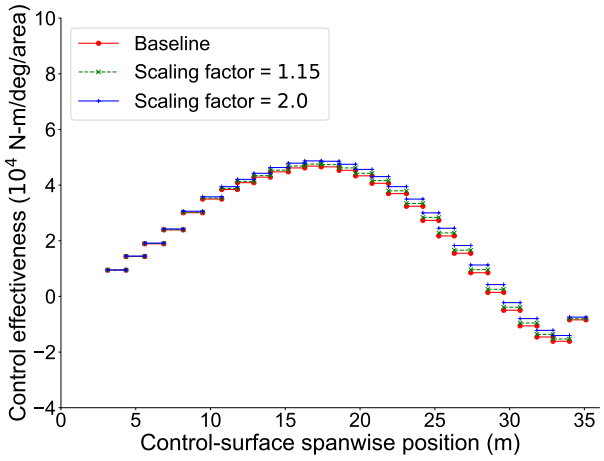

(c) Torsion stiffness, $M_\infty = 0.65$

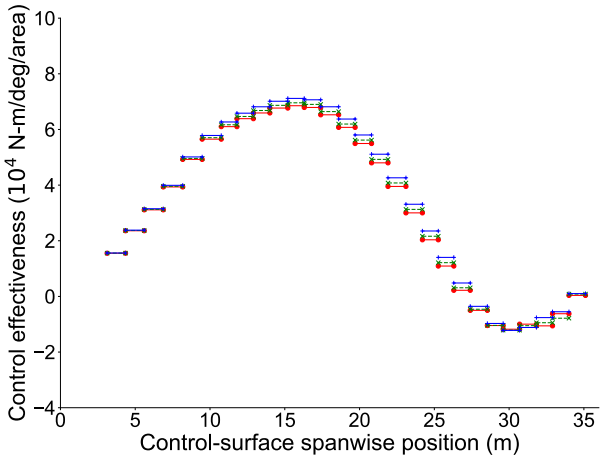

(d) Torsion stiffness, $M_\infty = 0.83$

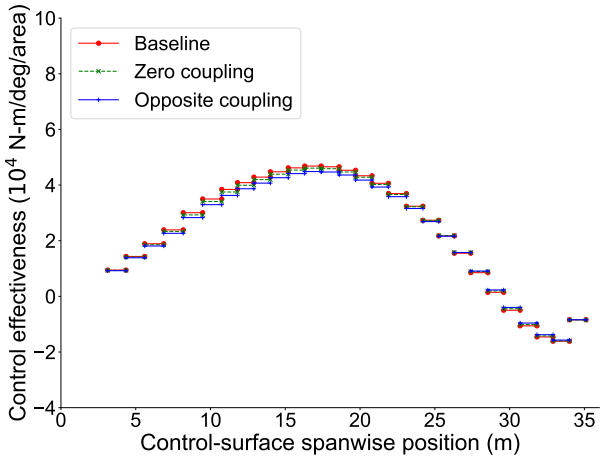

(e) Out-of-plane bending and torsion coupling, $M_\infty = 0.65$

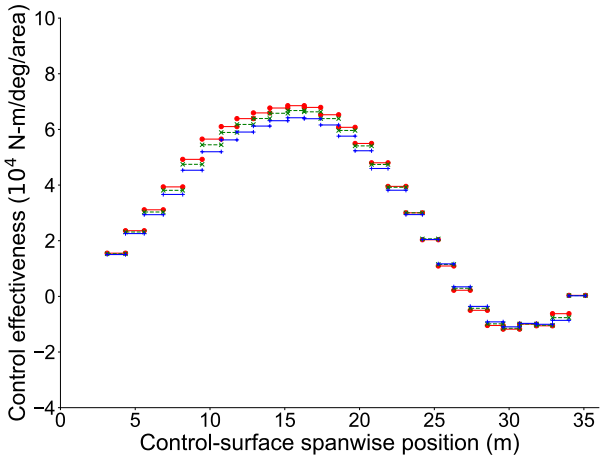

(f) Out-of-plane bending and torsion coupling, $M_\infty = 0.83$

Figure 4.6: VFA roll control effectiveness variation for uniform scaling of stiffness distributions.

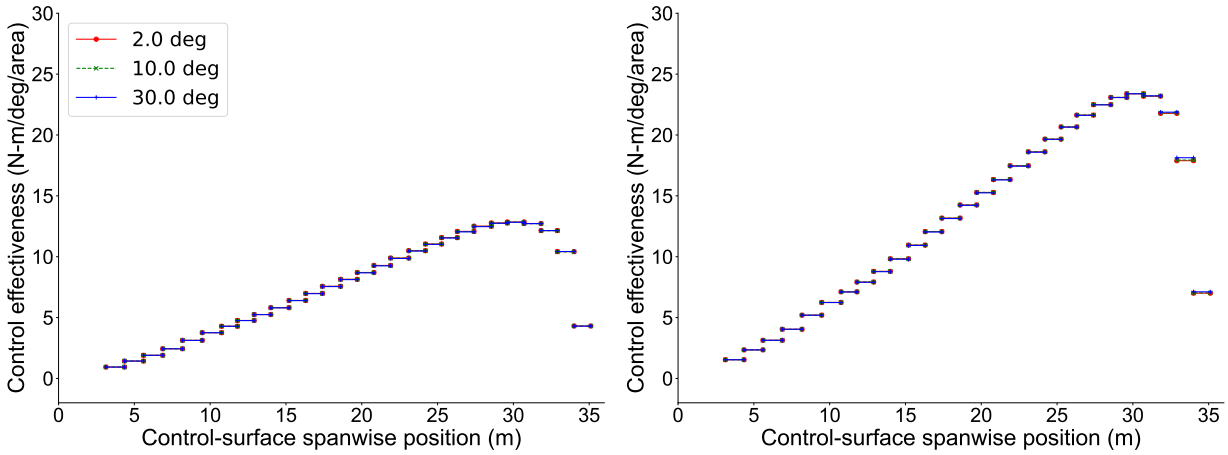

(a) Stiffened in out-of-plane bending, $M_\infty = 0.65$

(b) Stiffened in out-of-plane bending, $M_\infty = 0.83$

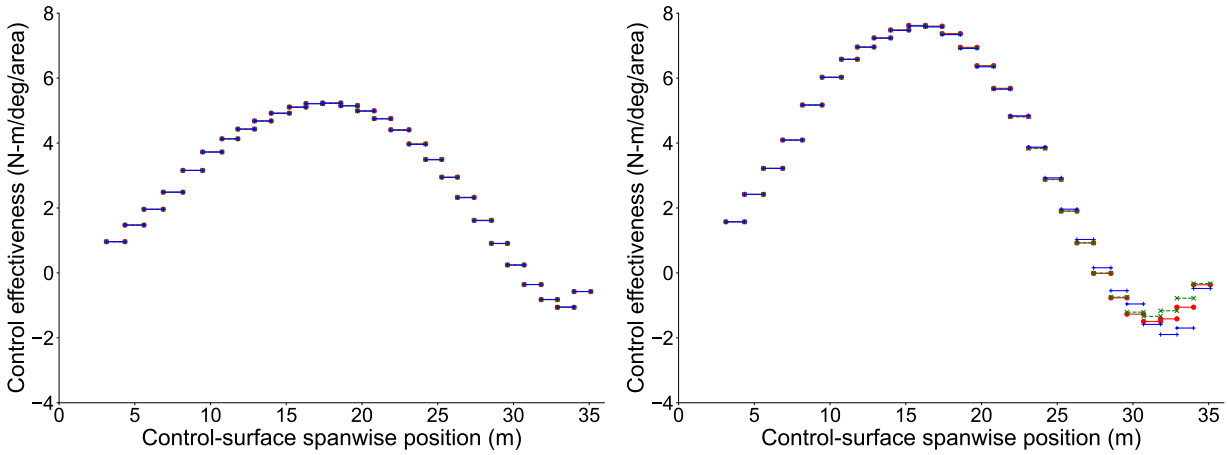

(c) Stiffened in torsion, $M_\infty = 0.65$

(d) Stiffened in torsion, $M_\infty = 0.83$

Figure 4.7: VFA roll control effectiveness variation for a stiffened wing.

shortening effects are neglected and the Jacobians used for updating the deformed configuration are evaluated in the undeformed shape. The case of non-follower aerodynamic loads neglects the change in orientation of these loads consistent with the deformed shape. The assumptions of linear kinematics and non-follower aerodynamics together correspond to a traditional linear aeroelastic analysis.

Figure 4.8 shows the results at $M_\infty = 0.65$. The FA roll response for both inboard and outboard ailerons is not impacted by the geometrically nonlinear effects. Similar behavior is observed for the VFA test case for both aileron configurations, with only slight differences at high deflection angles based on the choice of nonlinear versus linear kinematics. The impact of assuming follower or non-follower aerodynamics is negligible. These results are motivated by smaller deflections of the wing at this flight condition where linear assumptions is valid. Figure 4.9 shows the results for the $M_\infty = 0.83$. The impact of geometrically nonlinear effects is more pronounced due to the larger wing deflections. There are small variations at higher aileron deflections of the outboard ailerons for the FA test case based on the type of kinematic descriptions selected. Similar behavior is observed for the aileron configuration 2 of the VFA test case. The maximum impact, however, is observed for the aileron configuration 1 of the VFA test case. The response of the outboard ailerons for this configuration varies significantly with the type of kinematics and direction of aerodynamic loads. The roll response is lower in the case of linear kinematics and non-follower aerodynamic loads. In fact, the outboard ailerons are not in reversal when considering nonlinear kinematics and follower aerodynamics, while a reversal is predicted when considering linear kinematics or non-follower aerodynamics.

The impact of geometrically nonlinear effects is appreciable only for the outboard ailerons at flight conditions with significant wing deflections. Because the outboard ailerons have lower control effectiveness, they are unlikely to be deployed as primary control surfaces for roll maneuvers. However, there is a growing interest in exploring outboard ailerons in combination with inboard ailerons for load alleviation. For this applications, one has to consider geometrically nonlinear effects to capture the aileron response. Neglecting these effects may predict lower control effectiveness or reversal, leading to control inputs that are detrimental to load alleviation.

4.2.4 Dynamic Analysis

The influence of aileron spanwise placement is further investigated by means of dynamic simulations for selected aileron layouts chosen based on the static results of Sec. 4.2.3. The selected layouts are shown in Fig. 4.10.

For the FA test case, the selected layouts assume the segments from #16 to #18 (inboard aileron configuration, or layout #1) and the segments from #13 to #15 (outboard aileron configuration, or

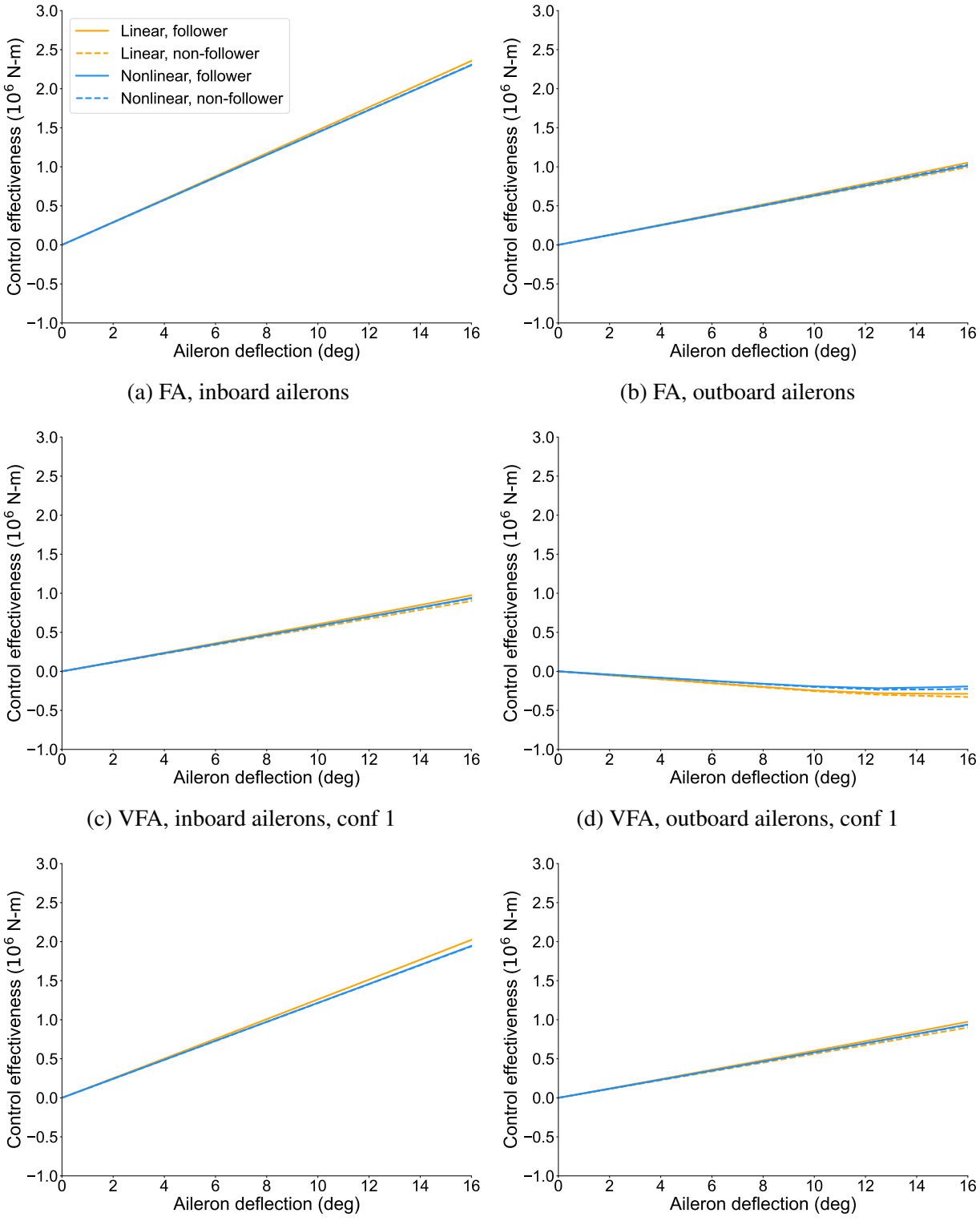

(a) FA, inboard ailerons

(b) FA, outboard ailerons

(c) VFA, inboard ailerons, conf 1

(d) VFA, outboard ailerons, conf 1

(e) VFA, inboard ailerons, conf 2

(f) VFA, outboard ailerons, conf 2

Figure 4.8: Impact of geometrically nonlinear effects on roll control effectiveness, $M_\infty = 0.65$.

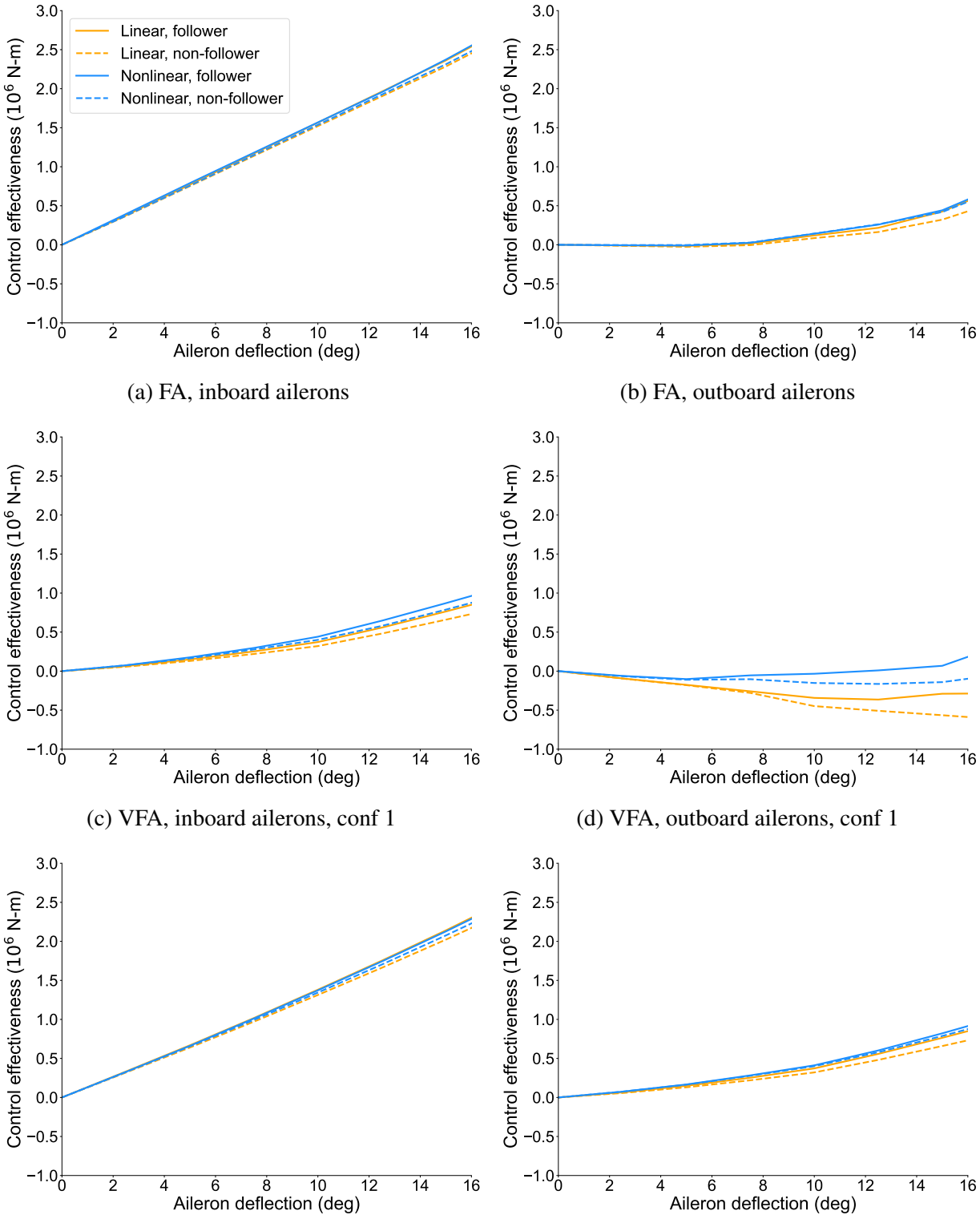

(a) FA, inboard ailerons

(b) FA, outboard ailerons

(c) VFA, inboard ailerons, conf 1

(d) VFA, outboard ailerons, conf 1

(e) VFA, inboard ailerons, conf 2

(f) VFA, outboard ailerons, conf 2

Figure 4.9: Impact of geometrically nonlinear effects on roll control effectiveness, $M_\infty = 0.83$.

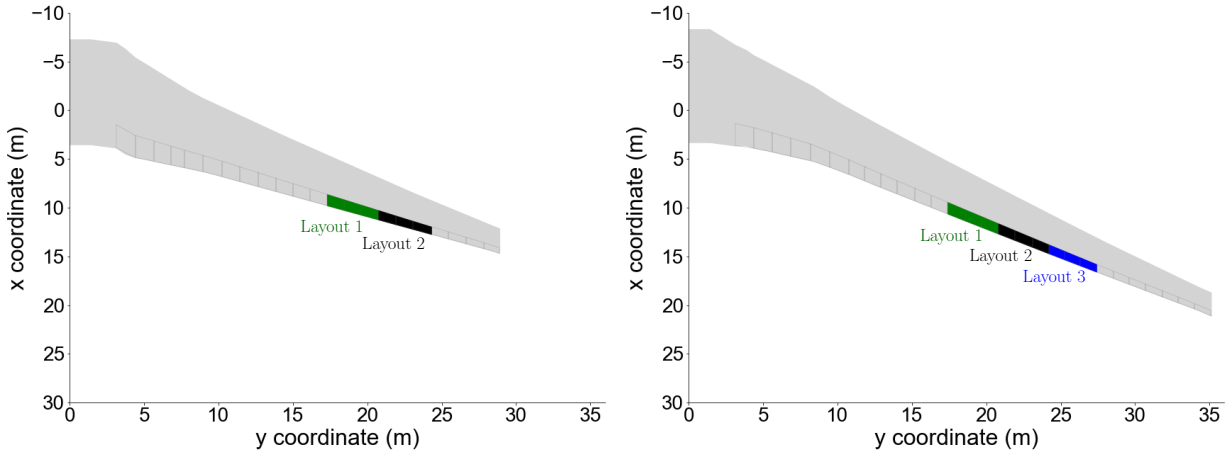

(a) FA test case

(b) VFA test case

Figure 4.10: Aileron layouts considered in dynamic analyses.

layout #2), which has higher aileron effectiveness while remaining at a similar spanwise location. For the VFA test case, layout #1 and layout #2 span the same spanwise locations from the wing root as for the FA. An additional case is considered where the control surface spans segments from #19 to #21 (layout #3). Although it has lower aileron effectiveness, this case is considered as this layout is at approximately the same non-dimensional spanwise location as the FA baseline aileron layout #2, resulting in a more outboard dimensional placement due to the longer VFA wing span. A further inboard layout is not considered in the dynamic studies because of practical constraints that may prevent placing ailerons this far inboard. Furthermore, control effectiveness only increases moderately for control surface segments inboard of the layout #1 (see Fig. 4.4), then it decreases as moving closer to the wing root.

The dynamic roll responses of the FA and VFA test cases are compared for a bank-to-bank maneuver commanded by applying an anti-symmetric control-surface deflection starting from a trimmed level flight condition at 1 g. The time history of the deflection applied to the right wing control surface is shown in Fig. 4.11. This time history is determined so that the FA with layout #2, which corresponds to the FA baseline aileron configuration, meets the roll maneuverability requirement reported in the regulations [53]. With the anti-symmetric input in Fig. 4.13 applied to layout #2, the FA performs the bank-to-bank maneuver in 9.5 seconds at $M_\infty = 0.65$. The same input is applied to all the FA and VFA aileron layouts to compare the roll responses.

The static analyses showed the impact of wing flexibility on control effectiveness of the VFA test case compared with the FA test case. For dynamic maneuvers, the higher roll moment of inertia of the VFA test case also impacts the roll rate. Additionally, as explained in Sec. 4.1, the roll rate also depends on the roll damping, which increases with the wingspan. For a rigid

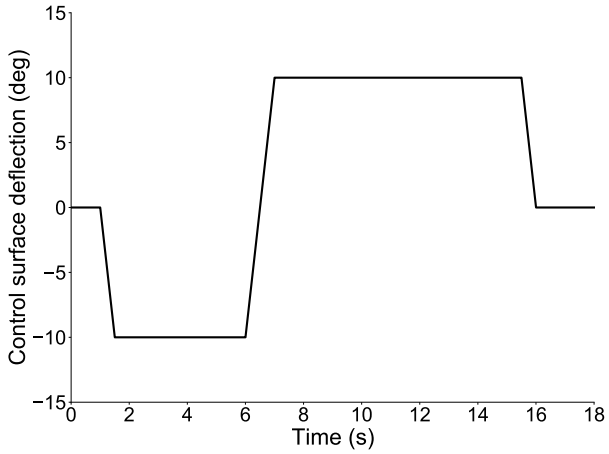

Figure 4.11: Right control-surface deflection.

wing, the relationship of roll damping with wingspan can be established analytically. For a flexible wing, aeroelastic deflections and washout effects (in the presence of sweep) alter the roll damping. Therefore, dynamic roll responses of FA and VFA test case are first compared for different layouts for the case of rigid wing in Fig. 4.12. This corresponds to isolating the impact of the longer wing span of the VFA test case, which increases the roll moment of inertia and the roll damping, without considering its indirect impact on the roll damping due to the higher flexibility. The roll response for the rigid wing is simulated for only a step input (the first five seconds of the bank-to-bank input in Fig. 4.11). This is because, at $M_\infty = 0.83$, the roll angle increases significantly for a rigid wing, resulting in the aircraft nearing a 90-degree roll angle. For a rigid wing at $M_\infty = 0.65$, the VFA develops a smaller steady roll rate compared with the FA due to the larger roll inertia and increased roll damping, which come from the longer span. However, the ailerons of the VFA test case have larger areas than the ones of the FA, so developing higher roll moment (see Fig. 4.5). For the given control surface deflection, the detrimental impact of the larger roll moment of inertia and roll damping is higher at $M_\infty = 0.65$, making the VFA test case roll more slowly. At $M_\infty = 0.83$, the higher roll moments developed by the VFA have a more prominent effect and the FA and VFA test cases have a comparable roll response. For this case that considers a rigid wing, there are no differences in the response with the spanwise placement of the selected aileron layouts. This is because the higher roll control effectiveness associated with a more inboard placement is counter balanced by the longer moment arm of an outboard placement.

Figures 4.13 show bank-to-bank maneuvers for the case of flexible wings. At $M_\infty = 0.65$, FA develops the required 60-deg roll angle change faster when deflecting the ailerons for layout #1 than for layout #2, consistently with the static results. The VFA has a slower roll response than the FA for both the aileron layouts #1 and #2 at $M_\infty = 0.65$ due to a larger roll moment of inertia by the longer wing span. The VFA with layout #3 maneuvers much more slowly and

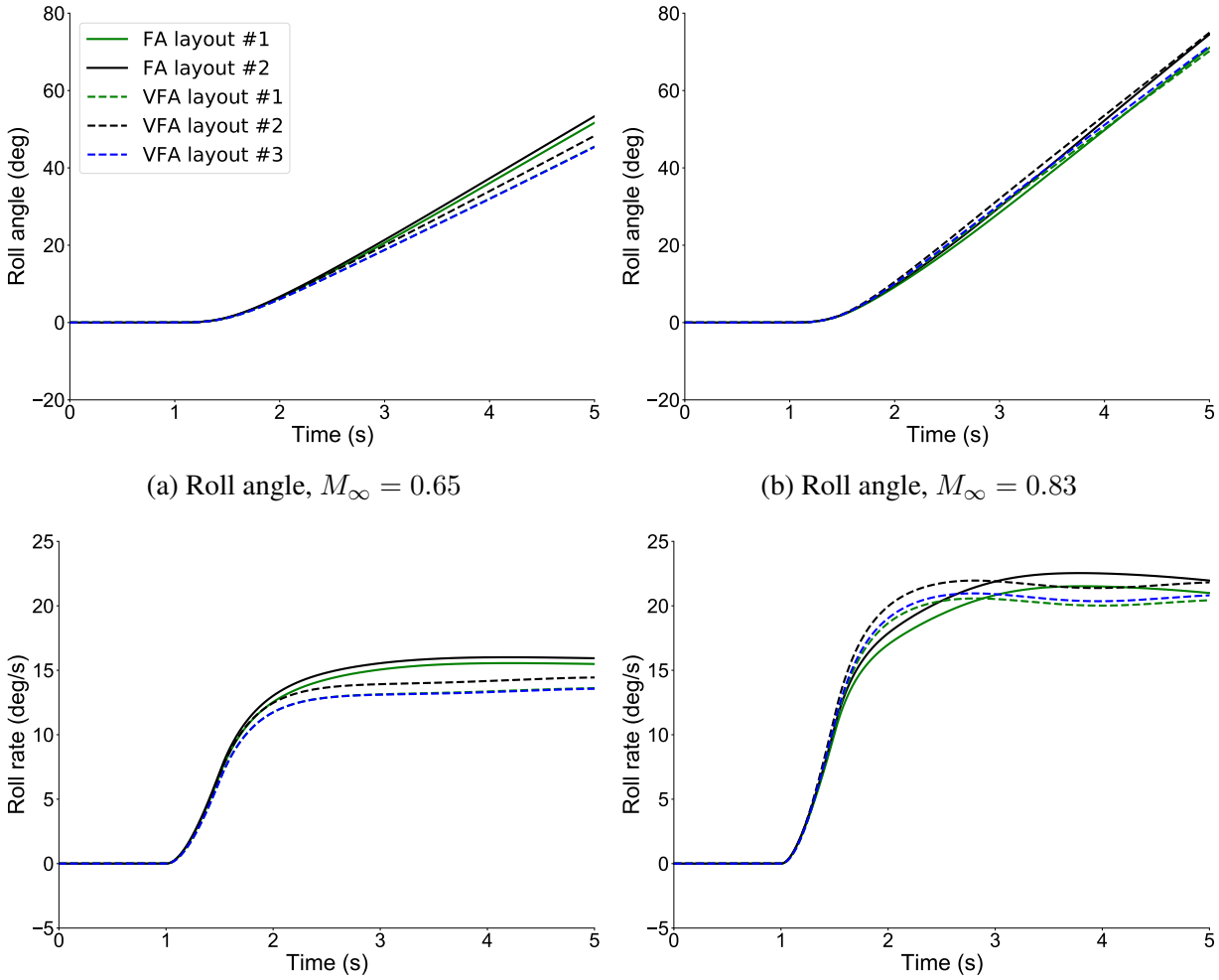

(a) Roll angle, $M_\infty = 0.65$

(b) Roll angle, $M_\infty = 0.83$

(c) Roll rate, $M_\infty = 0.65$

(d) Roll rate, $M_\infty = 0.83$

Figure 4.12: VFA vs. FA step input maneuver (rigid wing).

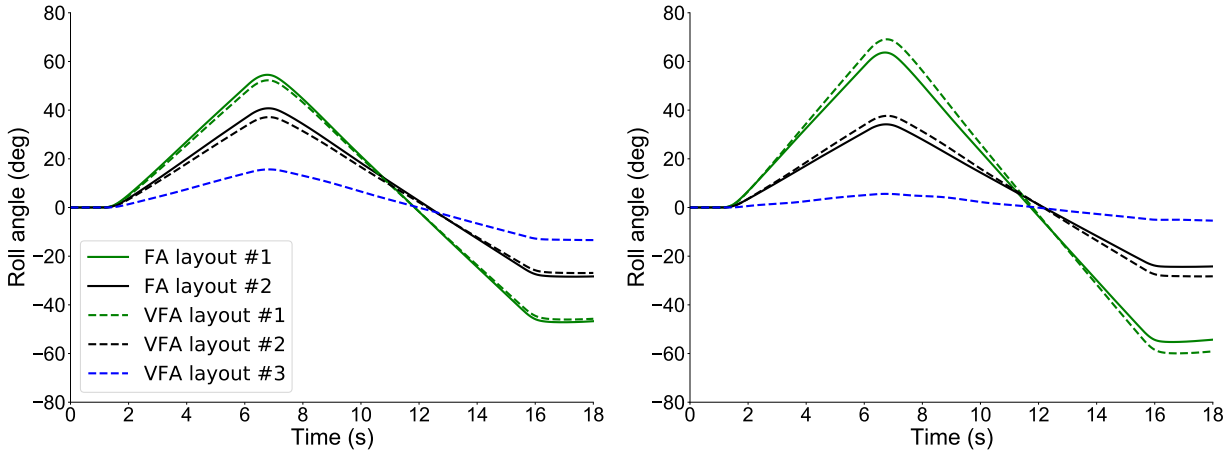

(a) Roll angle, $M_\infty = 0.65$

(b) Roll angle, $M_\infty = 0.83$

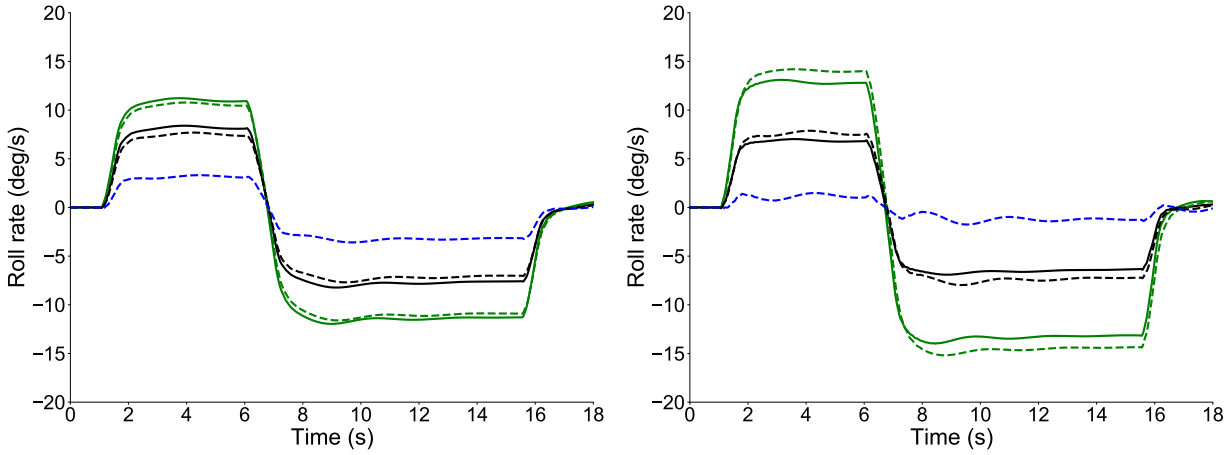

(c) Roll rate, $M_\infty = 0.65$

(d) Roll rate, $M_\infty = 0.83$

Figure 4.13: VFA vs. FA bank-to-bank maneuver.

would require a much higher control surface deflection to meet the certification criterion, which might not be practically feasible with limitations on the hinge loads, actuation bandwidth etc. The results at $M_\infty = 0.83$ show that the VFA test case has higher roll maneuverability when deflecting aileron layouts #1 and #2 compared with the FA test case. The VFA ailerons have comparable effectiveness than the corresponding FA ailerons at $M_\infty = 0.83$, as shown in Fig. 4.5b. However, roll damping effects are smaller for the VFA test case due to the washout effects in the wingtip region, which are more pronounced at this flight condition. The higher impact of aeroelastic effects at this flight condition can also be appreciated by the higher roll maneuverability of the most inboard placement (layout #1) at this flight condition compared with $M_\infty = 0.65$. On the other hand, a lower maneuverability for layouts #2 and #3 is observed at this flight conditions because these regions are subjected to higher out-of-plane deflections, which impact control effectiveness.

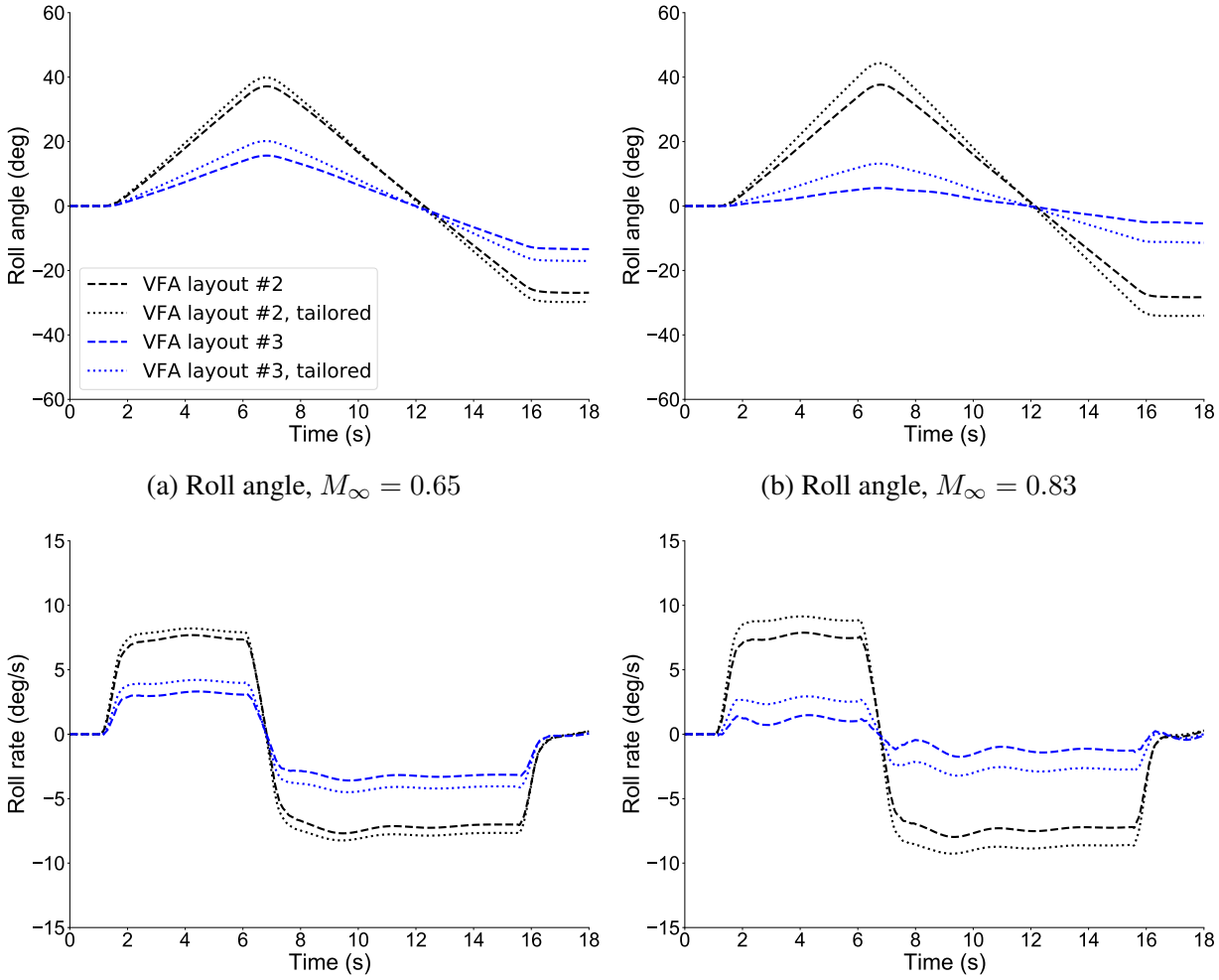

(a) Roll angle, $M_\infty = 0.65$

(b) Roll angle, $M_\infty = 0.83$

(c) Roll rate, $M_\infty = 0.65$

(d) Roll rate, $M_\infty = 0.83$

Figure 4.14: VFA bank-to-bank maneuver with aeroelastically tailored wingbox.

For the VFA, aileron effectiveness decreases considerably for layout #3 due to aeroelastic effects, resulting in a very slow roll maneuver compared to the other configurations.

Figures 4.14 shows results for the selected layouts combined with wingbox passive aeroelastic tailoring. Based on the parametric studies in Sec. 4.2.4, modified wingbox designs are considered where the out-of-plane bending and torsion stiffness are increased by 15% uniformly along the span. The roll maneuvers in Fig. 4.13 are then repeated for the VFA test case considering the aeroelastically tailored wingbox and by deflecting aileron layouts #2 and #3. At both the flight conditions, the VFA test case with a tailored wingbox shows faster the roll response compared with baseline wingbox. Higher improvements are observed for the more outboard located layout #3. The impact of wingbox passive aeroelastic tailoring becomes stronger at $M_\infty = 0.83$. However, applying wingbox passive aeroelastic tailoring is not sufficient to improve the roll response for the

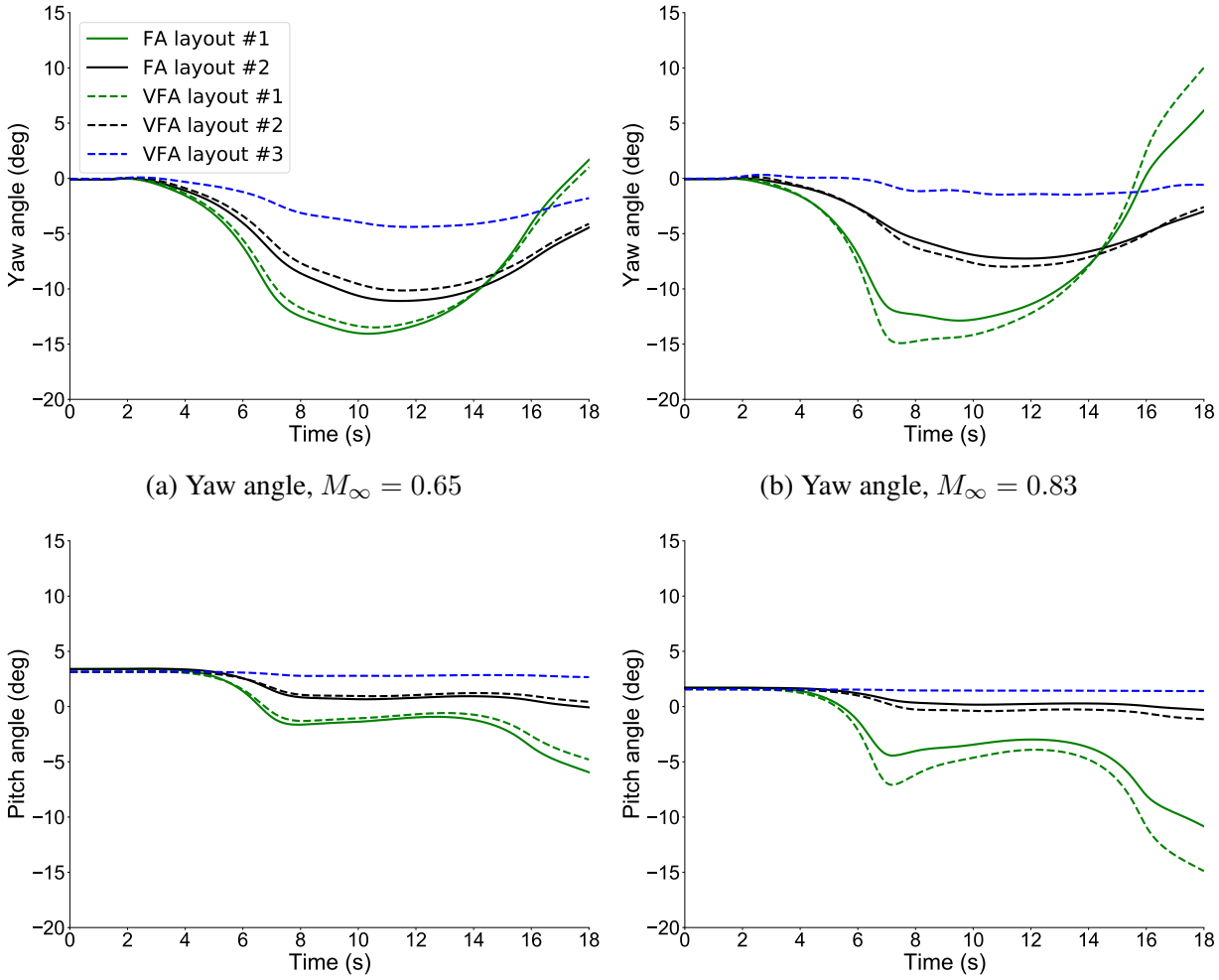

(a) Yaw angle, $M_\infty = 0.65$

(b) Yaw angle, $M_\infty = 0.83$

(c) Pitch angle, $M_\infty = .65$

(d) Pitch angle, $M_\infty = 0.83$

Figure 4.15: VFA vs. FA bank-to-bank maneuver (lateral/longitudinal response).

case of aileron layout #3 so it is comparable with the response of the more inboard aileron layout #2. Finally, Fig. 4.15 shows results for the effect of different control surface placements on the lateral and longitudinal response of the aircraft during the roll maneuver considered in this section. The impact on the longitudinal response is more minor, especially for the layout #2 and #3. An inboard placement creates a higher effect of adverse yaw. At $M_\infty = 0.83$, higher variations in pitch and yaw are observed for the VFA test case with the most inboard layout.

This section investigated the impact of the spanwise placement of trailing-edge control surfaces on roll maneuverability. The studies in the remainder of the chapter will investigate the effect of the spanwise placement of trailing-edge control surfaces on maneuver load alleviation. The feasibility of deploying leading-edge control surfaces and FFWTs for improving roll maneuverability will also be investigated.

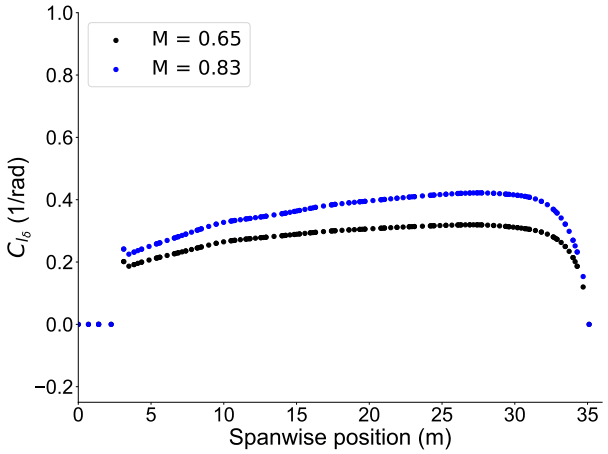

Figure 4.16: VFA spanwise variation of c_{l_δ} for leading-edge control surfaces.

4.3 Leading-Edge Control Surfaces

This section compares the roll maneuverability and load alleviation capabilities of leading-and trailing-edge control surfaces for the VFA test case. The impact of the spanwise placement of leading-edge control surfaces will be examined against the trailing-edge control surfaces.

First, Sec. 4.3.1 details the control surface modeling. Sec. 4.3.2 presents static results for varying control-surface placement. Finally, Sec. 4.3.3 presents dynamic simulations of roll maneuvers for selected control-surface layouts.

4.3.1 Analysis Setup

The control-surface derivatives for the leading-edge control surfaces are obtained from a literature ratio between the trailing- and leading-edge values [71]. The ratio of the leading- to trailing-edge C_{l_δ} values is assumed as 0.074 and the one between the C_{m_δ} values is assumed to be -0.251. The control-surface chord to wing chord fraction is 0.10 for the leading-edge control surfaces. Figure 4.16 shows the variation of the c_{l_δ} along the VFA wing span for two flight conditions $M_\infty = 0.65, 0.83$ using the assumed parameters. The c_{m_δ} is a constant value equal to 0.16 rad^{-1}. Similar to the trailing-edge control surfaces in Fig. 4.1, the VFA test case is subdivided into multiple segments associated with the leading-edge control surfaces that can deflect individually. Fig. 4.17 shows the trailing- and leading-edge control surfaces that are located at same spanwise location as reported in Table 4.1.

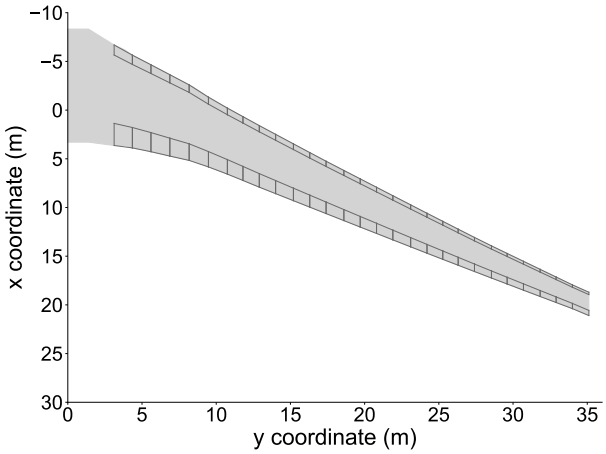

Figure 4.17: Leading-edge vs. trailing-edge control-surface spanwise definition for the VFA test case.

4.3.2 Static Analysis

The effect of leading-edge control surfaces on load alleviation compared to trailing-edge control surfaces is studied by quantifying the out-of-plane bending and torsion moment variation at the wing root. The roll control effectiveness (defined in Sec. 4.2.3) is also presented to explore the trade-off between maneuverability and load alleviation. The trailing-edge results for control effectiveness are shown again to highlight the differences.

A spanwise placement study for the leading- and trailing-edge control surfaces is presented. Wing root bending and torsion moment variation and roll control effectiveness are compared for given deflections of each leading- and trailing-edge control surface defined in Fig. 4.17. The loads are shown at the wing root because trends are similar for other locations. Similar to the roll control effectiveness, the wing root moment variations are normalized by the control-surface deflection angle and area. The sign of the roll control effectiveness is such that a negative sign means control reversal. A negative value of bending or torsion moment variation indicates load alleviation with respect to the loads at the static aeroelastic solution without deflected control surfaces.

First, the roll control effectiveness of the leading- and trailing-edge control surfaces are compared in Fig. 4.18 considering the wing as rigid. Horizontal bars denote the control-surface spanwise location. For both flight conditions, roll control effectiveness peaks when deflecting control surfaces at 85% of the semispan. Similar to results in Sec. 4.2.3, there is a trade-off between the increase in the moment arm and the drop in c_{l_δ} (see Fig. 4.17) toward the wingtip. Roll control effectiveness of trailing-edge control surfaces is an order of magnitude higher than the one of leading-edge control surfaces due to their larger control-surface derivatives. Higher dynamic pressure increases control effectiveness because the rigid wing generates more lift for the same

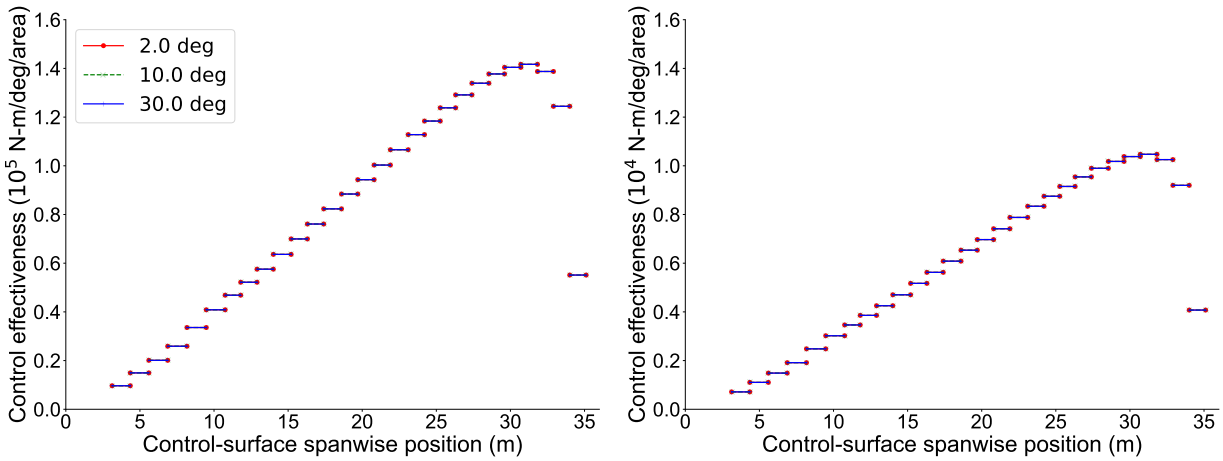

(a) Trailing-edge control surfaces, $M_\infty = 0.65$

(b) Leading-edge control surfaces, $M_\infty = 0.65$

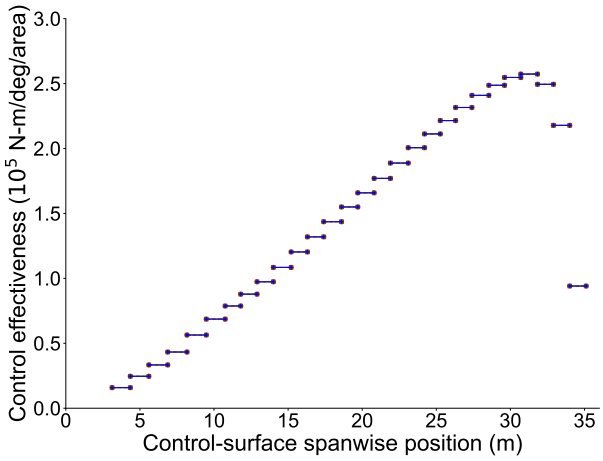

(c) Trailing-edge control surfaces, $M_\infty = 0.83$

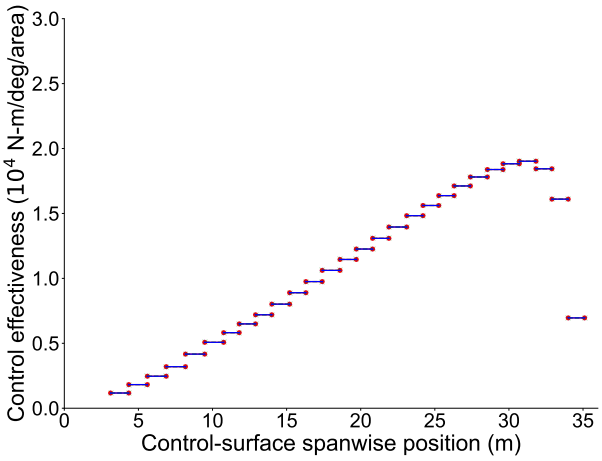

(d) Leading-edge control surfaces, $M_\infty = 0.83$

Figure 4.18: Roll control effectiveness as a function of control-surface spanwise placement (rigid wing).

control-surface deflection. For this rigid case, control effectiveness is the same regardless of the control-surface deflection due to the lack of aeroelastic effects.

The results for the wing considered as flexible are shown in Figs. 4.19 to 4.19. In this case, the roll control effectiveness peaks around the same spanwise location for both types of control surfaces. For a flexible wing, the roll aerodynamic moment is impacted by the loss in lift due to wash-out effects and the increase in lift due to control-surface deflection, the latter being the only contribution for a rigid wing. At a given flight condition, larger wing aeroelastic deflections towards the wingtip cause more substantial wash-out effects in that region. This makes roll control effectiveness drop when deflecting control surfaces outboard of the midspan despite their longer moment arm. Also, compared to the rigid wing, the difference between the maximum control

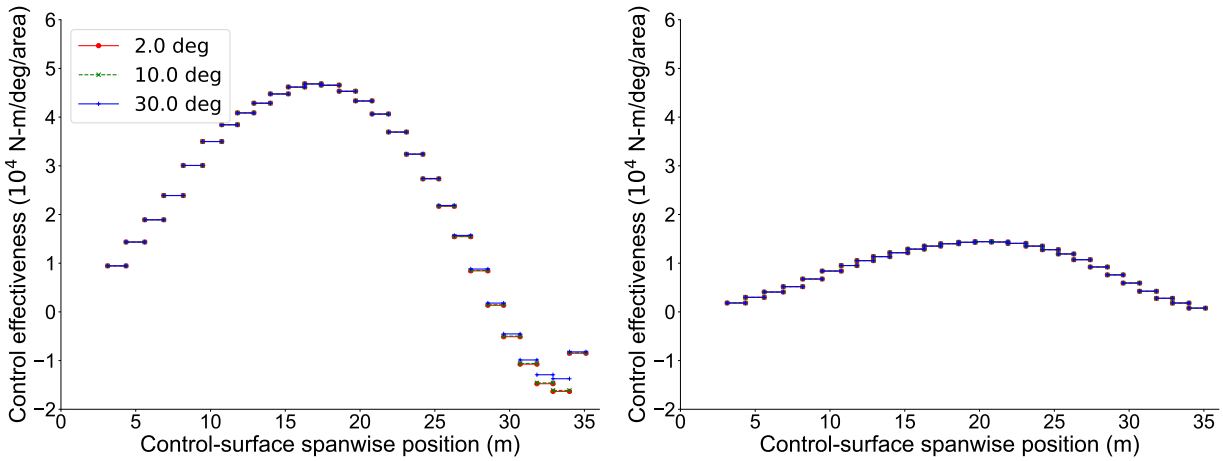

(a) Trailing-edge control surfaces, $M_\infty = 0.65$

(b) Leading-edge control surfaces, $M_\infty = 0.65$

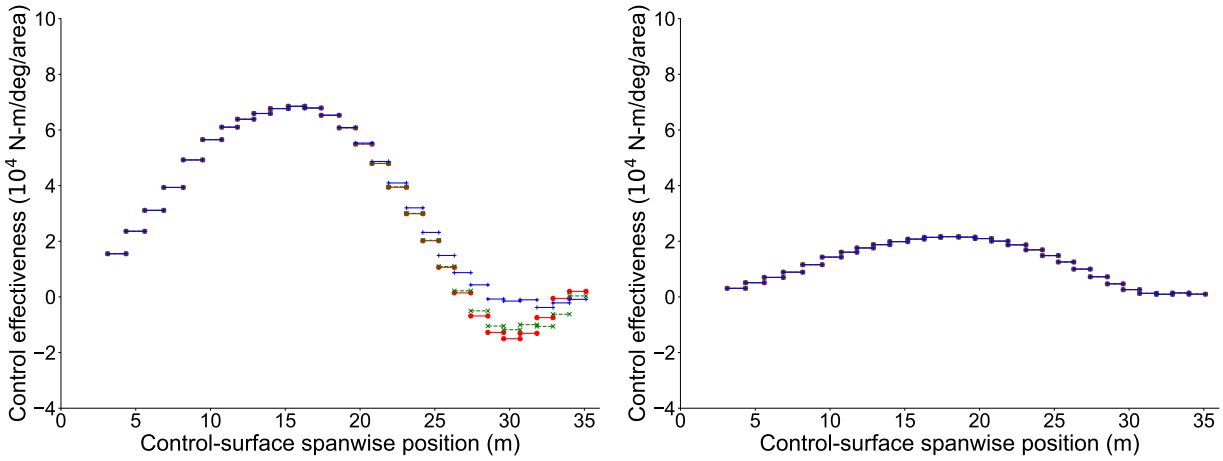

(c) Trailing-edge control surfaces, $M_\infty = 0.83$

(d) Leading-edge control surfaces, $M_\infty = 0.83$

Figure 4.19: Roll control effectiveness as a function of control-surface spanwise placement (flexible wing).

effectiveness of the trailing-edge control surfaces compared to the leading-edge control surfaces is lower. This is motivated by a lower drop in the effectiveness of the leading-edge control surfaces due to their pitching moment, which counters the washout effects. At higher dynamic pressure, trailing-edge control surfaces show stronger nonlinear effects, though control reversal is avoided for certain deflections near the wingtip (Fig. 4.19c). This behavior is motivated by the low torsional stiffness as explained in Sec. 4.2. The leading-edge control surfaces show no control reversal and behave linearly for varying control-surface deflection. This is motivated by their smaller roll control effectiveness than the trailing-edge control surfaces at the same spanwise locations due to lower control-surface derivatives. Also, leading-edge control surfaces produce a positive moment, which counteracts wash-out effects and prevents reversal.

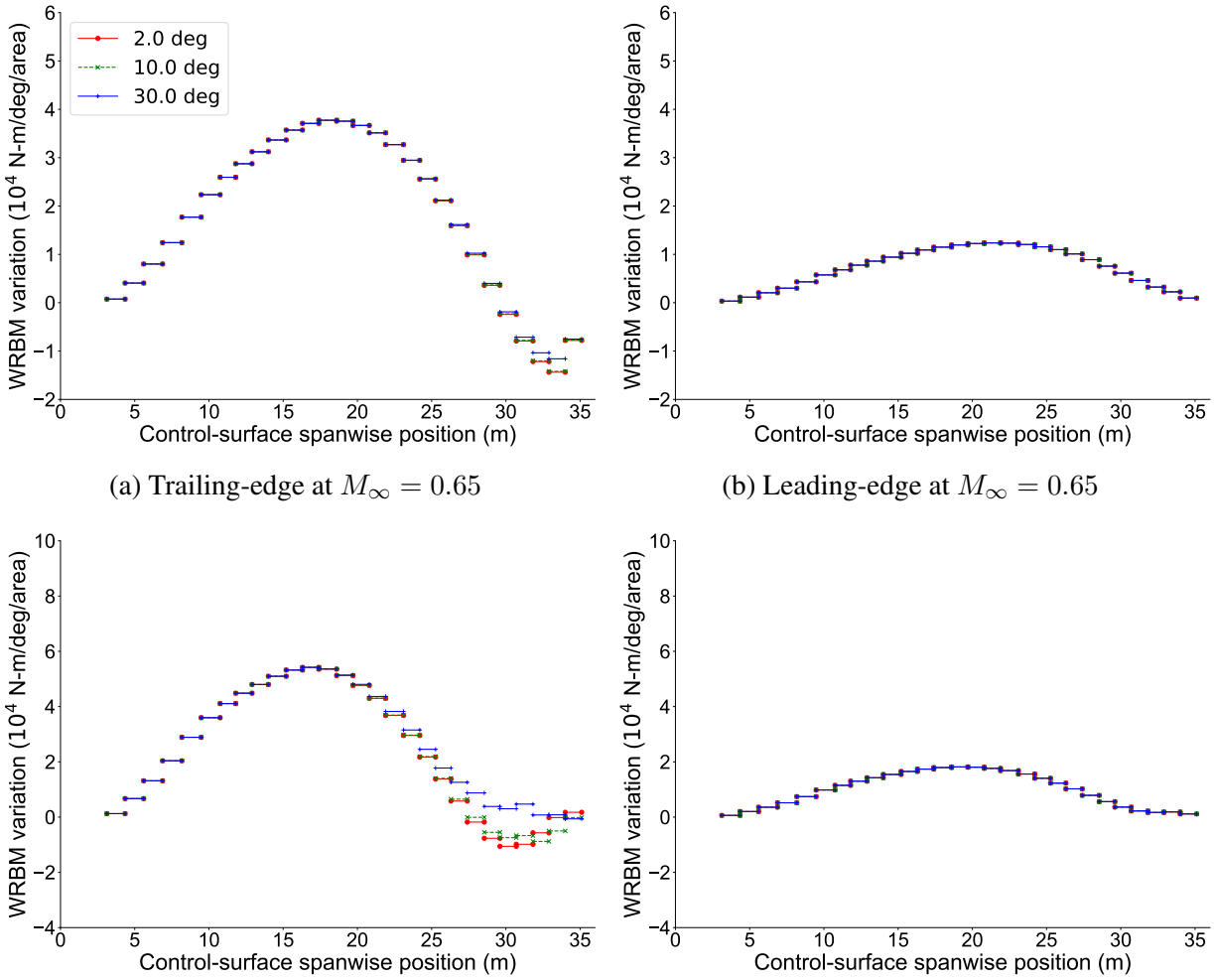

(a) Trailing-edge at $M_\infty = 0.65$

(b) Leading-edge at $M_\infty = 0.65$

(c) Trailing-edge at $M_\infty = 0.83$

(d) Leading-edge at $M_\infty = 0.83$

Figure 4.20: Out-of-plane wing root bending moment variation as a function of control-surface spanwise placement (flexible VFA wing).

Figures 4.20 to 4.21 show that the WRBM (wing root bending moment) and WRTM (wing root torsion moment) variation follows the roll control effectiveness trend. Deflecting control surfaces with higher effectiveness increases loads: the balance between alleviating loads and increasing effectiveness drives the optimal control-surface placement along the span (in addition to other factors such as hinge moments, control-surface mass etc.). Deflecting a leading-edge control surface at the wingtip alleviates out-of-plane wing root bending moment while avoiding control reversal that would be experienced by a trailing-edge control surface at the same location.

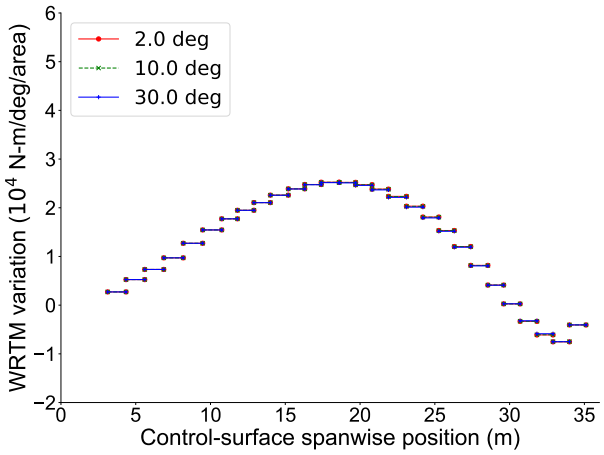

(a) Trailing-edge at $M_\infty = 0.65$

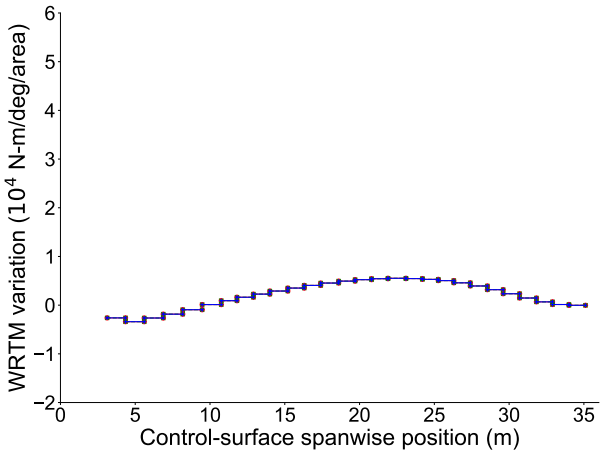

(b) Leading-edge at $M_\infty = 0.65$

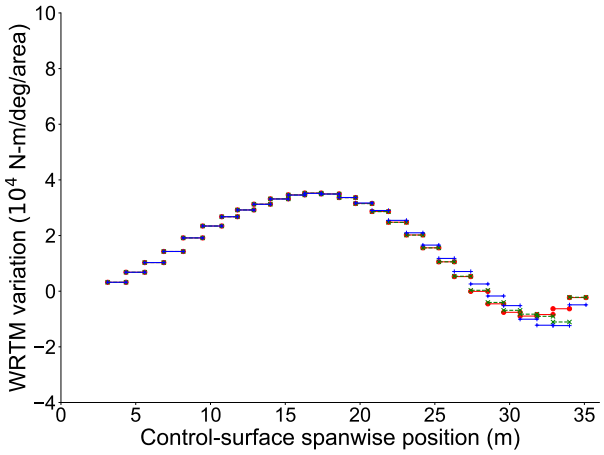

(c) Trailing-edge at $M_\infty = 0.83$

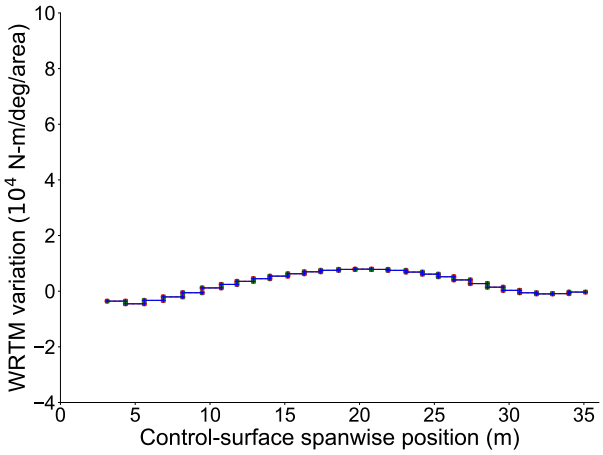

(d) Leading-edge at $M_\infty = 0.83$

Figure 4.21: Wing root torsion moment variation as a function of control-surface spanwise placement (flexible VFA wing).

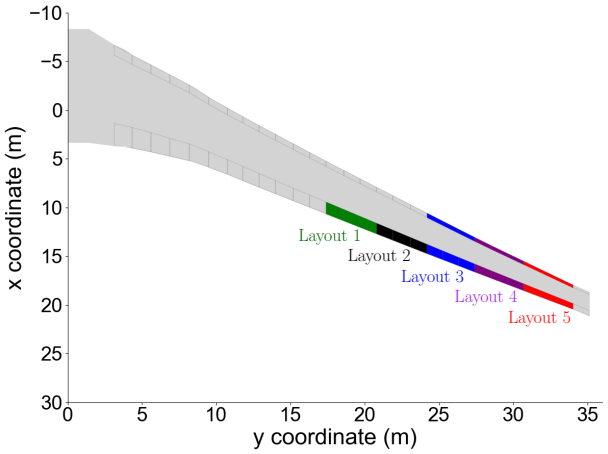

Figure 4.22: Selected control surface layouts for dynamic studies.

4.3.3 Dynamic Analysis

To further investigate the impact of leading- and trailing-edge control surface placement, dynamic analyses are conducted for selected layouts as defined in Fig. 4.22. Two layouts are selected in both the inboard and outboard regions. The inboard layouts signify regions till the end of layout #3, which is close to the tip of the FA test case (see Table 4.1).

Placing a control surface further than layout #5 results in a non-converged numerical solution within the simulation; hence, only two layouts are further considered in the outboard region for this study. The two inboard layouts are selected in the region where maximum control effectiveness is obtained from the static studies. The dynamic analyses consider the same input as studies in Sec. 4.2.4 (see Fig. 4.11).

Results for the selected inboard layouts at $M_\infty = 0.65, 0.83$ are shown in Figs. 4.24 and 4.23. At lower dynamic pressure, smaller loads and slower roll maneuvers are obtained. The inboard leading-edge control surfaces are ineffective compared to the trailing-edge control surfaces at the lower dynamic pressure condition. However, for layout #3 at $M_\infty = 0.83$, the leading-edge control surface roll response is comparable to the trailing-edge control surface while producing smaller loads at the wing root. The more inboard layout #2 produces the highest loads at the wing root and a larger roll angle and roll rate. These trends are consistent with the static results. Figure. 4.25 shows another comparison for the layout #2 with leading-edge control surfaces deflected by 25 degrees compared to the trailing-edge control surfaces deflected by 10 degrees. As expected, the roll maneuverability of the leading-edge control surfaces improves (still lower than trailing-edge control surfaces). However, while the bending loads at the root have also scaled, the torsional loads remain significantly lower than the trailing-edge control surfaces. These results show that even with similar roll control effectiveness, torsional loads can be alleviated by deploying leading-

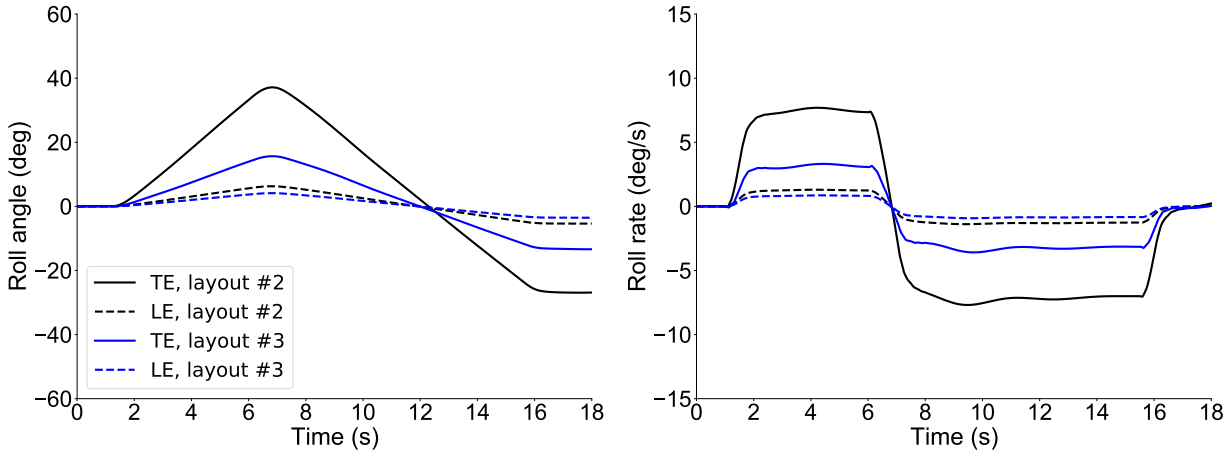

(a) Roll angle

(b) Roll rate

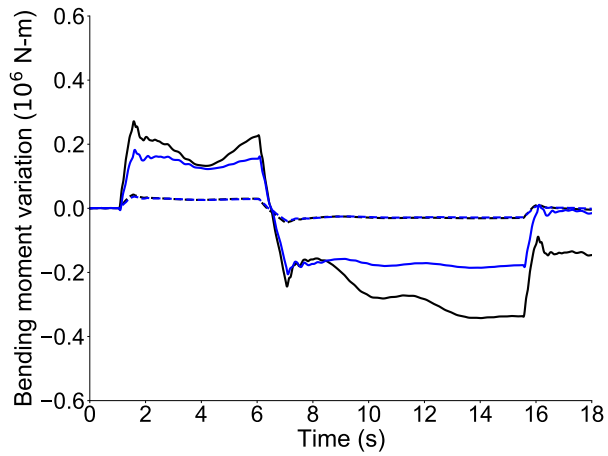

(c) Wing root out-of-plane bending moment

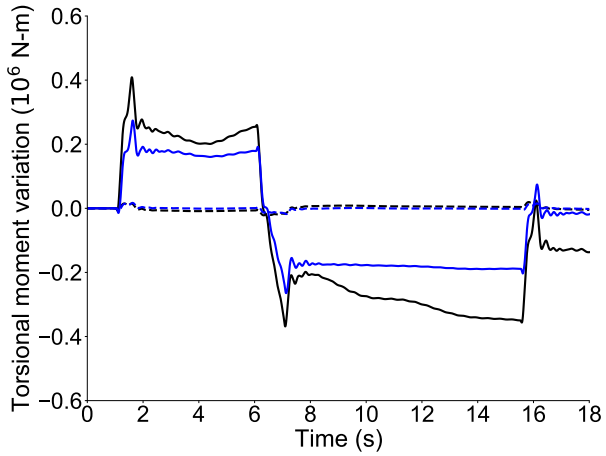

(d) Wing root torsion moment

Figure 4.23: Roll maneuver with inboard control surfaces at $M_\infty = 0.65$.

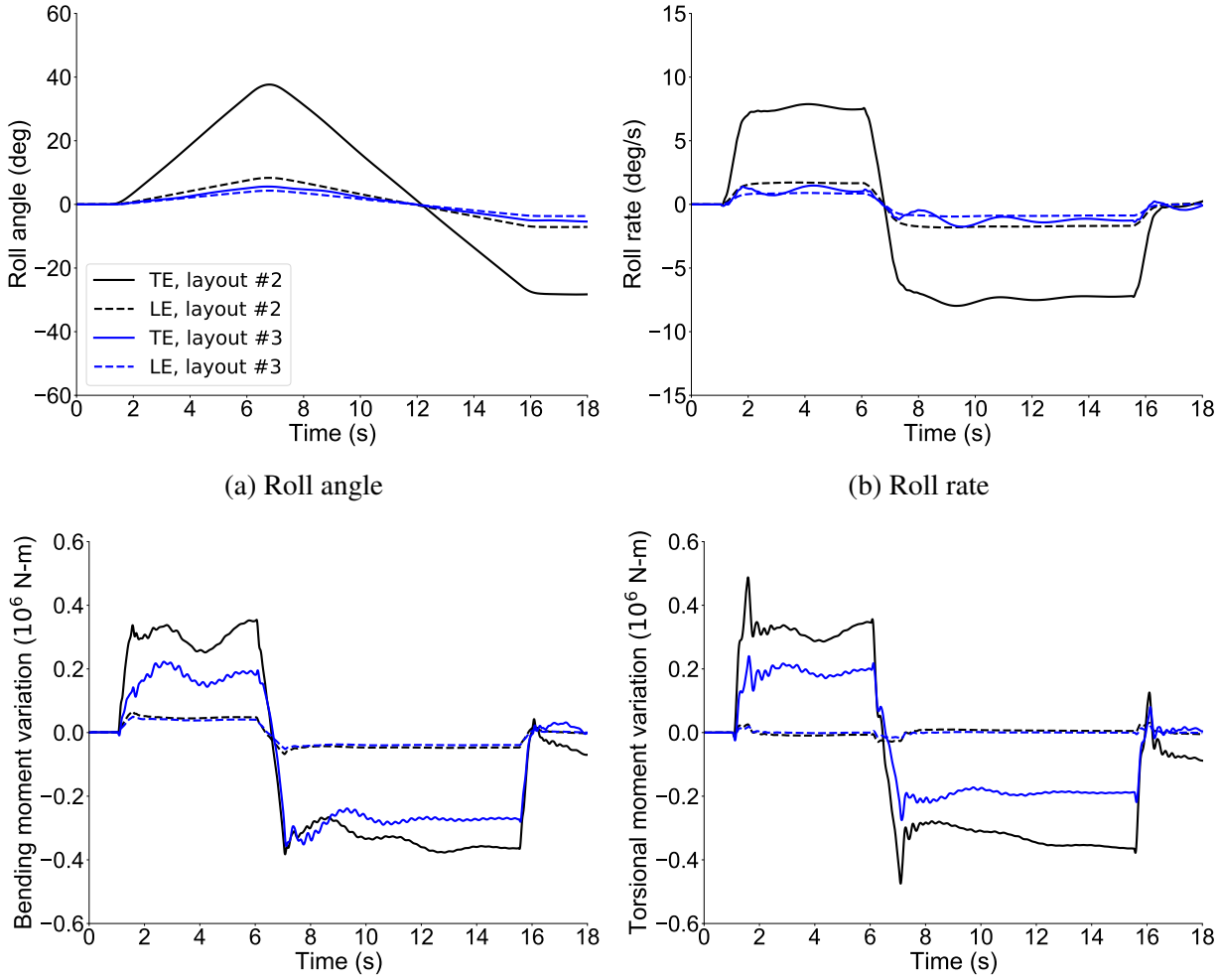

(a) Roll angle

(b) Roll rate

(c) Wing root out-of-plane bending moment

(d) Wing root torsion moment

Figure 4.24: Roll maneuver with inboard control surfaces at $M_\infty = 0.83$.

edge control surfaces.

Results for the outboard layouts are shown in Fig. 4.26 for $M_\infty = 0.65, 0.83$. The outboard layouts are less effective than the inboard ones, as seen with the static results. For layout #4, the leading-edge control surfaces give a faster roll response and produce lower loads at the wing root. In contrast, the outboard trailing-edge control surfaces are in reversal. In fact, for the most outboard layout, #5, the trailing-edge deployed in the opposite direction enables higher maneuverability while producing lower loads. However, at $M_\infty = 0.83$, the simulation with trailing-edge control surfaces diverges (see Fig. 4.27).

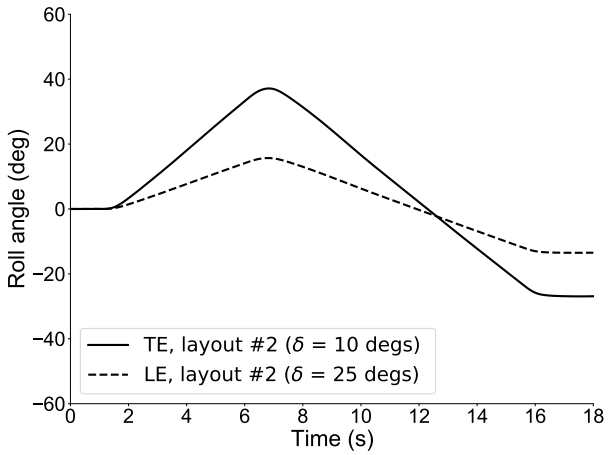

(a) Roll angle, $M_\infty = 0.65$

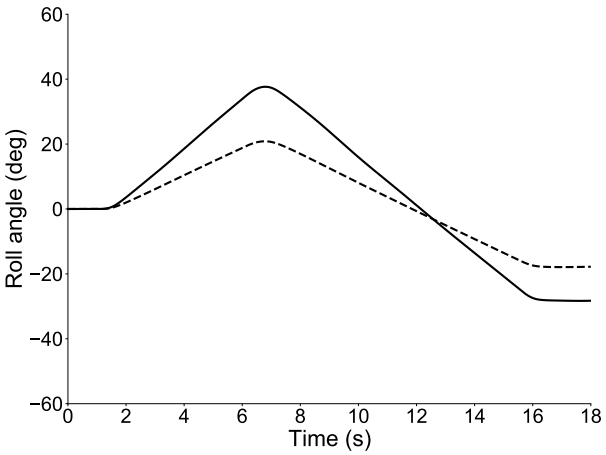

(b) Roll angle, $M_\infty = 0.83$

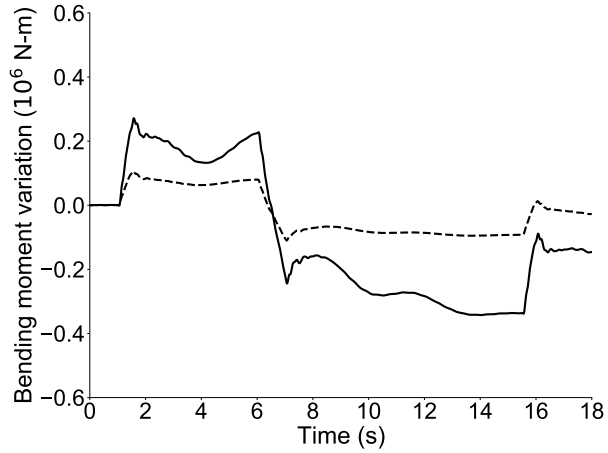

(c) Wing root out-of-plane bending moment, $M_\infty = 0.65$

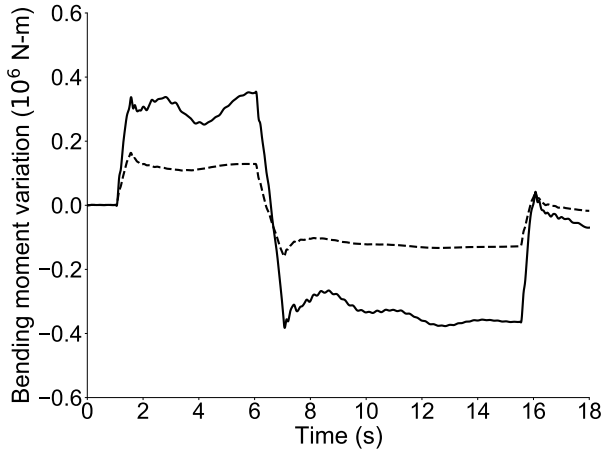

(d) Wing root out-of-plane bending moment, $M_\infty = 0.83$

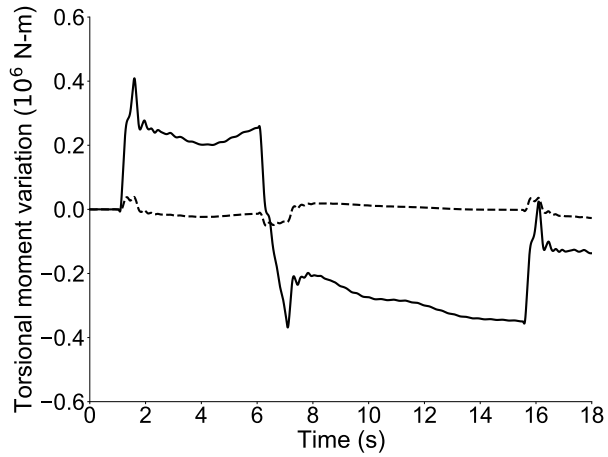

(e) Wing root torsion moment, $M_\infty = 0.65$

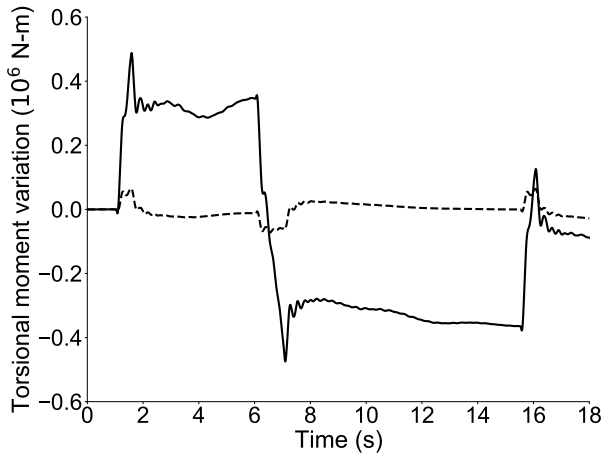

(f) Wing root torsion moment, $M_\infty = 0.83$

Figure 4.25: Roll maneuver with layout #2, TE deflected 10 degs vs. LE deflected 25 degs.

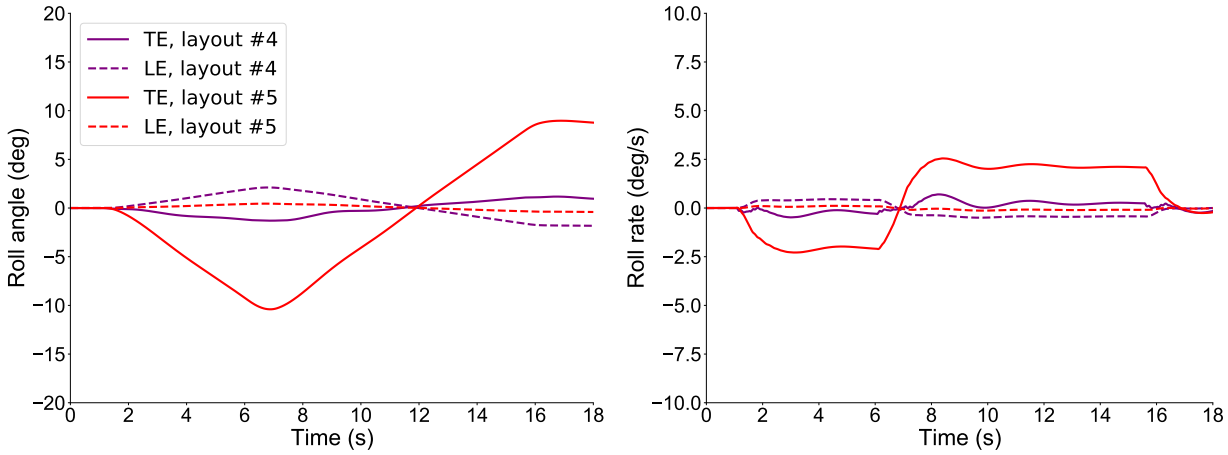

(a) Roll angle

(b) Roll rate

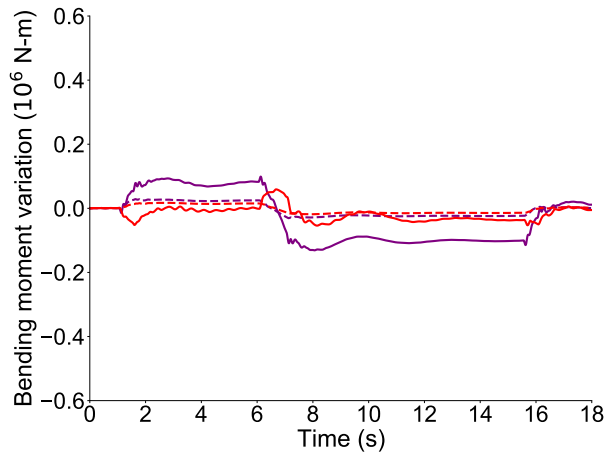

(c) Wing root out-of-plane bending moment

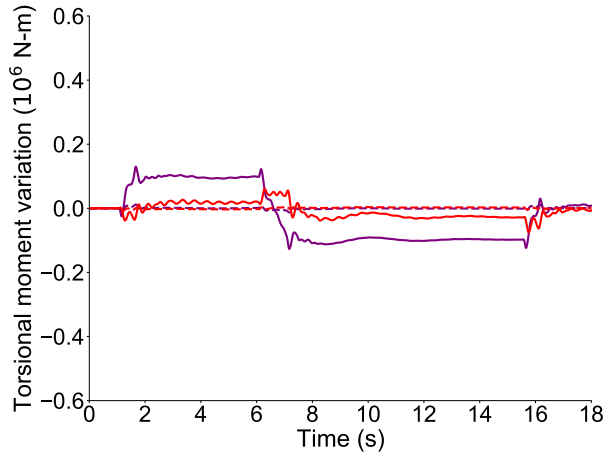

(d) Wing root torsion moment

Figure 4.26: Roll maneuver with outboard control surfaces at $M_\infty = 0.65$.

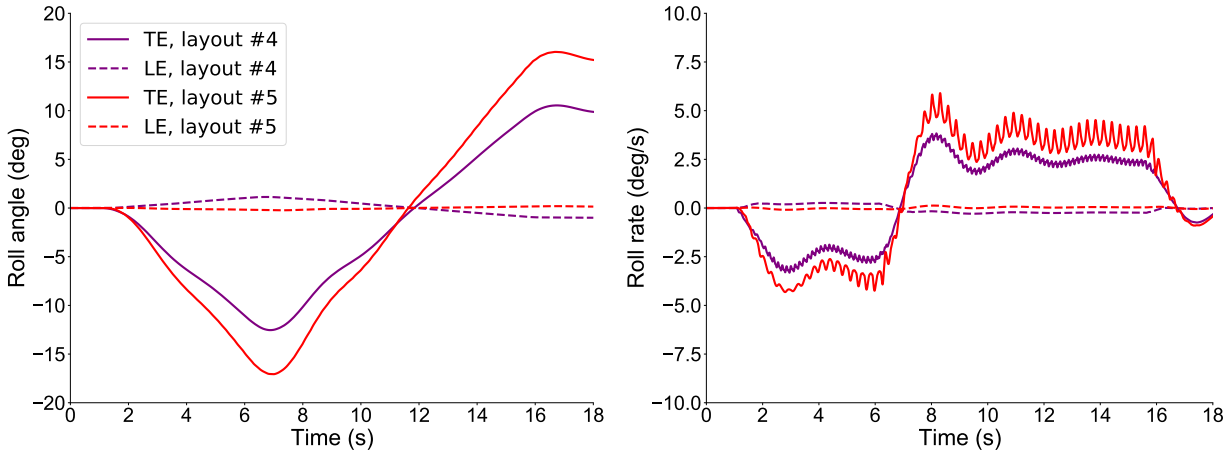

(a) Roll angle

(b) Roll rate

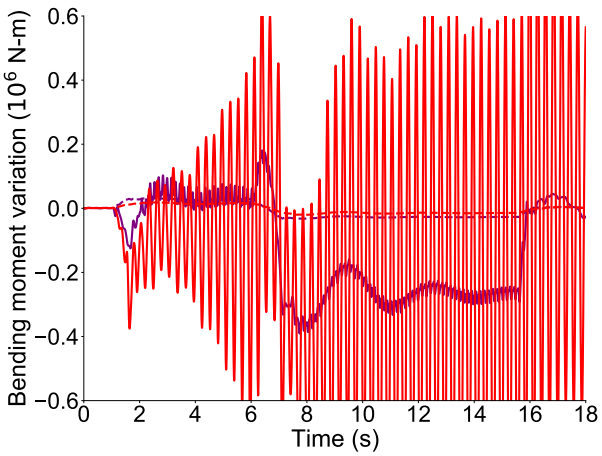

(c) Wing root out-of-plane bending moment

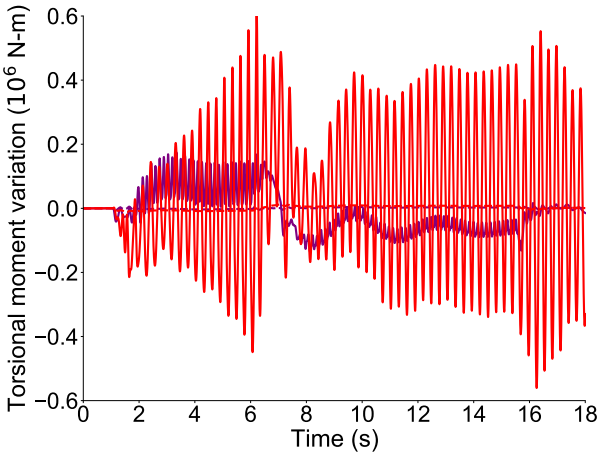

(d) Wing root torsion moment

Figure 4.27: Roll maneuver with outboard control surfaces at $M_\infty = 0.83$.

4.4 Flared Folding Wingtips

This section investigates the roll maneuverability and maneuver load alleviation resulting from deploying trailing- and leading-edge control surfaces along with FFWTs. Sections 4.2 to 4.3 investigated the influence of the spanwise placement of trailing- and leading-edge control surfaces on roll maneuverability of a HARW aircraft. Roll responses for multiple layouts, with and without wingbox passive aeroelastic tailoring, were discussed to highlight the best design practices for improving roll maneuverability in future civil transport aircraft with HARWs. Results showed that trailing-edge control surfaces of HARW aircraft should not be placed at a larger distance from the wing root than in aircraft with regular wing aspect ratios to provide adequate roll maneuverability. Moving the control surfaces toward the wing midspan maximizes aileron effectiveness and roll maneuverability.

The simulations also showed that inboard leading-edge control surfaces are less effective than trailing-edge control surfaces at the same spanwise locations; however, outboard leading-edge control surfaces may provide higher load alleviation capability than their trailing-edge counterparts while avoiding control reversal. The impact of wingbox passive aeroelastic tailoring was also investigated. The results showed that increasing the wingbox out-of-plane bending stiffness and implementing a positive coupling between out-of-plane bending and torsion help increase aileron effectiveness and, thus, roll maneuverability. However, the benefits of wingbox passive aeroelastic tailoring are modest for practical variations in the stiffness properties and become very slight for more inboard aileron placements and at lower dynamic pressure conditions.

These studies highlighted the requirement of an inboard aileron placement in HARW aircraft to meet certification requirements for roll maneuverability. However, an inboard aileron placement will create additional challenges. The results showed that an inboard placement generated higher loads since the wing root bending moment variation followed the same trend as control effectiveness. An inboard aileron placement will also result in a larger control surface area because the hinge line is typically located at a constant wing chord percentage from the trailing-edge at different spanwise locations. A larger control surface area means a heavier control surface and related actuation system. Additionally, an inboard placement might not be a practical choice given other design constraints (placement of different control effectors, fuel storage, etc.). Finally, the results from the previous studies showed a higher variation in the pitch and yaw of the aircraft when a roll maneuver was performed with a more inboard control surface layout.

This section looks at a possible solution to these challenges by investigating the impact of the combined deployment of trailing- and leading-edge control surfaces with FFWTs. An aspect of particular interest is how to best leverage the benefits of trailing- and leading-edge control surfaces, FFWTs, and wingbox passive aeroelastic tailoring to enhance roll maneuverability in these aircraft

Table 4.2: Folding wingtip parameters.

Parameter	Unit	Value
Length	% semispan	22
Flare angle	deg	10, 25
Hinge stiffness	Nm/rad	5×10^5, 0.0

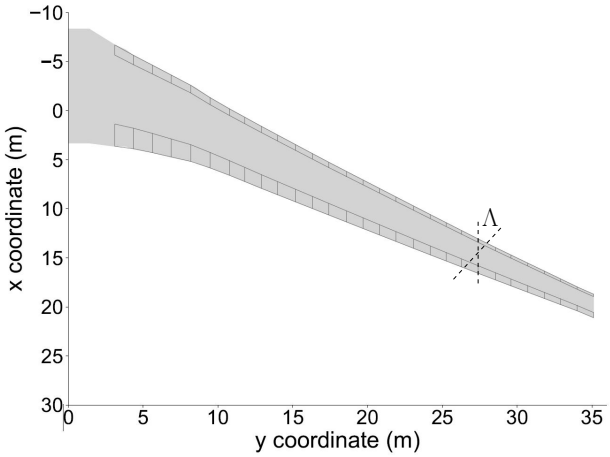

Figure 4.28: Control-surface spanwise definition and position of the FFWT's hinge.

while providing load alleviation.

The studies are conducted for the VFA test case with the FFWTs spanning approximately 22% of the semispan. This corresponds to the hinge line in Fig. 4.28 located approximately at the wingtip of the FA test case. The flare angle Λ denotes the angle between the hinge line and the flow direction and is positive for an outward hinge line orientation. The assumed hinge parameters are summarized in Table 4.2.

Static analyses will investigate the impact of varying control-surface placement and wingtip hinge stiffness in Sec. 4.4.1. Then, for selected layouts based on static results, the studies will investigate roll maneuvers with the simultaneous deployment of trailing- and leading-edge control surfaces and FFWTs in Sec. 4.4.2.

4.4.1 Static Analysis

The impact of FFWTs on control effectiveness and load alleviation is studied by deflecting different trailing- and leading-edge control surfaces for varying hinge stiffness values (see Table 4.2). The static analyses consider a root-clamped wing at a rigid (wing-root) angle of attack of 2 deg, similar to the results in the previous section. The results are presented for the out-of-plane bending and torsion moment variation at the wing root. The roll control effectiveness is also presented to

explore the trade-off between higher maneuverability and load alleviation. A negative value of the bending or torsion moment variation signify load alleviation. Only control surfaces inboard of the wingtip hinge are considered in these investigations.

First, the out-of-plane wing root bending moments for the wing considered as rigid and for the varying hinge stiffness values are compared with the rigid hinge case (fixed wingtip) for two flare angles, $\Lambda = 10, 25$ deg. Results for only the trailing-edge control surfaces are presented since similar behavior is observed for the leading-edge control surfaces for a rigid wing. For the rigid hinge, the wing root bending moment variation increases when deflecting control surfaces towards the wingtip (Fig. 4.29).

For a free hinge, lift decreases outboard of the hinge due to the FFWT rotation (see Fig. 4.30). The net positive root bending moment due to a given control-surface deflection is highest towards the wingtip due to the larger moment arm. However, the increase in bending moment due to control surface deflection is smaller than the reduction in bending moment due to the FFWT. Since loads are normalized by the control-surface area, load alleviation increases from root to tip as the control-surface area decreases. Lowering hinge stiffness increases the load alleviation due to the folding wingtip as a result of its larger passive rotation, with more load alleviation at higher dynamic pressure. The smaller the flare angle, the smaller the load alleviation. The wing root bending moment does not practically change with the flare angle for the lower dynamic pressure (see Figs. 4.29a and 4.29b) as the load alleviation is driven by the hinge stiffness (Ref. [36]). Hence, only the smaller flare angle ($\Lambda = 10°$) is considered for the subsequent results. The results obtained considering the wing as flexible are shown in Figs. 4.31 and 4.32. At $M_\infty = 0.65$, load alleviation trends align to the rigid wing case as shown in Figs. 4.31a and 4.31c.

For the leading-edge control surfaces, the load alleviation trends are similar to the results observed for the trailing-edge control surfaces with a rigid wing. This is motivated by the smaller contribution to the bending moment by the control-surface deflection compared to the reduction in the bending moment due to the FFWT. This also reflects in the increase in load alleviation towards the wingtip since the results are normalized by the control-surface area. At $M_\infty = 0.83$, an opposite trend is observed in Figs. 4.31b and 4.31d as the free folding wingtip increases loads. Figure. 4.31 shows a similar trend for the roll control effectiveness. The increase in loads when allowing for FFWT at higher dynamic pressure can be explained by the lift coefficient variation along the span for a flexible wing with no control surfaces deflected (Fig. 4.33). For the rigid wing, lift reduces in the wingtip region due to the hinge rotation as shown in Figs. 4.30a and 4.30b. For a flexible wing, lift increases inboard of the hinge while it decreases in the wingtip region (see Figs. 4.33a and 4.33b). At lower dynamic pressure (Fig. 4.33a), there is a net decrease in lift resulting in load alleviation. This can be also explained by the static aeroelastic deformed shapes in Fig. 4.34a. Lower hinge stiffness causes the folding wingtip to rotate more inboard, causing the

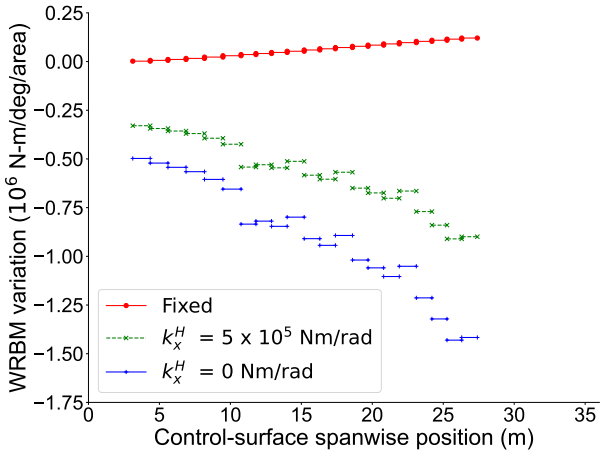

(a) Trailing-edge control surfaces, $M_\infty = 0.65, \Lambda = 10°$

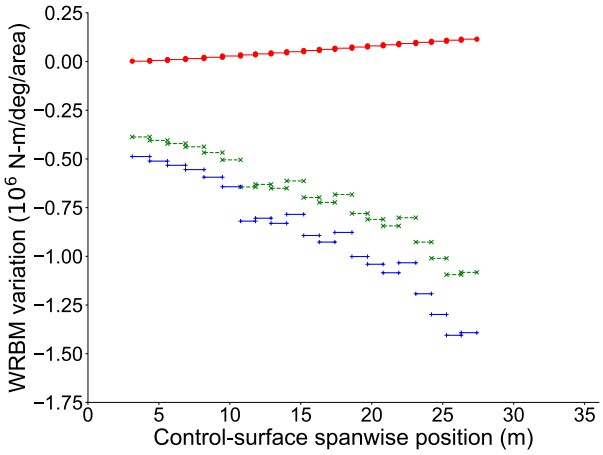

(b) Trailing-edge control surfaces, $M_\infty = 0.65, \Lambda = 25°$

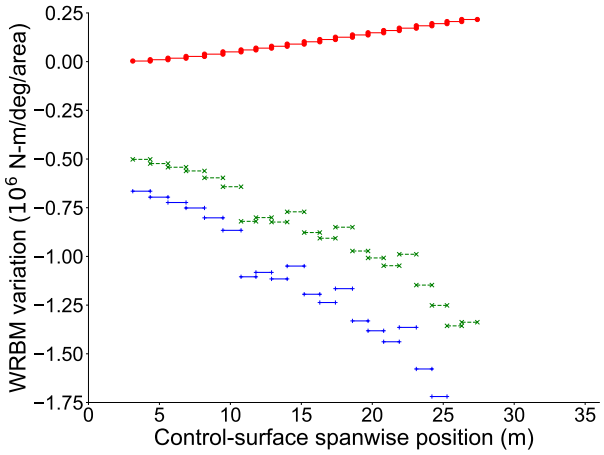

(c) Trailing-edge control surfaces, $M_\infty = 0.83, \Lambda = 10°$

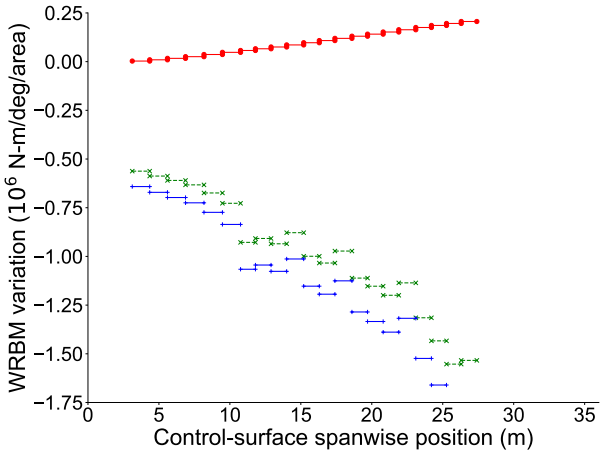

(d) Trailing-edge control surfaces, $M_\infty = 0.83, \Lambda = 25°$

Figure 4.29: Out-of-plane wing root bending moment variation as a function of control-surface spanwise placement with FFWT (rigid VFA wing).

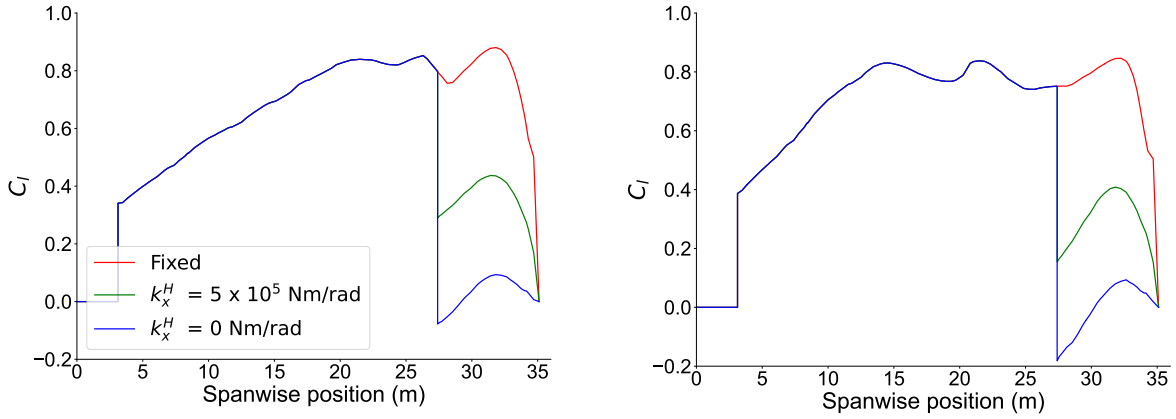

(a) $M_\infty = 0.65, \Lambda = 10°$ (b) $M_\infty = 0.83, \Lambda = 10°$

Figure 4.30: Lift coefficient spanwise variation with FFWTs (rigid VFA wing).

main wing to deflect less than for a rigid hinge. At higher dynamic pressure, stronger wash-out effects toward the wingtip cause the folding wingtip to rotate less. This decreases the reduction in the local angle of attack compared with the increase in lift inboard of the hinge. Hence, there is a net increase in the loads at the root.

To explore this mechanism, results for a partially rigid wing are shown in Fig. 4.35. For a wing stiffened in torsion or with zero out-of-plane bending and torsion stiffness coupling, the increase in lift inboard of the hinge due to wingtip rotation is still observed. For a wing stiffened in out-of-plane bending stiffness, the lift distribution shows a similar response as the rigid wing. These results show that the lower out-of-plane bending stiffness drives the increase in lift inboard of the hinge in a swept wing. A swept-wing flexible in out-of-plane bending stiffness, even with the wing stiffened in torsion, bends less as the wingtip is offloaded due to the folding wingtip's upward rotation. As the out-of-plane bending is reduced inboard, the washout effects increase the angle of attack inboard. The impact of this effect is more substantial at higher dynamic pressure conditions due to the stronger aeroelastic effects. Finally, results for a stiffened wing are shown in Fig. 4.36. Figures 4.36a and 4.36c show results for the baseline wing while Figs. 4.36b and 4.36d for a stiffer variant where out-of-plane bending stiffness is scaled by a uniform factor equal to 1.75 along the span. As the wing gets stiffer, allowing a free folding wingtip gives the same load alleviation trend as in the results at $M_\infty = 0.65$. These results show the importance of considering different wing flexibility levels when exploring folding wingtips as load alleviation devices. These results are in contrast with the ones from previous work that focused on configurations with moderate flexibility and/or aspect ratios [35, 36, 108].

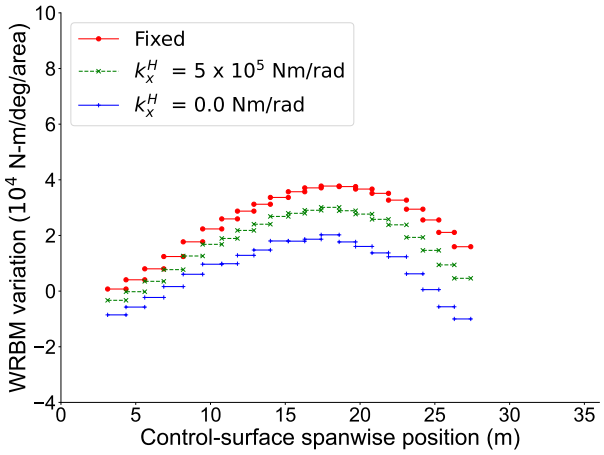

(a) Trailing-edge control surfaces, $M_\infty = 0.65, \Lambda = 10°$

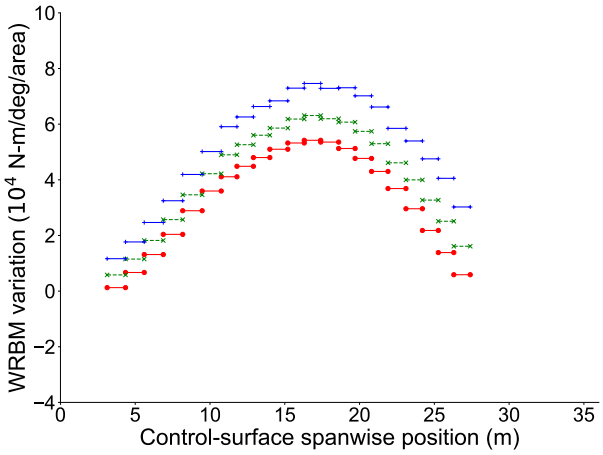

(b) Trailing-edge control surfaces, $M_\infty = 0.83, \Lambda = 10°$

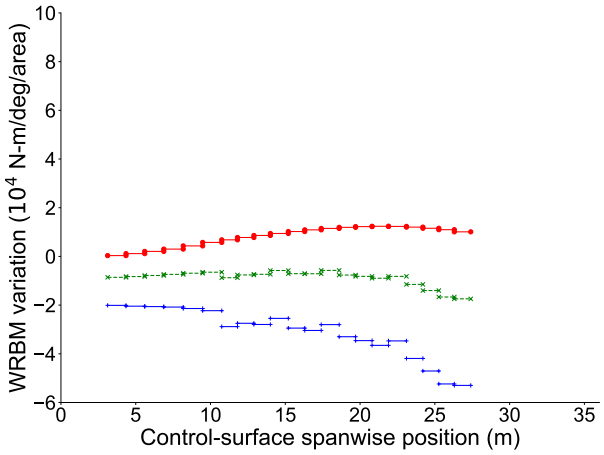

(c) Leading-edge control surfaces, $M_\infty = 0.65, \Lambda = 10°$

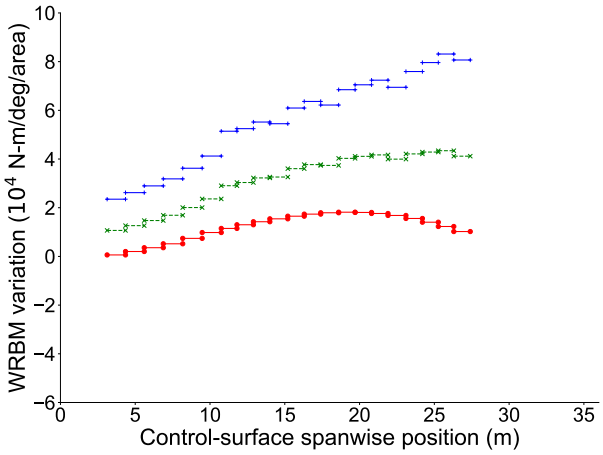

(d) Leading control surfaces, $M_\infty = 0.83, \Lambda = 10°$

Figure 4.31: Out-of-plane wing root bending moment variation as a function of control-surface spanwise placement with FFWTs (flexible VFA wing).

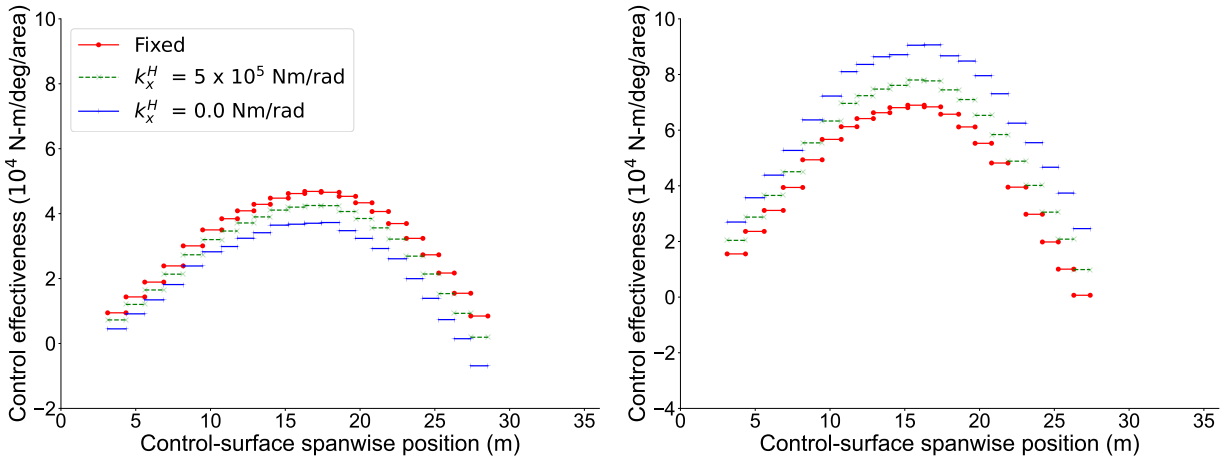

(a) Trailing-edge control surfaces, $M_\infty = 0.65, \Lambda = 10°$

(b) Trailing-edge control surfaces, $M_\infty = 0.83, \Lambda = 10°$

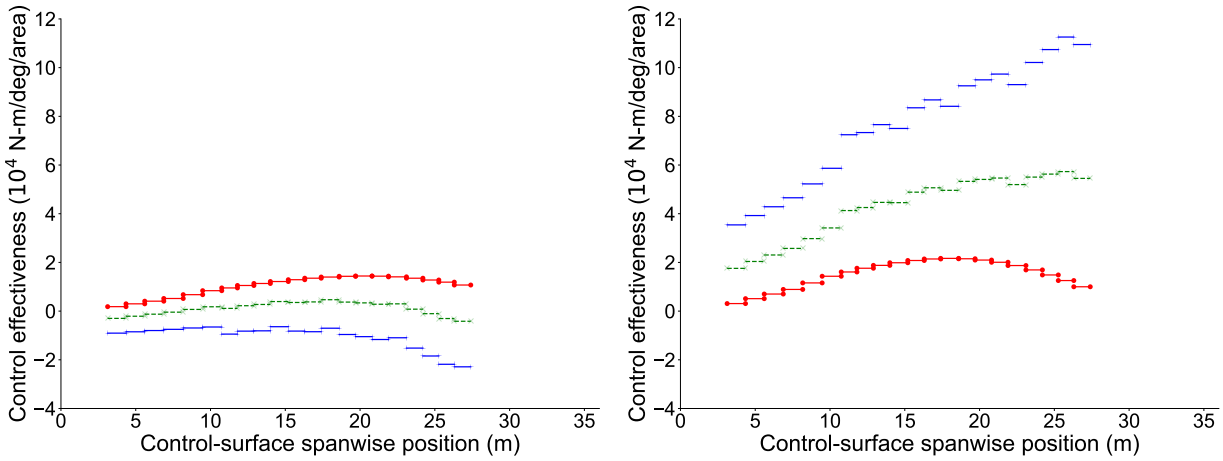

(c) Leading-edge control surfaces, $M_\infty = 0.65, \Lambda = 10°$

(d) Leading-edge control surfaces, $M_\infty = 0.83, \Lambda = 10°$

Figure 4.32: Roll control effectiveness as a function of control-surface spanwise placement with FFWTs (flexible VFA wing).

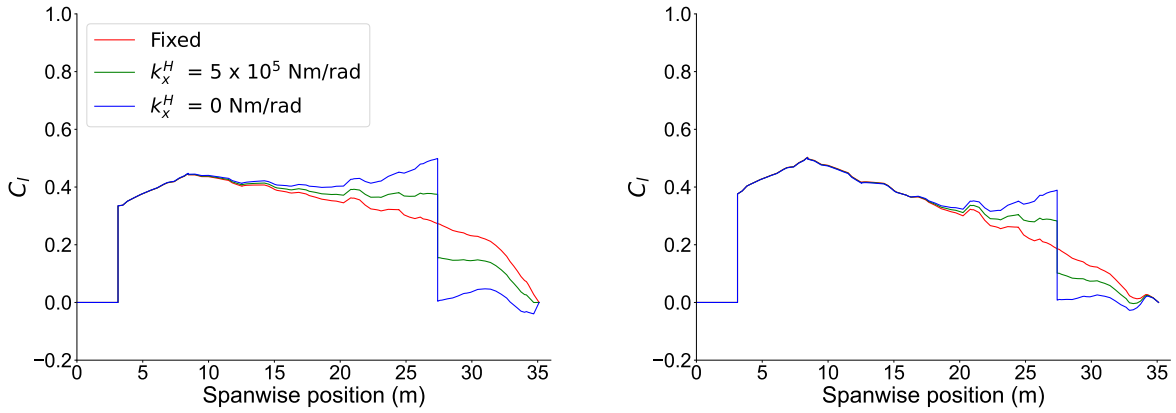

(a) $M_\infty = 0.65, \Lambda = 10°$ (b) $M_\infty = 0.83, \Lambda = 10°$

Figure 4.33: Lift coefficient spanwise variation with FFWTs (flexible VFA wing).

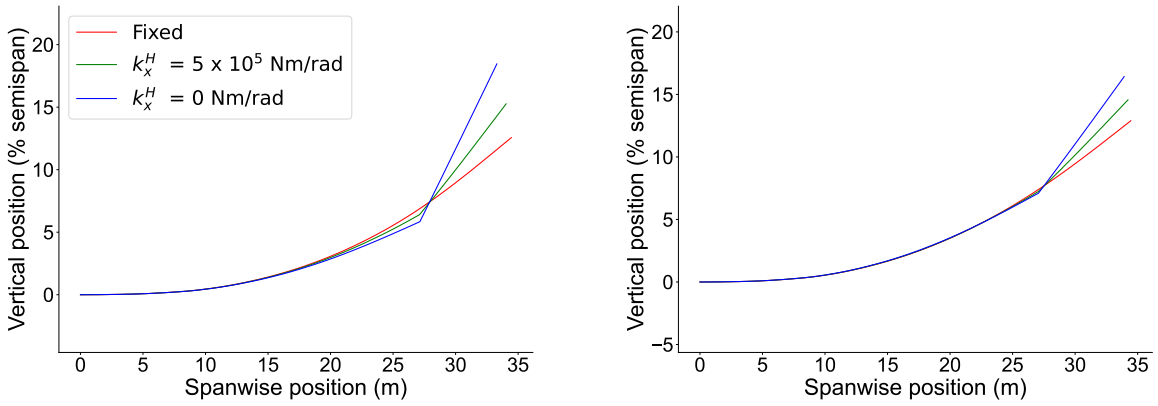

(a) $M_\infty = 0.65, \Lambda = 10°$ (b) $M_\infty = 0.83, \Lambda = 10°$

Figure 4.34: Static aeroelastic deformed shapes with FFWTs (flexible VFA wing).

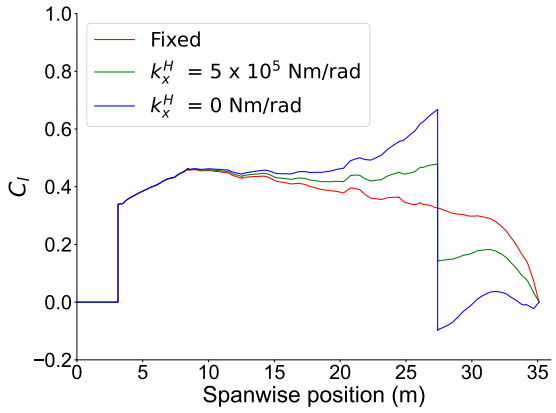

(a) Stiffened in torsion, $M_\infty = 0.65$

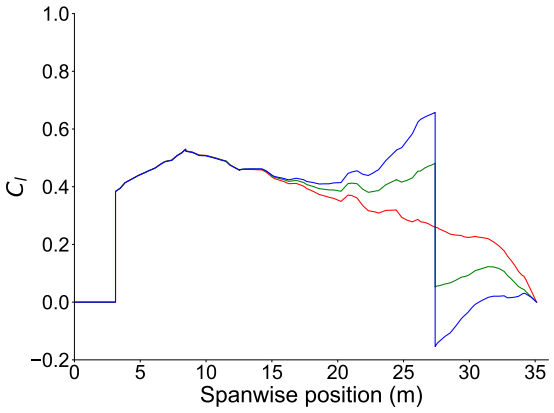

(b) Stiffened in torsion, $M_\infty = 0.83$

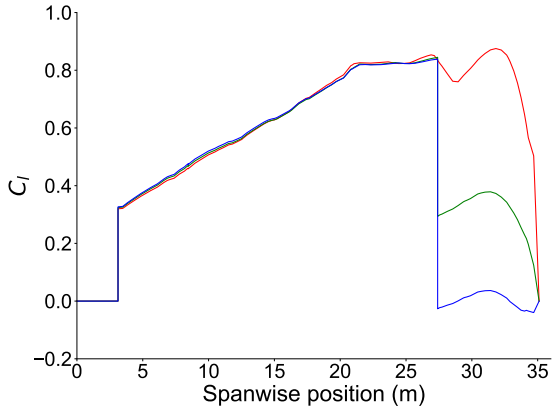

(c) Stiffened in out-of-plane bending,$M_\infty = 0.65$

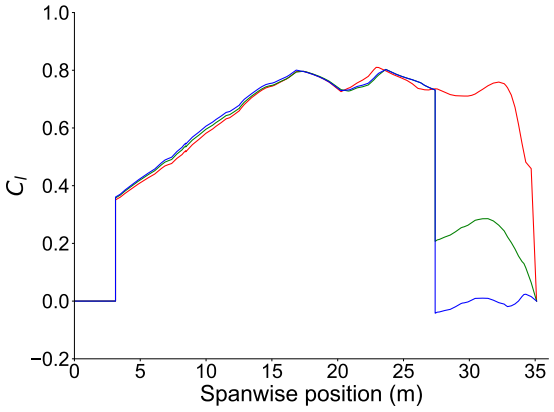

(d) Stiffened in out-of-plane bending,$M_\infty = 0.83$,

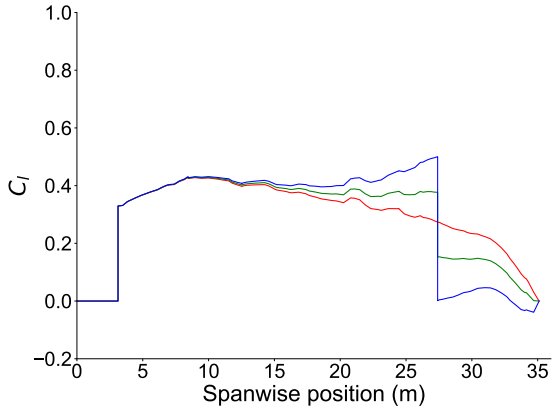

(e) Zero bending/torsion coupling, $M_\infty = 0.65$

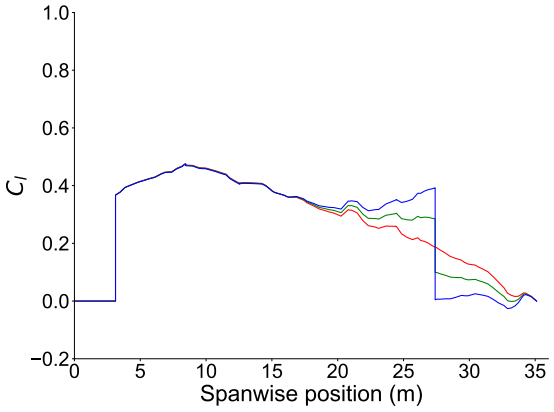

(f) Zero bending/torsion coupling, $M_\infty = 0.83$

Figure 4.35: Lift coefficient spanwise variation with FFWTs (partially rigid wing), $\Lambda = 10°$.

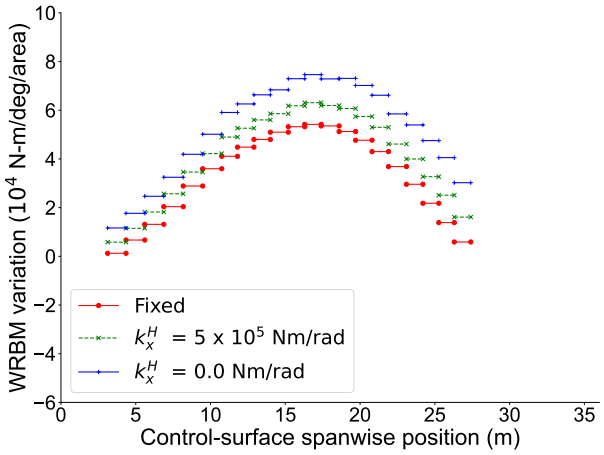

(a) Trailing-edge control surfaces, $M_\infty = 0.83$, baseline

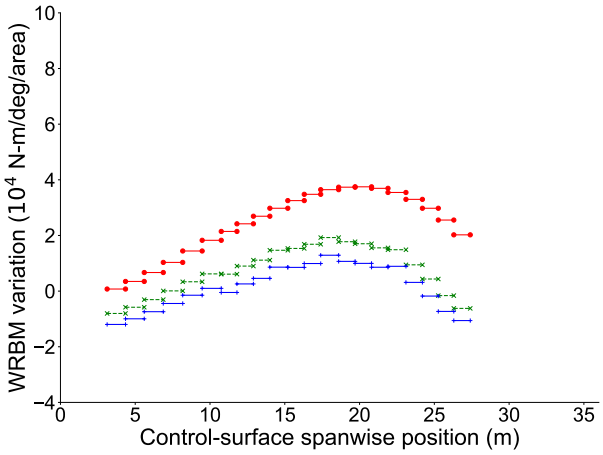

(b) Trailing-edge control surfaces, $M_\infty = 0.83$, stiffened

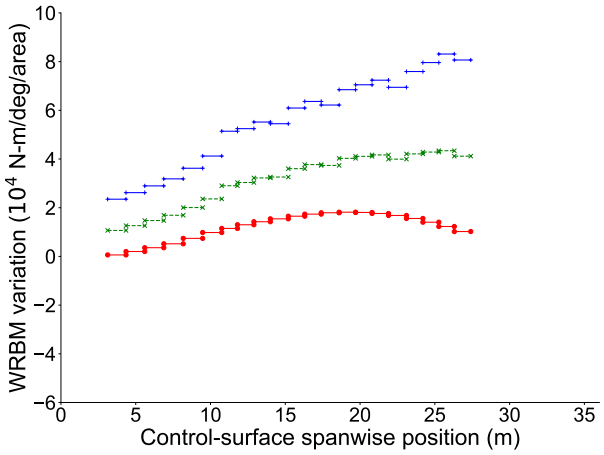

(c) Leading-edge control surfaces, $M_\infty = 0.83$, baseline

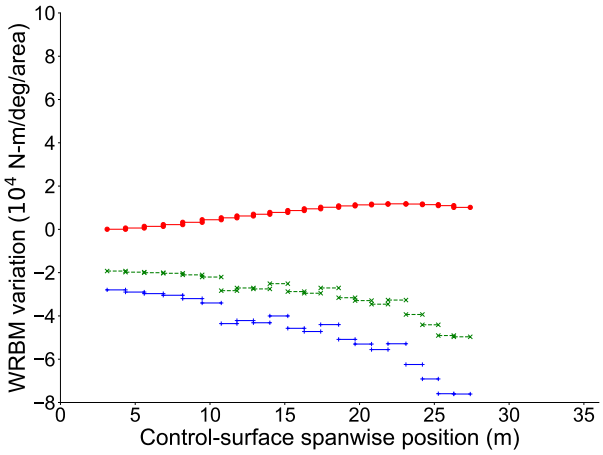

(d) Leading-edge control surfaces, $M_\infty = 0.83$, stiffened

Figure 4.36: Out-of-plane wing root bending moment variation as a function of control-surface spanwise placement with FFWTs, $\Lambda = 10^\circ$ (stiffened VFA wing).

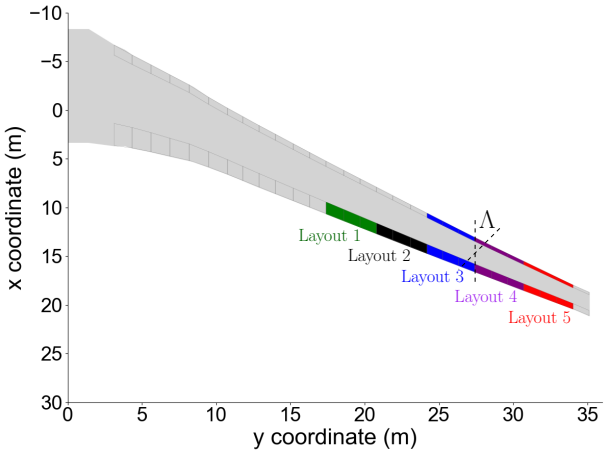

Figure 4.37: Selected control surface layouts for dynamic studies.

4.4.2 Dynamic Analysis

This section investigates roll maneuvers with the simultaneous deployment of trailing- and leading-edge control surfaces and FFWTs. Sections 4.4.2.1 and 4.4.2.2 present the results for selected trailing- and leading-edge control-surface layouts, respectively. The selected layouts considered are based on the static results. These selected layouts are shown in Fig. 4.37. The hinge line located at the end of layout #3 or the start of layout #4. Dynamic responses of the VFA test case are simulated by releasing the FFWTs during flight. This is achieved by setting the hinge stiffness to K^H_{HH} = 0.0 Nm/rad, with damping D^H_{HH} = 10.0 kNms/rad. The results consider a flare angle $\Lambda = 10$ deg and are compared with the previous case where the wingtip is locked in its flat position during flight (see Sec. 4.12).

The dynamic roll responses are investigated for a bank-to-bank maneuver commanded by applying an anti-symmetric control-surface input starting from a trimmed flight condition. The time history of the input applied to the left wing control surface is shown in Fig. 4.37. The same control surface input is applied to all the selected layouts to compare the resulting roll maneuvers. All simulations start from a trimmed condition during which the FFWTs are free to rotate until static equilibrium is reached and are locked when a dynamic simulation starts about the trimmed state. The wingtips are released at $t = 0.5$ s, with the roll maneuver starting at $t = 1.0$ s. The bank-to-bank maneuvers commanded by deploying different control surfaces with free FFWTs are compared against the case where the FFWTs are fixed (locked) in their flat position associated with the original wing geometry during the trim and dynamic simulation.

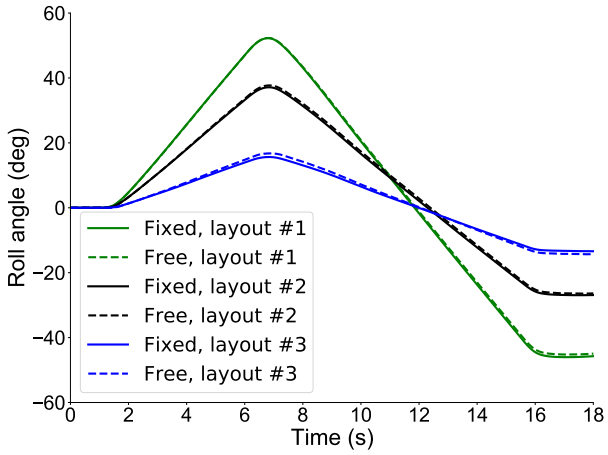

(a) Roll angle

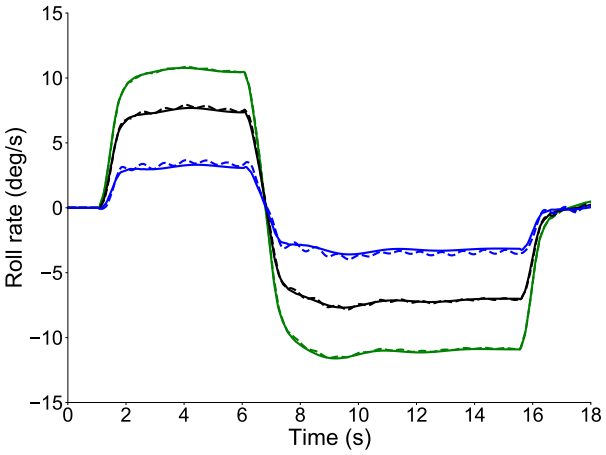

(b) Roll rate

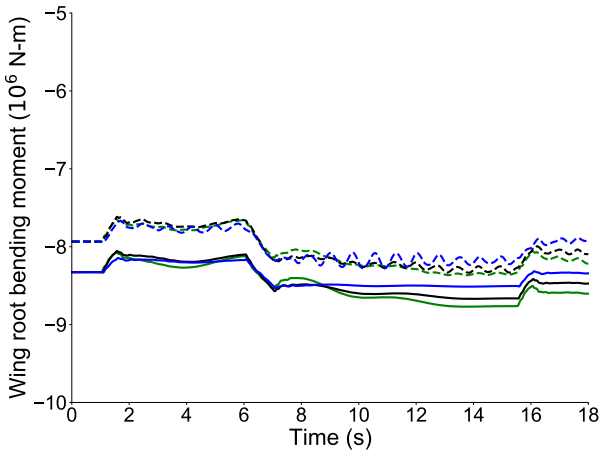

(c) Wing root out-of-plane bending moment

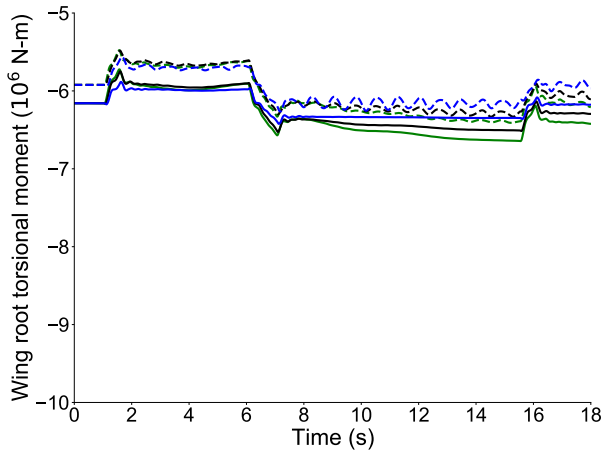

(d) Wing root torsion moment

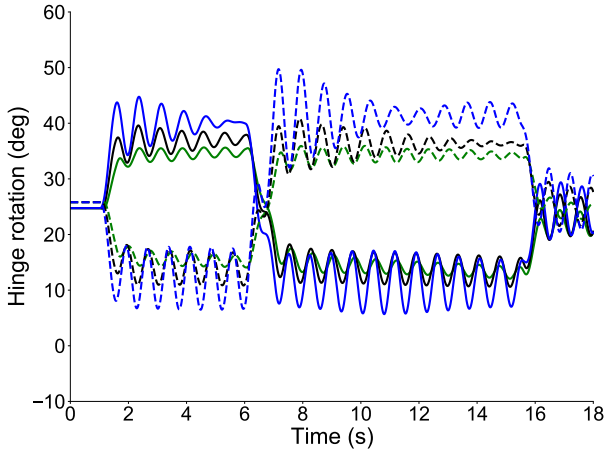

(e) Hinge rotation

Figure 4.38: Roll maneuver with inboard trailing-edge control surfaces and fixed/free FFWTs at $M_\infty = 0.65$.

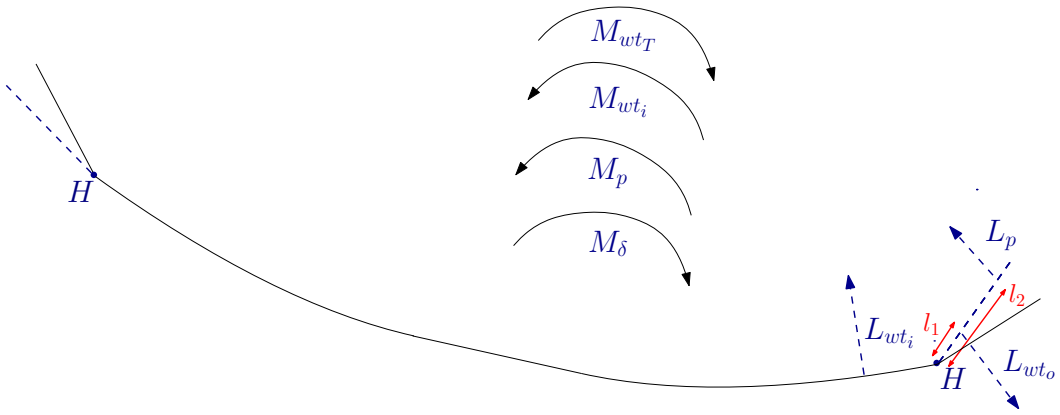

Figure 4.39: Simplified mechanism for roll with trailing-edge control surfaces inboard of the FFWTs.

4.4.2.1 Trailing-Edge Control Surfaces and Flared Folding Wingtips

Figure 4.38 compares the roll maneuvers for the case of the three layouts inboard of the hinge at $M_\infty = 0.65$. For all the three layouts, deploying FFWTs offers negligible benefits in term of the roll rate (see Fig. 4.38a) and roll angle (see Fig. 4.38b) developed during the maneuver. However, a load alleviation benefit is observed at the wing root, where lower out-of-plane bending and torsion moments are developed when FFWTs are deployed (see Figs. 4.38c and 4.38d). The load alleviation benefits remain roughly constant for different layouts. A maximum of 4% for the out-of-plane bending moment and 3.5% for the torsion moment is achieved when the FFWTs are deployed. The load alleviation benefits also remain almost constant throughout the simulation, with the maximum difference originating from the fact that loads are alleviated when the aircraft is trimmed with FFWTs free to rotate. Despite a difference in the hinge rotation observed with the three layouts (see Fig. 4.38e), the maximum load alleviation benefit originates from the difference in the trimmed configuration compared to the fixed hinge case. A higher variation in hinge rotation is observed for the layout #3 adjacent to the FFWT hinge position.

The impact of the FFWTs can be explained by understanding how the roll maneuver is impacted when FFWTs are deployed for an inboard control-surface layout, as shown in Fig. 4.39. The different forces and their corresponding moments acting on the right half-wing during a roll maneuver are illustrated to explain the results. The left wing develops anti-symmetric loads and moments, therefore only the effect on the right half-wing is shown. In a roll maneuver, the lift distribution created by the anti-symmetric aileron input produces a rolling moment (M_δ). The results studied here show a positive roll moment according to the flight dynamics convention, with the right wing going down while the left wing lifts up. The rolling motion induces an increase in the

angle of attack on the right wing and a decrease on the left wing. This change in the angle of attack creates a moment in the opposite direction, called roll damping, induced by the roll rate (M_p). A simplified expression for the roll damping shows that the roll damping increases with the roll rate and wingspan. For a rigid wing, the maximum change in the angle of attack associated with the roll damping occurs at the wingtip. However, for a flexible wing, the maximum change is more inboard due to the reduction in the local angle of attack toward the wingtips caused by washout effects.

The dynamic roll maneuver studies consider a control-surface input applied at a trimmed flight condition. The aircraft has a different trim shape when the FFWTs are deployed. During a roll maneuver with FFWTs free to rotate, the roll damping induced due to the roll rate causes an increase in the lift on the right wingtip and a decrease in the lift on the left wingtip ($L_p > 0$ on the right wingtip). Since we consider a hinge with zero hinge stiffness, the net bending moment about the hinge remains zero ($M_H = 0$). Therefore, to compensate for the increase in the lift on the right wingtip, the right wingtip rotates more to reduce the angle of attack outboard of the hinge. Therefore, with respect to the trimmed condition, a delta decrease in lift outboard of the right wing is generated (L_{wt_o}). This helps in alleviating the roll damping, enhancing roll maneuverability.

While the hinge does not transfer any bending moments, the shear forces are transmitted. Depending on the direction of the shear force, either a moment aiding the roll or resisting the roll is created. This depends on the relative position of the wingtip's center of gravity (not shown in Fig. 4.39) and the position of the wingtip's center of lift. The position of the wingtip's center of lift depends on the net delta change in the lift due to the roll rate (L_p) and the change in the lift due to the wingtip rotation (L_{wt_o}). In this case, a higher reduction in lift due to the wingtip motion will be required to balance the increase in lift due to the roll rate (since $l_2 > l_1$). This will result in a positive moment (M_{wt_T}) due to the opposing shear force transmitted through the right hinge, which enhances roll maneuverability.

For a rigid wing, the wingtips enhance roll maneuverability by reducing the roll damping (due to the zero moment transfer through the hinge) or with the help of the shear force due to the wingtip rotation if the sign of the shear force transmitted through the hinge creates a positive roll moment.

However, there is an another factor to consider during the roll maneuver with FFWTs free to rotate for a flexible wing: the moment due to the change in lift observed inboard of the hinge due to the wingtip rotation (M_{wt_i}). This increase in the lift inboard of the hinge was observed in the static analyses. The reduction in the lift outboard of the hinge is accompanied by an increase in the lift inboard of the hinge for a flexible wing with FFWTs. As the right wingtip rotates more while the left one rotates less, a moment resisting the roll is created due to the increase in the lift inboard of the right wingtip and a decrease in the lift inboard of the left wingtip. This reduces both the load alleviation benefits and the roll maneuverability of the aircraft.

Therefore, for a flexible aircraft rolling with FFWTs free to rotate, we have the following factors impacting the results:

- M_δ: Roll moment due to the anti-symmetric control surface deflection
- M_p: Roll moment due to the roll rate or roll damping
  - Folding wingtips may help alleviate the roll damping effect due to non-transfer of bending moments through a zero stiffness hinge ($M_H = 0.0$)
- M_{wt_T}: Roll moment due to the transmission of shear forces through the hinge
  - Depending on the magnitude and direction of the shear force, M_{wt_T} will either increase or alleviate the effect of the roll damping
  - Magnitude and sign of the shear force depends on the following:
    * wingtip's center of gravity
    * change in lift due to wingtip rotation (L_{wt_i})
    * change in lift due to roll rate (L_p)
    * control surface deflection in the case of an outboard layout (L_δ)
- M_{wt_i}: Roll moment due to the increase in lift inboard of the hinge

For the results at $M_\infty = 0.65$, the increase in roll damping due to the above factors cancels out the alleviation due to the wingtip deployment. Hence, no appreciable benefit is achieved by releasing the FFWTs at this flight condition. To explore the impact of wing flexibility, Sec. 4.4.2.3 will analyze the roll maneuvers with increasing wing stiffness.

The results for $M_\infty = 0.83$ for inboard layouts are shown next in Fig. 4.40. At this flight condition, deploying the FFWTs degrades roll maneuverability. Similar to the results at $M_\infty = 0.65$, the maximum effect is observed for the layout closest to the hinge (layout #3). This is because the wingtips develop larger variations in hinge rotation when they are deployed with layout #3 as shown in Fig. 4.40e. The hinge rotation angle at the trim for this flight condition is lower than the low dynamic pressure condition. This results in a lower reduction in the angle of attack outboard of the hinge but with an increase in the lift inboard of the hinge. This contributes to the negligible differences observed in the loads developed at the wing root. On the other hand, the load alleviation trends are similar to those observed in the static results.

The poor roll maneuverability with the FFWTs for this flight condition can be explained by examining the impact of the four moments induced during a roll maneuver, as discussed above. At this flight condition, due to stronger washout effects, the increase in the lift on the right wing due to the roll damping is shifted inboard. This inboard shift of the incremental lift due to the roll

rate requires (see Fig 4.39, L_p, shift inboard) a smaller delta change in the lift due to the wingtip (L_{wt_o}) to satisfy the hinge condition ($M_H = 0$). Therefore, the right wingtip rotates less than at the $M_\infty = 0.65$ flight condition. While a reduction in roll damping is still achieved due to the non-transfer of bending moments through the zero stiffness hinge, the net shear force transferred through the hinge is also reduced. Therefore, the positive contribution on the roll due to the moment induced by the hinge shear forces is reduced at this flight condition.

However, the main contribution to the reduction in roll maneuverability with folding wingtips at this flight condition is caused by the increase in the roll damping due to the increase in lift inboard of the wingtip (M_{wt_i}). This can also be observed by the poor load alleviation at this flight condition. The increase in the lift inboard of the hinge has a higher contribution to the wing root bending moment, which neutralizes any benefits due to the reduction in the lift outboard of the hinge.

Overall, for the HARW test case considered in this work and the wingtip parameters (wingtip mass distribution and length), the FFWTs do not provide any benefits for enhancing roll maneuverability. Load alleviation benefits are only achieved at the lower dynamic pressure. The maximum effect of the FFWTs is observed when deployed with the control surface close to the hinge (inboard).

Next, Figs. 4.42 and 4.43 show the response of the layouts outboard of the hinge with and without FFWTs. For these layouts, the outboard control surfaces are in reversal due to the strong washout effects near the wingtip. This was also observed in the static results. The outboard layouts remain in reversal even when the folding wingtips are deployed (see Figs. 4.42a and 4.43a). For the results at $M_\infty = 0.65$, the layout closest to the hinge develops a higher roll angle (but in reversal) when the FFWTs are deployed (see Figs. 4.42a). The control reversal is also reflected in the reversal of the hinge rotation, where the right wingtip has a reduction in the fold angle while the left wingtip exhibits an increase in the fold angle (see Fig. 4.42c). The hinge rotation is only shown for layout #4 since the wingtip gets unstable for the further outboard placement with layout #5. This can be observed from the oscillations in the roll rate developed with the deployment of FFWTs and layout #5 (see Fig. 4.42b). The roll response for these two layouts with folding wingtips can be explained considering the moments induced by the different factors, shown in Fig. 4.41. Since the outboard layouts considered here are in reversal, the rolling damping resisting the roll rate induces a decrease in the lift, L_p on the right wing. Note that the control surface is producing a negative lift, L_δ on the right wingtip due to the commanded deflection despite the reversal. The right wingtip then starts to reduce its fold angle to induce a net positive lift to satisfy the zero stiffness hinge requirement. This causes a positive shear force transmitted through the hinge, which aids the roll (in reversal). This results in a higher roll angle for the layout #4 when folding wingtips are deployed. Note that the change in the hinge rotation angle (see Fig. 4.42c) is

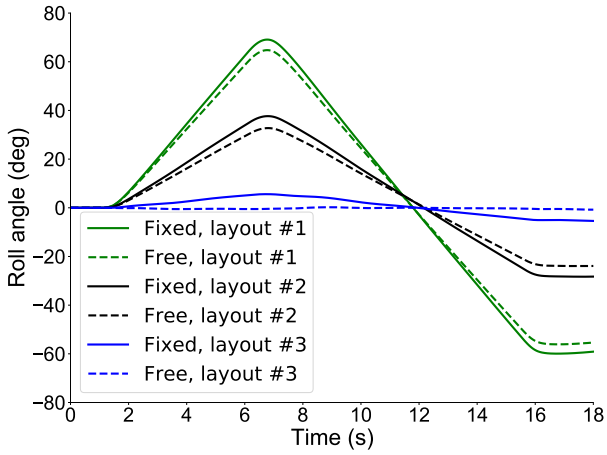

(a) Roll angle

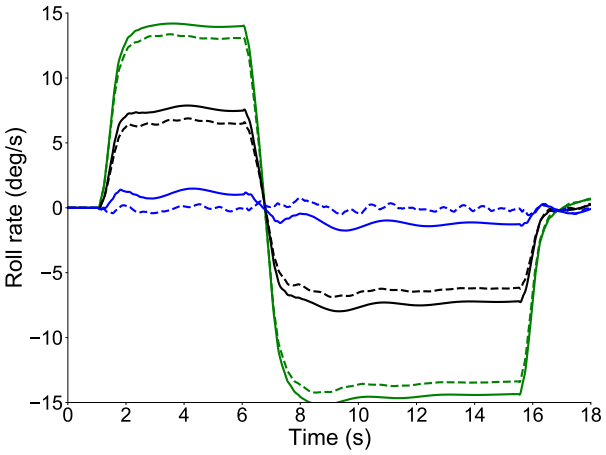

(b) Roll rate

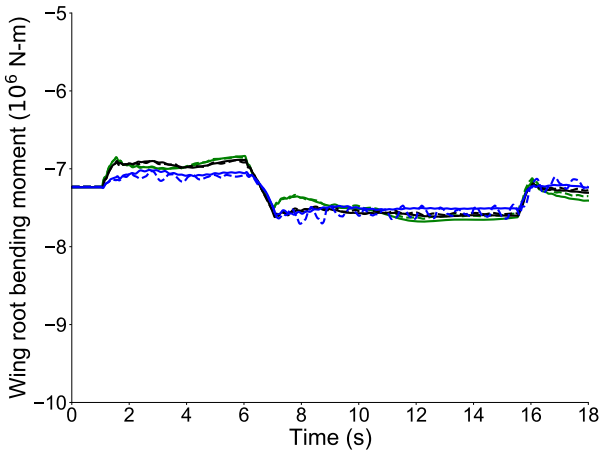

(c) Wing root out-of-plane bending moment

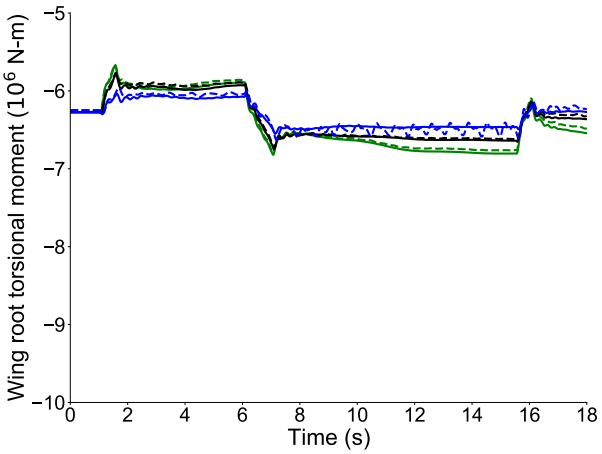

(d) Wing root torsion moment

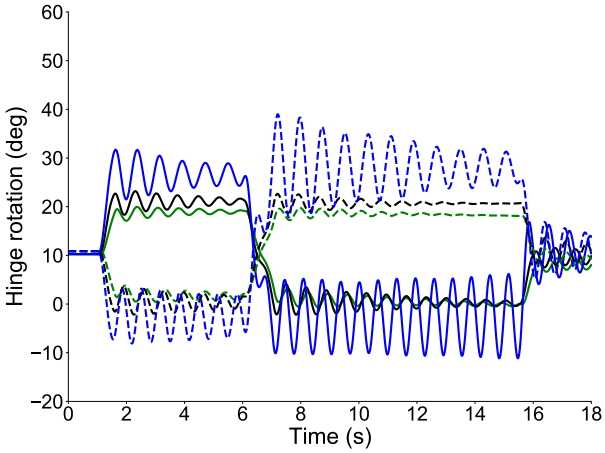

(e) Hinge rotation

Figure 4.40: Roll maneuver with inboard trailing-edge control surfaces and fixed/free FFWTs at $M_\infty = 0.83$.

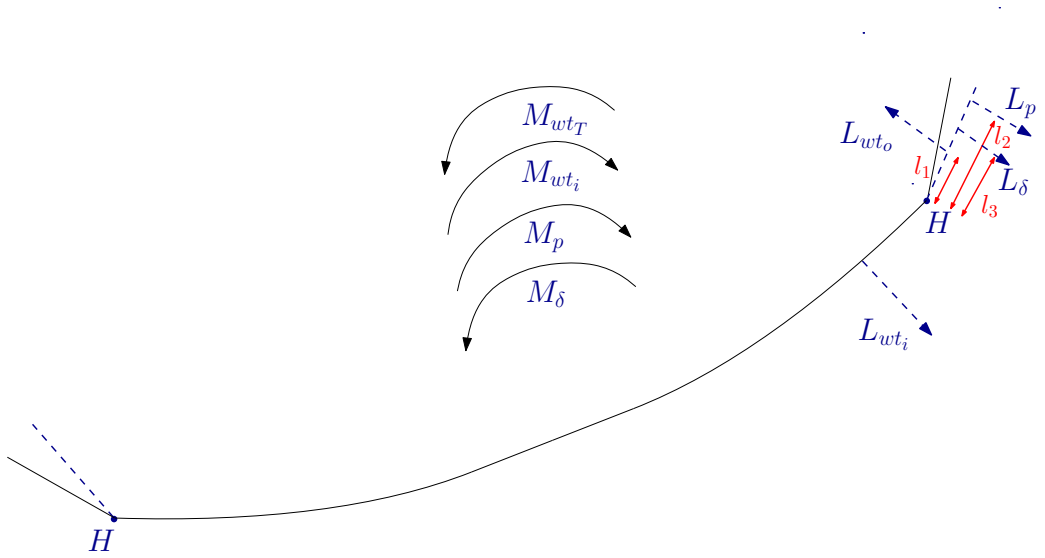

Figure 4.41: Simplified mechanism for roll with trailing-edge control surfaces outboard of the FFWTs.

smaller for outboard layouts than the inboard layouts. This is due to the strong washout effects in the wingtip region, which are exaggerated due to the aileron deflection. This makes it difficult for the right wingtip to decrease its angle of attack by folding less. For the most outboard placement with layout #5, this is further impacted, and the wingtip becomes unstable as it's unable to satisfy the zero bending moment about the hinge.

The results for $M_\infty = 0.83$ are shown by Fig. 4.43. The stronger washout effects at this flight condition induce wingtip instability even for the layout #4. Figure 4.44 shows the result with a smaller control surface deflection of 5 degrees. Reducing the change in lift commanded by the control-surface, helps in avoiding the instability at $M_\infty = 0.65$ with the most outboard layout but with a smaller roll response. However, at $M_\infty = 0.83$, the most outboard layout is still unstable (see Fig. 4.44d). These results highlight the issues with deploying a control surface outboard of the FFWT's hinge for a roll maneuver at higher dynamic pressure conditions.

4.4.2.2 Leading-Edge Control Surfaces and Flared Folding Wingtips

Results for the selected leading-edge layouts deployed together with FFWTs are shown in Figs. 4.46 and 4.47 for $M_\infty = 0.65$ and $M_\infty = 0.83$ respectively. These selected layouts are based on the results in Sec. 4.12. The leading-edge control surfaces are mostly ineffective compared to the trailing-edge control surfaces for more inboard locations. Leading-edge control surfaces have comparable control effectiveness at these selected layouts and avoid control reversal. The load alleviation trends with the leading-edge control surfaces follow the same trend as the trailing-edge control surfaces. This is expected since the significant impact on load alleviation comes from the

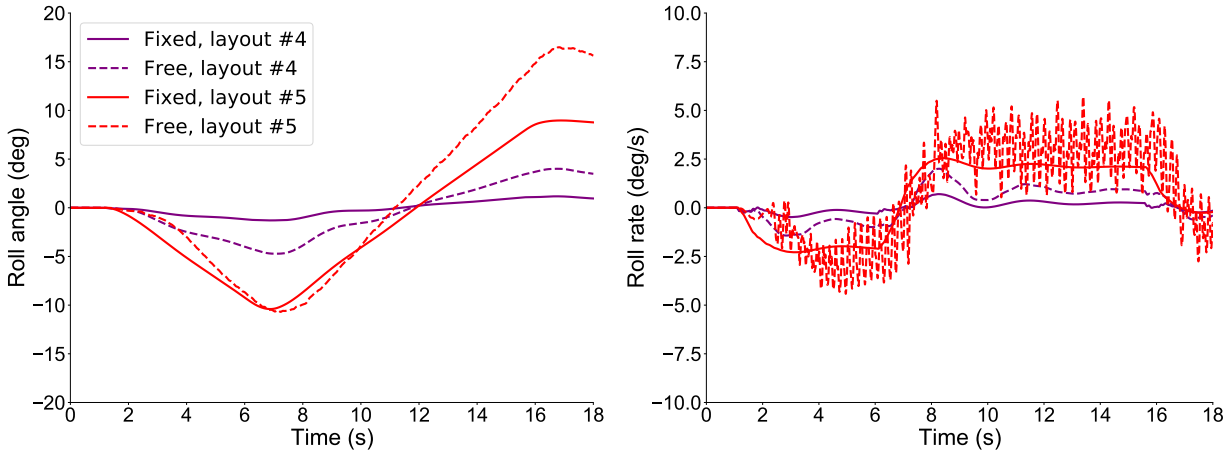

(a) Roll angle

(b) Roll rate

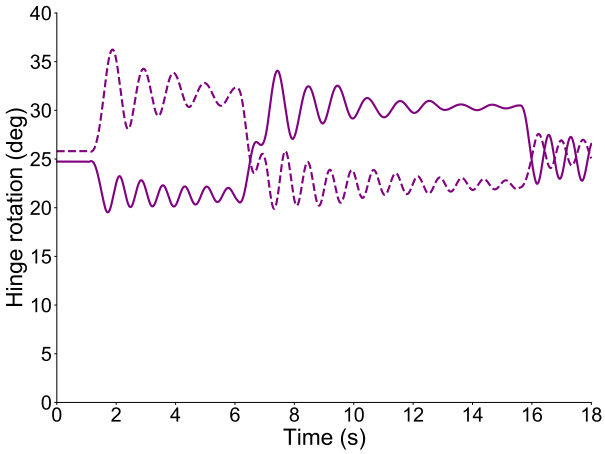

(c) Hinge rotation (layout #4 only)

Figure 4.42: Roll maneuver with outboard trailing-edge control surfaces and fixed/free FFWTs at $M_\infty = 0.65$.

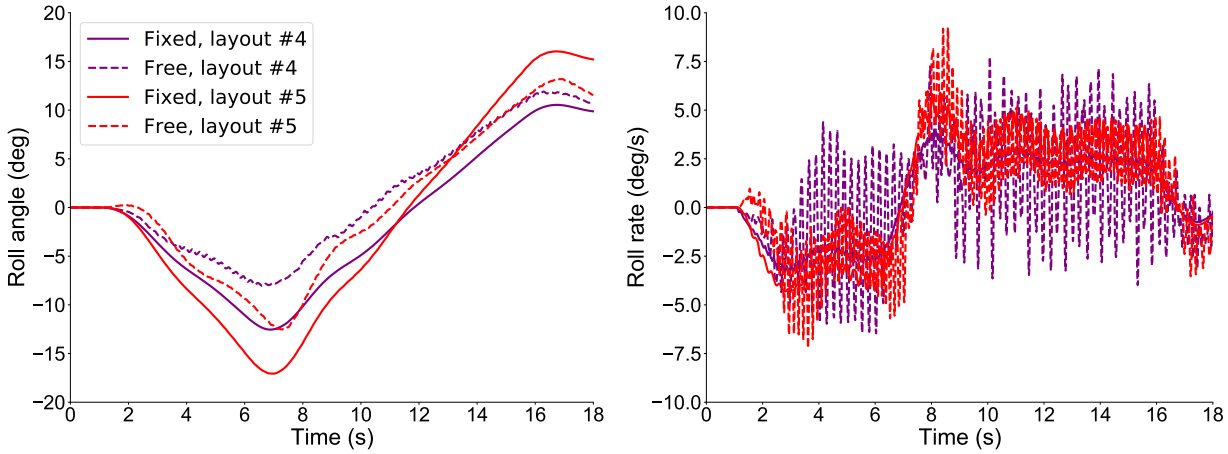

(a) Roll angle

(b) Roll rate

Figure 4.43: Roll maneuver with outboard trailing-edge control surfaces and fixed/free FFWTs at $M_\infty = 0.83$.

difference in the trimmed configuration (the same for the two different surfaces). The trends for the layout #3, inboard of the wingtip hinge, are similar to trends of the corresponding trailing-edge control-surface layout. At $M_\infty = 0.65$, there is no appreciable improvement in the roll response (Fig. 4.46a) but there is a slight degradation at $M_\infty = 0.83$. However, while for trailing-edge control surfaces, the variation in the hinge rotation for layout #3 was substantial, the variation in hinge rotation for the same layout with leading-edge control surfaces is negligible (Fig. 4.46e vs. Fig. 4.38e). Also, note that for the leading-edge control surfaces, the layouts are not in reversal, but the hinge rotation follows the opposite trend compared to the trailing-edge control surfaces. The right wingtip rotates less for a positive roll moment, while the left wingtip rotates more. The highest variation in hinge rotation is observed for the most outboard layout (layout #5). This reflects in the roll response as well.

For layout #4, the hinge rotates less than layout #5. The roll response for this layout at $M_\infty = 0.65$ shows a degraded roll response when folding wingtips are deployed compared to the fixed hinge case. This behavior can be explained by the Fig. 4.45. An increase in roll damping is created for a positive roll on the right wingtip. At this flight condition, the increase in the lift due to roll damping (L_p) is expected to be more outboard. There is also a delta decrease in the lift due to the leading-edge control-surface (L_δ), which acts more inboard of the wingtip for the layout #4. There is a net increase in the lift outboard of the hinge from the wingtip rotation (right wingtip rotates less), to maintain the zero stiffness hinge requirement. This contributes to a moment (M_{wt_T}) opposing the roll moment. Since there is a load alleviation benefit at this flight condition, the effect of this moment opposing the roll moment is larger than the moment (M_{wt_i}) aiding the roll due to

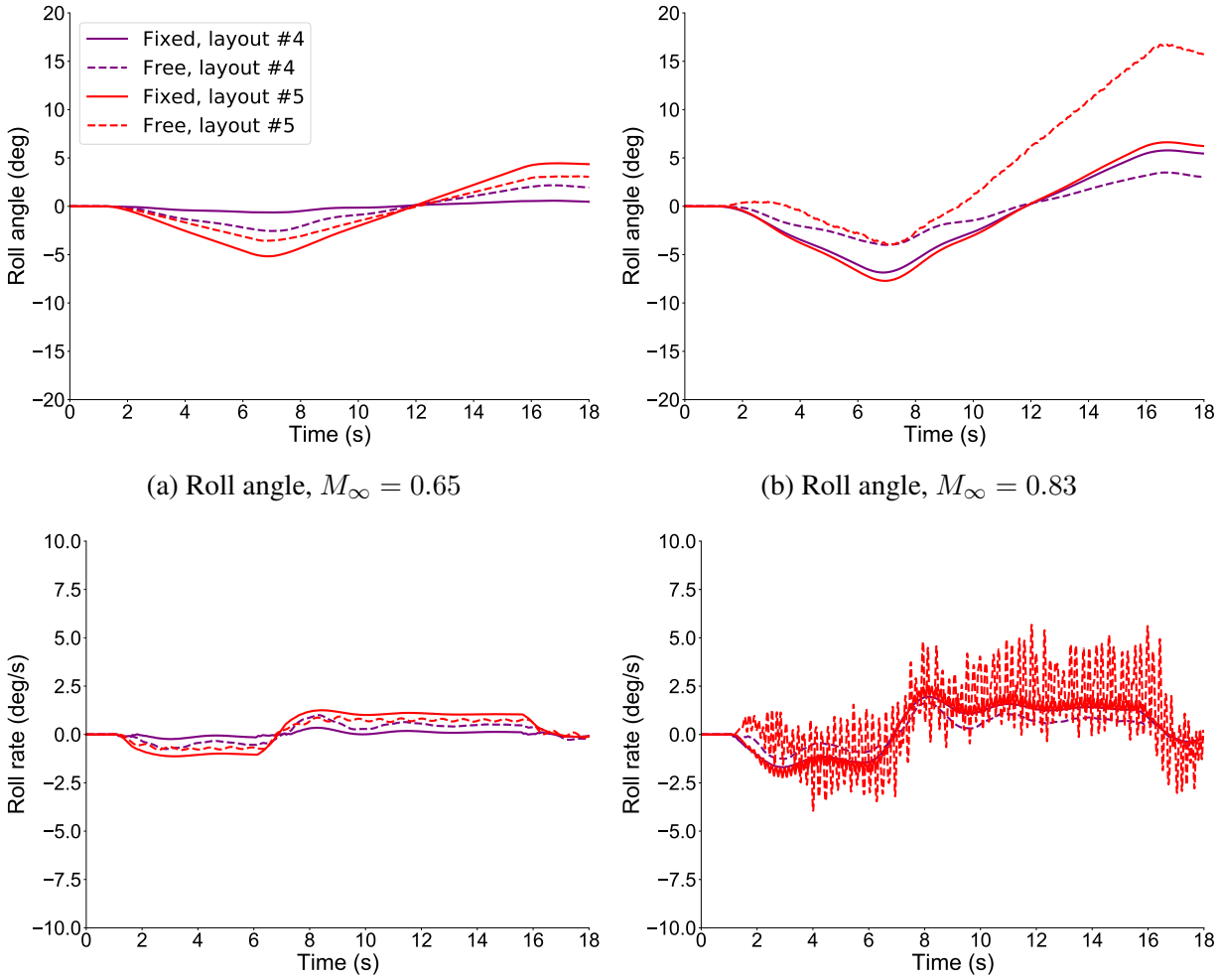

(a) Roll angle, $M_\infty = 0.65$

(b) Roll angle, $M_\infty = 0.83$

(c) Roll rate, $M_\infty = 0.65$

(d) Roll rate, $M_\infty = 0.83$

Figure 4.44: Roll maneuver with outboard trailing-edge control surfaces ($\delta = 5°$) and fixed/free FFWTs.

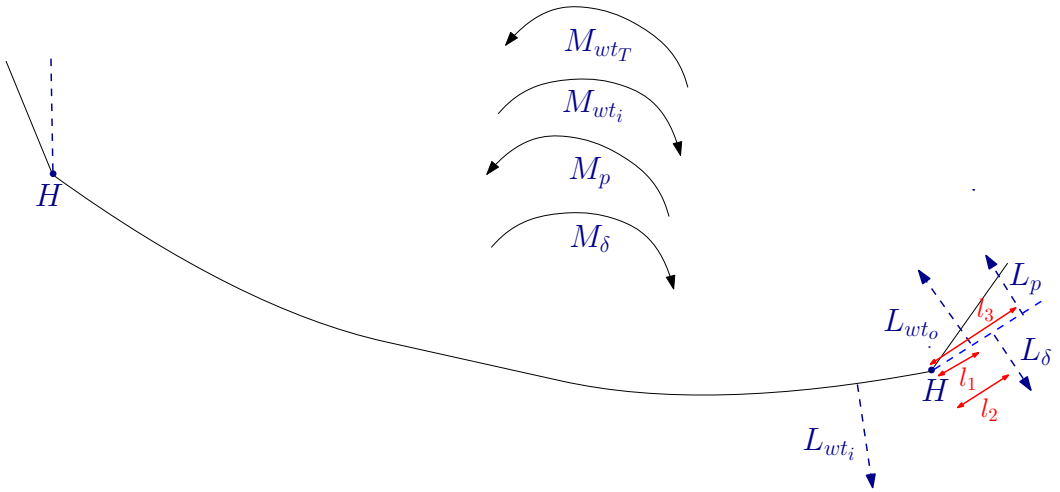

Figure 4.45: Simplified mechanism for roll with leading-edge control surfaces outboard of the FFWTs.

the change in lift inboard caused by the wingtip rotation.

In contrast, at $M_\infty = 0.83$, there is an improvement in the roll response for the layout #4. There is a higher variation in the hinge rotation at this flight condition than at the lower dynamic pressure condition. This can be explained by the net increase in the lift (L_p) due to the roll damping to be lower in magnitude and shifted more inboard at higher dynamic pressure conditions due to strong washout effects. Since the delta change in lift due to the leading-edge control-surface deflection remains the same, the right wingtip rotates more to balance the bending moment about the hinge. This creates a higher roll damping due to the shear forces transmitted through the hinge. However, the effect of increase in roll moment due to the change in lift inboard (M_{wt_o}) has a higher impact at this flight condition. This is also reflected in the similar load alleviation effects with folding wingtips compared to the fixed hinge case. For layout #5, there is an improvement in the roll response at both the flight conditions when folding wingtips are deployed. A more significant improvement in the roll response is observed for the $M_\infty = 0.83$ flight condition due to the higher hinge rotation variation and a more substantial contribution of the change in lift inboard due to the wingtip rotation, which aids the roll. Finally, Fig. 4.48 presents the results for the case where the leading-edge layouts outboard of FFWT are deflected higher by a value of 25 degrees. The response at a higher control-surface deflection is showed to further investigate if the instability observed with trailing-edge control surfaces was due to the larger change in lift because of their higher control-surface derivatives value. Even at higher control-surface deflections, the leading-edge control surfaces are stable and provide higher roll maneuverability than the trailing-edge control surfaces at the same spanwise position. In fact, deploying FFWTs increases their

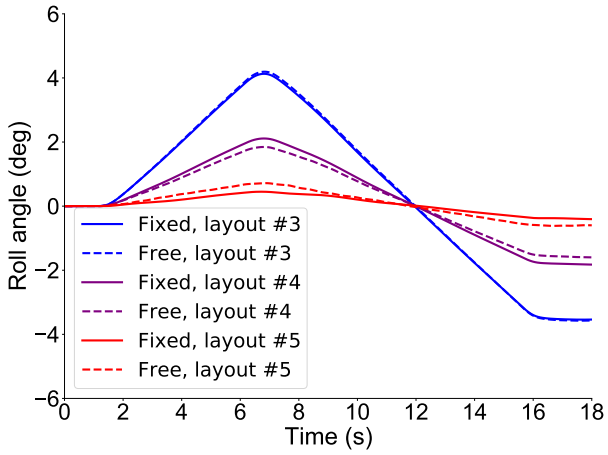

(a) Roll angle

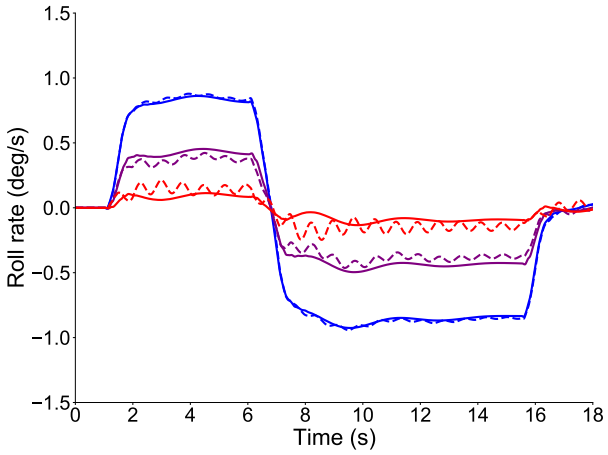

(b) Roll rate

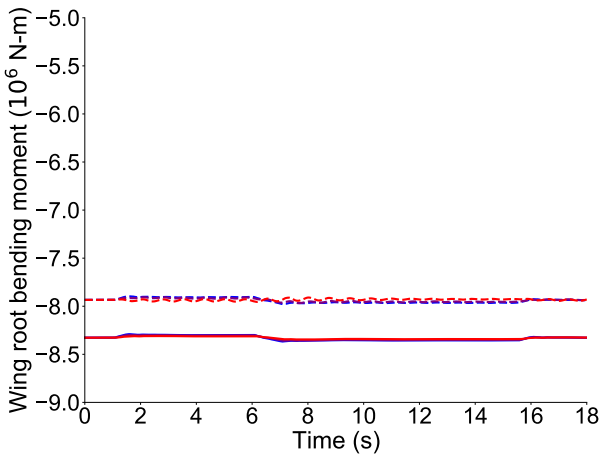

(c) Wing root out-of-plane bending moment

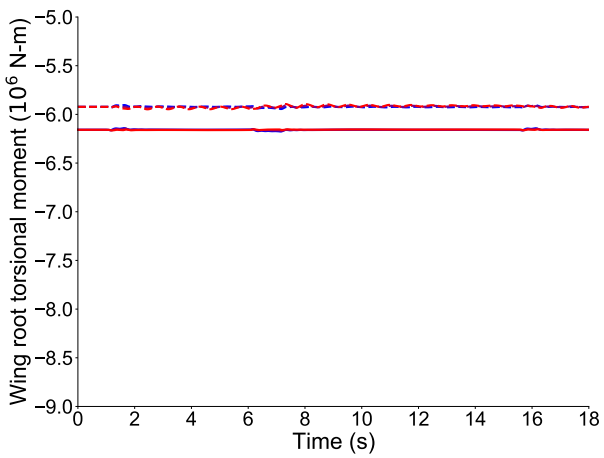

(d) Wing root torsion moment

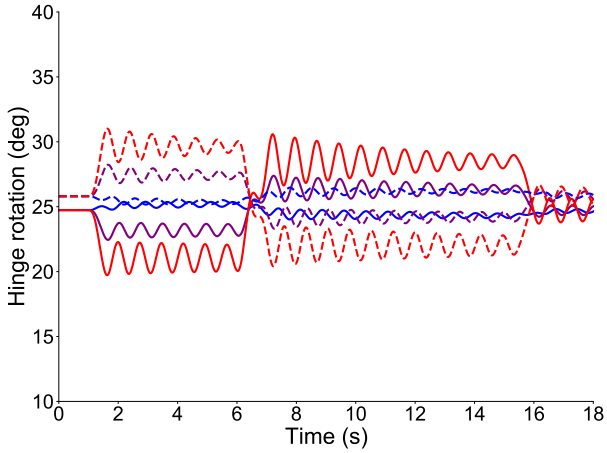

(e) Hinge rotation

Figure 4.46: Roll maneuver with leading-edge control surfaces and fixed/free FFWTs at $M_\infty = 0.65$.

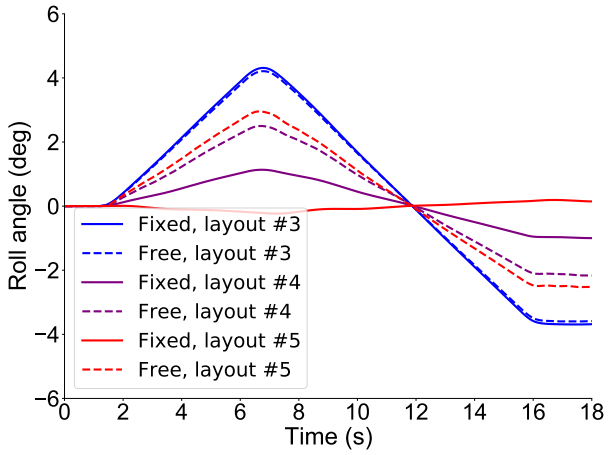

(a) Roll angle

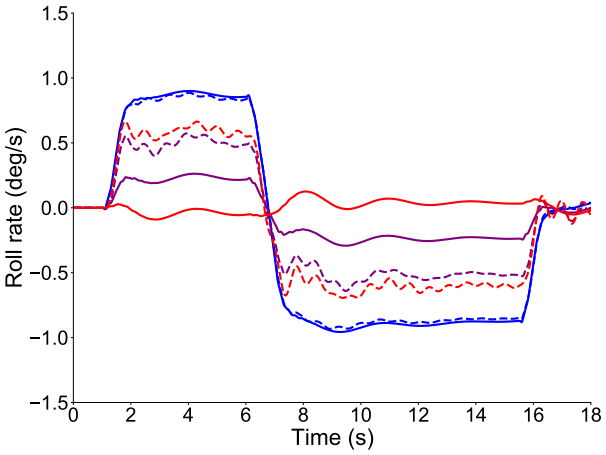

(b) Roll rate

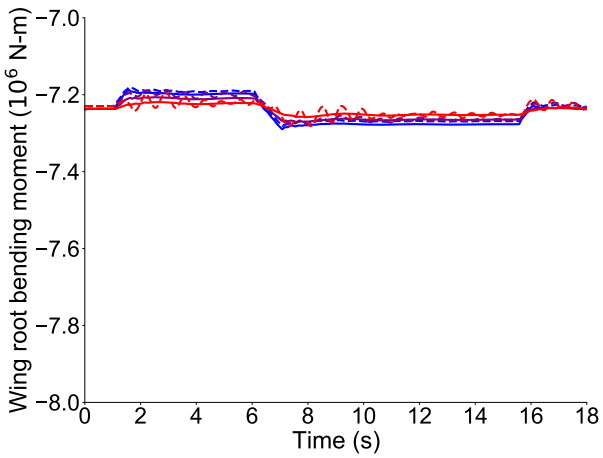

(c) Wing root out-of-plane bending moment

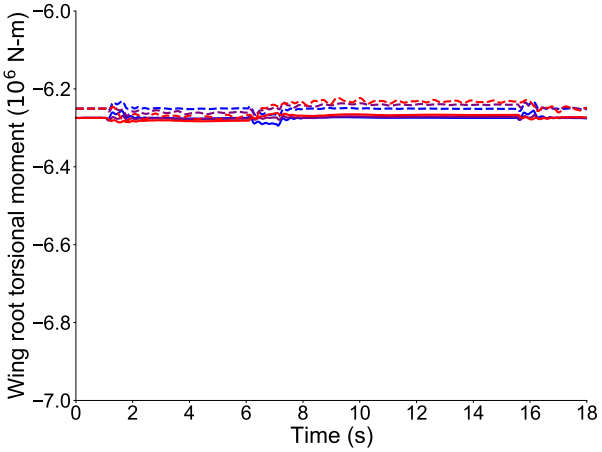

(d) Wing root torsion moment

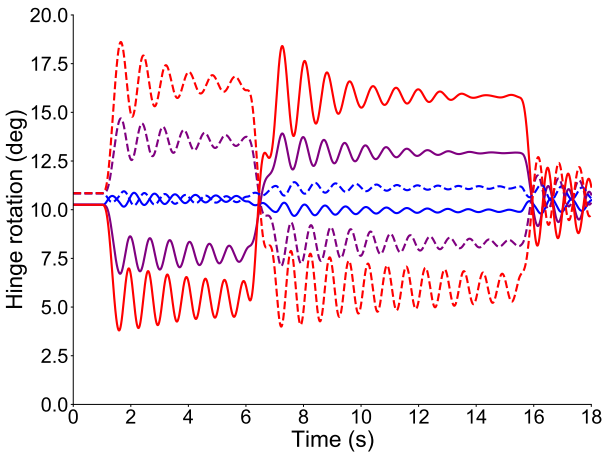

(e) Hinge rotation

Figure 4.47: Roll maneuver with leading-edge control surfaces and fixed/free FFWTs at $M_\infty = 0.83$.

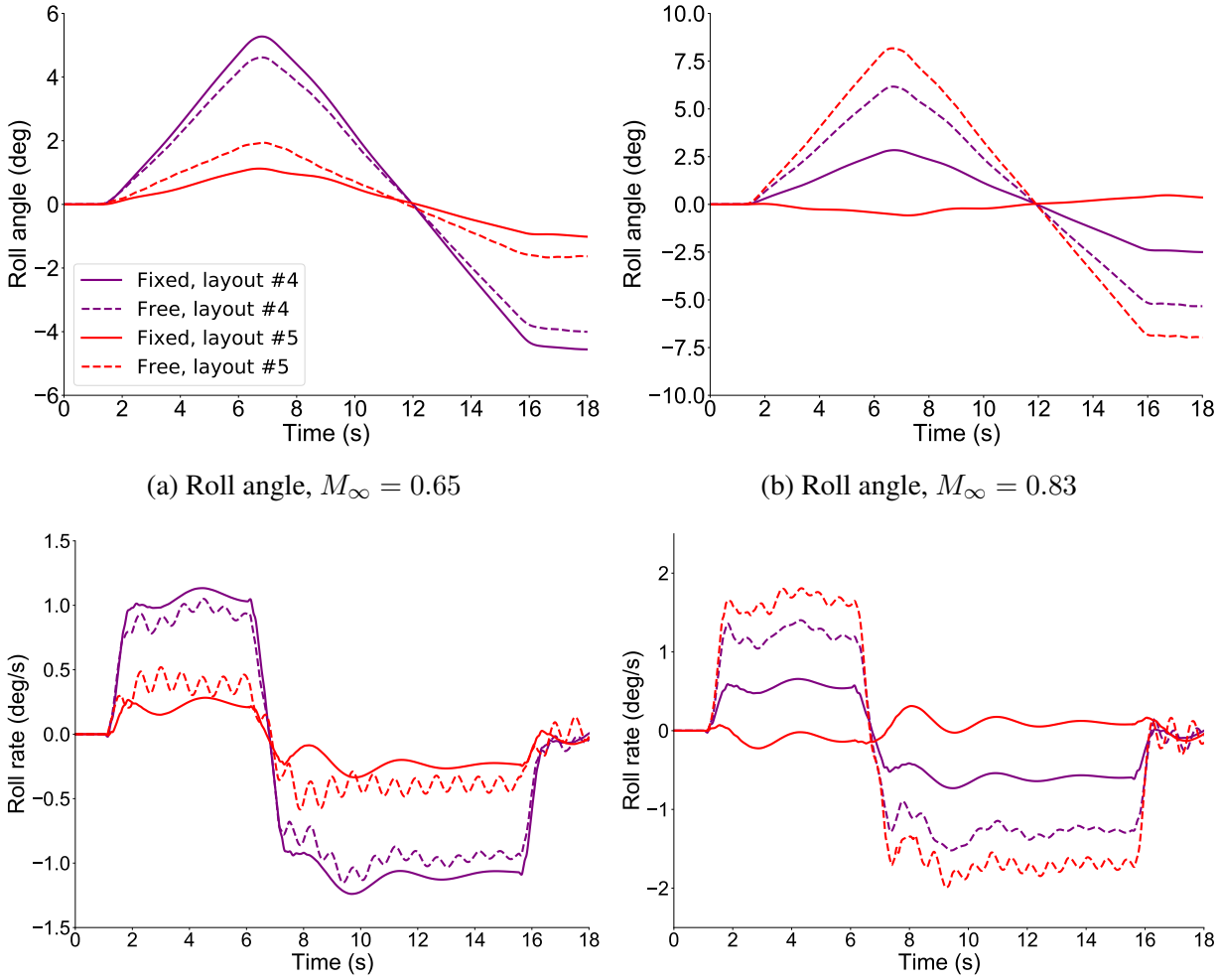

(a) Roll angle, $M_\infty = 0.65$

(b) Roll angle, $M_\infty = 0.83$

(c) Roll rate, $M_\infty = 0.65$

(d) Roll rate, $M_\infty = 0.83$

Figure 4.48: Roll maneuver with leading-edge control surfaces ($\delta = 25°$) and fixed/free FFWTs.

maneuverability for the most outboard layout #5 at $M_\infty = 0.65$ and for both the layouts #4 and #5 at $M_\infty = 0.83$.

4.4.2.3 Impact of Wingbox Passive Aeroelastic Tailoring

In this section, dynamic analyses are conducted for a variation in the wing stiffness. The major stiffness components impacting the roll response are the out-of-plane bending stiffness, torsion stiffness, and their associated coupling term. Results for the individual variation of the out-of-plane bending and torsion stiffness are discussed in this section (the coupling term had no significant impact).

Figs. 4.49 and 4.50 compare the results for a stiffened wing with a 15% increase in its out-of-plane bending stiffness. At the lower dynamic pressure condition ($M_\infty = 0.65$), there is an

improvement in the roll response for each layout when the FFWTs are deployed (see Fig. 4.50a). This contrasts with the baseline stiffness case (Fig. 4.38), where there was no change in the response when the folding wingtips were deployed. There is also a higher load alleviation benefit for the stiffened wing compared to the baseline wing stiffness case. This is caused due to a lower increase in the lift inboard of the hinge due to wingtip rotation. Hence, this helps in reducing the roll damping further for a stiffened wing. However, at the higher dynamic pressure condition (see Fig. 4.50), the folding wingtips are still unable to improve the roll maneuverability even when the stiffness of the wing is increased by 15%. There is also no significant improvement in the loads with the wingtip deployment.

Next, Fig. 4.51 shows the impact of increasing out-of-plane bending stiffness on the outboard trailing-edge control surfaces. For both flight conditions, the wing stiffness increase is insufficient to overcome the strong washout effects for the most outboard placement (layout #5). Therefore, the layout #5 remains in reversal, and the instability due to the FFWT motion is also observed. In contrast, at the low dynamic pressure condition for the layout #4 (see Fig. 4.51a), the control surface is no longer in reversal for the case of a fixed hinge. However, if the FFWT is deployed with layout #4 for a stiffened wing, we get control surface reversal. Although, the free folding wingtip instability is avoided in this case.

If the wing stiffness is increased further, the roll maneuverability with the folding wingtips improves significantly (as observed in some previous studies in the literature [34]). Results for the inboard layouts at $M_\infty = 0.65, 0.83$ are shown in Figs. 4.52 and 4.53 for a 75% increase in the out-of-plane bending stiffness. A 75% increase in the stiffness is not feasible, but the results are shown here to comment on the impact of wing flexibility on the wingtips' roll maneuverability. Fig. 4.52a shows the improvement in the roll angle when the FFWTs are deployed compared to the fixed hinge case. The maximum effect is observed for the layout closest to the hinge (layout #3). For this layout, the maximum roll angle obtained with the combined deployment of the FFWT is comparable to the roll angle obtained with the most inboard placement with layout #1. There is almost a 100% increase in the terminal roll rate developed for the layout #3 when deployed together with the FFWT.

At the higher dynamic pressure condition (see Fig. 4.53), there is less improvement in the roll response compared to the lower dynamic pressure condition (Fig. 4.52). However, the improvement is still significant. Note that a stiffened wing also has a load alleviation benefit observed at this flight condition. This is similar to the trend observed during the static analyses with FFWTs.

The effect of increasing torsional stiffness on the roll response is shown in Fig. 4.54. For both the flight conditions, there is an improvement in the roll response for the fixed case compared to the baseline stiffness (see Figs. 4.38 and 4.40). However, increasing the torsional stiffness alone has no impact on the roll maneuver of the wing with folding wingtips relative to the fixed hinge case. The

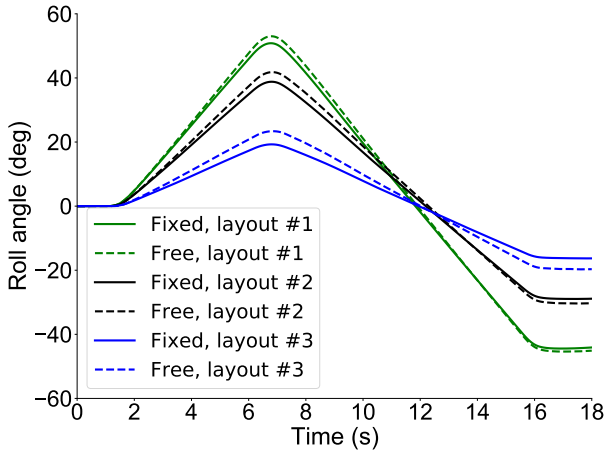

(a) Roll angle

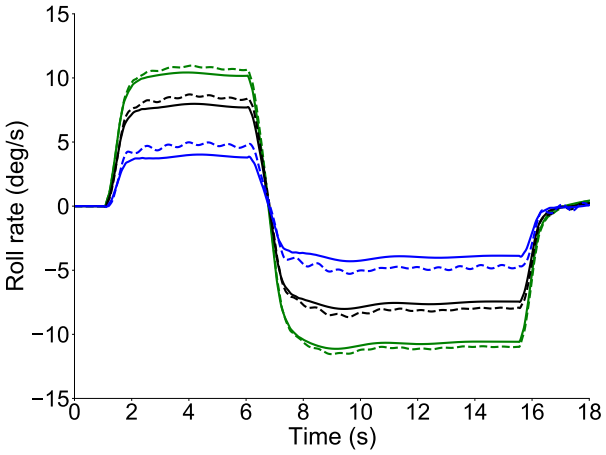

(b) Roll rate

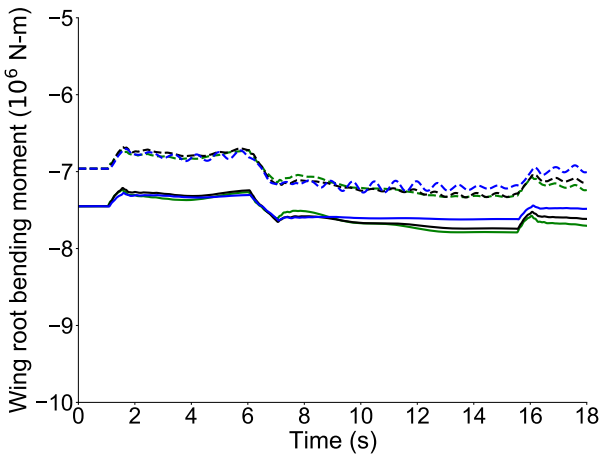

(c) Wing root out-of-plane bending moment

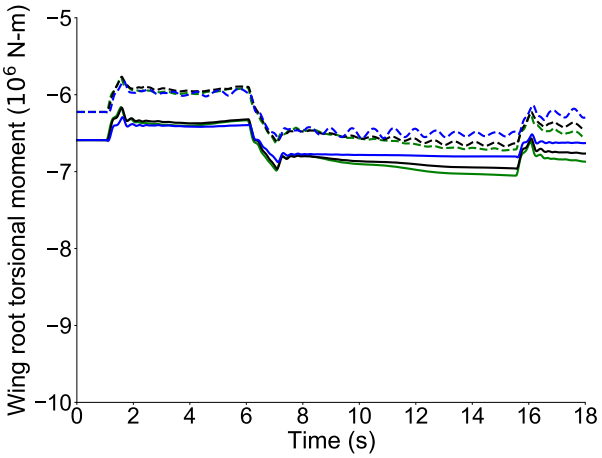

(d) Wing root torsion moment

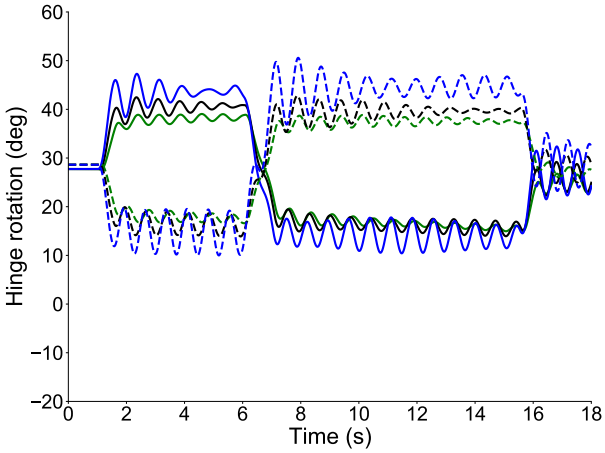

(e) Hinge rotation

Figure 4.49: Roll maneuver with inboard trailing-edge control surfaces, out-of-plane bending stiffness (1.15×), $M_\infty = 0.65$.

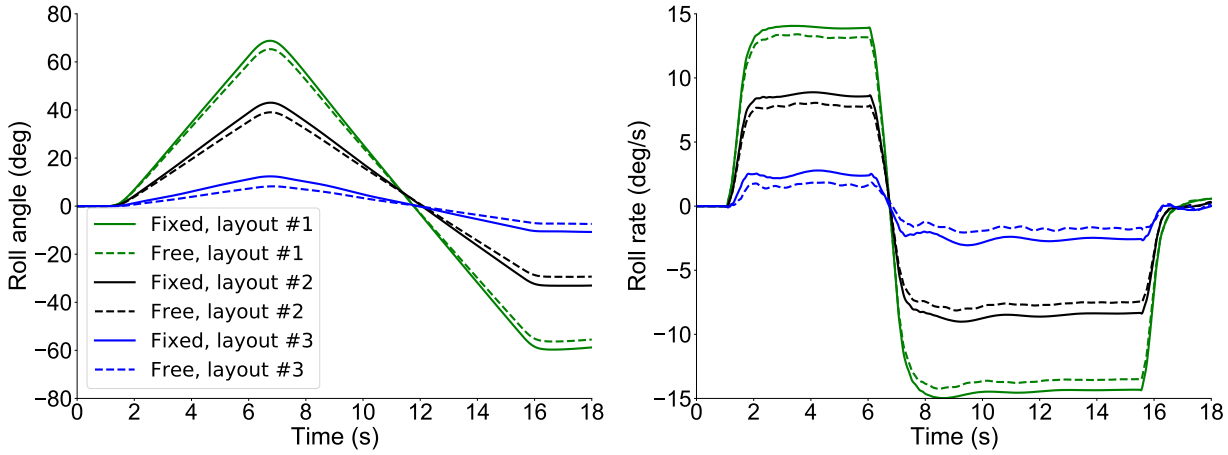

(a) Roll angle

(b) Roll rate

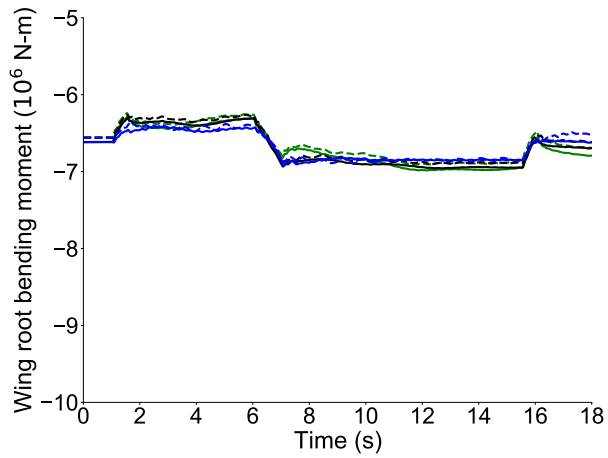

(c) Wing root out-of-plane bending moment

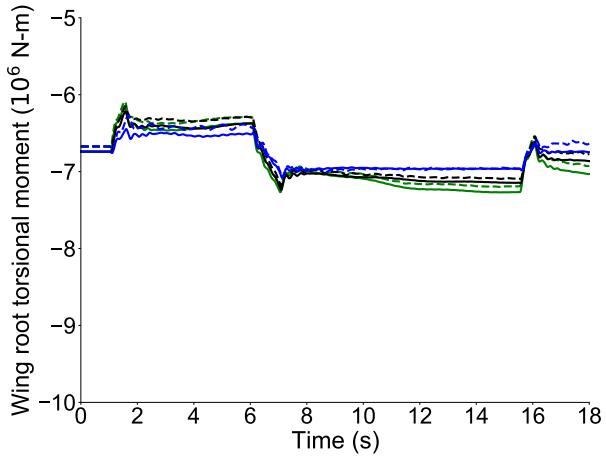

(d) Wing root torsion moment

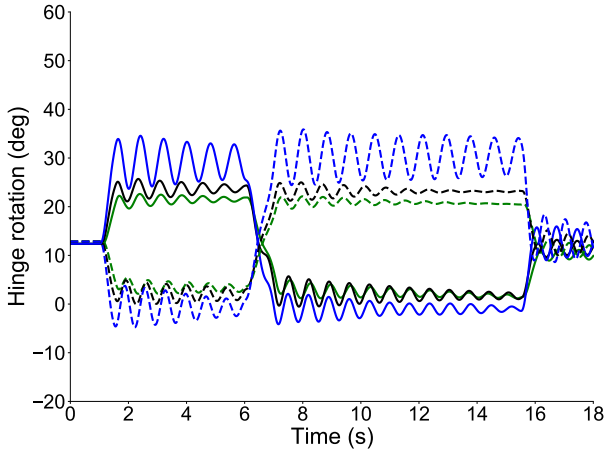

(e) Hinge rotation

Figure 4.50: Roll maneuver with inboard trailing-edge control surfaces, out-of-plane bending stiffness (1.15×), $M_\infty = 0.83$.

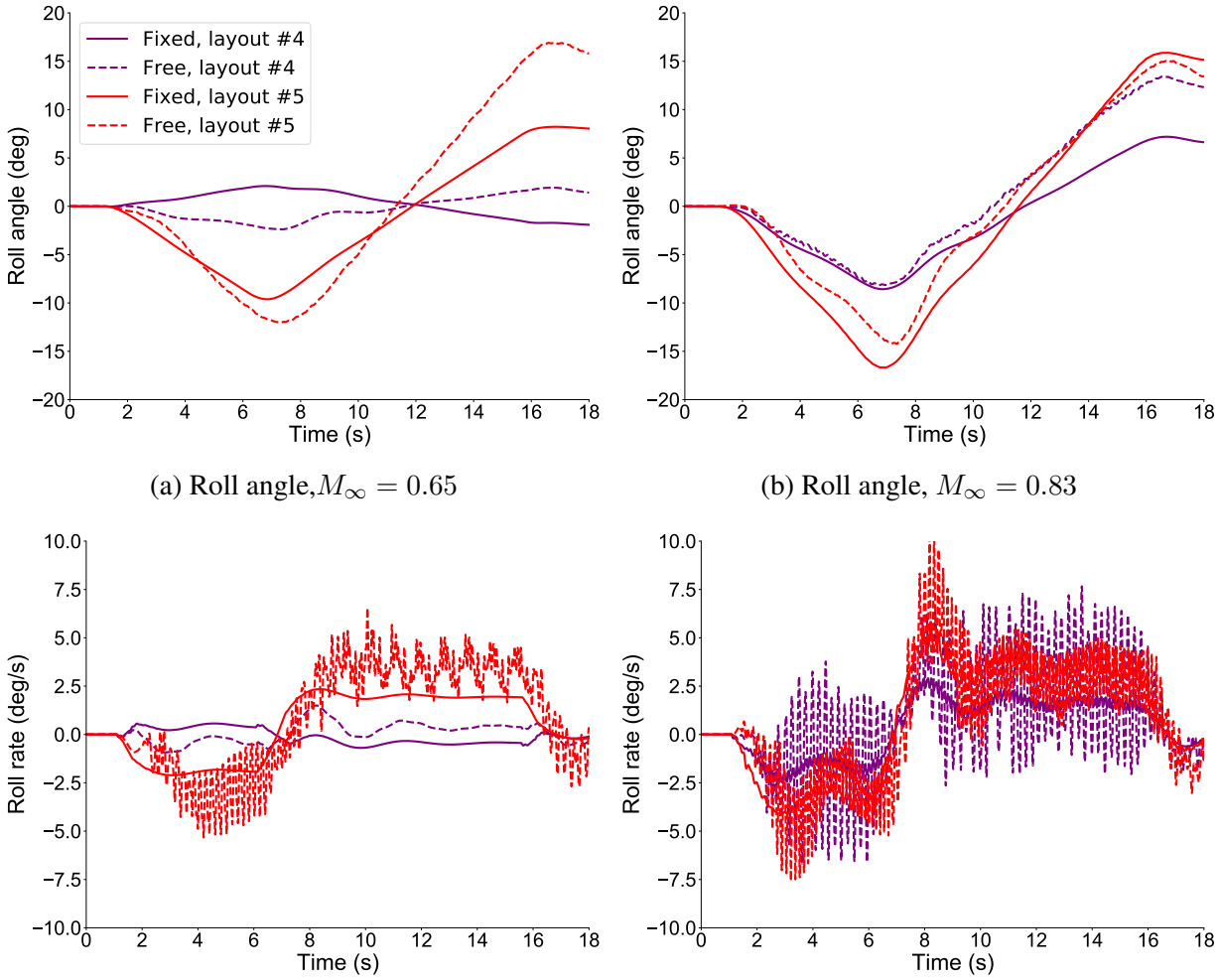

(a) Roll angle,$M_\infty = 0.65$

(b) Roll angle, $M_\infty = 0.83$

(c) Roll rate,$M_\infty = 0.65$

(d) Roll rate, $M_\infty = 0.83$

Figure 4.51: Roll maneuver with outboard trailing-edge control surfaces, out-of-plane bending stiffness (1.15×).

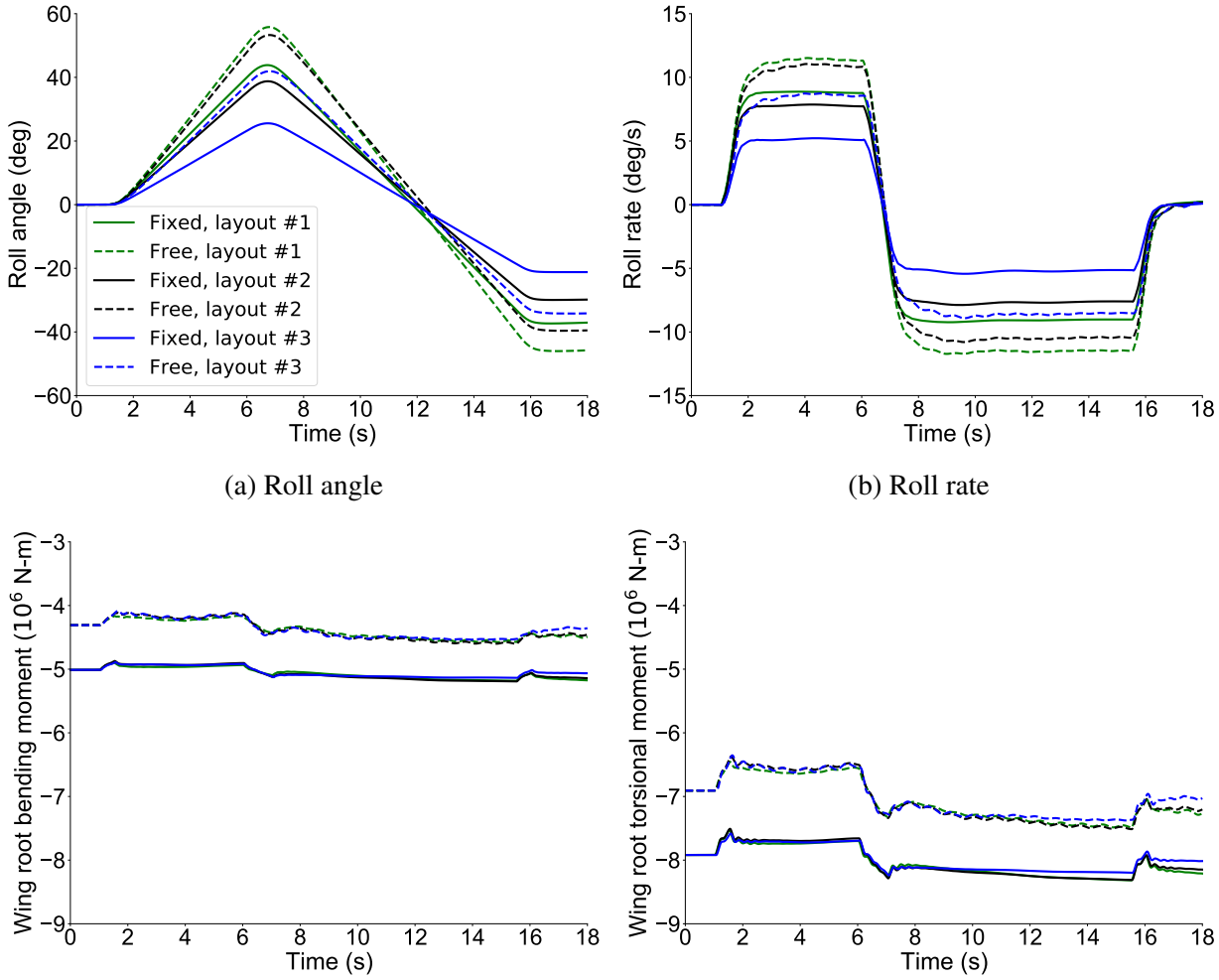

(a) Roll angle

(b) Roll rate

(c) Wing root out-of-plane bending moment

(d) Wing root torsion moment

Figure 4.52: Roll maneuver with inboard trailing-edge control surfaces, out-of-plane bending stiffness (1.75×), $M_\infty = 0.65$.

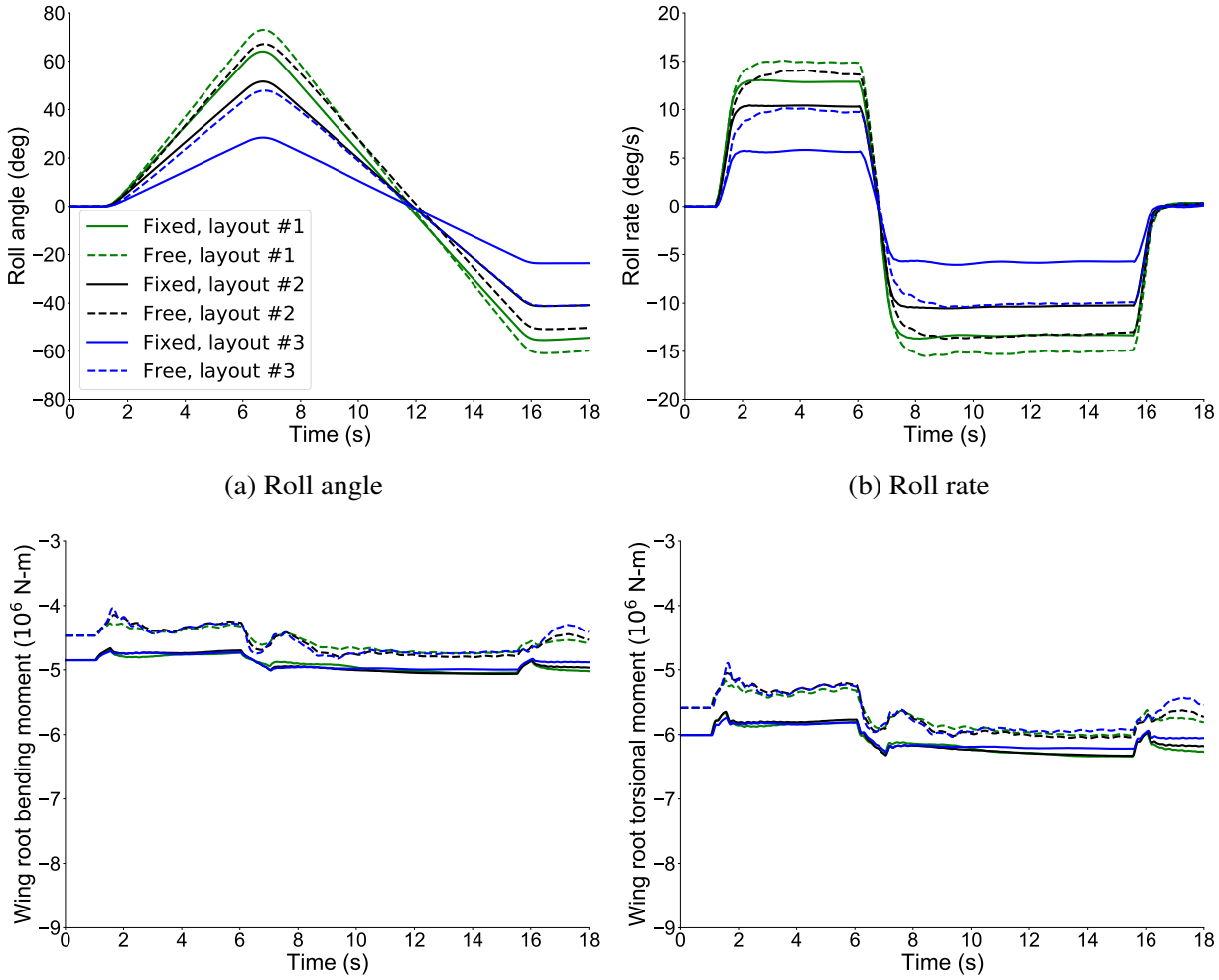

(a) Roll angle

(b) Roll rate

(c) Wing root out-of-plane bending moment

(d) Wing root torsion moment

Figure 4.53: Roll maneuver with inboard trailing-edge control surfaces, out-of-plane bending stiffness (1.75×), $M_\infty = 0.83$.

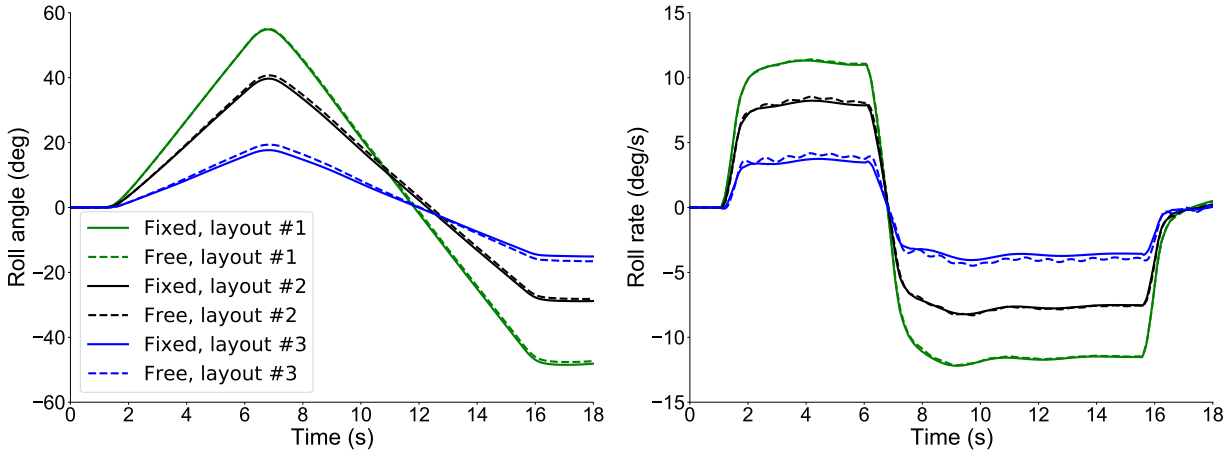

(a) Roll angle, $M_\infty = 0.65$

(b) Roll rate, $M_\infty = 0.65$

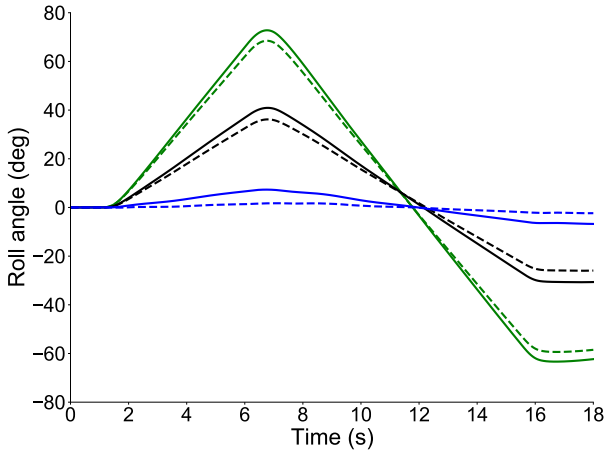

(c) Roll angle, $M_\infty = 0.83$

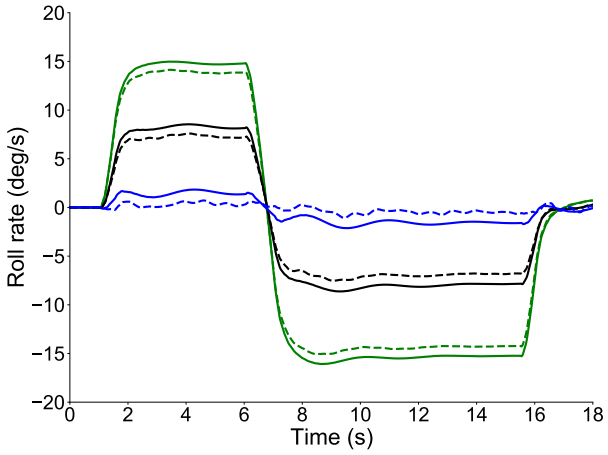

(d) Roll rate, $M_\infty = 0.83$

Figure 4.54: Roll maneuver with inboard trailing-edge control surfaces, torsional stiffness (1.75×).

trends remain similar to the one observed for the baseline wing flexibility. This is expected since the significant driving factor for the washout effects is large out-of-plane bending deformation due to higher out-of-plane bending flexibility.

4.5 Summary

This chapter investigated the roll maneuverability and load alleviation performance of trailing- and leading-edge control surfaces and FFWTs in a HARW aircraft representing a potential future civil transport configuration. Analyses were conducted on the VFA test case for two flight conditions at $M_\infty = 0.65$, a relatively low dynamic pressure case, and at a typical cruise condition at $M_\infty = 0.83$. The effect of wingbox passive aeroelastic tailoring was also investigated.

First, the impact of the spanwise placement of trailing-edge control surfaces on roll maneuverability of a VFA HARW civil transport aircraft test case compared to a contemporary FA test case with a regular wing aspect. The static and dynamic roll response analyses showed that the VFA trailing-edge control surfaces should not be placed farther from the wing root than the FA to achieve comparable roll maneuverability. The results also showed that the benefits of wingbox passive aeroelastic tailoring are modest for practical variations in the stiffness properties and become very slight for more inboard aileron placements and at lower dynamic pressure. The impact of geometrically nonlinear effects on roll control effectiveness was also investigated. The results showed the impact of nonlinear effects was limited to outboard trailing-edge control surfaces and at higher dynamic pressure conditions where the aeroelastic effects are more prominent.

Second, this chapter compared the roll maneuverability and load alleviation performance of leading-and trailing-edge control surfaces. The static spanwise placement study showed maximum roll control effectiveness could be achieved by placing the control surfaces at the midspan for both leading- and trailing-edge control surfaces. However, the peak effectiveness placement also corresponds to the placement resulting in the highest loads at the wing root. Inboard leading-edge control surfaces are ineffective compared to trailing-edge control surfaces at the same spanwise location. On the other hand, for an outboard control surface placement, a leading-edge control surface provides higher load alleviation while avoiding reversal. At higher dynamic pressure, trailing-edge control surfaces exhibit a strong nonlinear response. Dynamic analyses were conducted for selected control surfaces, confirming the static trends.

Third, the impact of deploying FFWTs with trailing- and leading-edge control surfaces was also investigated. The results showed that releasing a FFWT while deploying the control surfaces alleviates bending moment at the wing root due to the reduction in the local angle of attack outboard of the hinge. However, for a flexible wing, this is accompanied by an increase in the local angle of attack inboard of the hinge. Load alleviation occurs if the moment contribution due to the increase in loads inboard remains smaller than the moment contribution due to the decrease in loads outboard. This is the case at lower dynamic pressures while releasing the folding wingtip causes higher loads at higher dynamic pressures due to the level of wing flexibility. This mechanism was investigated further by analyzing the impact of wing stiffness on the load alleviation performance of FFWTs. It was found that the wing's out-of-plane bending stiffness had a significant impact. The dynamic analyses showed that the FFWTs could not enhance the roll maneuverability of a very flexible HARW for a control surface layout placed inboard of the hinge. The roll maneuverability degrades at high dynamic pressure conditions if FFWTs are deployed. This was observed for both the trailing- and leading-edge control surfaces. As observed in the static results, the load alleviation benefit of FFWTs during a roll maneuver is limited to low dynamic pressure conditions where the aeroelastic effects are weaker.

The effect of FFWTs was also analyzed for outboard layouts of trailing- and leading-edge control surfaces. The outboard trailing-edge layouts with or without FFWTs are in reversal due to strong washout effects. Deploying FFWTs with outboard trailing-edge control surfaces led to a free wingtip instability. In contrast, deploying FFWTs with leading-edge control surfaces improved the roll maneuverability for the case of the most outboard layout.

Similar to static results, the significant effect on enhancing the roll maneuverability was observed by increasing the out-of-plane bending stiffness of the wing. Increasing the torsional or the coupling term was found to have a negligible impact. For practical variations in the wing stiffness (+15%), there was a slight improvement in the roll maneuverability for the case of the inboard trailing-edge control surface deployed with FFWTs at the lower dynamic pressure condition. However, a 15% increase in stiffness was insufficient to improve the roll maneuverability at the higher dynamic pressure condition. Increasing the wing stiffness by 75% showed almost a 100% increase in the roll maneuverability of the folding wingtips. A 75% increase in out-of-plane bending stiffness corresponds to the VFA test case with the first-out-of-plane bending frequency similar to the baseline FA test case.

CHAPTER 5

Gust Load Alleviation and Ride Qualities

This chapter addresses the second and third objectives of the thesis by investigating gust load alleviation and ride qualities in transonic HARW aircraft. For this purpose, the response of the VFA is simulated flying through different gust disturbances. First, the impact of geometrically nonlinear effects is investigated by considering linear kinematics and non-follower aerodynamics. Next, the impact of wing and fuselage flexibility on ride qualities is investigated. This is followed by analyzing the gust response of the VFA test case with and without FFWTs to analyze the impact of these devices on load alleviation and ride qualities.

This chapter is organized as follows: Sec. 5.1 provides an overview of the studies in this chapter. Sec. 5.2 investigates the gust response of the VFA test case and highlights the impact of geometrically nonlinear effects. This is followed by Sec. 4.3 which analyze the ride qualities. Finally, Sec. 4.5 summarizes the chapter.

5.1 Analysis Setup

The studies in this chapter consider continuous and discrete gust inputs. The discrete gust input is described by a "1-cosine" vertical gust input with penetrative effects as shown in Fig. 5.1. The gust profile is defined by the following expression [53]:

$$U_{gust} = \frac{U_{ds}}{2}[1 - cos(\frac{\pi S}{H})], \tag{5.1}$$

where U_{ds} is the design gust speed, S is the gust penetrative distance ($0 < S < 2H$) and H is the gust length which can vary from 9 m to 107 m. The design gust speed is a function of the gust length and weight of the aircraft. The studies in this work consider a gust length of $H = 9, 60, 107$ m and the design gust speed of $U_{ds} = 6.9, 9.5, 10.4$ m/s respectively.

The continuous gust disturbance is generated by the one-dimensional von Kármán spectrum.

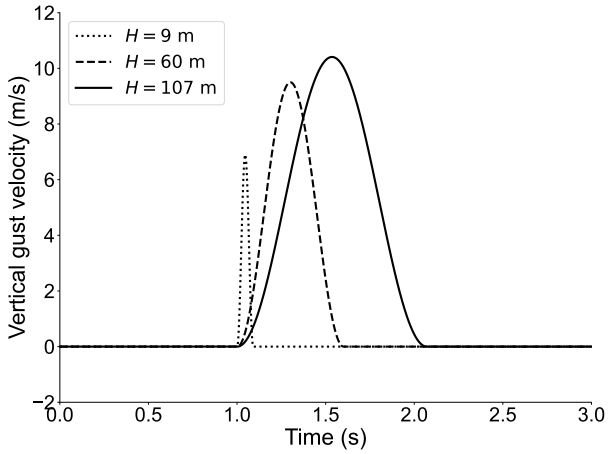

Figure 5.1: Time-domain signal for "1-cosine."

The von Kármán is prescribed with power spectral density Φ given by:

$$\Phi(\Omega) = \frac{L}{\pi} \frac{1 + \frac{8}{3}(1.339L\Omega)^2}{\left[1 + (1.339L\Omega)^2\right]^{\frac{11}{6}}} , \tag{5.2}$$

where Ω is the reduced frequency and $L = 762$ m is the scale of turbulence considered. Figure 5.2 and shows the time signal associated for the gust vertical velocity. The studies with FFWTs consider the wingtip location at approximately at spanwise location corresponding to baseline FA wingtip (same as the maneuver load alleviation studies in Sec. 4.4.1).

5.2 Gust Load Alleviation

This section discusses the impact of gust disturbance on the loads generated at the wingroot of the VFA test case. Section 5.2.1 discusses the impact of geometrically nonlinear effects on the gust response. Next, Sec. 5.2.2 discusses the impact of FFWTs on gust load alleviation along with the impact of wing flexibility on their performance.

5.2.1 Impact of Geometrically Nonlinear Effects

This section investigates the impact of geometrically nonlinear effects on the gust response of transonic HARW aircraft. The gust response of the VFA test case is simulated with different combinations of linear/nonlinear kinematics and follower/non-follower aerodynamics. The response to discrete vertical gust is shown in Figs. 5.3 and 5.4. A higher pitch angle and vertical tip displacement are observed at both flight conditions with non-follower aerodynamics and linear kinematics.

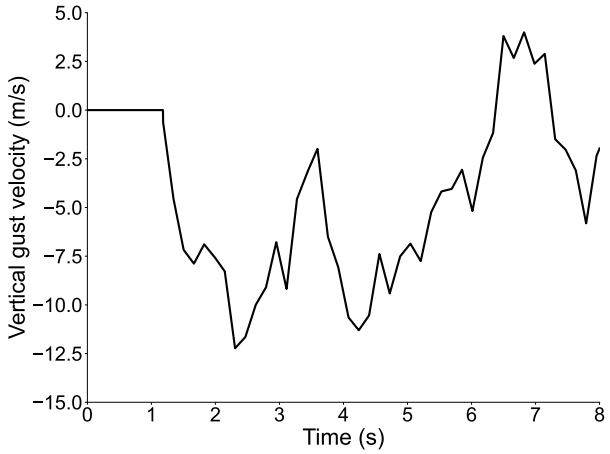

Figure 5.2: Time-domain signal for a von Kármán vertical gust disturbance.

The impact of considering non-follower aerodynamics is higher. This is reflected in the evaluation of loads at the wing root in Fig. 5.4. Higher loads are predicted if linear kinematics and non-follower aerodynamics are considered. The difference in the loads evaluation is higher at $M_\infty = 0.83$.

Similar behavior is observed with the continuous vertical gust in Figs. 5.5 and 5.6. A higher difference in the evaluation of loads is observed for a model considering nonlinear kinematics with follower aerodynamics compared to linear kinematics with non-follower aerodynamics. These results highlight the impact of geometrically nonlinear effects on the gust response of a VFA test case. While a conservative estimation of loads with a linear analysis will provide higher safety margins, it will also impact the aircraft's performance. The subsequent studies in this chapter consider nonlinear kinematics and follower aerodynamics in the gust response analyses.

5.2.2 Impact of Flared Folding Wingtips

This section presents the results of the investigations to study the gust load alleviation capabilities of the FFWTs. Dynamic simulations of the VFA test case with and without FFWTs are presented for two flight conditions as described in Sec. 4.2.1. The case where FFWTs are fixed (locked) signifies their flat position associated with the original wing geometry during the trim and dynamic simulations, similar to results in Sec. 5.2.1. The case with free FFWTs signifies the solution starting from a trimmed condition. The FFWTs are free to rotate until static equilibrium is reached and are locked when a dynamic simulation starts about the trimmed state. The FFWTs are released at $t = 0.5$ s, with the gust disturbance starting at $t = 1.0$ s. All the simulations with free FFWTs set the hinge stiffness to K^H_{HH} = 0.0 Nm/rad, with damping D^H_{HH} = 10.0 kNms/rad and a flare

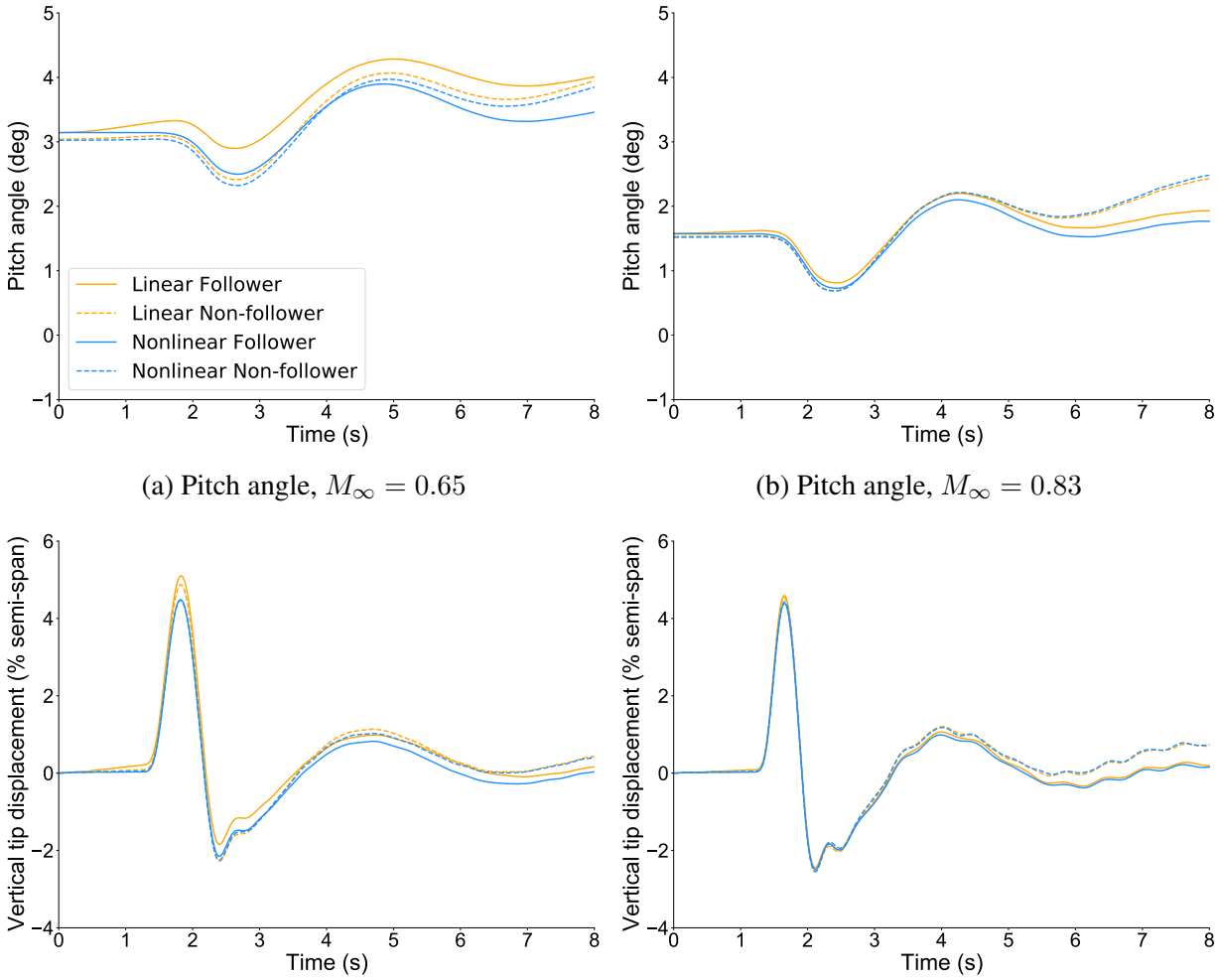

(a) Pitch angle, $M_\infty = 0.65$

(b) Pitch angle, $M_\infty = 0.83$

(c) Vertical tip displacement, $M_\infty = 0.65$

(d) Vertical tip displacement, $M_\infty = 0.83$

Figure 5.3: Impact of geometrically nonlinear effects on VFA response to discrete vertical gust ($H = 107$ m).

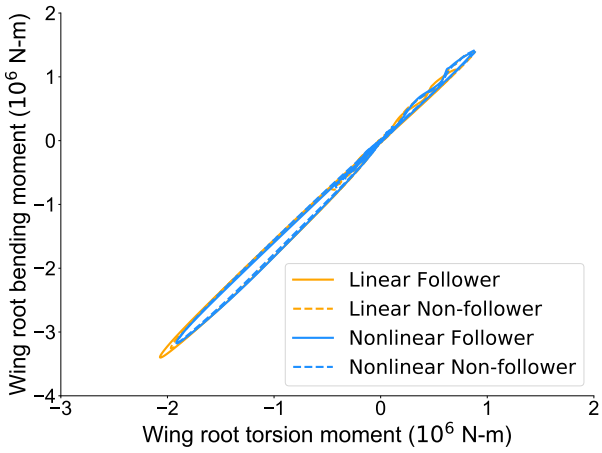

(a) Out-of-plane-bending vs. torsion, $M_\infty = 0.65$

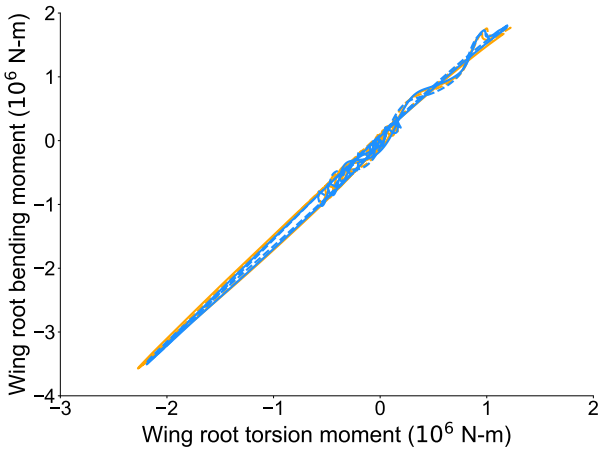

(b) Out-of-plane-bending vs. torsion, $M_\infty = 0.83$

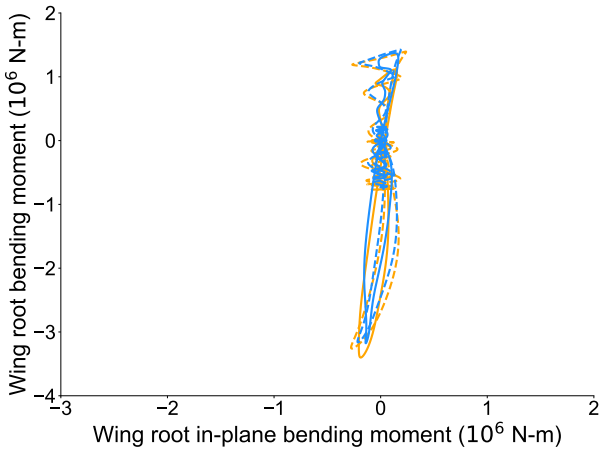

(c) Out-of-plane vs. in-plane bending, $M_\infty = 0.65$

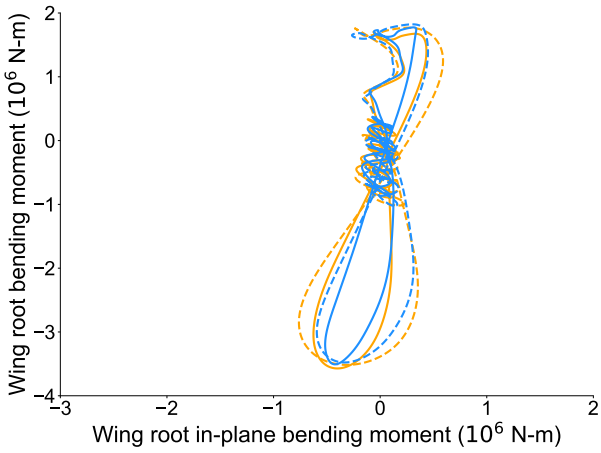

(d) Out-of-plane vs. in-plane bending, $M_\infty = 0.83$

Figure 5.4: Impact of geometrically nonlinear effects on VFA loads with discrete vertical gust ($H = 107$ m).

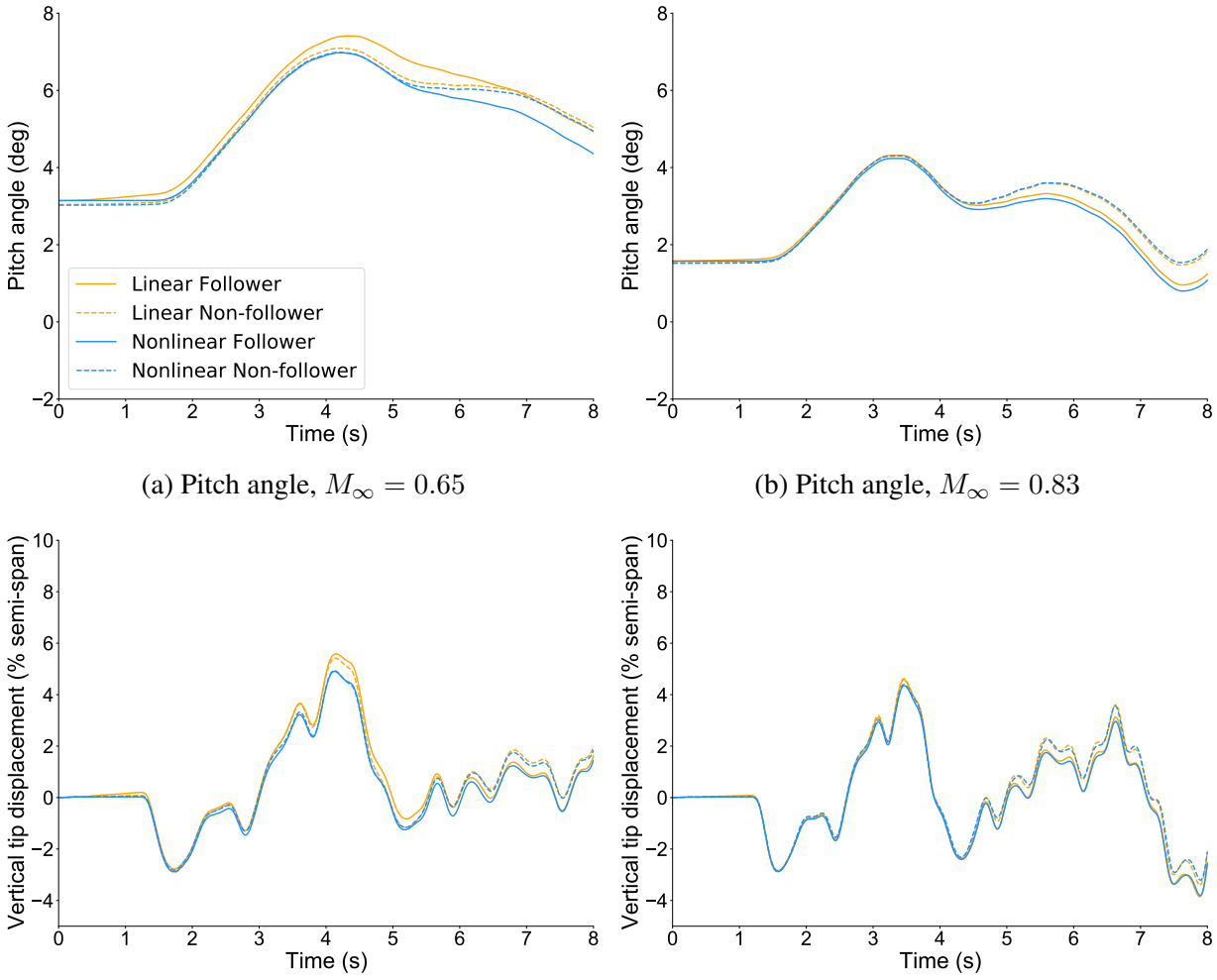

(a) Pitch angle, $M_\infty = 0.65$

(b) Pitch angle, $M_\infty = 0.83$

(c) Vertical tip displacement, $M_\infty = 0.65$

(d) Vertical tip displacement, $M_\infty = 0.83$

Figure 5.5: Impact of geometrically nonlinear effects on VFA response to continuous vertical gust.

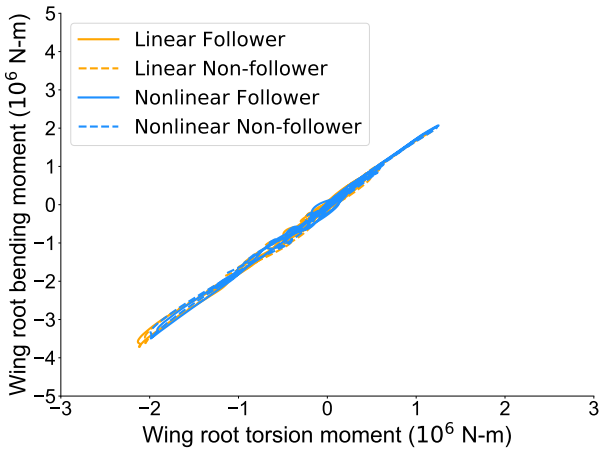

(a) Out-of-plane-bending vs. torsion, $M_\infty = 0.65$

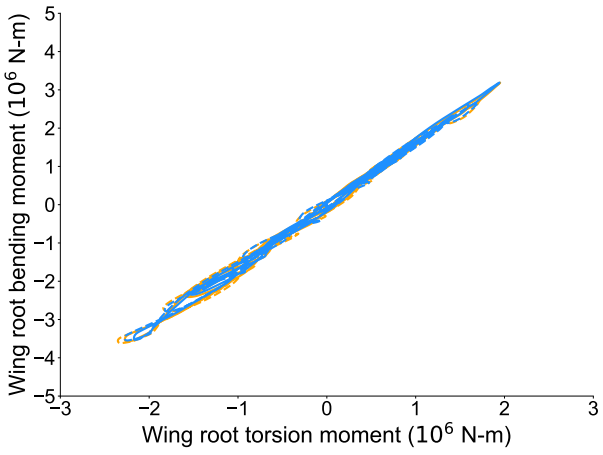

(b) Out-of-plane-bending vs. torsion, $M_\infty = 0.83$

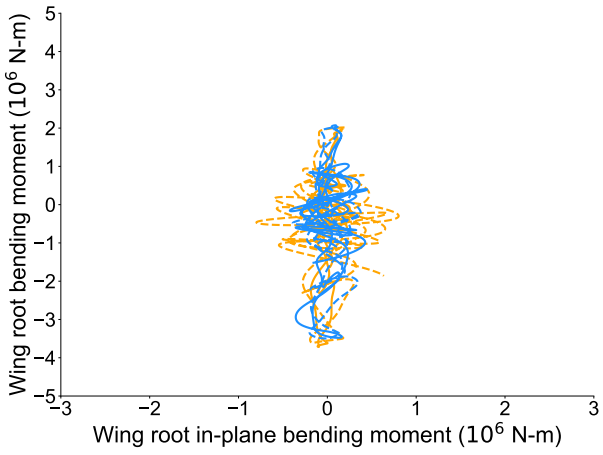

(c) Out-of-plane vs. in-plane bending, $M_\infty = 0.65$

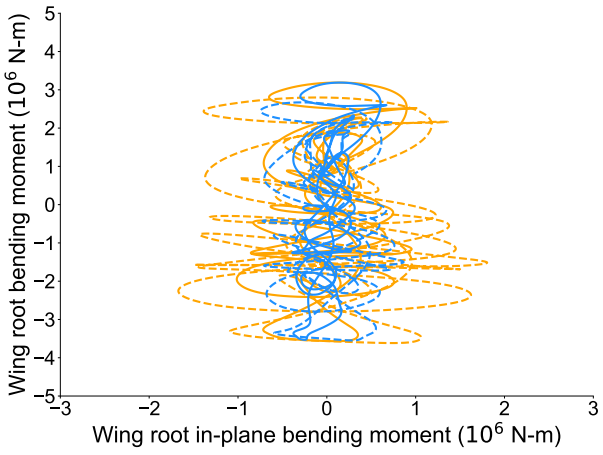

(d) Out-of-plane vs. in-plane bending, $M_\infty = 0.83$

Figure 5.6: Impact of geometrically nonlinear effects on VFA loads with continuous vertical gust.

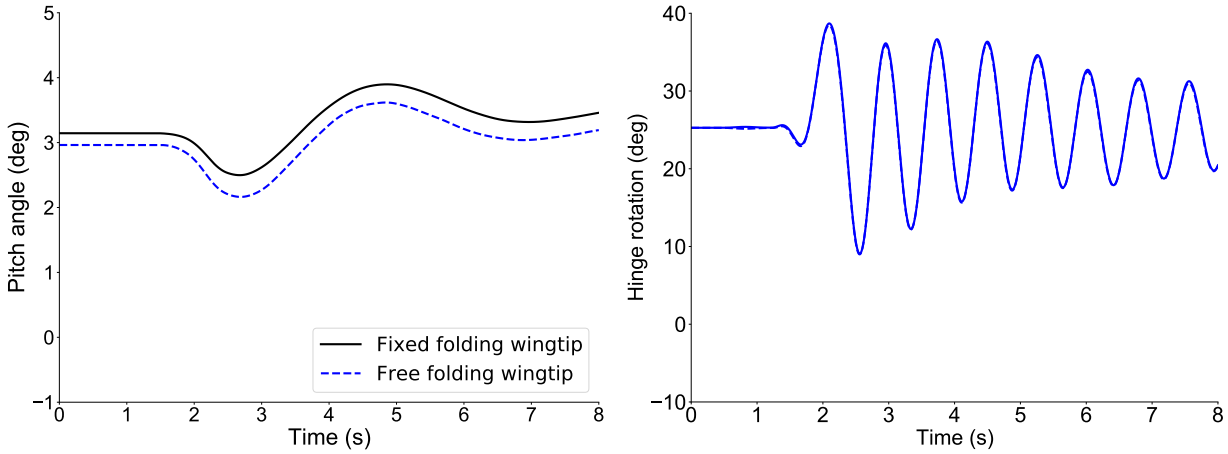

(a) Pitch angle

(b) Hinge rotation

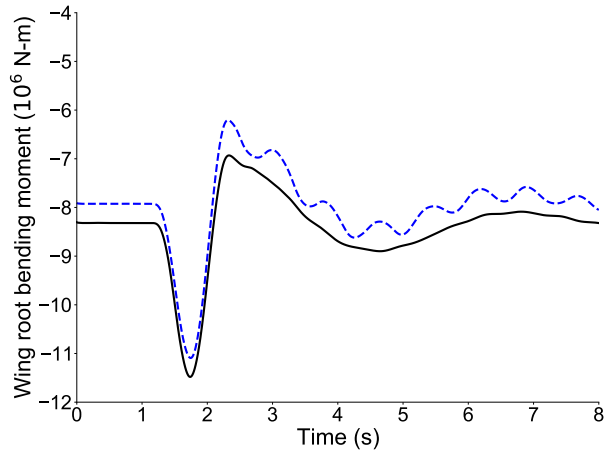

(c) Wing root out-of-plane bending moment

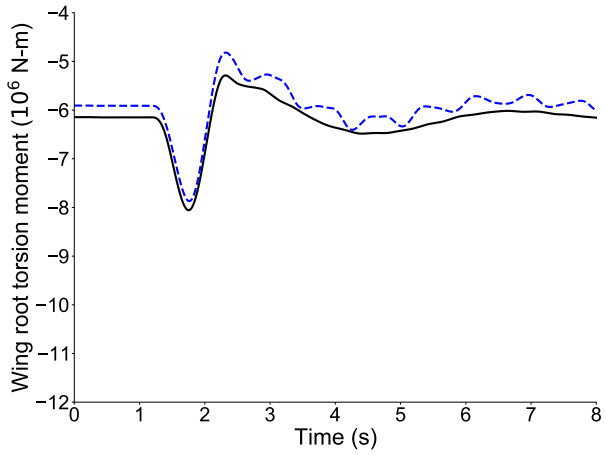

(d) Wing root torsion moment

Figure 5.7: VFA response to discrete vertical gust ($H = 107$ m) with deployed FFWTs, $M_\infty = 0.65$.

angle $\Lambda = 10$ deg. The impact of varying flare angles is not shown here since its impact on load alleviation was found insignificant 4.4.1. The results for the baseline stiffness are described in this section, followed by the impact of wing stiffness in Sec. 5.3.1.

First, the results for the "1-cosine" vertical gust input are shown in Figs. 5.7 and 5.8 for a gust length of $H = 107$ m. At $M_\infty = 0.65$, deploying FFWTs offers load alleviation benefits by reducing the out-of-plane moment at the wing root. The pitch angle is also reduced. The hinge rotation for the right and left wingtips show an oscillatory behavior. Note that in the case of a gust disturbance, both the wingtips rotate upwards. An increase in hinge rotation alleviates load by decreasing more lift outboard of the hinge while the opposite is true when the hinge rotation decreases. In contrast, at the high dynamic pressure condition (see Fig. 5.8), there is negligible impact

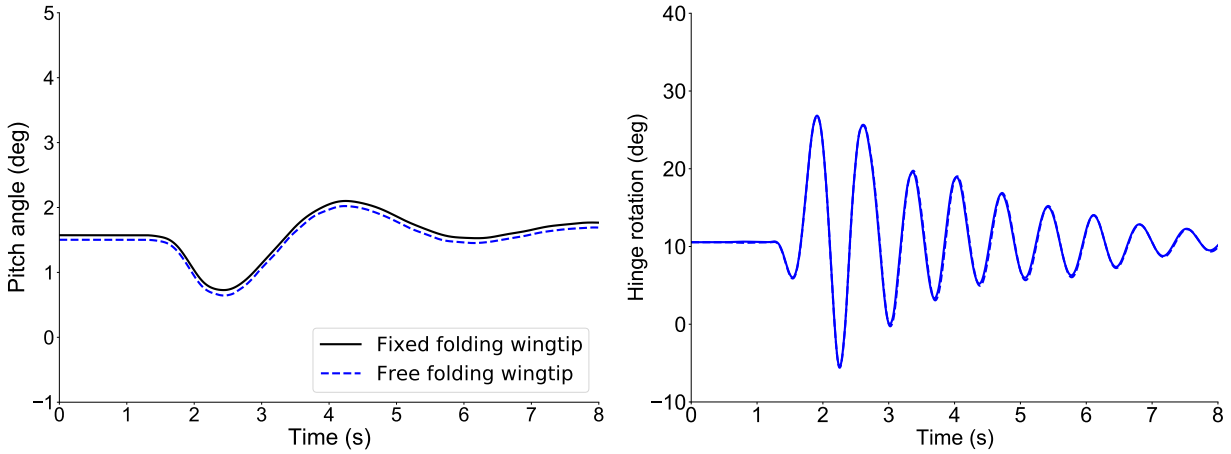

(a) Pitch angle

(b) Hinge rotation

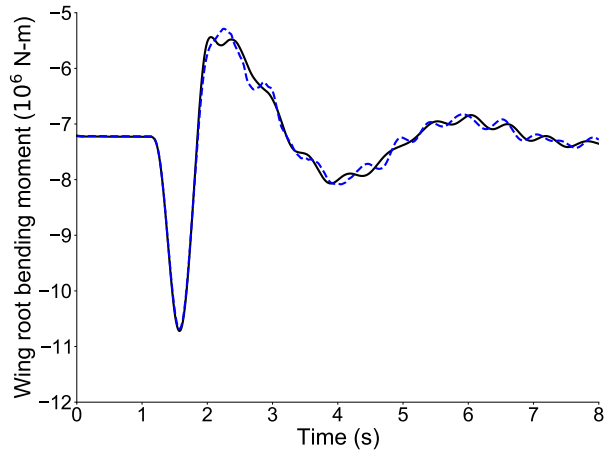

(c) Wing root out-of-plane bending moment

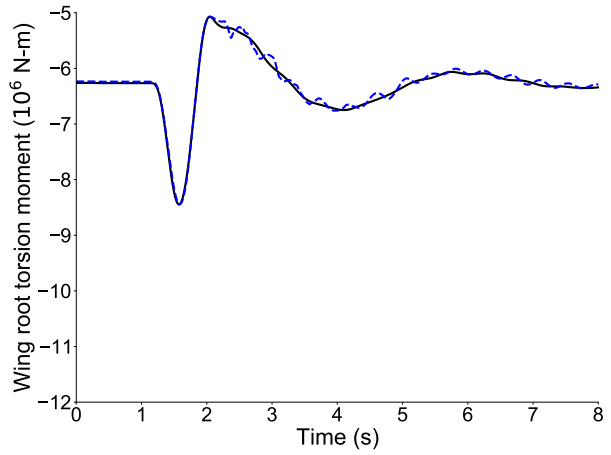

(d) Wing root torsion moment

Figure 5.8: VFA response to discrete vertical gust ($H = 107$ m) with deployed FFWTs, $M_\infty = 0.83$.

on the response and loads due to the wingtip rotation. These results also align with observations of maneuver load alleviation studies 4.4.2. The strong aeroelastic effects at this flight condition reduce the load alleviation performance by increasing substantial lift inboard of the hinge.

The load alleviation performance of folding wingtips for varying gust lengths is shown in Fig. 5.9 for $H = 60, 9$ m at $M_\infty = 0.65$. While the load performance benefit has no significant difference, the overall loads and oscillations are reduced for the shortest gust length considered. The results for $M_\infty = 0.83$ are not shown due to the poor load alleviation performance observed with the $H = 107$ m case.

Next, the results for the continuous gust input are shown in Figs. 5.10 and 5.11. Similar behavior is observed for the two different gust inputs. At $M_\infty = 0.65$, the FFWTs respond to the

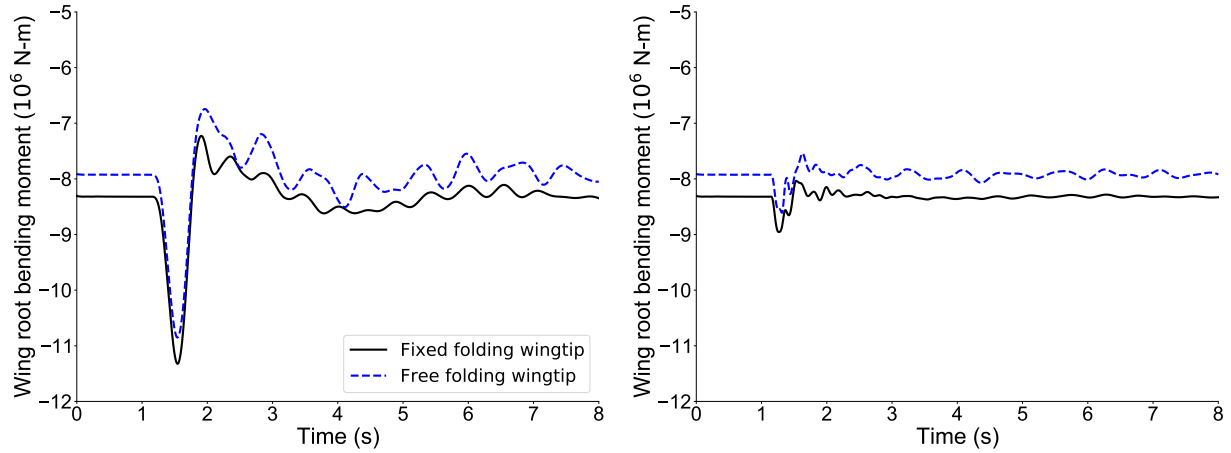

(a) Wing root out-of-plane bending moment, $H = 60$ m

(b) Wing root out-of-plane bending moment, $H = 9$ m

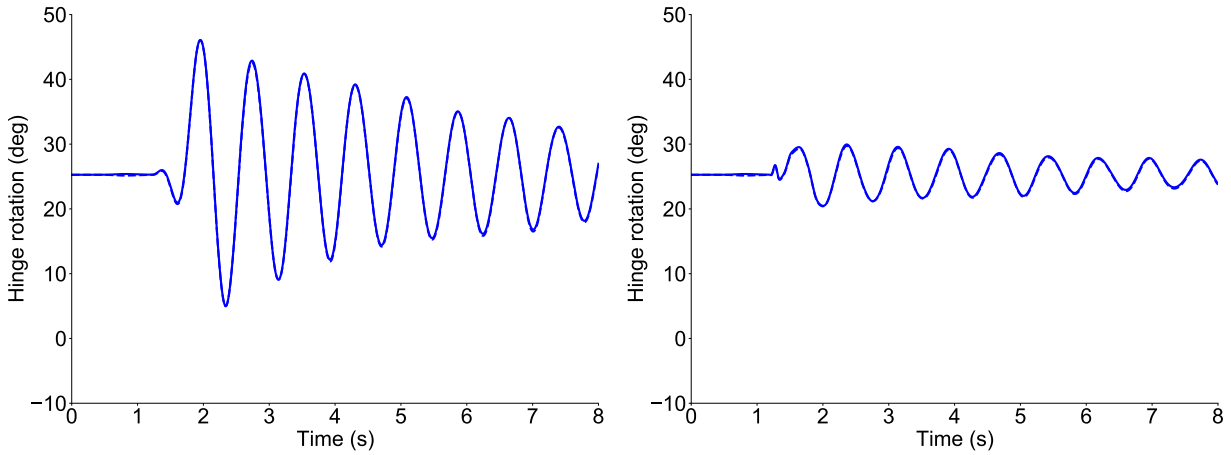

(c) Hinge rotation, $H = 60$ m

(d) Hinge rotation, $H = 9$ m

Figure 5.9: VFA response to discrete vertical gust with deployed FFWTs, varying gust length, $M_\infty = 0.65$.

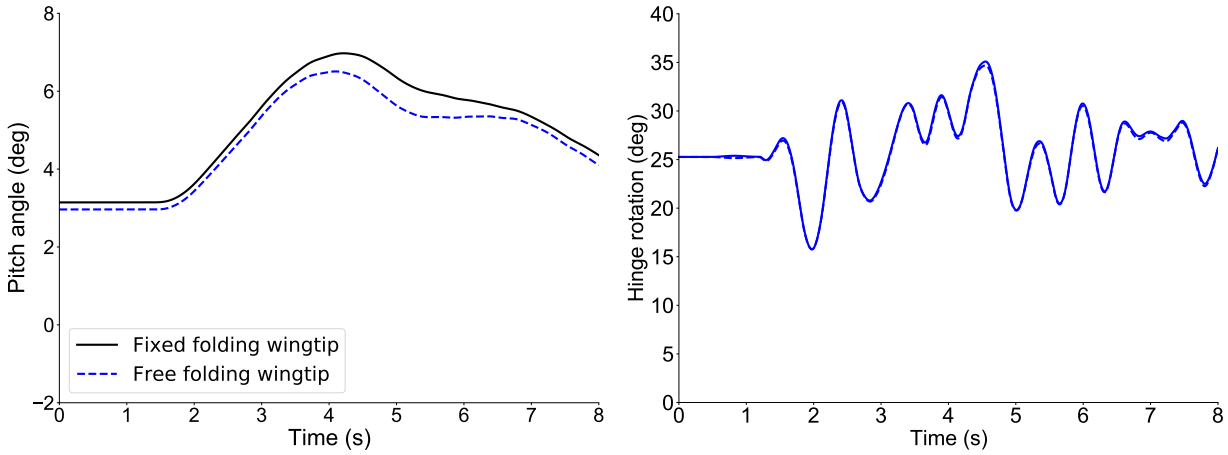

(a) Pitch angle

(b) Hinge rotation

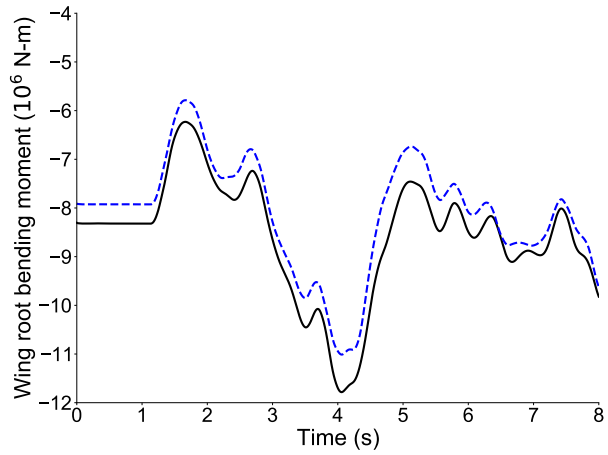

(c) Wing root out-of-plane bending moment

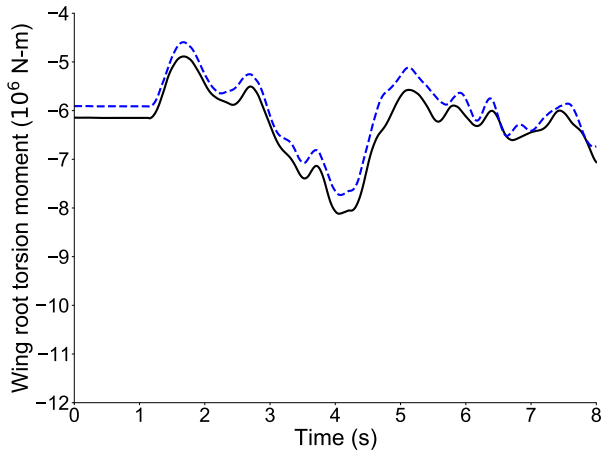

(d) Wing root torsion moment

Figure 5.10: VFA response to continuous vertical gust with deployed FFWTs, $M_\infty = 0.65$.

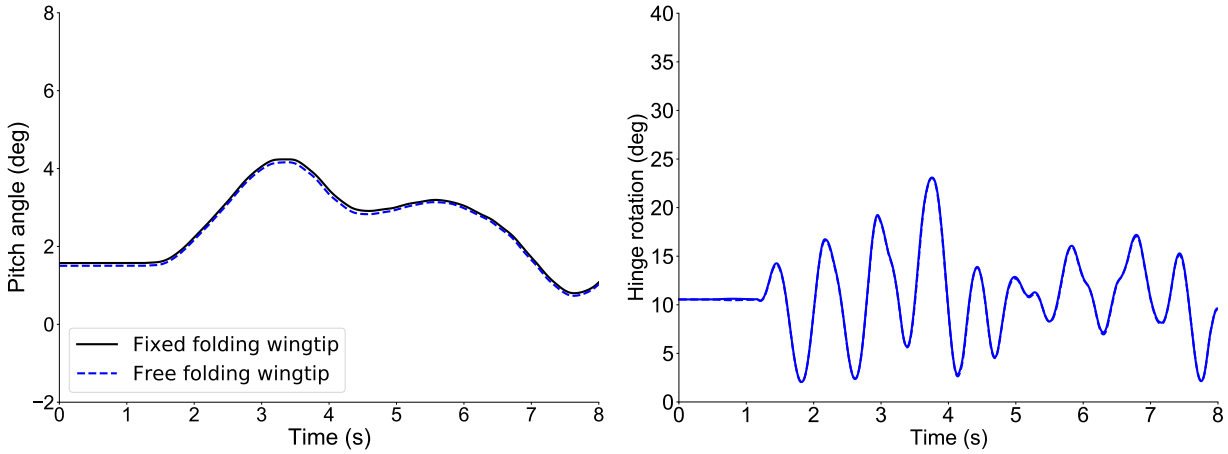

(a) Pitch angle

(b) Hinge rotation

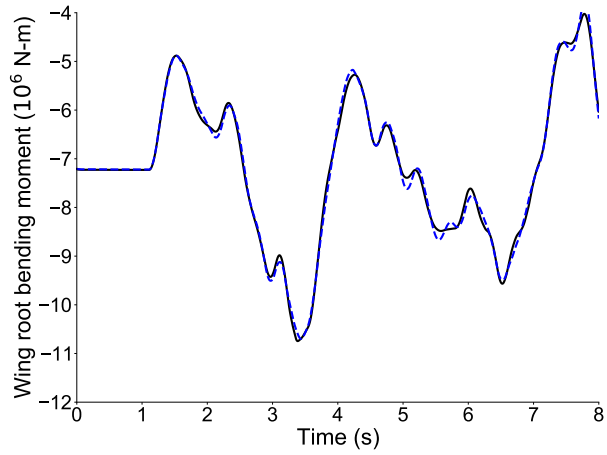

(c) Wing root out-of-plane bending moment

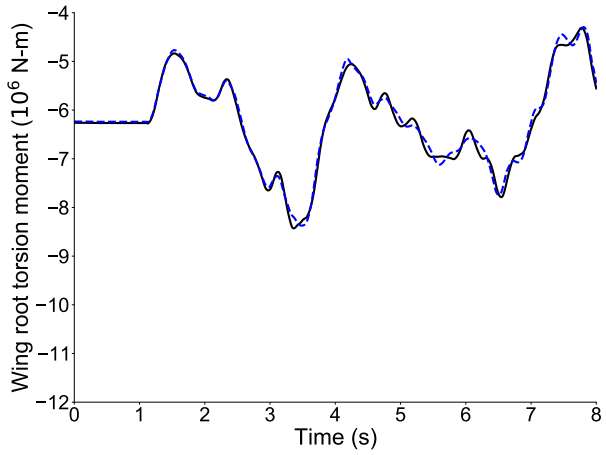

(d) Wing root torsion moment

Figure 5.11: VFA response to continuous vertical gust with deployed FFWTs, $M_\infty = 0.83$.

gust disturbance by rotating about the hinge. The flare angle and the wingtip's upward deflection reduce the angle of attack outboard of the hinge, alleviating the loads at the wing root as shown in Figs. 5.10c and 5.10d. A difference in hinge rotation is observed between the two gust inputs due to the nature of the applied gust velocity field. The discrete gust input resulted in an oscillatory behavior of the hinge rotations, which peaked at the time of the gust input application and then had a slow decay with time (see Fig 5.10b). In contrast, the hinge rotation developed a non-sinusoidal response with the continuous gust input. A similar motion of the wingtip is observed at $M_\infty = 0.83$. However, as seen with the discrete gust, the FFWT rotates less at this flight condition due to stronger wash-out effects toward the wingtip. This contributed to poor load alleviation performance of the FFWTs.

Next, the impact of wing flexibility on the load alleviation performance of the FFWTs is in-

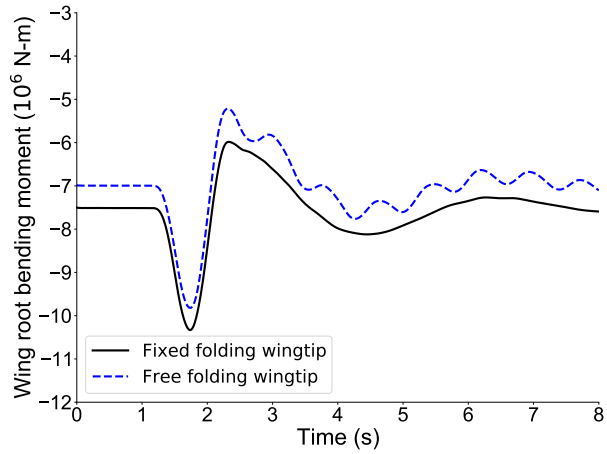

(a) Wing root out-of-plane bending moment, case 1

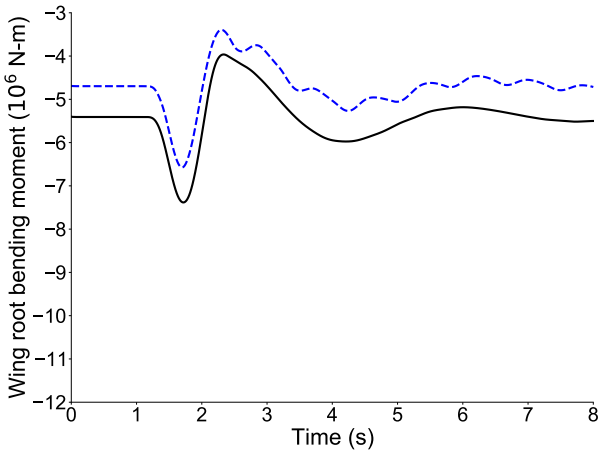

(b) Wing root out-of-plane bending moment, case 2

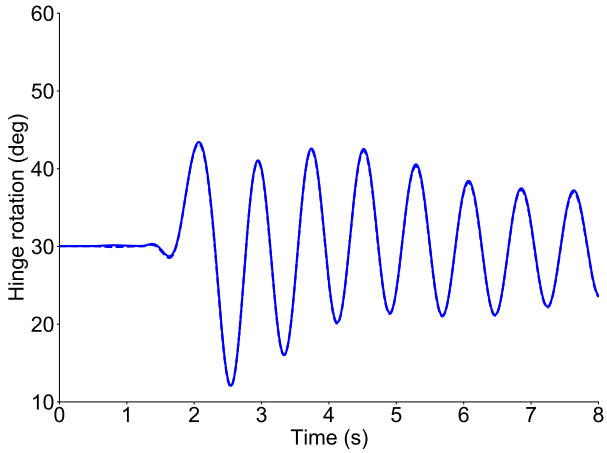

(c) Hinge rotation, case 1

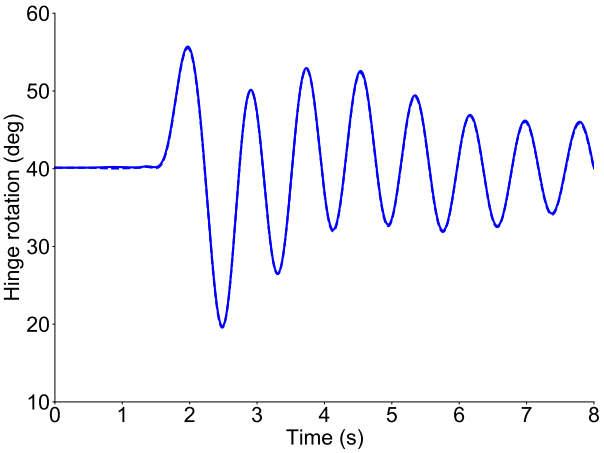

(d) Hinge rotation, case 2

Figure 5.12: VFA response to discrete gust ($H = 107$ m) with deployed FFWTs, varying wing stiffness, $M_\infty = 0.65$.

vestigated. The results are presented for two cases: case 1 corresponds to a practical variation in the out-of-plane bending stiffness (15%) and; case 2 corresponds to a 75% increase in the out-of-plane bending stiffness representing a stiffened version of the VFA test case with the first bending frequency close to the baseline FA test case. Results are presented for both the gust inputs. The discrete gust input results consider only the longest gust input ($H = 107$ m).

Figs. 5.12 and 5.13 compares the load alleviation and hinge rotation for the two wing stiffness case. Comparing these results with the baseline stiffness (see Fig. 5.7) for the lower dynamic pressure condition, a higher load reduction is observed as the stiffness of the wing is increased. The wingtip rotates more at the trim and during the gust encounter. This helps increase the load alleviation due to a higher reduction in lift outboard of the hinge. Further, as the wing stiffness

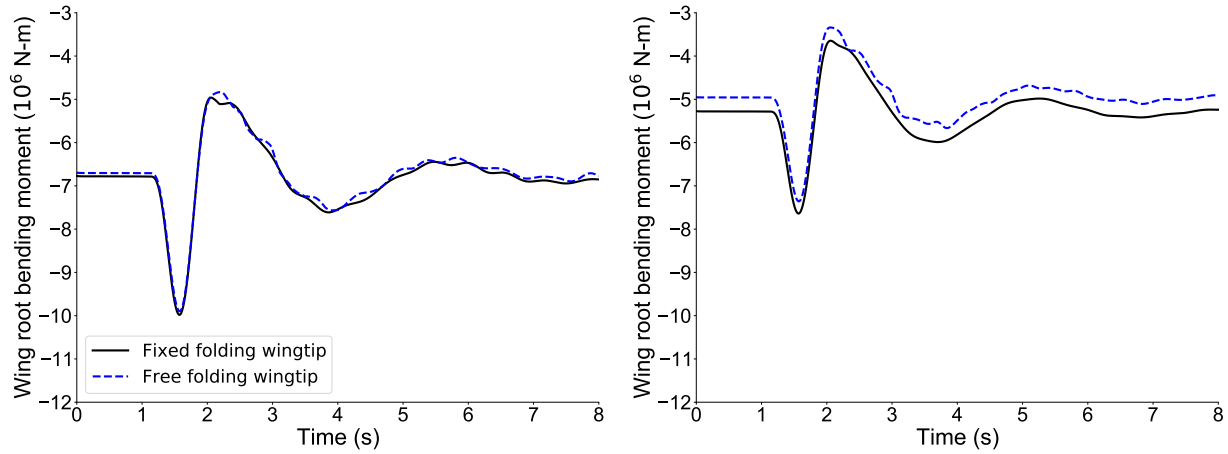

(a) Wing root out-of-plane bending moment, case 1

(b) Wing root out-of-plane bending moment, case 2

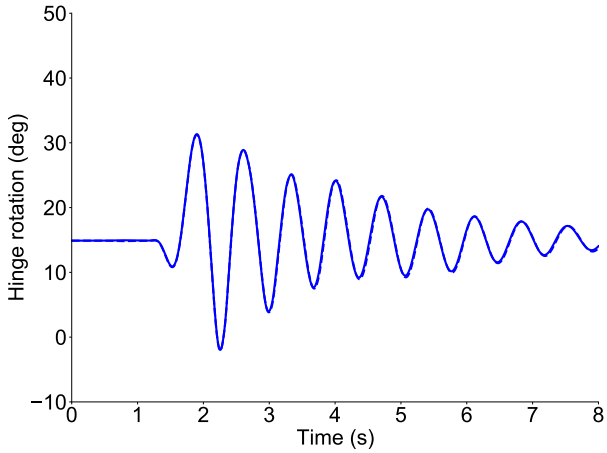

(c) Hinge rotation, case 1

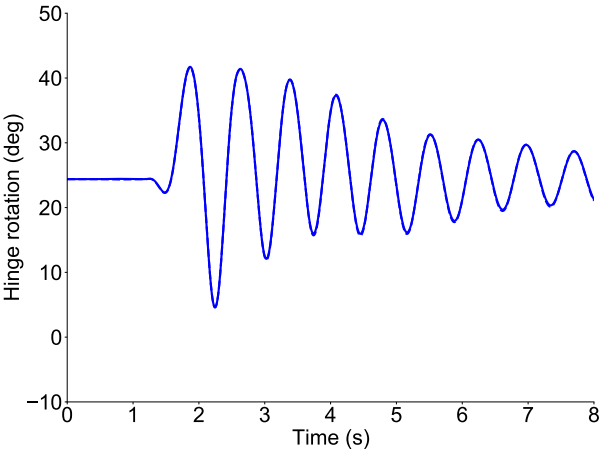

(d) Hinge rotation, case 2

Figure 5.13: VFA response to discrete gust ($H = 107$ m) with deployed FFWTs, varying wing stiffness, $M_\infty = 0.83$.

increase, the aeroelastic effects become milder, resulting in a smaller increase in lift inboard of the hinge. This higher reduction in lift outboard and a lower increase in lift inboard of the hinge contribute to the improvement of FFWT's load alleviation performance. A lower impact of wing stiffness is observed at $M_\infty = 0.83$. The 15% increase in wing stiffness is not significant at this flight condition to improve load alleviation, as shown in Fig. 5.13a. However, for stiffness case 2, the 75% increase in wing stiffness shows a significant load reduction at this flight condition. The impact of wing stiffness is also observed with increased hinge rotation.

Finally, the impact of wing stiffness is also shown for the continuous gust input in Figs. 5.14 and 5.15. The overall trends in the load alleviation remain the same as observed for the results with the discrete gust. At $M_\infty = 0.65$, higher load alleviation benefits are observed as the stiffness

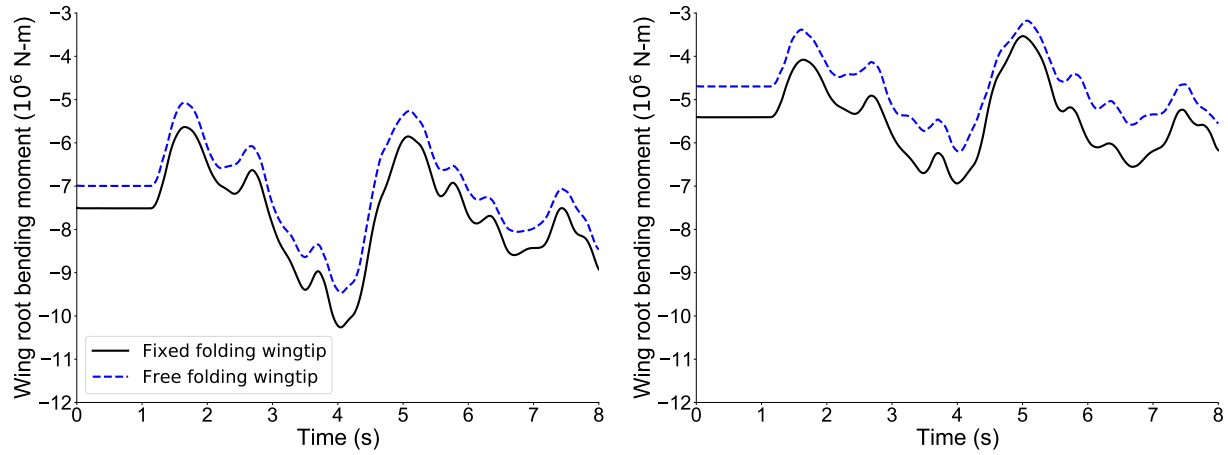

(a) Wing root out-of-plane bending moment, case 1

(b) Wing root out-of-plane bending moment, case 2

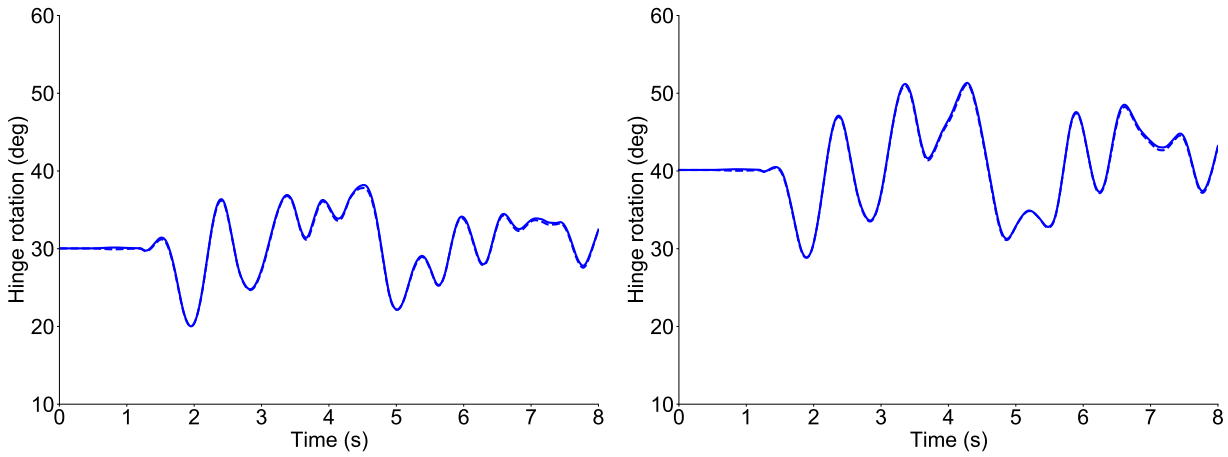

(c) Hinge rotation, case 1

(d) Hinge rotation, case 2

Figure 5.14: VFA response to continuous gust with deployed FFWTs, varying wing stiffness, $M_\infty = 0.65$.

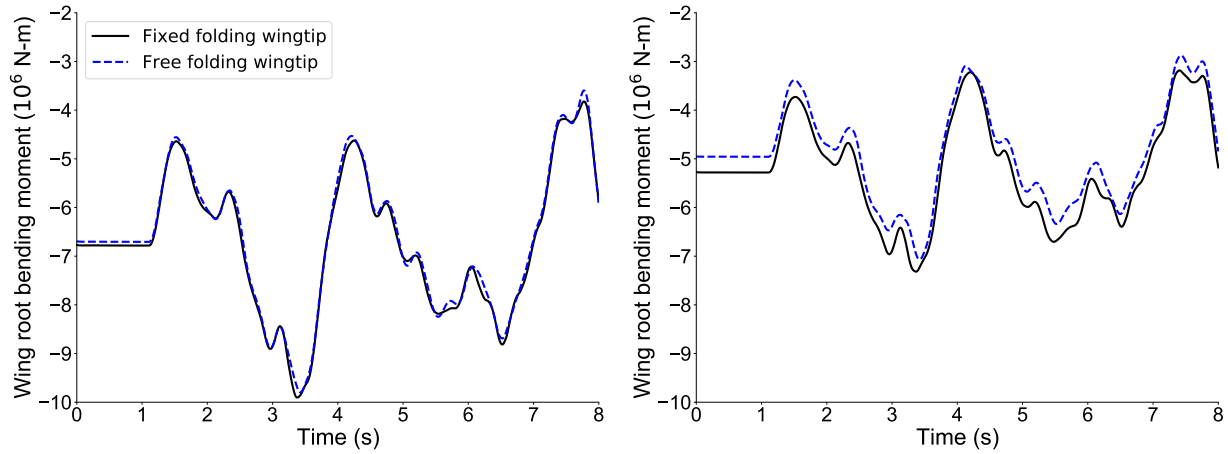

(a) Wing root out-of-plane bending moment, case 1

(b) Wing root out-of-plane bending moment, case 2

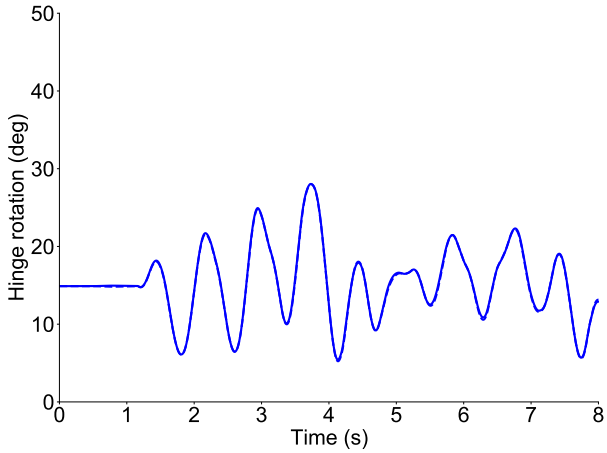

(c) Hinge rotation, case 1

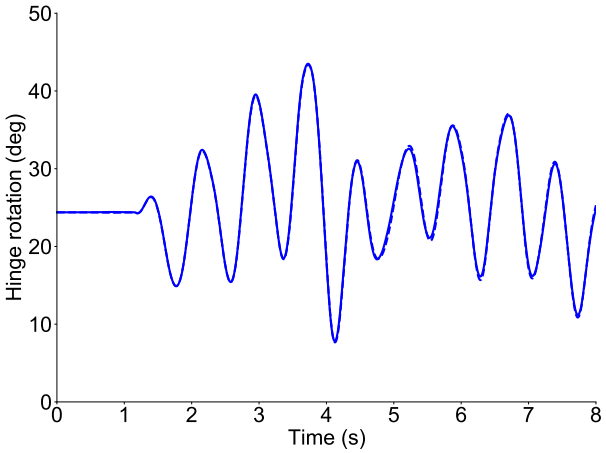

(d) Hinge rotation, case 2

Figure 5.15: VFA response to continuous gust with deployed FFWTs, varying wing stiffness, $M_\infty = 0.83$.

increases, while at $M_\infty = 0.83$, a significant load alleviation is observed only with the higher increase in wing stiffness (case 2). These results are consistent with the maneuver load alleviation results (see Sec. 4.4.2), which showed that the FFWTs effectiveness in reducing loads varies with the level of wing flexibility and the flight condition.

5.3 Ride Qualities

Table 5.1 lists the accelerometers placed at various points of interest along the fuselage. The accelerometers #1 and #6 are placed at an offset from the fuselage beam reference axis, while the others are placed along the reference axis. The ride qualities are evaluated for only the continuous

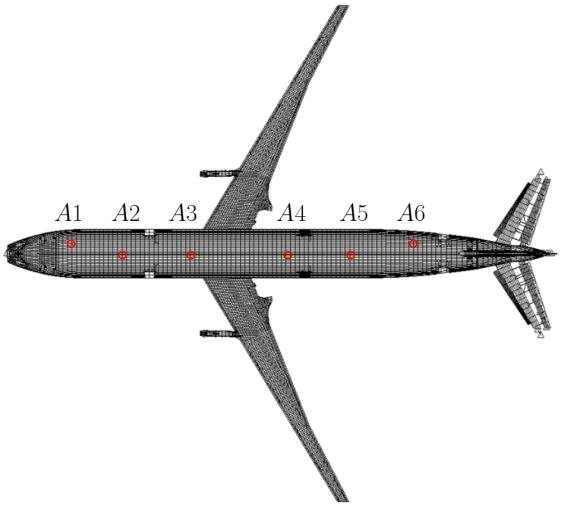

Figure 5.16: Positions of the accelerometers along the fuselage.

Table 5.1: Coordinates of the accelerometers in the aircraft B frame.

Label	x (m)	y (m)	z (m)
A1	-24.00	1.10	1.05
A2	-12.02	0.00	0.98
A3	-4.05	0.00	0.98
A4	4.42	0.00	0.98
A5	20.00	0.00	0.98
A6	28.71	1.10	0.31

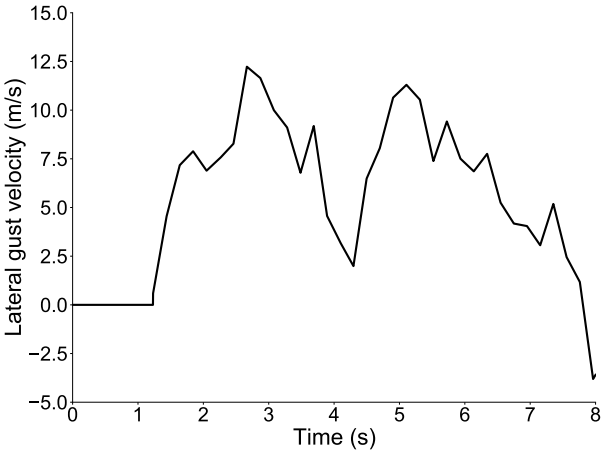

Figure 5.17: Time-domain signal for a von Kármán lateral gust disturbance.

gust model since it can excite different frequencies during the simulation. The studies consider a vertical and lateral gust input. Figure 5.17 and shows the time signal associated for the gust lateral velocity.

The discussion of ride quality results is as follows: Sec. 5.3.1 shows the impact of wing flexibility on the ride qualities and Sec. 5.3.1 presents the results investigating the impact of FFWTs on ride qualities of the VFA test case.

5.3.1 Impact of Wing and Fuselage Flexibility

The ride qualities of the VFA test case are compared with the FA test case to show the impact of a very flexible HARW. Then the impact of wing and fuselage flexibility is analyzed. The results for the vertical and lateral gust inputs are presented in Sec. 5.3.1.1 and Sec. 5.3.1.2 respectively.

5.3.1.1 Vertical Gust

Figure 5.18 compares the vertical accelerations for each sensor and test case for the two flight conditions. The $M_\infty = 0.83$ flight condition is associated with higher accelerations causing higher discomfort, as shown by the higher ride quality metric values in Table 5.2 and 5.3. The last column in the tables lists the percentage variation of the ride quality metric for the VFA test case relative to the FA for a given sensor. A percentage decrease means that the VFA has a lower ride quality metric value than the FA, that is, improved ride qualities. A percentage increase means that the VFA has a higher value of the ride quality metric, meaning degraded ride qualities.

For both test cases, vertical accelerations are highest toward the tail (A5 and A6), leading to higher values of the ride quality metric and increasing discomfort. At $M_\infty = 0.83$, the VFA

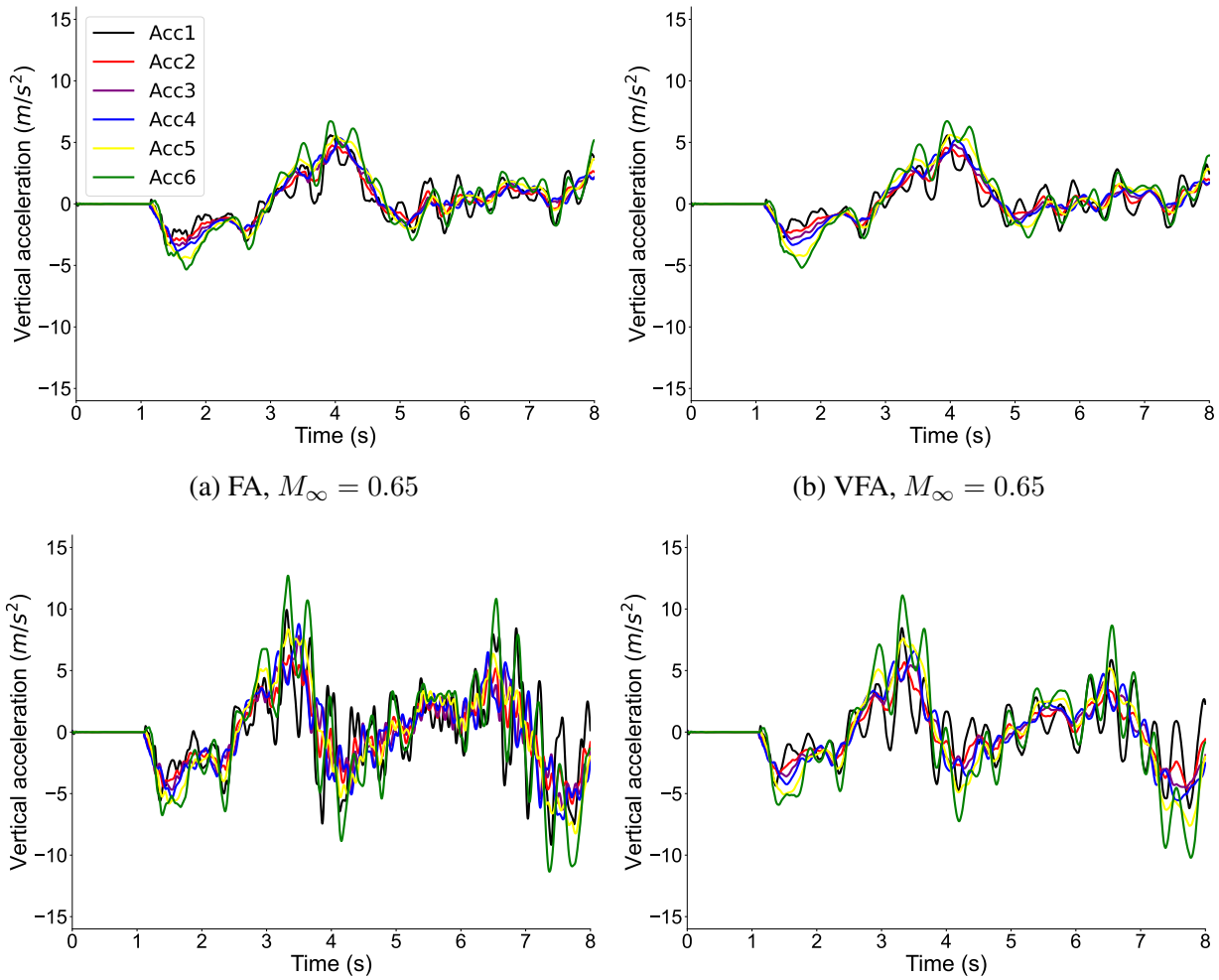

(a) FA, $M_\infty = 0.65$

(b) VFA, $M_\infty = 0.65$

(c) FA, $M_\infty = 0.83$

(d) VFA, $M_\infty = 0.83$

Figure 5.18: VFA vs. FA vertical accelerations at various locations during the vertical gust encounter.

Table 5.2: VFA vs. FA ride quality metric (m/s^2) during the vertical gust encounter, $M_\infty = 0.65$.

Sensor	FA	VFA	Variation (%)
A1	0.491	0.439	−10.50
A2	0.469	0.421	−10.10
A3	0.494	0.452	−8.53
A4	0.534	0.500	−6.48
A5	0.622	0.604	−2.85
A6	0.704	0.690	−2.09

Table 5.3: VFA vs. FA ride quality metric (m/s^2) during the vertical gust encounter, $M_\infty = 0.83$.

Sensor	FA	VFA	Variation (%)
A1	0.913	0.667	−27.00
A2	0.715	0.575	−19.63
A3	0.790	0.649	−17.85
A4	0.878	0.753	−14.29
A5	1.018	0.947	−7.01
A6	1.284	1.153	−10.20

shows lower accelerations than the FA due to the higher flexibility and larger inertia associated with the HARW test case. This translates to lower ride quality metric values for each sensor (Table 5.3), meaning enhanced ride qualities. The difference in the ride quality metric is higher for the sensors in front of the fuselage. At $M_\infty = 0.65$, the difference in the acceleration levels and ride quality metric values between the two test cases is smaller. At this flight condition, the acceleration alleviation effect due to the increased flexibility of the HARW is less pronounced. Moving from the nose toward the tail causes smaller and smaller differences in the vertical accelerations between the two configurations.

Figure 5.19 compares the ride quality metric for the VFA with varying wing flexibility levels. The stiffened variant case 2 has the out-of-plane bending and torsion stiffness distributions scaled by constant factors of 1.75 and 1.5, respectively. This shifts the first few frequencies in the same range as the FA test case to isolate the impact of the higher wing aspect ratio. The stiffened variant 1 has the out-of-plane bending and torsion stiffness distributions scaled by constant factors of 1.15 and 1.15, respectively. The trend for the different accelerometers is not monotonic. The rigid wing case shows a higher ride quality metric for both flight conditions than the flexible wing case. The stiffened variant case 2 experiences higher accelerations than its rigid counterpart except for the sensors at the front of the fuselage (A1 to A3). The discomfort at the front of the fuselage (A1) remains higher with the flexible wing than with the stiffened wing. The stiffened variant case 1 experiences lower accelerations than its rigid counterpart. However, it experiences higher accelerations than its flexible counterpart except for the sensors at the front of the fuselage (A1 to A2). The discomfort at the front of the fuselage (A1) remains higher with the flexible wing than with the stiffened wings.

These trends are similar for the two flight conditions, though the numerical values of the ride quality metric vary. These results considered the fuselage as a flexible member. The results considering the fuselage as a rigid member are shown in Fig. 5.20. The impact of fuselage flexibility on the ride quality metric is shown for the VFA with varying wing flexibility levels. For a flexible

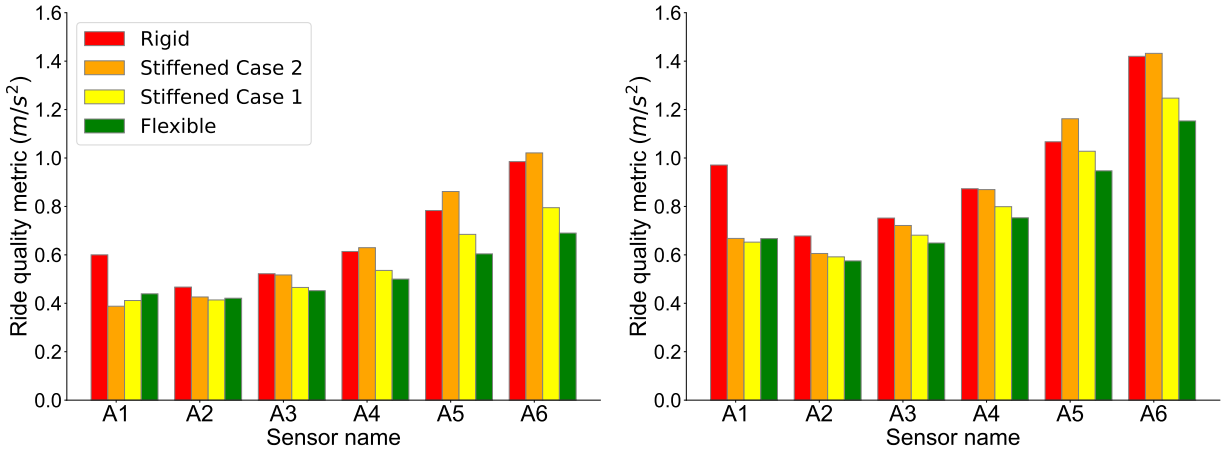

(a) $M_\infty = 0.65$ (b) $M_\infty = 0.83$

Figure 5.19: Ride quality metric for different VFA wing variants, vertical gust.

fuselage, all the wing variants showed an increase in the ride quality metric towards the tail except for the sensor located at the front fuselage (A1). In contrast, for a rigid fuselage, there is a trend of increasing ride quality metric towards the tail for all the sensors. The interaction of fuselage flexibility with wing flexibility impacts the ride quality metric. The highest impact is observed for the nose fuselage due to the fuselage flexibility. A higher comfort is predicted for the sensors in front of the fuselage if the flexibility effects are not considered. There is also a minor variation in the ride quality metric of a given sensor location for different VFA wing variants for a rigid fuselage.

The results suggest that wing and fuselage flexibility must be accounted for in the ride quality metric evaluation. The interaction between the fuselage and wing flexibility may play a detrimental or beneficial role in ride qualities, depending on its level and the location along the aircraft.

5.3.1.2 Lateral Gust

Figure 5.21 compares the lateral accelerations for each sensor and aircraft for the two flight conditions. Similar to the results for the vertical gust, the $M_\infty = 0.83$ flight condition is associated with higher accelerations causing higher discomfort, as shown by the higher ride quality metric values in Table 5.4 and 5.5.

For both test cases, lateral accelerations are highest toward the ends (A1 and A6), leading to higher values of the ride quality metric and hence higher discomfort. This can be explained by looking at the response of the aircraft to a lateral gust in Fig. 5.28. The lateral gust induces a roll and a yaw motion towards the right wing. This causes higher accelerations towards the ends of the

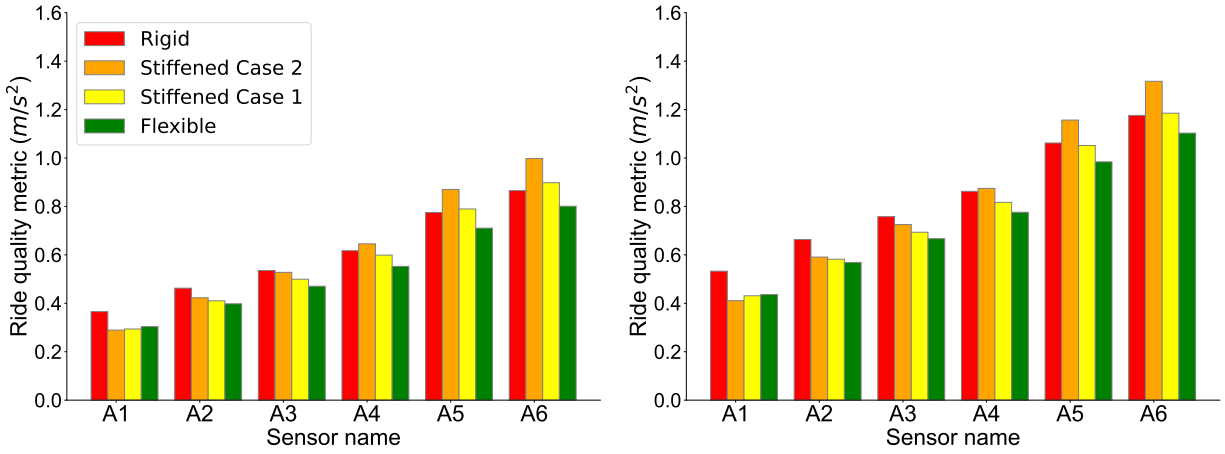

(a) $M_\infty = 0.65$ (b) $M_\infty = 0.83$

Figure 5.20: Ride quality metric for different VFA wing variants, vertical gust (rigid fuselage).

Table 5.4: VFA vs. FA ride quality metric (m/s^2) during the lateral gust encounter, $M_\infty = 0.65$.

Sensor	FA	VFA	Variation (%)
A1	0.667	0.585	−12.32
A2	0.274	0.252	−7.96
A3	0.107	0.111	3.52
A4	0.173	0.155	−10.39
A5	0.458	0.443	−3.29
A6	0.701	0.656	−6.42

fuselage because of the lateral motion. At $M_\infty = 0.65$, the VFA shows lower accelerations than the FA except for the sensor located near the fuselage wing intersection (A3), though numerically they have a similar value (Table 5.4). At this flight condition, the trends are similar to the vertical gust input.

At $M_\infty = 0.83$, the difference in the acceleration levels and ride quality metric values between the two test cases is similar towards the rear fuselage wit lower ride quality metric for the VFA test case. A higher difference is observed for the sensors located near the fuselage wing intersection (A3 and A4), though qualitatively the ride quality metric is much smaller than at the fuselage ends. There is an increase in discomfort at the sensor located towards the tip of the nose fuselage (A1) and near the fuselage wing intersection (A3 and A4) for the VFA than the FA. At this flight condition, the acceleration alleviation effect due to the increased flexibility of the VFA is less pronounced.

To further investigate the ride qualities of the VFA test case under lateral gust loads, Fig. 5.22

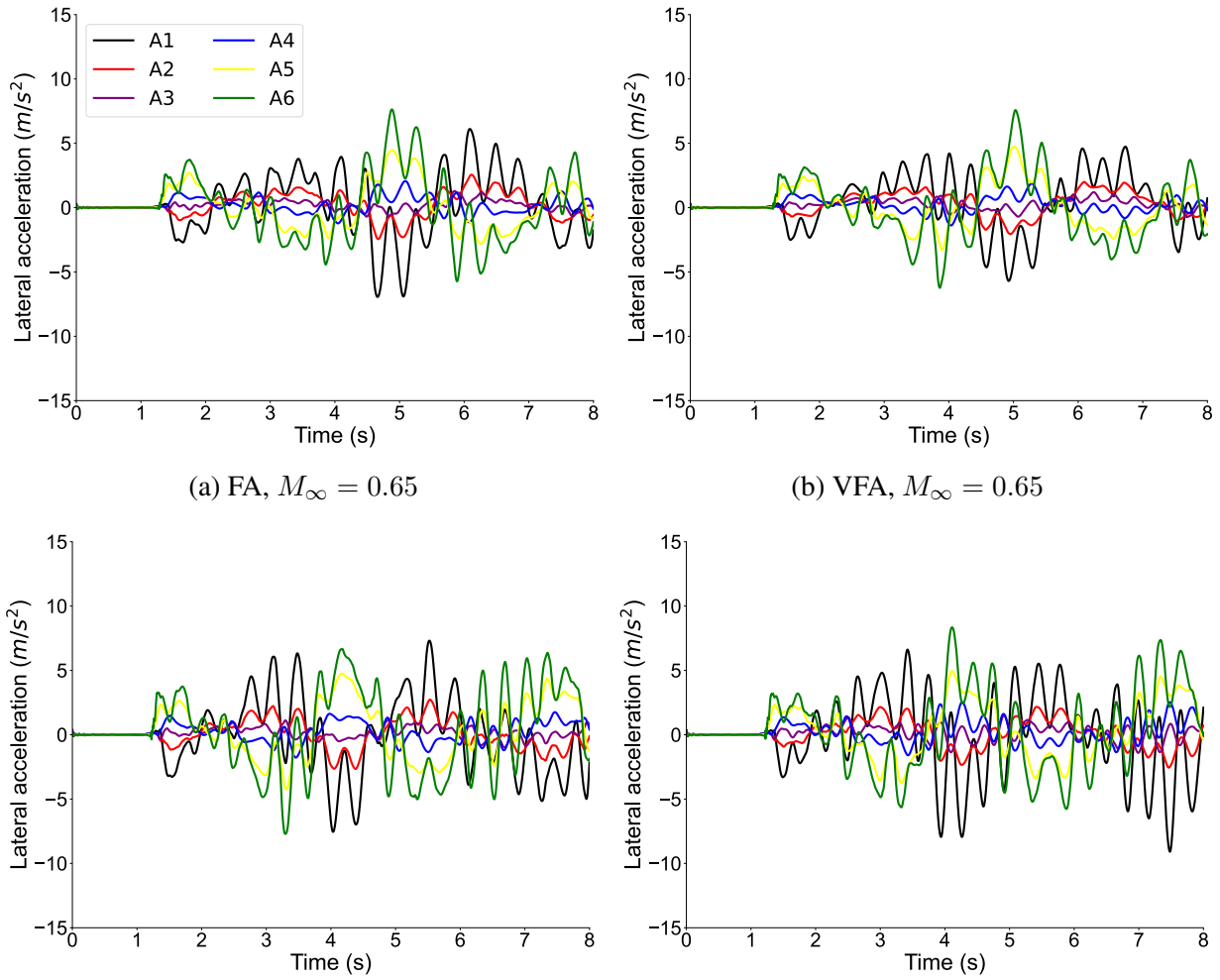

(a) FA, $M_\infty = 0.65$

(b) VFA, $M_\infty = 0.65$

(c) FA, $M_\infty = 0.83$

(d) VFA, $M_\infty = 0.83$

Figure 5.21: VFA vs. FA lateral accelerations at various locations during the lateral gust encounter.

Table 5.5: VFA vs. FA ride quality metric (m/s^2) during the lateral gust encounter, $M_\infty = 0.83$.

Sensor	FA	VFA	Variation (%)
A1	0.775	0.856	10.47
A2	0.306	0.293	−4.07
A3	0.116	0.152	31.55
A4	0.212	0.236	11.52
A5	0.573	0.559	−2.48
A6	0.881	0.849	−3.55

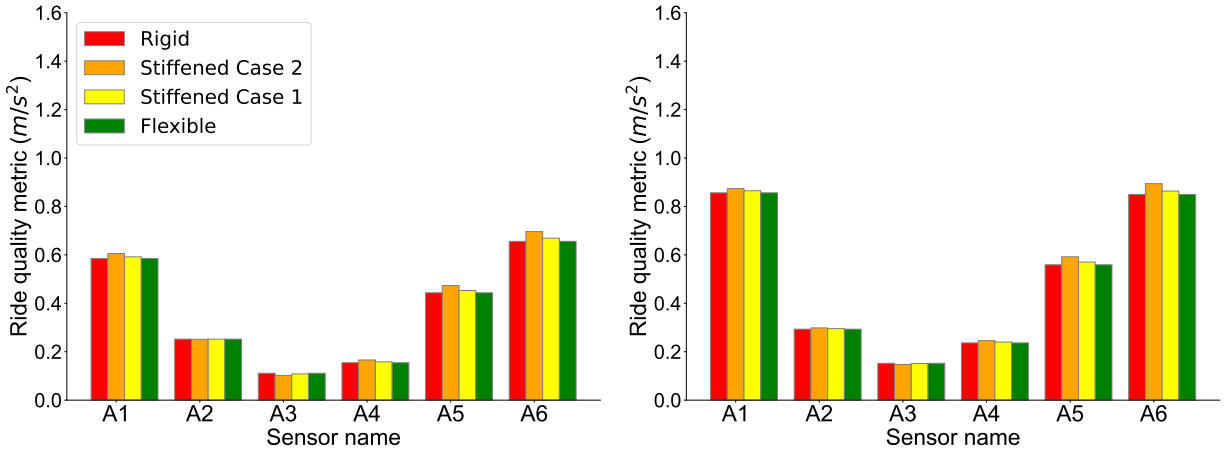

(a) $M_\infty = 0.65$ (b) $M_\infty = 0.83$

Figure 5.22: Ride quality metric for different VFA wing variants, lateral gust.

compares the ride quality metric for the VFA with varying wing stiffness considering a flexible fuselage. The impact of different wing flexibility levels is not significant for a lateral gust specially for the sensors located in the center of the fuselage. This is observed for both flight conditions. For the sensors located at the ends, there is a trend of increasing discomfort with wing flexibility and then a reduction in discomfort as the flexibility of the wing is increased further. However, the differences remain smaller than the results for a vertical gust. Figure 5.23 compares the ride quality metric for the VFA with varying wing stiffness considering a rigid fuselage. For a rigid fuselage, there is a higher variation in the ride quality metric for varying VFA wing flexibility levels towards the fuselage ends. There is a trend of decrease in ride quality metric, implying higher comfort with increasing wing flexibility. The difference is highest towards the fuselage tail (sensors A5 and A6). Overall, similar to the results with the vertical gust, a lower discomfort is evaluated when a rigid fuselage is considered.

5.3.2 Impact of Flared Folding Wingtips

The impact of FFWTs on the ride qualities of the VFA test case are compared presented in this section. The results for the vertical and lateral gust inputs are presented in Sec. 5.3.2.1 and Sec. 5.3.2.2 respectively.

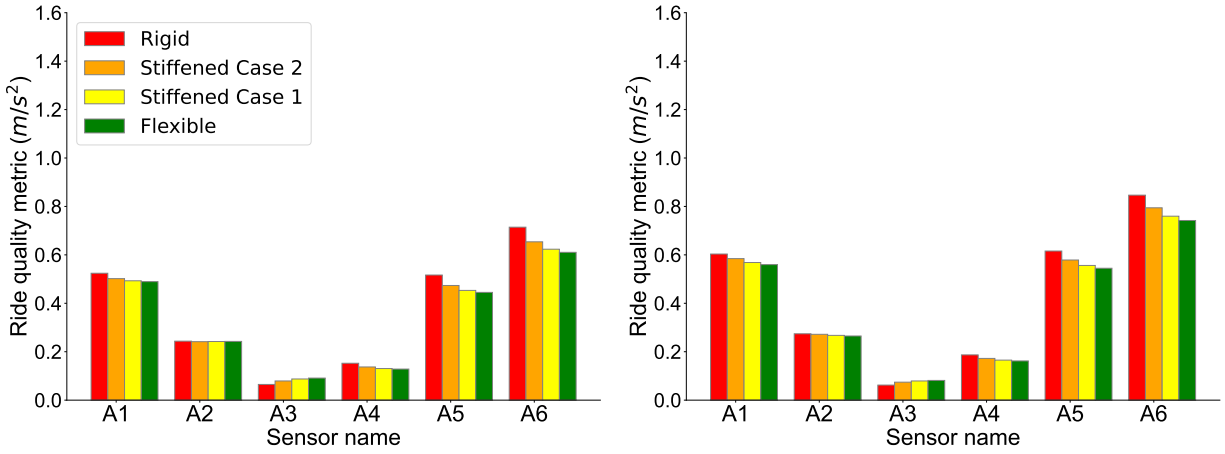

(a) $M_\infty = 0.65$ (b) $M_\infty = 0.83$

Figure 5.23: Ride quality metric for different VFA wing variants, lateral gust (rigid fuselage).

5.3.2.1 Vertical Gust

Section 5.2.2 shown the VFA response to a continuous vertical gust with FFWTs is shown for different flight conditions in Sec. 5.2.2. Table 5.6 and 5.7 list the ride quality metric at $M_\infty = 0.65, 0.83$. The flapping motion of the free wingtip in response to the gust disturbance causes higher accelerations in the fuselage, also shown in Fig. 5.24. These accelerations result in a higher value of ride quality metric and increased discomfort when the folding wingtips are released. This degradation effect is highest for the front accelerometer (A1), where the maximum benefit of the wing flexibility was observed when moving from FA to VFA (see Tables 5.2 and 5.3). This degradation of ride qualities can also be motivated by the decrease in frequency separation between the fuselage and the wing when FFWTs are deployed (see Table 3.10). However, the ride quality metric for the VFA with free folding wingtips remains lower than for the FA, whose wing span corresponds to the span of the VFA wing at the wingtip hinge line. This is observed for all the sensors except toward the tail (A5 and A6) at $M_\infty = 0.65$ as shown in Fig. 5.25.

Additionally, Table 5.8 summarizes the impact of the flare angle by comparing results for $\Lambda = 10$ and 20 deg. The results are presented only for $M_\infty = 0.65$ because there is no load alleviation benefit from releasing the FFWTs at $M_\infty = 0.83$. Ride qualities degrade with the flare angle, as expected since this leads to higher load alleviation. This is also shown by the dynamic responses in Fig. 5.10. The wingtip position and hinge rotation angle show larger-amplitude oscillations at $\Lambda = 20$ deg, so reducing comfort. To further investigate the impact of the flare angle of the FFWTs on the ride quality metric, Fig. 5.27 shows the comparison for varying flare angles between $\Lambda = 10$ and 20 deg. There is no significant impact of varying the flare angle on the ride qualities except at

Table 5.6: Impact of deploying FFWTs on VFA ride quality metric (m/s^2), vertical gust $M_\infty = 0.65$.

Sensor	Fixed	Free	Variation (%)
A1	0.439	0.479	9.10
A2	0.421	0.419	−0.49
A3	0.452	0.453	0.10
A4	0.500	0.509	1.76
A5	0.604	0.623	3.11
A6	0.690	0.730	5.85

Table 5.7: Impact of deploying FFWTs on VFA ride quality metric (m/s^2), vertical gust, $M_\infty = 0.83$.

Sensor	Fixed	Free	Variation (%)
A1	0.667	0.730	9.55
A2	0.575	0.582	1.23
A3	0.649	0.659	1.48
A4	0.753	0.767	1.94
A5	0.947	0.956	1.00
A6	1.153	1.182	2.44

Table 5.8: Impact of flare angle on the VFA ride quality metric (m/s^2), vertical gust, $M_\infty = 0.65$.

	Flare angle (deg)		
Sensor	10	20	Variation (%)
A1	0.479	0.610	27.20
A2	0.419	0.440	4.89
A3	0.453	0.466	3.01
A4	0.509	0.525	3.25
A5	0.623	0.637	2.18
A6	0.730	0.768	5.26

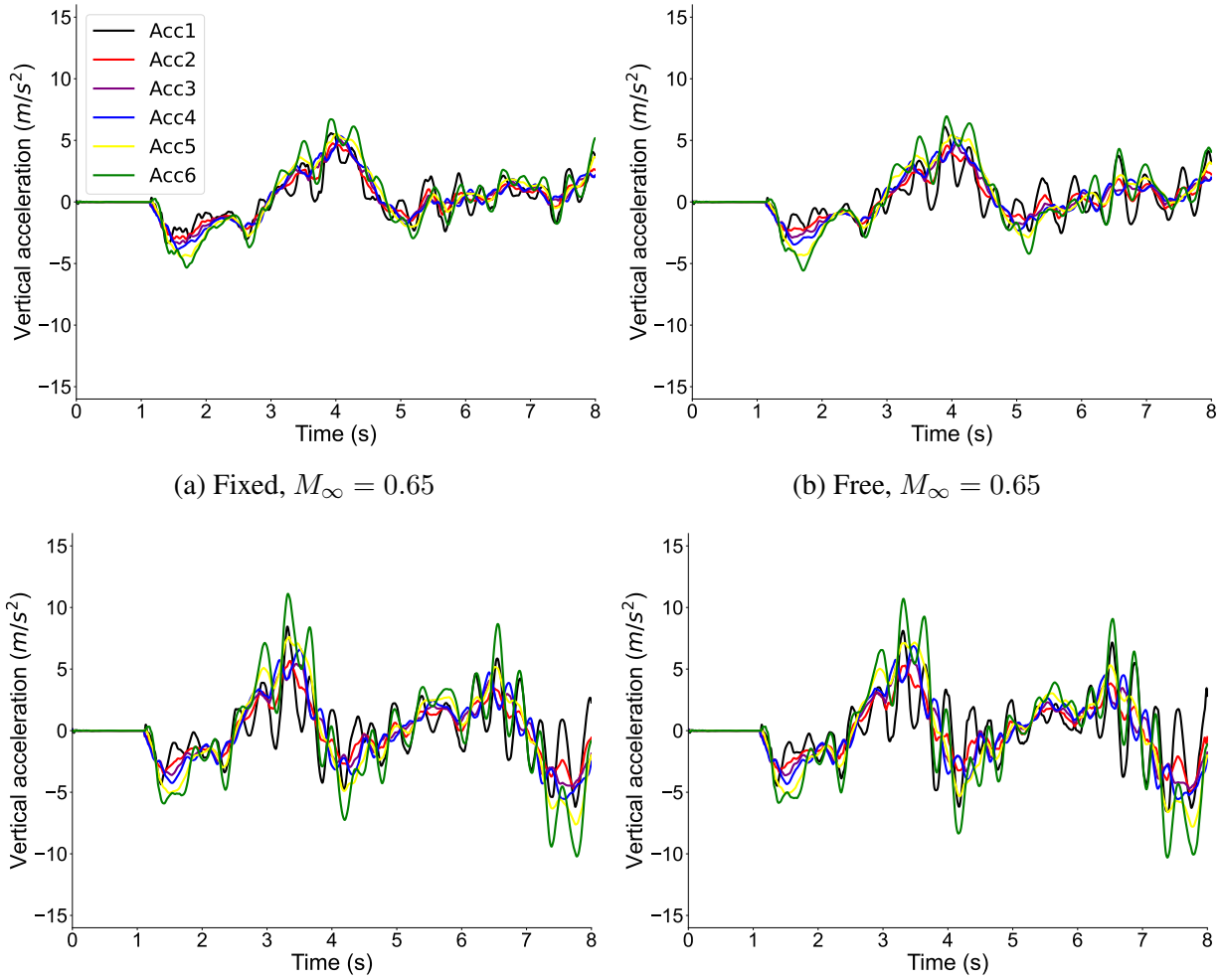

(a) Fixed, $M_\infty = 0.65$

(b) Free, $M_\infty = 0.65$

(c) Fixed, $M_\infty = 0.83$

(d) Free, $M_\infty = 0.83$

Figure 5.24: VFA vertical accelerations at various locations with deployed FFWTs, vertical gust.

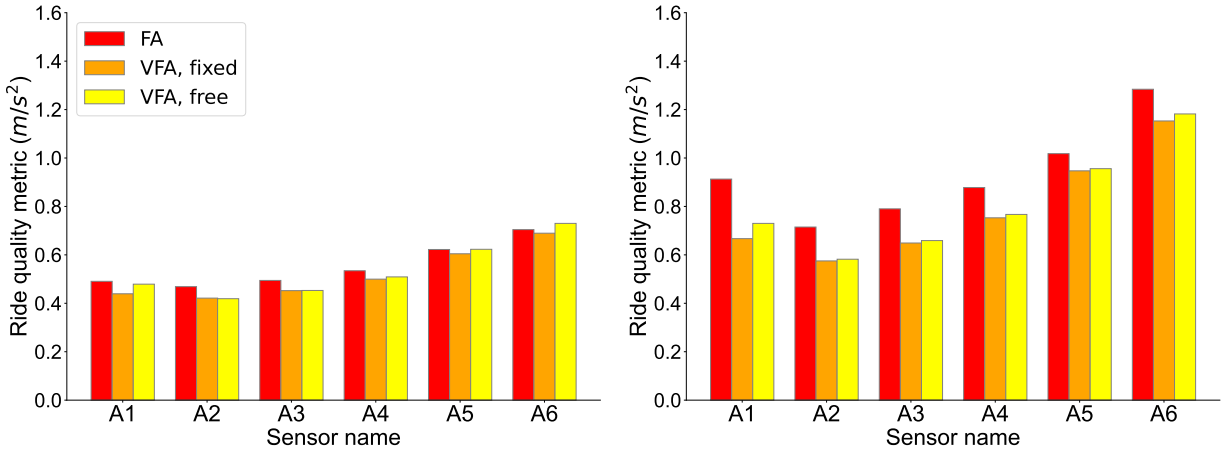

(a) $M_\infty = 0.65$ (b) $M_\infty = 0.83$

Figure 5.25: Ride quality metric for FA, VFA (fixed FFWTs), and VFA (free FFWTs), vertical gust.

values closer to $\Lambda = 20$ deg, where there is a free wingtip instability as shown by Fig. 5.26.

5.3.2.2 Lateral Gust

The results for the continuous lateral gust input are shown in Figs. 5.28 and 5.29. In response to a lateral gust, the aircraft experiences a rolling and an in-plane motion towards the right wing. At $M_\infty = 0.65$, the FFWTs responds to the gust disturbance by rotating about the hinge. As the aircraft rolls towards the right, the hinge rotation increases for the left wing while reducing for the right wing. This creates a net higher lift on the right wing and the wingtip motion tries to resist the rolling motion induced by the lateral gust. This can be seen by a slightly smaller roll angles with the free wingtips (see Fig. 5.28e). However, this favorable impact of the wingtip motion is only observed for the sensors located in the front fuselage (A1 to A43) as shown in the Table 5.9. The sensors located towards the rear fuselage (A4 to A6) show higher discomfort due to the flapping motion of the wingtip similar to the vertical gust. The impact on load alleviation remains the same as seen for the previous results at this flight condition.

A similar motion of the wingtip is observed at $M_\infty = 0.83$. However, as seen with the previous results, the FFWT rotates less at this flight condition due to the presence of stronger wash-out effects toward the wingtip. This contributed to poor load alleviation performance of the FFWTs. However, the anti-symmetric motion of the wingtip at this flight condition causes a higher improvement in the comfort for the sensors located towards the front fuselage and a smaller increase in discomfort for the sensors located towards the rear fuselage (see Table 5.10). Finally Fig. 5.31

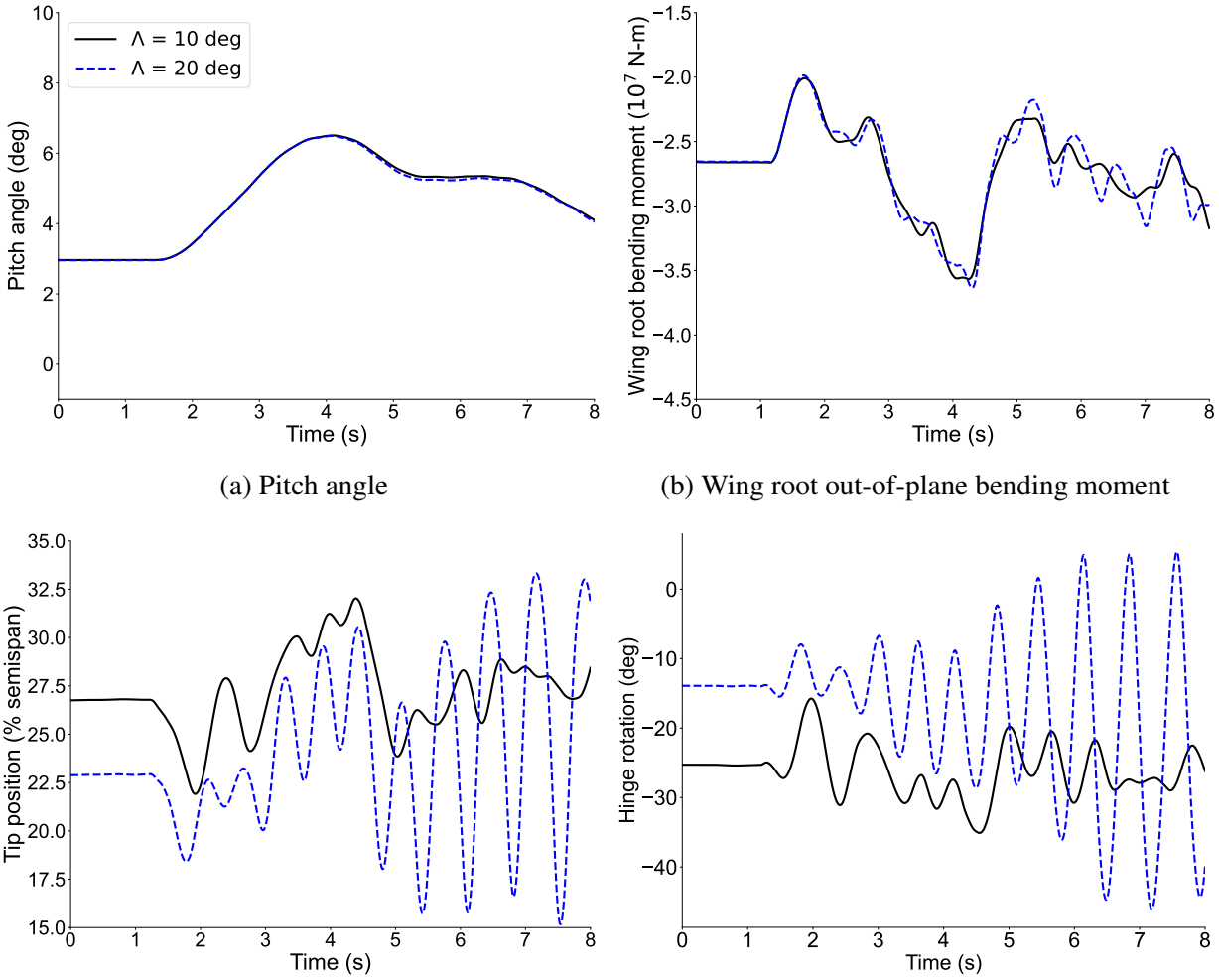

(a) Pitch angle

(b) Wing root out-of-plane bending moment

(c) Vertical tip position

(d) Hinge rotation

Figure 5.26: Gust response of the VFA with varying flare angle, vertical gust $M_\infty = 0.65$.

Table 5.9: Impact of deploying FFWTs on VFA ride quality metric (m/s^2), lateral gust, $M_\infty = 0.65$.

Sensor	Fixed	Free	Variation (%)
A1	0.585	0.573	−2.08
A2	0.252	0.251	−0.49
A3	0.111	0.108	−2.47
A4	0.155	0.155	0.22
A5	0.443	0.459	3.52
A6	0.656	0.690	5.13

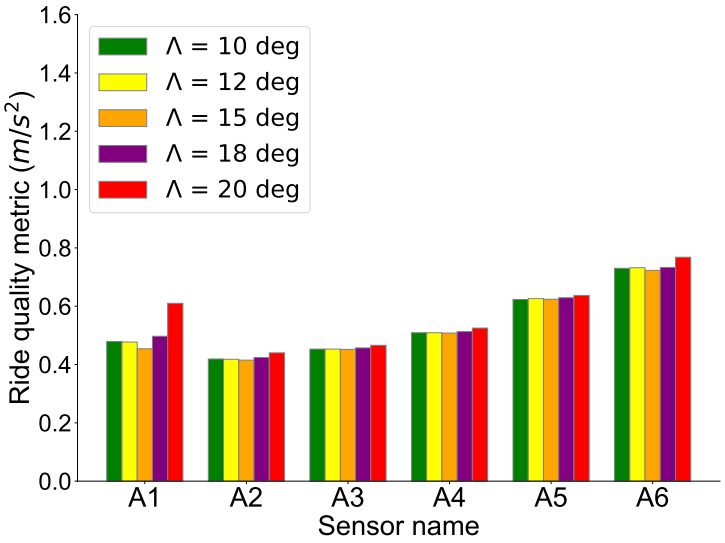

Figure 5.27: Impact of flare angle on the VFA ride quality metric (m/s^2), vertical gust, $M_\infty = 0.65$.

Table 5.10: Impact of deploying FFWTs on VFA ride quality metric (m/s^2), lateral gust, $M_\infty = 0.83$.

Sensor	Fixed	Free	Variation (%)
A1	0.856	0.798	−6.79
A2	0.293	0.285	−2.69
A3	0.152	0.141	−7.38
A4	0.236	0.227	−4.09
A5	0.559	0.567	1.45
A6	0.849	0.860	1.29

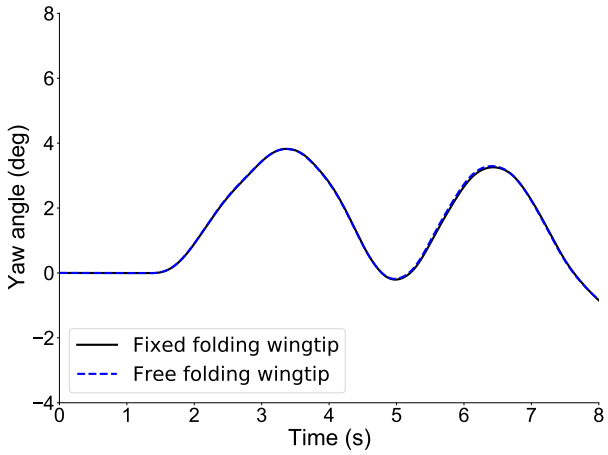

(a) Yaw angle

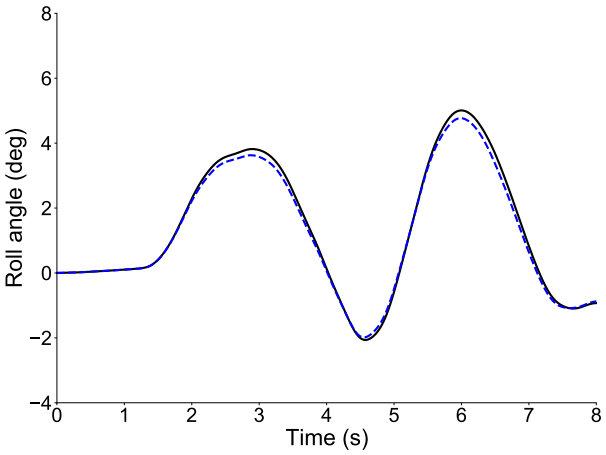

(b) Roll angle

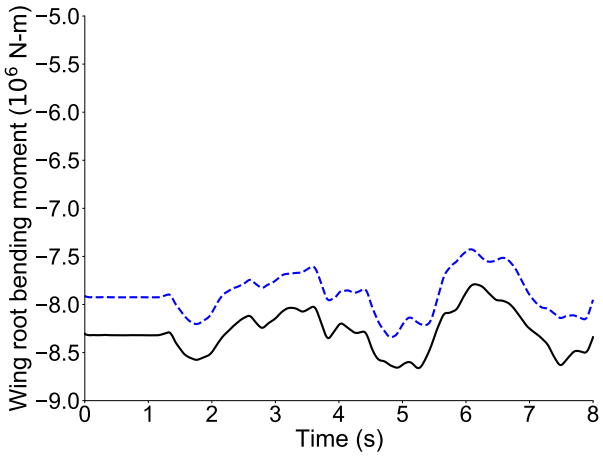

(c) Wing root out-of-plane bending moment

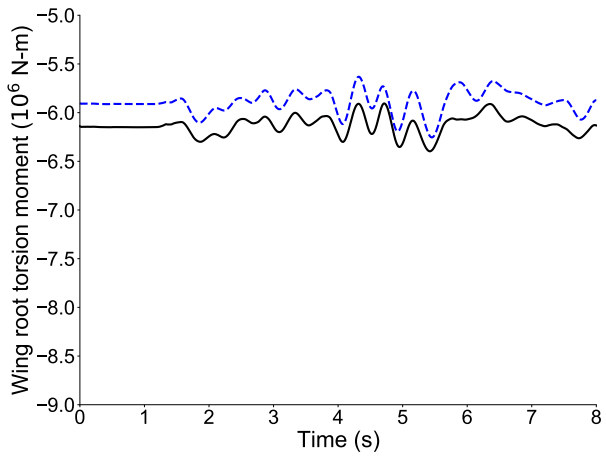

(d) Wing root torsion moment

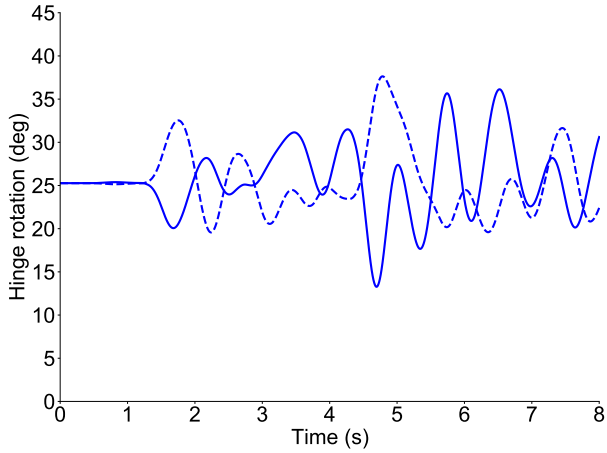

(e) Hinge rotation

Figure 5.28: VFA response to continuous lateral gust with deployed FFWTs, $M_\infty = 0.65$.

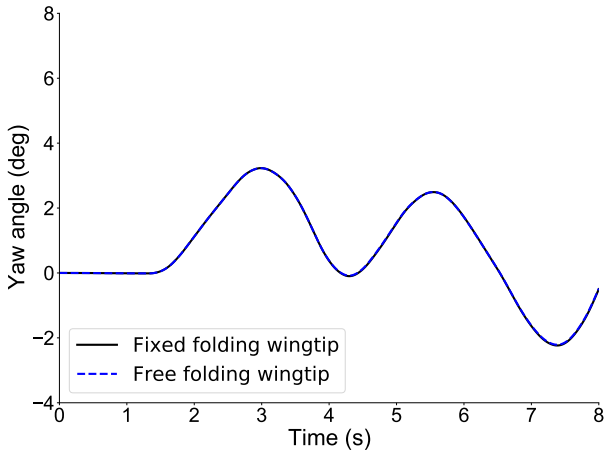

(a) Yaw angle

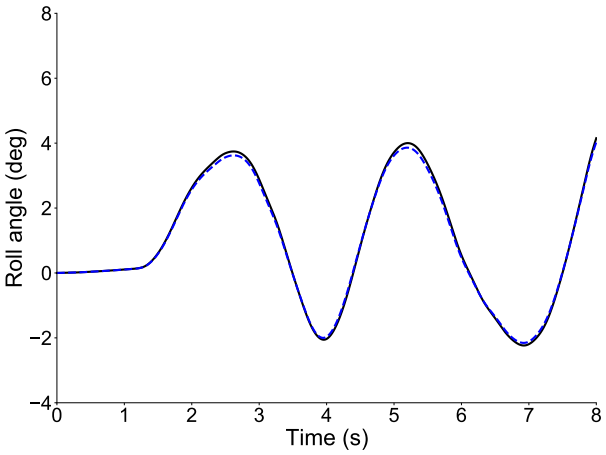

(b) Roll angle

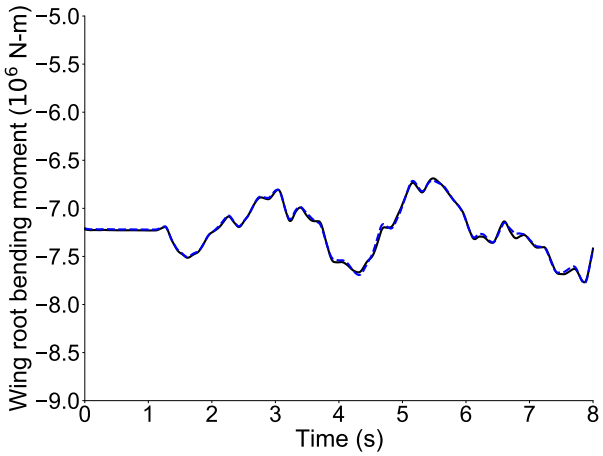

(c) Wing root out-of-plane bending moment

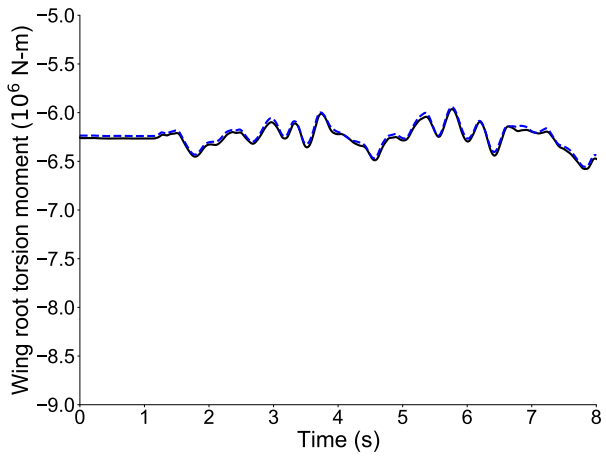

(d) Wing root torsion moment

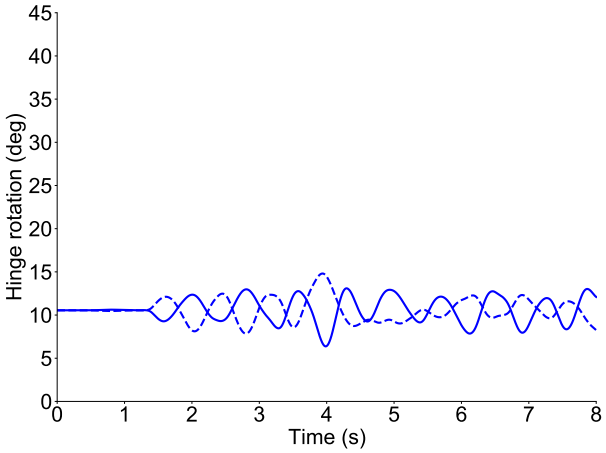

(e) Hinge rotation

Figure 5.29: VFA response to continuous lateral gust with deployed FFWTs, $M_\infty = 0.83$.

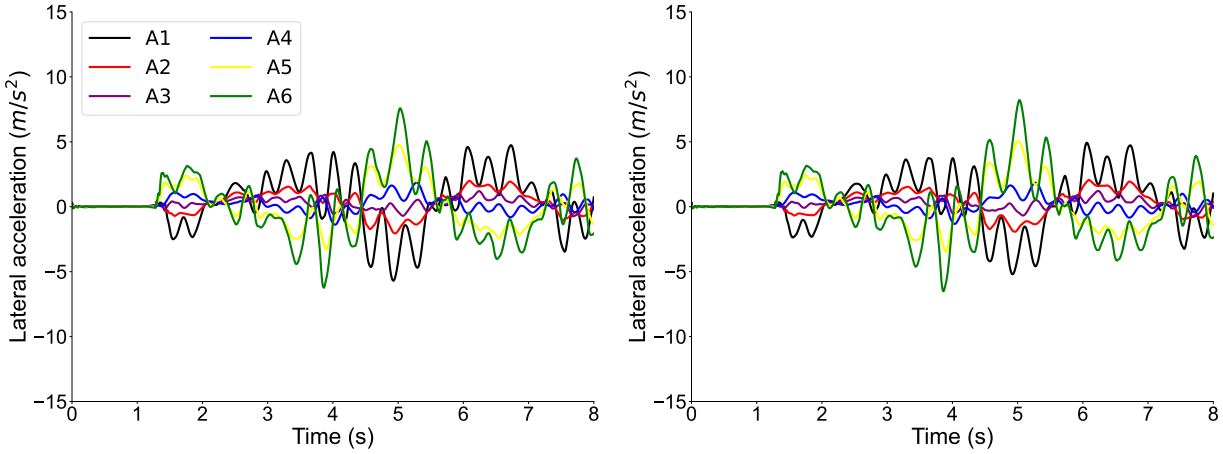

(a) Fixed, $M_\infty = 0.65$

(b) Free, $M_\infty = 0.65$

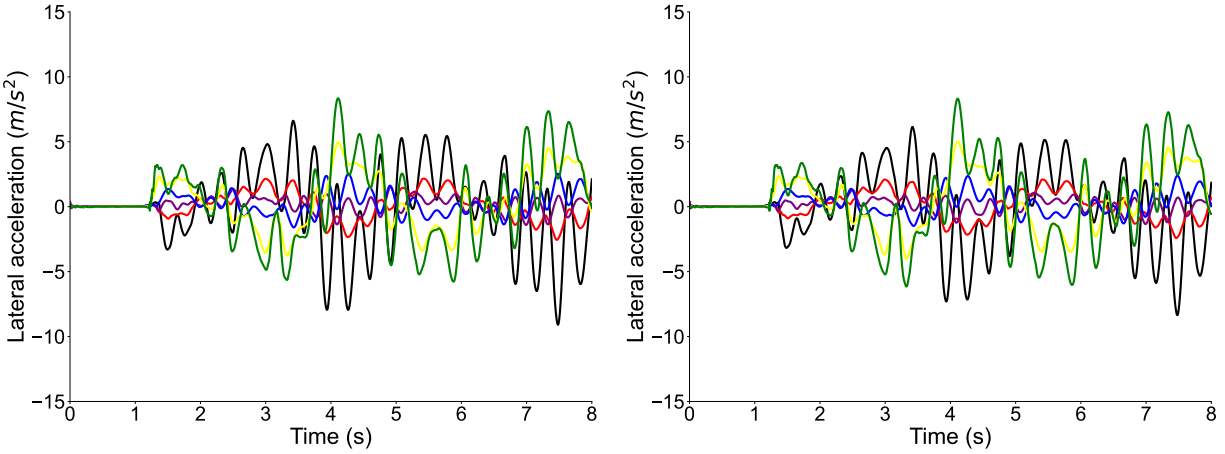

(c) Fixed, $M_\infty = 0.83$

(d) Free, $M_\infty = 0.83$

Figure 5.30: VFA lateral accelerations at various locations with deployed FFWTs, lateral gust.

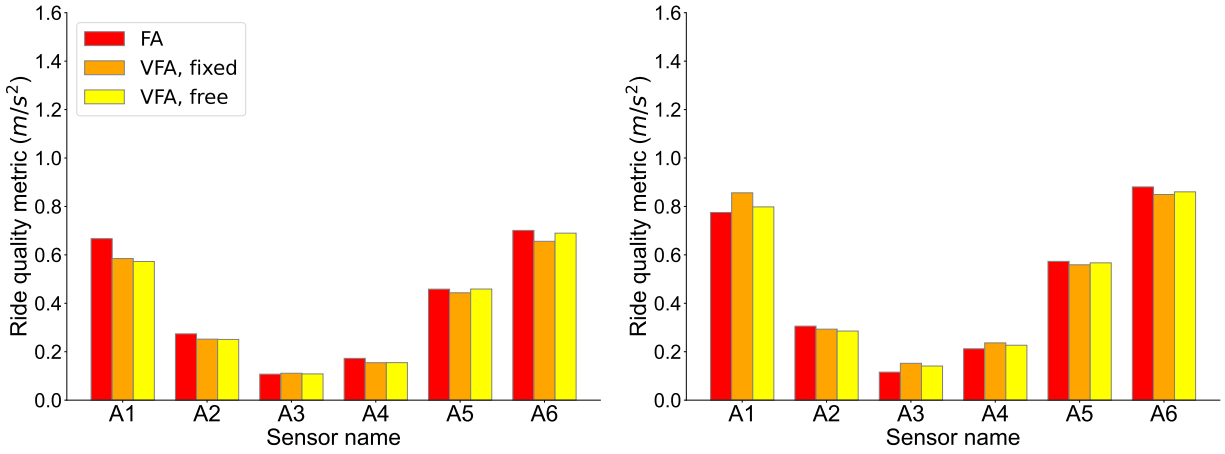

(a) $M_\infty = 0.65$ (b) $M_\infty = 0.83$

Figure 5.31: Ride quality metric for FA, VFA (fixed FFWTs), and VFA (free FFWTs), lateral gust.

shows the comparison of ride quality metric for the FA test case against the VFA test case with and without FFWTs. At $M_\infty = 0.65$, the ride qualities of the VFA test case with FFWT's remain lower than the FA test case for all the sensors. At $M_\infty = 0.83$, the ride qualities of the VFA test case with FFWT's also remain lower than the FA test case except for the sensor (A1) near the front fuselage. However, for this sensor the deployment of FFWTs improve the ride qualities of the VFA test case that was deteriorated compared to the FA test case. These results show that the load alleviation benefits of FFWTs impact the ride qualities at flight conditions where these devices effectively alleviate loads (e.g., $M_\infty = 0.65$ in these studies). At flight conditions where wash-out effects are such that FFWTs do not virtually change the loads, releasing these devices still reduces ride quality. However, this is valid only for the vertical gusts. FFWTs improve the comfort when lateral gusts are considered, even at higher dynamic pressure conditions where the impact of aeroelastic effects is more substantial. The range of flight conditions where FFWTs are deployed for load alleviation should be assessed based on the level of wing flexibility and strength of wash-out effects and the impact on ride qualities for different types of gust disturbances. Overall, the VFA with FFWTs shows mostly lower or similar ride qualities as the FA test case, with vertical and lateral gust disturbances.

5.4 Summary

This chapter investigated the gust load alleviation and ride qualities of transonic HARW aircraft representing a potential future civil transport configuration. Gust responses of the aircraft were

simulated in a nonlinear aeroelastic-flight dynamics framework to assess the impact of wing flexibility and FFWTs on ride qualities. The gust responses considered continuous and discrete penetrative gust models and two flight conditions, a relatively low dynamic pressure case and a typical cruise condition. The VFA test case (HARW configuration) was found to have better ride qualities than the FA test case (a baseline aircraft with a regular wing aspect ratio) during vertical gusts. Wing flexibility was found to reduce accelerations in front of the fuselage, so improving ride qualities at those locations during the vertical gusts. In contrast, for a lateral gust, the VFA showed an increase in ride quality metric toward the front fuselage at the higher dynamic pressure condition. For all other locations and at lower dynamic pressure condition, the VFA showed a lower ride quality metric value, therefore higher comfort.

The trend of increasing comfort with increasing flexibility was also observed when comparing the HARW configuration against a rigid-wing variant with the same aspect ratio. However, compared to a stiffened-wing variant, a non-monotonic trend was observed in the ride quality metric depending on the sensor location. This was observed for both vertical and lateral gusts. The impact of fuselage flexibility was also investigated. For a rigid fuselage, a lower ride quality metric value was observed for all the sensor locations, thereby showing an increase in comfort when a rigid fuselage is considered in the analysis.

Deploying FFWTs was found to degrade ride qualities of the HARW configuration due to increased accelerations at the fuselage caused by the wingtip flapping motion for a vertical gust. This is also motivated by the decrease in the frequency separation between the fuselage and the wing when FFWTs are deployed. Maximum degradation was observed toward the nose fuselage. In contrast, FFWTs improved the ride comfort towards the front fuselage during a lateral gust. While deploying FFWTs degraded ride qualities at both flight conditions, it alleviated the bending moment at the wing root at lower dynamic pressure. On the other hand, no load alleviation benefit was observed at the cruise condition on top of degraded ride qualities. Overall, the ride quality of the VFA with FFWTs remains lower or similar to the ride quality of the FA.

CHAPTER 6

Concluding Remarks

This chapter summarizes the work performed and provides the main conclusions and key contributions of this dissertation. Recommendations for future research are also described.

6.1 Summary and Main Conclusions

This dissertation addressed open questions related to roll maneuverability, load alleviation, and ride qualities of transonic HARW aircraft. The studies were enabled by UM/NAST, a coupled nonlinear aeroelastic-flight dynamics simulation framework with the ability to model different control effectors and simulate flexible and very flexible aircraft in free flight. As part of this work, the framework was enhanced with the capability to model FFWTs and evaluate an acceleration-based ride quality metric. Aeroelastic test cases of flexible and very flexible HARW aircraft with distributed trailing- and leading-edge control surfaces were developed to study the impact of higher wing flexibility due to the increased span. These test cases represent a baseline aircraft with a regular wing aspect ratio and a HARW aircraft representing a potential future civil transport configuration. The main findings under the three research objectives are summarized below:

- **To investigate questions regarding roll maneuverability in transonic HARW aircraft**

  - *What is the impact of aileron placement on the static and dynamic roll response?*

    The static spanwise placement study of trailing-edge control surfaces showed peak roll control effectiveness at approximately 50% semispan of the VFA (HARW) test case. For the FA test case, the peak effectiveness spanwise location corresponds to 60% of the semispan. The outboard control surfaces were less effective because of the increasing wash-out effect resulting from larger aeroelastic deflections. This effect was found to be more pronounced in the outboard regions of the VFA test case, where strong nonlinear effects and control reversal were observed, especially at $M_\infty = 0.83$. The dynamic analyses considered a bank-to-bank maneuver similar to the one for roll capability

certification of civil transport aircraft. The dynamic roll response analyses showed that the VFA trailing-edge control surfaces need to be placed at the same distance from the wing root as the FA to achieve comparable roll maneuverability. However, a higher impact of adverse yaw was observed for an inboard placement.

– *What are the benefits and limitations of varying aileron placement versus tailoring the wingbox for improving roll maneuverability?*

  The roll maneuverability can be improved by increasing the wingbox out-of-plane bending stiffness and providing a positive coupling between out-of-plane bending and torsion. The out-of-plane bending stiffness has the highest impact. However, the benefits of wingbox passive aeroelastic tailoring are not significant for inboard control-surface layouts. With practical variations in the stiffness properties, the improvement in roll maneuverability is not comparable to the impact of an inboard control surface placement. However, there are challenges with both these approaches. Increasing wing stiffness will also increase the weight, which was not accounted in this study. An inboard trailing-edge control surface also created additional issues. These were discussed in Sec. 4.4.

– *Can unconventional control effectors like leading-edge control surfaces and FFWTs improve roll maneuverability?*

  * What is the best spanwise placement of a leading-edge control surface?
    The spanwise placement with highest roll control effectiveness of a leading-edge control surface is similar to a trailing-edge control surface. For the relative value of control derivatives between leading- and trailing-edge control surfaces considered in this study, inboard leading-edge control surfaces are ineffective compared to trailing-edge control surfaces. However, outboard leading-edge control surfaces can provide comparable roll maneuverability while avoiding higher loads and control reversal.
  * What is the impact of deploying FFWTs with the different spanwise placement of trailing- and leading-edge control surfaces?
    Deploying FFWTs with a trailing- or leading-edge control surface inboard of the hinge shows no improvement in the roll maneuverability at lower dynamic pressure conditions for the VFA test case. The roll maneuverability is degraded at high dynamic pressure conditions if FFWTs are deployed. In contrast, if the FFWTs are deployed for a stiffened wing, the roll maneuverability is enhanced with higher impact at the lower dynamic pressure conditions. FFWTs help in reducing roll

damping by not transmitting any bending loads through the hinge. However, for a very flexible swept wing, this benefit comes with an increase in lift inboard of the hinge, which increases the roll damping. Increasing the out-of-plane bending stiffness of the wing reduces the washout effects, which decreases the impact of the roll damping due to the increase in lift inboard of the hinge. Deploying FFWTs with a trailing-edge control surface located outboard of the hinge (on the FFWT) induces free wingtip instability, especially for the most outboard located layout. The instability can be avoided by reducing the commanded deflections, which results in a very slow roll maneuver. In contrast, deploying FFWTs with leading-edge control surface outboard of the hinge improves the roll maneuverability even at higher dynamic pressure conditions.

- **To investigate questions regarding load alleviation in transonic HARW aircraft**
  - *What is the impact of the wing flexibility on the load alleviation performance of FFWTs?*

    FFWTs alleviate loads by reducing the angle of attack outboard of the hinge when they rotate upwards for a positive flare angle. The offloading of the wingtip reduces the upwards deflections of the main wing. This increases the angle of attack inboard due to the washout effects in a flexible swept wing. Hence, FFWTs will alleviate loads when the moment due to the lift outboard of the hinge overcomes the moment due to lift gain inboard of the hinge. Increasing wing stiffness improves the load alleviation performance, but the impact is smaller for practical variations in stiffness properties. It was also observed that the difference in the trim shape with FFWTs significantly affects the load alleviation performance for both MLA and GLA.
  - *What is the impact of considering different flight conditions on the load alleviation performance of FFWTs?*

    For the VFA test case, loads are alleviated only at lower dynamic pressure conditions where the aeroelastic effects are milder. However, for a typical cruise flight condition, the strong aeroelastic effects reduce their load alleviation performance despite the wingtip's upward rotation. At this flight condition, the wingtip rotates by a smaller angle. Therefore, a smaller reduction in loads is obtained with the FFWTs. At the same time, there is a more significant increase in lift inboard, which reduces the load alleviation performance. The impact of increasing the stiffness of the wing was also smaller at higher dynamic pressure conditions. For a stiffened wing, a 13% decrease in wing root bending moment was observed at the lower dynamic pressure condition. On the

other hand, only 6% reduction in the loads was observed at higher dynamic pressure conditions.

These results show the importance of considering the wing flexibility and different flight conditions when exploring FFWTs as load alleviation devices.

- **To investigate questions regarding ride qualities of transonic HARW aircraft**
  - *How does wing flexibility impact ride qualities?*

    The ride qualities of the VFA HARW test case were compared against the FA test case with a regular aspect ratio. The ride quality metric was analyzed for both vertical and lateral gust inputs. For a vertical gust input, the VFA test had a lower ride quality metric value than the FA test case, meaning higher comfort with the VFA test case. This was motivated by the higher wing flexibility and inertia of the VFA test case. Similar results were obtained for the lateral gust except for increased discomfort near the front fuselage at higher dynamic pressure conditions with the VFA test case. The impact of wing flexibility was investigated for the VFA test case with varying wing flexibility levels. For a vertical gust, the trend of the ride quality metric with the wing flexibility of the VFA test case was not monotonic. Moving toward the tail, the ride quality first decreases with wing flexibility but then improves beyond a flexibility level. The opposite behavior was observed for the front fuselage. For a lateral gust, the impact of wing flexibility showed smaller variations in the ride quality metric. The studies also showed that fuselage flexibility should be considered when evaluating ride qualities—neglecting fuselage flexibility results in a lower ride quality metric value, meaning a higher comfort is predicted. This behavior was observed at both flight conditions even though the absolute values of the ride quality metric change.
  - *How do FFWTs impact ride qualities?*

    The impact of FFWTs on ride qualities was investigated by releasing the wingtip during the gust response. For a vertical gust, the motion of the FFWTs induced additional vibrations that increased the ride quality metric, increasing discomfort. There was no significant impact on increasing the flare angle on ride qualities except at an angle where the wingtip becomes unstable. This was observed for a flare angle of 20 deg, where the ride qualities deteriorated due to the increase in wingtip rotations. For a lateral gust, the right and the left FFWTs showed an anti-symmetric rotation in response to the roll and yaw motion of the aircraft. This helps in alleviating accelerations towards the front fuselage when FFWTs are deployed. Overall, for both cases, the ride quality

metric for the VFA test case with FFWTs remains lower or comparable to the FA test case.

6.2 Key Contributions

This dissertation provided the following key contributions:

- Developed and implemented the theoretical formulation of FFWTs as flexible control effectors within a fully coupled nonlinear aeroelastic-flight dynamics framework. This capability enabled the static and dynamic analyses of these devices in free flight while capturing the coupling among nonlinear structural dynamics, rigid-body dynamics, and aerodynamics in the behavior of very flexible HARW aircraft [7].

- Provided new insights about the impact of deploying FFWTs in very flexible transonic HARW aircraft. The effect of wingbox passive aeroelastic tailoring was also investigated to highlight the impact of stronger aeroelastic effects on the poor load alleviation and roll performance of FFWTs in the presence of increased wing flexibility or at higher dynamic pressure conditions. These results were in contrast with previous studies that were conducted on relatively stiffer wings.

- Provided new knowledge on the relative ride qualities of very flexible transonic HARW aircraft under gust loads. The results compared the ride qualities of a HARW and a regular aspect ratio wing aircraft. The impact of deploying FFWTs on ride qualities was also investigated. The studies highlighted the effect of frequency separation between the fuselage and the wing on the aircraft ride qualities with and without FFWTs.

- Enabled a linearized kinematics mode within the nonlinear simulation framework to investigate the impact of geometrically nonlinear effects on the roll control effectiveness of trailing-edge control surfaces and gust response of very flexible HARW aircraft.

- Implemented enhancements for extracting the stiffness properties of an equivalent beam representation of a given GFEM. This capability allows modeling a GFEM of an industrial aircraft model as a set of equivalent beam models for nonlinear aerostructural analyses. This was developed as part of the UM/EF2S framework and used to create the aircraft test cases studied in this dissertation.

6.3 Recommendations for Future Research

Some topics have been identified throughout this work that can be pursued for future research.

- Additional investigations should focus on improving accuracy and robustness of the UM/EF2S process for industrial models of components such as fuselage or, in general, for GFEM with more complex geometries and property distributions. The current UM/EF2S framework can condense GFEMs of wings into equivalent-beam models with lower errors than for fuselage components. For instance, a maximum error of 2% was observed in the modal frequency comparison of the HARW beam model against its GFEM for the first 10 modes. In contrast, errors in the range of 8-11% were observed for fuselage components.

- The control-surface placement studies should explore the feasibility of an inboard control-surface placement. The studies should consider the impact of the mass and inertia of the different control surface layouts and the implications for hinge loads. Additionally, the analyses need to be conducted with an actuator dynamics model.

- The evaluation of control-surface aerodynamic derivatives for leading- and trailing-edge control surfaces through CFD analyses could be considered. This will allow capturing the impact on the aerodynamic loads of neighboring control surfaces for a given control surface deflection.

- MLA and GLA studies with the combined deployment of trailing- and leading-edge control surfaces can be investigated to leverage the load alleviation performance of leading-edge control surfaces.

- The current investigations considered quasi-steady transonic effects. While this approach is reasonable, for instance, for roll maneuver, gust load alleviation and ride quality studies should be revisited with an updated aerodynamic model that captures unsteady transonic effects.

- The aerodynamic model in this work is based on the reference trimmed geometry without considering the impact of wingtip rotation. Future studies should consider the impact of large wingtip rotations in the aerodynamic model for the various investigations.

- Future studies should consider of FFWT the impact on flutter and post-flutter response. Time-domain flutter and post-flutter calculations are possible with the current implementation in UM/NAST. However, additional developments are required for frequency-domain flutter calculations with FFWTs. Additionally, the studies did not consider the impact of

FFWTs inertia distributions and length. Extensive design space exploration in this area is recommended.

- The studies in this worked showed the detrimental impact of aeroelastic effects on the performance of FFWTs under high dynamic pressure conditions and increased wing flexibility. Future work can address optimization of transonic HARW aircraft with FFWTs with constraints on control authority, MLA/GLA, ride and handling qualities, and other metrics.
- The impact of geometrically nonlinear effects on the FFWT's response should be investigated.
- Wind-tunnel testing of a very flexible swept wing with FFWTs and distributed control surfaces can help provide additional insights and validate the numerical results.
- The impact of the FFWT's release time should be explored in future studies. An actuation model for the release of the FFWTs in a dynamic simulation can be developed. Additionally, the impact of the possible failure of the lock and release mechanism of FFWTs on the aircraft's dynamic response can be investigated.
- The ride quality metric evaluation can be improved by weighting different frequencies according to their impact on humans comfort, allowing for a more realistic ride quality assessment. Additionally, extensive investigations should be conducted to isolate the impact of wing and fuselage flexibility on the ride qualities, with and without FFWTs.

APPENDIX A

Control-Surface Flexibility

A flexible control surface is modeled as a beam-type member connected to a parent fixed wingbox or tailbox member at discrete points along the hinge line, as shown in Fig. A.1. The structural properties of the control surface are obtained by reducing its three-dimensional built-up finite element model to an equivalent beam-type representation associated to a chosen reference axis (blue line in Fig. A.1). This description can be captured directly in the original strain-based structural formulation implemented into UM/NAST. However, three theoretical developments are needed for connecting an isolated flexible control-surface member to its parent (wingbox or tailbox) member: 1) kinematic laws for recovering the position and orientation of the hinge line, which generally does not coincide with the reference axis of the parent member or the control surface; 2) boundary conditions to constrain the relative motions of the parent member and of the control surface at the hinge connection points; and 3) internal virtual work to capture elastic reactions and dissipation that may arise to relative motions at the hinge. These extensions are developed in Secs. A.1 to A.4.

A.1 Hinge Fundamental Description and Kinematics

Consider the fixed member and the control surface in Fig. A.1. The two members are connected at a discrete number of spanwise locations along the hinge line. Each connection is modeled by two coincident points, one on the parent member and the other on the control surface. The projections of these points intersect the parent-member reference axis at a point u within the mth element and the control-surface reference axis at a point v within the nth element. The h vectors at these points are h_{mu} and h_{nv}, respectively, while the θ vectors are θ_{mu} and θ_{nv}, respectively. The h and θ vectors at the coincident hinge points are denoted by h^H_{mu} and θ^H_{mu} (point on the fixed member) and h^H_{nv} and θ^H_{nv} (point on the control surface). For simplicity, the points mu and nv are here assumed to coincide with finite element nodes. The general case where these points have arbitrary locations within the mth and nth elements is treated in Sec. A.4.

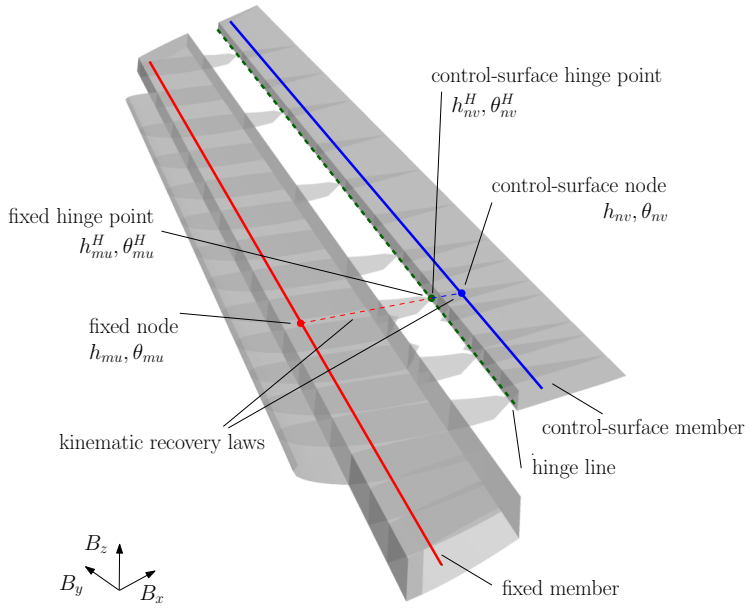

(a)

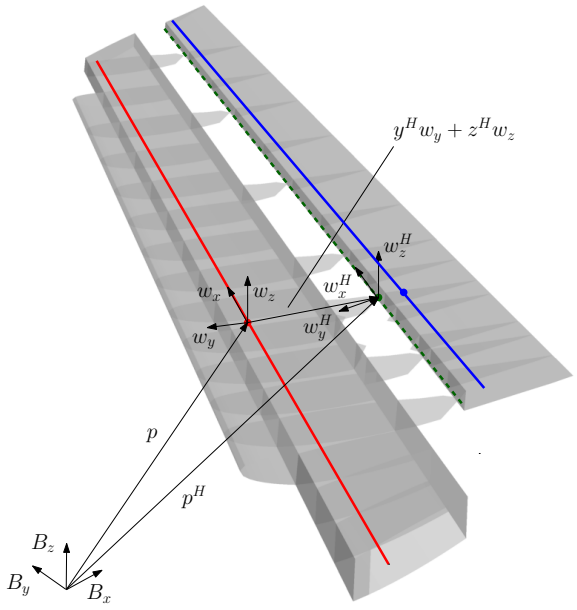

(b)

Figure A.1: Equivalent beam-type representation of a wingbox with a flexible control surface.

Since points along the hinge belong to the same rigid cross sections as their projections onto the fixed member and control-surface member reference axes, they are subject to the same rotations. Therefore, one has:

$$\begin{aligned} \theta^H_{mu} &= \theta_{mu}, \qquad & \theta^H_{nv} &= \theta_{nv}, \\ J^H_{\theta\varepsilon_{mu}} &= J_{\theta\varepsilon_{mu}}, \qquad & J^H_{\theta\varepsilon_{nv}} &= J_{\theta\varepsilon_{nv}}, \end{aligned} \tag{A.1}$$

where $J_{\theta\varepsilon_{mu}}$ and $J_{\theta\varepsilon_{nv}}$ are the $3 \times 4N$ blocks corresponding to the nodes mu and nv in the model Jacobian matrix $J_{\theta\varepsilon}$ in Eq. (2.13). The position and orientation of the hinge points are given by:

$$h^H_{mu} = \left\{ \begin{array}{c} p^H_{mu} \\ w^H_{x_{mu}} \\ w^H_{y_{mu}} \\ w^H_{z_{mu}} \end{array} \right\} \neq h_{mu}, \qquad h^H_{nv} = \left\{ \begin{array}{c} p^H_{nv} \\ w^H_{x_{nv}} \\ w^H_{y_{nv}} \\ w^H_{z_{nv}} \end{array} \right\} \neq h_{nv}. \tag{A.2}$$

Specifically, the positions of the hinge points are given by:

$$\begin{aligned} p^H_{mu} &= p_{mu} + y^H_{mu} w_{y_{mu}} + z^H_{mu} w_{z_{mu}}, \\ p^H_{nv} &= p_{nv} + y^H_{nv} w_{y_{nv}} + z^H_{nv} w_{z_{nv}}, \end{aligned} \tag{A.3}$$

where the distances y^H_{mu}, y^H_{nv}, z^H_{mu}, and z^H_{nv} are known from the hinge geometry and are constant in time. The orientations of w^H_{mu} and w^H_{nv} upon initialization are such that the $w^H_{x_{mu}}$ and $w^H_{x_{nv}}$ unit vectors are along the hinge line, while the other two unit vectors are along any pair of orthogonal directions in the normal plane. Note that the w^H_{mu} and w^H_{nv} frames do not generally coincide with the w_{mu} and w_{nv} frames. However, the orientations of the w^H_{mu} and w^H_{nv} frames with respect to the w_{mu} and w_{nv} frames, respectively, are known from the hinge geometry and related by:

$$w^H_{i_{mu}} = C^{Hw}_{mu} w_{i_{mu}}, \qquad w^H_{i_{nv}} = C^{Hw}_{nv} w_{i_{nv}}, \tag{A.4}$$

where $i = x, y, z$. The rotation matrices C^{Hw}_{mu} and C^{Hw}_{nv} transform the w_{mu} and w_{nv} frames into the w^H_{mu} and w^H_{nv} frames, respectively. These matrices are evaluated in undeformed configuration and, under the assumption of rigid cross-sections, they remain constant in time.

Using Eqs. (A.3) and (A.4), the column vectors h^H_{mu} and h^H_{nv} can be written as

$$h^H_{mu} = D^H_{mu} h_{mu}, \qquad h^H_{nv} = D^H_{nv} h_{nv}, \tag{A.5}$$

with

$$D^H_{mu} = \begin{bmatrix} I_3 & 0_3 & y^H_{mu} I_3 & z^H_{mu} I_3 \\ 0_3 & C^{Hw}_{mu} & 0_3 & 0_3 \\ 0_3 & 0_3 & C^{Hw}_{mu} & 0_3 \\ 0_3 & 0_3 & 0_3 & C^{Hw}_{mu} \end{bmatrix}, \quad D^H_{nv} = \begin{bmatrix} I_3 & 0_3 & y^H_{nv} I_3 & z^H_{nv} I_3 \\ 0_3 & C^{Hw}_{nv} & 0_3 & 0_3 \\ 0_3 & 0_3 & C^{Hw}_{nv} & 0_3 \\ 0_3 & 0_3 & 0_3 & C^{Hw}_{nv} \end{bmatrix}, \tag{A.6}$$

where I_3 is a 3×3 identity matrix, 0_3 is a 3×3 zero matrix. The matrices in Eq. (A.6) are known from the hinge line position and orientation in undeformed configuration and they are constant in time. The recovery law in Eq. (A.5) yields

$$J^H_{h\varepsilon_{mu}} = D^H_{mu} J_{h\varepsilon_{mu}}, \qquad J^H_{h\varepsilon_{nv}} = D^H_{nv} J_{h\varepsilon_{nv}}, \tag{A.7}$$

where $J_{h\varepsilon_{mu}}$ and $J_{h\varepsilon_{nv}}$ are the $12 \times 4N$ matrices corresponding to the nodes mu and nv in the model Jacobian matrix $J_{h\varepsilon}$ given in Eq. (2.13).

A.2 Hinge Boundary Conditions

Hinge boundary conditions are enforced by extending the formulation presented in Ref. [97] for modeling relative constraints. These constraints allow to model configurations where two members connect at a common node, such as joined-wing aircraft. However, hinge constraints are enforced at pairs of coincident hinge points that are not finite element nodes and do not belong to a reference beam axis. Depending on the hinge kinematic characteristics, certain position and rotation components of the hinge points are enforced to be equal at all times.

With reference to Fig. A.1, hinge constraints are modeled by enforcing the relations

$$B^H_h (h^H_{mu} - h^H_{nv}) = 0, \qquad B^H_\theta (\theta^H_{mu} - \theta^H_{nv}) = 0. \tag{A.8}$$

In Eq. (A.8), B^H_h is a boolean matrix that selects the constrained position components, that is, elements of p^H_{mu} and p^H_{nv} that are enforced to be equal at any time, B^H_θ selects the constrained components of θ^H_{mu} and θ^H_{nv}. Typically, coincident hinge connection points are enforced to keep the same positions at any time, while the rotation about the hinge axis is left free or commanded by enforcing a known prescribed relative rotation of the control-surface member with respect to the parent member. These conditions dictate the size and structure of the matrices B^H_h and B^H_θ such that they select the position and rotation components subject to the hinge constraint.

Following Ref. [97], the constraints in Eq. (A.8) are introduced into the discretized energy

functional using Lagrange multipliers. This leads to the constrained energy functional variation

$$\begin{aligned}\delta\Pi_c &= \delta\Pi + \delta\lambda_{hc,h}^T B_h^H (h_{mu}^H - h_{nv}^H) + \delta\lambda_{hc,\theta}^T [B_\theta^H (\theta_{mu}^H - \theta_{nv}^H)] \\ &\quad + \delta\varepsilon^T \left[B_h^H \left(D_{mu}^H J_{h\varepsilon_{mu}} - D_{nv}^H J_{h\varepsilon_{nv}}\right)\right]^T \lambda_{hc,h} + \delta\varepsilon^T \left[B_\theta^H \left(J_{\theta\varepsilon_{mu}} - J_{\theta\varepsilon_{nv}}\right)\right]^T \lambda_{hc,\theta},\end{aligned} \tag{A.9}$$

where the unconstrained energy functional variation is

$$\delta\Pi = \delta h^T M\ddot{h} + \delta\varepsilon^T C\dot{\varepsilon} + \delta\varepsilon^T K(\varepsilon - \varepsilon^0) + \tag{A.10}$$

$$+\delta h^T N\, g - \delta p^T (B^F F^{distr} + F^{pt}) - \delta\theta^T (B^M M^{distr} + M^{pt}), \tag{A.11}$$

and $\lambda_{hc,h}$ and $\lambda_{hc,\theta}$ are the column vectors of Lagrange multipliers for the position and rotation hinge constraints (A.8).

The unconstrained contribution in Eq. (A.9) is rewritten in terms of strain DOFs. The hinge constraints is developed using an iterative procedure [97] because the vectors h and θ are nonlinear functions of the strain vector. At the iteration $j+1$, the contribution due to the hinge position constraint is

$$\delta\lambda_{hc,h_{j+1}}^T B_h^H (h_{mu_{j+1}}^H - h_{nv_{j+1}}^H) + \delta\varepsilon_{j+1}^T \left[B_h^H \left(D_{mu}^H J_{h\varepsilon_{mu}} - D_{nv}^H J_{h\varepsilon_{nv}}\right)\right]_j^T \lambda_{hc,h_{j+1}}, \tag{A.12}$$

where

$$\begin{aligned} h_{mu_{j+1}}^H &= h_{mu_j}^H + (D_{mu}^H J_{h\varepsilon_{mu}})_j \left(\varepsilon_{j+1} - \varepsilon_j\right), \\ h_{nv_{j+1}}^H &= h_{nv_j}^H + (D_{nv}^H J_{h\varepsilon_{nv}})_j \left(\varepsilon_{j+1} - \varepsilon_j\right). \end{aligned} \tag{A.13}$$

The hinge rotation constraint is treated similarly, giving

$$\delta\lambda_{hc,\theta_{j+1}}^T [B_\theta^H (\theta_{mu_{j+1}}^H - \theta_{nv_{j+1}}^H) - \overline{\Delta\theta}_{mu,nv_{j+1}}^H] + \delta\varepsilon_{j+1}^T \left[B_\theta^H \left(J_{\theta\varepsilon_{mu}} - J_{\theta\varepsilon_{nv}}\right)\right]_j^T \lambda_{hc,\theta_{j+1}}, \tag{A.14}$$

where

$$\begin{aligned} \theta_{mu_{j+1}}^H &= \theta_{mu_j}^H + (J_{\theta\varepsilon_{mu}})_j \left(\varepsilon_{j+1} - \varepsilon_j\right), \\ \theta_{nv_{j+1}}^H &= \theta_{nv_j}^H + (J_{\theta\varepsilon_{nv}})_j \left(\varepsilon_{j+1} - \varepsilon_j\right). \end{aligned} \tag{A.15}$$

Substituting the Jacobians in Eq. (2.13) and Eqs. (A.12) to (A.15) into the constrained energy functional variation in Eq. (A.9) and setting it to zero gives the equations of motion

$$\begin{bmatrix} M_{FF_j} & M_{FB_j} & 0 \\ M_{BF_j} & M_{BB_j} & 0 \\ 0 & 0 & 0 \end{bmatrix} \ddot{q}_{j+1} + \begin{bmatrix} C_{FF_j} & C_{FB_j} & 0 \\ C_{BF_j} & C_{BB_j} & 0 \\ 0 & 0 & 0 \end{bmatrix} \dot{q}_{j+1} + \begin{bmatrix} K_{FF} & 0 & K_{hc_j}^T \\ 0 & 0 & 0 \\ K_{hc_j} & 0 & 0 \end{bmatrix} q_{j+1} = \begin{Bmatrix} R_{F_j} \\ R_{B_j} \\ R_{hc_j} \end{Bmatrix}, \tag{A.16}$$

where

$$\begin{aligned} \ddot{q}_{j+1}^T &= \left\{ \ddot{\varepsilon}_{j+1}^T,\, \dot{\beta}_{j+1}^T,\, \ddot{\lambda}_{hc_{j+1}}^T \right\}, \qquad \dot{q}_{j+1}^T = \left\{ \dot{\varepsilon}_{j+1}^T,\, \beta_{j+1}^T,\, \dot{\lambda}_{hc_{j+1}}^T \right\}, \\ q_{j+1}^T &= \left\{ \varepsilon_{j+1}^T,\, b_{j+1}^T,\, \lambda_{hc_{j+1}}^T \right\}, \qquad \lambda_{hc_{j+1}}^T = \left\{ \lambda_{hc,h_{j+1}}^T,\, \lambda_{hc,\theta_{j+1}}^T \right\}, \end{aligned} \tag{A.17}$$

and the hinge constraint stiffness and generalized load vector are

$$K_{hc_j} = \begin{bmatrix} B_h^H \left(D_{mu}^H J_{h\varepsilon_{mu}} - D_{nv}^H J_{h\varepsilon_{nv}} \right) \\ B_\theta^H \left(J_{\theta\varepsilon_{mu}} - J_{\theta\varepsilon_{nv}} \right) \end{bmatrix}_j, \qquad R_{hc_j} = K_{hc_j}\varepsilon_j - \begin{Bmatrix} B_h^H (h_{mu_j}^H - h_{nv_j}^H) \\ B_\theta^H (\theta_{mu_j}^H - \theta_{nv_j}^H) \end{Bmatrix}. \tag{A.18}$$

The matrix blocks in Eq. (A.16) are updated at each iteration, with the only exception of K_{FF}. Note that updating K_{hc_j} and R_{hc_j} requires to update only the Jacobians because the B_h^H, B_θ^H, D_{mu}^H, and D_{nv}^H matrices are all constant in time.

In the practice, a control-surface member is connected to a parent member at multiple locations. Therefore, the Lagrange multiplier vector will contain multipliers for each pair of constrained hinge connection points. Similarly, the hinge constraint stiffness matrix block and generalized load vector (A.17) will stack the associated Jacobians in the rows. Other types of constraints imposed on the model [97] such as relative constraints will also give additional Lagrange multipliers and matrix blocks in Eq. (A.16).

A.3 Hinge Loads

In a three-dimensional built-up finite element model of a component (e.g., wing) with a control surface, concentrated springs and dampers may be defined at the hinge connections to describe elastic reactions and dissipation that occur due to relative motions. To capture these effects in the beam-type representation of Fig. A.1, the following contributions are added to the internal virtual work terms:

$$\begin{aligned} \delta W_{H_{mu}}^{int} &= -\left(\delta\theta_{mu}^H\right)^T \left[K_{mu,nv}^H \left(\theta_{mu}^H - \theta_{nv}^H - \Delta\theta_{mu,nv}^0 \right) + C_{mu,nv}^H \left(\dot{\theta}_{mu}^H - \dot{\theta}_{nv}^H \right) \right] \\ &= -\delta\theta_{mu}^T \left[K_{mu,nv}^H \left(\theta_{mu} - \theta_{nv} - \Delta\theta_{mu,nv}^0 \right) + C_{mu,nv}^H \left(\dot{\theta}_{mu} - \dot{\theta}_{nv} \right) \right], \\ \delta W_{H_{nv}}^{int} &= -\left(\delta\theta_{nv}^H\right)^T \left[K_{mu,nv}^H \left(\theta_{nv}^H - \theta_{mu}^H - \Delta\theta_{nv,mu}^0 \right) + C_{mu,nv}^H \left(\dot{\theta}_{nv}^H - \dot{\theta}_{mu}^H \right) \right] \\ &= -\delta\theta_{nv}^T \left[K_{mu,nv}^H \left(\theta_{nv} - \theta_{mu} + \Delta\theta_{mu,nv}^0 \right) + C_{mu,nv}^H \left(\dot{\theta}_{nv} - \dot{\theta}_{mu} \right) \right], \end{aligned} \tag{A.19}$$

where $\Delta\theta_{mu,nv}^0 = -\Delta\theta_{nv,mu}^0$ is the built-in relative rotation vector of zero hinge elastic reaction at the current connection points. The hinge stiffness and damping matrices in Eq. (A.19) are derived by considering that rotations and rotation rates are resolved in the B frame, while the hinge

elastic and damping effects are conveniently modeled in the w^H frame. Therefore, the matrices in Eq. (A.19) take the forms

$$\begin{aligned} K^H_{mu,nv} &= \left(C^{HB}_{mu}\right)^T \begin{bmatrix} k^H_x & 0 & 0 \\ 0 & k^H_y & 0 \\ 0 & 0 & k^H_z \end{bmatrix}_{mu,nv} C^{HB}_{mu} = \left(C^{HB}_{nv}\right)^T \begin{bmatrix} k^H_x & 0 & 0 \\ 0 & k^H_y & 0 \\ 0 & 0 & k^H_z \end{bmatrix}_{mu,nv} C^{HB}_{nv}, \\ C^H_{mu,nv} &= \left(C^{HB}_{mu}\right)^T \begin{bmatrix} c^H_x & 0 & 0 \\ 0 & c^H_y & 0 \\ 0 & 0 & c^H_z \end{bmatrix}_{mu,nv} C^{HB}_{mu} = \left(C^{HB}_{nv}\right)^T \begin{bmatrix} c^H_x & 0 & 0 \\ 0 & c^H_y & 0 \\ 0 & 0 & c^H_z \end{bmatrix}_{mu,nv} C^{HB}_{nv}, \end{aligned} \tag{A.20}$$

where k^H_i and c^H_i $(i = x, y, z)$ are the torsion stiffness and viscous damping coefficients of the concentrated spring-damper elements at the hinge connections, respectively, and

$$C^{HB}_{mu} = C^{Hw}_{mu} C^{wB}_{mu}, \quad C^{HB}_{nv} = C^{Hw}_{nv} C^{wB}_{nv} \tag{A.21}$$

transform the B frame into the H frames at the coincident hinge connection points.

The total virtual work due to all the control surfaces in the model is obtained by summing contributions of the form in Eq. (A.20) for all the hinge connections, yielding

$$\delta W^{int}_H = -\delta\theta^T \left[K^H \left(\theta - \Delta\theta^0\right) + C^H \dot{\theta} \right], \tag{A.22}$$

where the matrices K^H and C^H and the column vector $\Delta\theta^0$ are obtained by assembling the nodal terms in Eq. (2.38).

The equations of motion including the hinge loads are obtained by rewriting Eq. (A.22) in terms of strains following the approach used in Sec. A.2. Assuming that the solution at the iteration j is known, the hinge virtual work at the iteration $j+1$ is

$$\delta W^{int}_{H_{j+1}} = -\delta\theta^T_{j+1} \left[K^H_j \left(\theta_{j+1} - \Delta\theta^0\right) + C^H_j \dot{\theta}_{j+1} \right], \tag{A.23}$$

where

$$\theta_{j+1} = \theta_j + \delta\theta_{j+1} = \theta_j + J_{\theta\varepsilon_j}(\varepsilon_{j+1} - \varepsilon_j). \tag{A.24}$$

The contribution due to the Jacobian $J_{\theta b}$ is neglected in Eq. (A.24), because only relative motions between the parent and control-surface members create hinge moments. Moreover, the sum of all these moments in the model cancels out, so that the contribution due to the Jacobian $J_{\theta b}$ is neglected when rewriting $\delta\theta^T_{j+1}$ as a function of the independent DOFs using Eq. (2.13). Considering these

properties and substituting Eq. (A.24) into Eq. (A.23), one obtains the equations of motion

$$\begin{bmatrix} M_{FF_j} & M_{FB_j} & 0 \\ M_{BF_j} & M_{BB_j} & 0 \\ 0 & 0 & 0 \end{bmatrix} \ddot{q}_{j+1} + \begin{bmatrix} \tilde{C}_{FF_j} & C_{FB_j} & 0 \\ C_{BF_j} & C_{BB_j} & 0 \\ 0 & 0 & 0 \end{bmatrix} \dot{q}_{j+1} + \begin{bmatrix} \tilde{K}_{FF_j} & 0 & K_{hc_j}^T \\ 0 & 0 & 0 \\ K_{hc_j} & 0 & 0 \end{bmatrix} q_{j+1} = \begin{Bmatrix} \tilde{R}_{F_j} \\ R_{B_j} \\ R_{hc_j} \end{Bmatrix}, \tag{A.25}$$

where

$$\begin{aligned} \tilde{C}_{FF_j} &= C_{FF_j} + \left(J_{\theta\varepsilon}^T C^H J_{\theta\varepsilon}\right)_j, \\ \tilde{K}_{FF_j} &= K_{FF} + \left(J_{\theta\varepsilon}^T K^H J_{\theta\varepsilon}\right)_j, \\ \tilde{R}_{F_j} &= R_{F_j} \ + \left(J_{\theta\varepsilon}^T K^H J_{\theta\varepsilon}\right)_j \varepsilon_j - \left(J_{\theta\varepsilon}^T K^H\right)_j \left(\theta_j - \Delta\theta^0\right). \end{aligned} \tag{A.26}$$

Flexible control surfaces affect the generalized mass, damping, and stiffness matrices in Eq. (A.25) through the equivalent beam properties of each control-surface member and also through the additional terms due to the hinge in Eqs. (A.17) and (A.26). Control-surface flexibility also affects the generalized loads both through the external loads applied directly on the control surfaces (for instance, due to aerodynamics) and through the hinge terms in Eqs. (A.17) and (A.26). All the matrix blocks and right-hand side column vector in Eq. (A.25) are updated at every time step, except for K_{FF}.

A.4 Hinge Point Projections at Arbitrary Reference Beam Axis Locations

In Secs. A.1 to A.3, the projections of the hinge connection points are assumed to intersect the reference axes of the parent member and of the control surface at points mu and nv coincident with nodes. However, these points will generally be at arbitrary locations within the mth and nth elements with offsets Δs_{mu} and Δs_{nv} from the first element nodes. This situation is shown in Fig. A.2 and can be treated using the kinematic relations presented.

The h vector at a generic location within a beam element is given by Eq. (2.22). Considering Fig. A.2, the hinge kinematic recovery laws in Eq. (A.5) are modified as

$$h_{mu}^H = D_{mu}^{Hw} h_{mu} = D_{mu}^{Hw} e^{G_{mu}} h_{m1}, \quad h_{nv}^H = D_{nv}^{Hw} h_{nv} = D_{nv}^{Hw} e^{G_{nv}} h_{n1}, \tag{A.27}$$

where $G_{mu} = \mathbb{K}_m \Delta s_{mu}$ and $G_{nv} = \mathbb{K}_n \Delta s_{nv}$, $\mathbb{K}_m$ and $\mathbb{K}_n$ are the matrices evaluated at the element m (fixed member) and n (control surface), respectively, and h_{m1} and h_{n1} are the h vectors at the first nodes of the elements m (fixed member) and n (control surface). The Jacobians associated to Eq. (A.27) can be still written as in Eq. (A.7), provided that the Jacobians $J_{h\varepsilon_{mu}}$ and $J_{h\varepsilon_{nv}}$ are

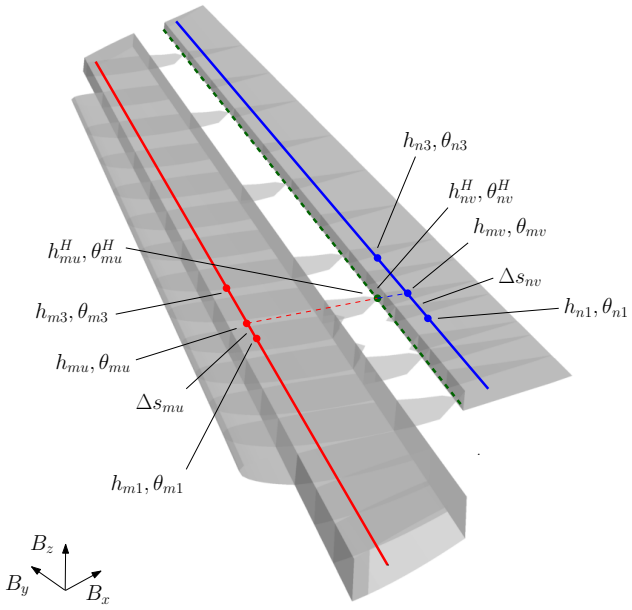

(a)

Figure A.2: Equivalent beam-type representation of a wingbox with a flexible control surface (general geometry).

evaluated as

$$
\begin{aligned}
J_{h\varepsilon_{mu}} &= \left[e^{G_{mu}} \frac{\partial h_{m1}}{\partial \varepsilon_1},\, e^{G_{mu}} \frac{\partial h_{m1}}{\partial \varepsilon_2}, \ldots, e^{G_{mu}} \frac{\partial h_{m1}}{\partial \varepsilon_l},\, \frac{\partial e^{G_{mu}}}{\partial \varepsilon_m} h_{m1},\, 0, \ldots,\, 0 \right], \\
J_{h\varepsilon_{nv}} &= \left[e^{G_{nv}} \frac{\partial h_{n1}}{\partial \varepsilon_1},\, e^{G_{nv}} \frac{\partial h_{n1}}{\partial \varepsilon_2}, \ldots, e^{G_{nv}} \frac{\partial h_{n1}}{\partial \varepsilon_m},\, \frac{\partial e^{G_{nv}}}{\partial \varepsilon_n} h_{n1},\, 0, \ldots,\, 0 \right].
\end{aligned}
\tag{A.28}
$$

All the terms but the quantities G_{mu}, G_{nv}, $\partial e^{G_{mu}}/\partial \varepsilon_m$, and $\partial e^{G_{nv}}/\partial \varepsilon_n$ are known from Eq. (2.13).

The θ column vector at a generic location within a beam element can be written as a linear combination of the nodal values because the strain-based formulation assumes constant curvatures along the element [97]. Therefore, one has

$$
\begin{aligned}
\theta^H_{mu} = \theta_{mu} &= \left(1 - \frac{\Delta s_{mu}}{\Delta s_m}\right) \theta_{m1} + \frac{\Delta s_{mu}}{\Delta s_m}\, \theta_{m3} = \eta_{m3}\, \theta_{m1} + \eta_{m1}\, \theta_{m3}, \\
\theta^H_{nv} = \theta_{nv} &= \left(1 - \frac{\Delta s_{nv}}{\Delta s_n}\right) \theta_{n1} + \frac{\Delta s_{nv}}{\Delta s_n}\, \theta_{n3} = \eta_{n3}\, \theta_{n1} + \eta_{n1}\, \theta_{n3}.
\end{aligned}
\tag{A.29}
$$

The quantities Δs_m and Δs_n are the lengths of the elements m and n, respectively, while $\eta_{m1} = \Delta s_{mu}/\Delta s_m$, $\eta_{m3} = 1 - \Delta s_{mu}/\Delta s_m$, $\eta_{n1} = \Delta s_{nv}/\Delta s_n$, $\eta_{n3} = 1 - \Delta s_{nv}/\Delta s_n$ are the

nondimensional offsets of the projected points mu and nv from the first and third nodes of the elements m and n, respectively. From Eq. (A.29) one obtains the Jacobians

$$\begin{aligned} J^H_{\theta\varepsilon_{mu}} &= J_{\theta\varepsilon_{mu}} = \eta_{m3}\, J_{\theta\varepsilon_{m1}} + \eta_{m1}\, J_{\theta\varepsilon_{m3}}, \\ J^H_{\theta\varepsilon_{nv}} &= J_{\theta\varepsilon_{nv}} = \eta_{n3}\, J_{\theta\varepsilon_{n1}} + \eta_{n1}\, J_{\theta\varepsilon_{n3}}, \end{aligned} \tag{A.30}$$

where $J_{\theta\varepsilon_{m1}}$, $J_{\theta\varepsilon_{m3}}$, $J_{\theta\varepsilon_{n1}}$, and $J_{\theta\varepsilon_{n3}}$ are the $3 \times 4N$ blocks of the model Jacobian $J_{\theta\varepsilon}$, Eq. (2.13), associated with the nodes $m1$, $m3$, $n1$, and $n3$, respectively.

Based on the above kinematic relations, the hinge boundary conditions lead to the same form of the equations of motion in Sec. A.2 provided that the hinge stiffness matrix is evaluated as

$$K_{hc_j} = \begin{bmatrix} B^H_h \left(D^H_{mu} e^{G_{mu}} J_{h\varepsilon_{mu}} - D^H_{nv} e^{G_{nv}} J_{h\varepsilon_{nv}} \right) \\ B^H_\theta \left(J_{\theta\varepsilon_{mu}} - J_{\theta\varepsilon_{nv}} \right) \end{bmatrix}_j , \tag{A.31}$$

where the Jacobians $J_{h\varepsilon_{mu}}$, $J_{h\varepsilon_{nv}}$, $J_{\theta\varepsilon_{mu}}$, and $J_{\theta\varepsilon_{nv}}$ are computed as in Eqs. (A.28) and Eq. (A.30).

Substituting Eqs. (A.29) and (A.30) into the hinge virtual works Eq. (A.19), the total virtual work due to all the hinge connection points can be still written as in Eq. (A.22). However, appropriate weights consistent with Eq. (A.29) are needed when assembling the contributions due to the hinge stiffness and damping matrices at each connection point into the full-model matrices. The same remarks applies to the Jacobians used for rewriting the total virtual work in terms of independent DOFs, which need to be computed as in Eq. (A.30).

APPENDIX B

Fuselage Aerodynamics

Aerodynamic loads on UM/NAST wing-type members subject to transonic flow conditions are currently computed using the method of segments and kriging surrogates [91, 65]. In this approach, the circulatory loads on each spanwise cross section (corresponding to a UM/NAST node) are computed using aerodynamic lift, drag, and pitching moment coefficients given by a kriging surrogate model as functions of the instantaneous Mach number M, local instantaneous effective angle of attack α_{eff}, and control-surface deflection δ_{CS}. Multiple control surfaces can be defined on the same cross section.

The aerodynamic loads at a point along the beam reference axis of a UM/NAST wing-type member are given in the local wind axes (a_1 frame, see Fig. B.1) by:

$$\begin{aligned} L &= \pi\rho b^2(-\ddot{z} + \dot{y}\dot{\alpha} - d\ddot{\alpha}) + \rho b\,\dot{y}^2\,c_L(M, \alpha_{\text{eff}}, \delta_{\text{CS}}), \\ D &= \rho b\,\dot{y}^2\,c_D(M, \alpha_{\text{eff}}, \delta_{\text{CS}}), \\ M &= \frac{\pi\rho b^3}{2}\left[\ddot{z} - 2\dot{y}\dot{\alpha} - (0.25b - d)\ddot{\alpha}\right] + 2\rho b^2\,\dot{y}^2\,c_M(M, \alpha_{\text{eff}}, \delta_{\text{CS}}), \end{aligned} \tag{B.1}$$

where L is lift per unit length (aerodynamic force component along a_{1_z}), D is drag per unit length (aerodynamic force component along $-a_{1_y}$), and M is the aerodynamic pitching moment per unit length about the quarter-chord point (aerodynamic moment component about a_{1_x}), ρ is the air density, b is the local half chord, d is the forward-positive dimensional offset of the beam reference axis from the half-chord point, $\dot{y}$ and $\dot{z}$ are the local horizontal and vertical velocity components in the airfoil chord frame (a frame, see Fig. B.2), $\dot{\alpha}$ is the local pitch velocity in that frame, and c_L, c_D, and c_M are the airfoil lift, drag, and pitching moment aerodynamic coefficients. The local instantaneous effective angle of attack in Eq. (B.1) is given by

$$\alpha_{\text{eff}} = \frac{-\dot{z} + (0.5b - d)\dot{\alpha}}{\dot{y}} \tag{B.2}$$

and is measured between the local velocity along a_{1_y} and the airfoil chord along a_y as shown in

Fig. B.1. Equation (B.2) does not include the unsteady effects due to the wake or compressibility lags.

A UM/NAST fuselage member is originally defined as a purely structural member that does not develop aerodynamic loads. In this work, UM/NAST is enhanced with the capability to account for fuselage aerodynamics. This is done under two assumptions: 1) the aerodynamic coefficients are given for each fuselage station that will be associated with a fuselage beam element, and 2) aerodynamic loads account for steady effects only. Moreover, while only the three aerodynamic load components (L, M, and D) are considered for wing-type members, fuselage members experience all six aerodynamic force and moment components.

The aerodynamic loads at a point along the fuselage stations are given in the local aerodynamic axes (a frame, see Fig. B.2) by

$$\begin{aligned}
F_x &= \frac{\rho r_f \dot{x}^2}{2} c_{F_x}(M, \alpha_{\text{eff}}) \ , \\
F_y &= \frac{\rho r_f \dot{x}^2}{2} c_{F_y}(M, \alpha_{\text{eff}}) \ , \\
F_z &= \frac{\rho r_f \dot{x}^2}{2} c_{F_z}(M, \alpha_{\text{eff}}) \ , \\
M_x &= \frac{\rho r_f^2 \dot{x}^2}{2} c_{M_x}(M, \alpha_{\text{eff}}) + d_y F_z - d_z F_y \ , \\
M_y &= \frac{\rho r_f^2 \dot{x}^2}{2} c_{M_y}(M, \alpha_{\text{eff}}) + d_z F_x \ , \\
M_z &= \frac{\rho r_f^2 \dot{x}^2}{2} c_{M_z}(M, \alpha_{\text{eff}}) - d_y F_x \ ,
\end{aligned} \tag{B.3}$$

where r_f is the local radius of a particular fuselage station, $\dot{x}$ is the local velocity component along the fuselage beam reference axis in its local frame (w frame, see Fig. B.3), d_y and d_z are the y and z offsets of the point of load calculation to the fuselage beam reference axis as shown in Fig. B.3; c_{F_z}, c_{F_x}, and c_{M_y} are the aerodynamic coefficients associated with longitudinal load components (analogous to the lift, drag, and pitching moment aerodynamic coefficients), while c_{F_y}, c_{M_x}, and c_{M_z} are the remaining aerodynamic coefficients associated with lateral load components.

The aerodynamic coefficients in Eq. (B.3) are functions of the local instantaneous effective angle of attack that for fuselage members is defined as

$$\alpha_{\text{eff}} = \frac{-\dot{z}}{\dot{x}}. \tag{B.4}$$

Other than on α_{eff}, the coefficients in Eq. (2.59) are also dependent on the local Mach number

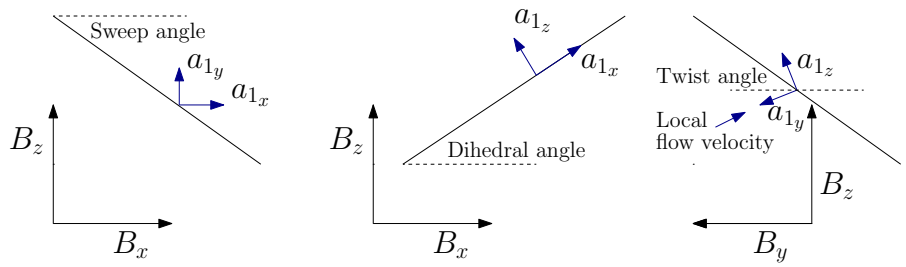

(a) Wing (top view) (b) Wing (rear view) (c) Wing (side view)

Figure B.1: Orientation of the local wind frame (a_1 frame) with respect to the global B frame for a generic UM/NAST wing node.

M. These dependencies are provided by a kriging surrogate model defined for each node along the fuselage beam reference axis and trained on a database of local aerodynamic coefficients from three-dimensional steady rigid CFD solutions obtained for different conditions of body angle of attack and Mach number. The aerodynamic coefficients in Eq. (B.3) for fuselage members would also depend on the instantaneous effective angle of sideslip β_{eff}.

To create the kriging surrogate models for a UM/NAST fuselage member, CFD solutions obtained for the training sets of body angle of attack and Mach number are "sliced" at the spanwise locations corresponding to the UM/NAST nodes for computing the aerodynamic coefficients at those locations.

These aerodynamic coefficients are fitted using the kriging technique [109] to create the nodal surrogates. The inputs to each nodal surrogate are the local M and α_{eff} values while the outputs are the nodal aerodynamic coefficients. The methodology is further described in Refs. [91, 65] and its application to modeling the XRF1 wing and horizontal tail aerodynamics is described in Ref. [90]. Note that each nodal surrogate takes the local angle of attack α_{eff} as the input during a simulation, which is generally different from the body angle of attack α because of the local incidence and the effect of flexible motion.

For giving correct results, the kriging nodal surrogates must be created consistently with Eq. (B.3). This means that each surrogate must return aerodynamic coefficients defined in the a frame at the corresponding UM/NAST node (see Fig. B.2), that is,

$$\begin{aligned} c_{F_x} &= \frac{2F_x}{\rho r_f \dot{x}^2}\,, \qquad c_{F_y} = \frac{2F_y}{\rho r_f \dot{x}^2}\,, \qquad c_{F_z} = \frac{2F_z}{2\rho r_f \dot{x}^2}\,, \\ c_{M_x} &= \frac{2M_x}{\rho r_f^2 \dot{x}^2}\,, \qquad c_{M_y} = \frac{2M_y}{\rho r_f^2 \dot{x}^2} \qquad c_{M_z} = \frac{2M_z}{2\rho r_f^2 \dot{x}^2}\,, \end{aligned} \tag{B.5}$$

where $\rho\dot{x}^2/2$ is the *local* dynamic pressure.

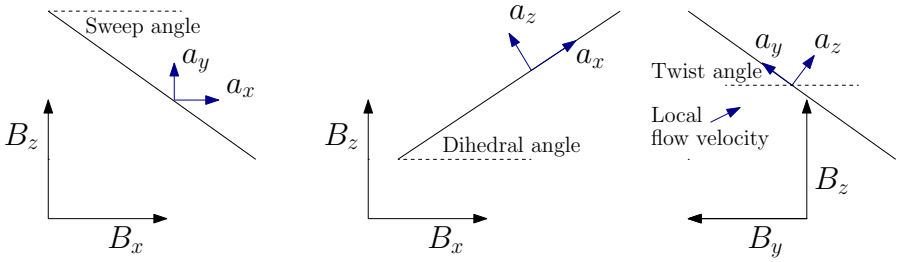

(a) Wing (top view) (b) Wing (rear view) (c) Wing (side view)

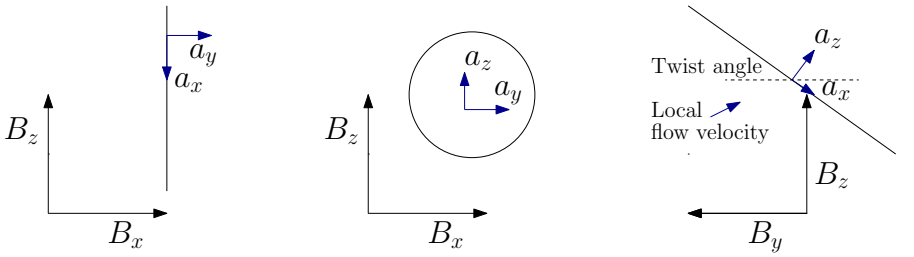

(d) Fuselage (top view) (e) Fuselage (rear view) (f) Fuselage (side view)

Figure B.2: Orientation of the local aerodynamic frame (a frame) when $(d_y, d_z) = (0, 0)$ and its connection with the global B frame for a generic UM/NAST wing and fuselage node. For the case of the fuselage, the a frame coincides with the w frame (structural frame).

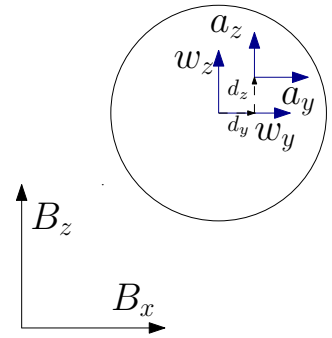

Figure B.3: Fuselage beam reference axis typically located at the fuselage station area centroid. While the aerodynamic coefficients should be also calculated at the fuselage area centroid, in general they could be given about a point offset from the beam reference line by (d_y, d_z). Regardless, the two coordinate frames, *i.e.*, a and w frames, remain aligned to each other.

APPENDIX C

Enhanced FEM2Stick

The University of Michigan's Enhanced FEM2Stick (UM/EF2S) is being developed to improve the evaluation of the equivalent beam stiffness properties by including the extraction of axial stiffness and corresponding coupling terms. The previous version of FEM2Stick (F2S) evaluates only a 3×3 cross-sectional stiffness matrix and hence only terms related to bending and torsion are calculated. Axial stiffness was not computed with F2S and was assumed infinite. On the other hand, the EF2S evaluates the complete 6×6 cross-sectional stiffness matrix. Terms related to axial stiffness are also evaluated. However, the 6×6 stiffness matrix is reduced to a 4×4 matrix as required by UM/NAST which includes the terms related to bending, torsion and axial stiffness.

C.1 Theoretical Formulation

It is required to reduce a given finite element method (FEM) model into an equivalent beam representation. Given a FEM model, we want to find out the stiffness properties of a beam which can model the behavior of the FEM model. In our case, the FEM model comes from MSC Nastran and the equivalent beam representation is to be modeled in UM/NAST. We want the stiffness of the beam in the UM/NAST compatible format. This requires the user to find the stiffness parameters in local coordinate frame for each beam element. In this FEM to beam stiffness reduction process, we will be doing the following major steps:

1. Defining the beam reference axis and number of reference nodes. Let's say the total number of beam reference nodes are $n + 1$, then the total number of elements will be n.

2. Apply six different static load cases at the tip of the FEM structure given by a force vector F^t. Using MSC Nastran's interpolation elements in the FEM, measure the displacement vector U for each reference node for the different load cases. Both F^t and U are in the global reference frame.

3. Using the information from the above steps, determine the following element stiffness matrix k for each element in its local beam reference axis.

This 6×6 stiffness matrix for each element is given by:

$$f^i = \begin{Bmatrix} f_x^i \\ f_y^i \\ f_z^i \\ m_x^i \\ m_y^i \\ m_z^i \end{Bmatrix} = k\epsilon, \tag{C.1}$$

where f^i, is a vector of internal force resultants withing an element in the local frame as a result of applied tip forces and ϵ is the strain vector in the element local frame.

Hence knowing the displacement vector u for the two ends of the element and using finite difference to calculate the derivatives, strain vector for the element can be calculated. It's important to note that the shear strains are not constant for an element and vary with the position along the element.

C.1.1 Evaluating the Local Internal Force Resultant Vector for an Element

We have the vector F^t, which for each six different static load case is given by:

$$F^t = \left\{ F_x^T \ 0 \ 0 \ 0 \ 0 \ 0 \right\}, \tag{C.2}$$

$$F^t = \left\{ 0 \ F_y^T \ 0 \ 0 \ 0 \ 0 \right\}, \tag{C.3}$$

$$F^t = \left\{ 0 \ 0 \ F_z^T \ 0 \ 0 \ 0 \right\}, \tag{C.4}$$

$$F^t = \left\{ 0 \ 0 \ 0 \ M_x^T \ 0 \ 0 \right\}, \tag{C.5}$$

$$F^t = \left\{ 0 \ 0 \ 0 \ 0 \ M_y^T \ 0 \right\} \tag{C.6}$$

and

$$F^t = \left\{ 0 \ 0 \ 0 \ 0 \ 0 \ M_z^T \right\}. \tag{C.7}$$

C.1.1.1 Load Cases Involving Tip Moments

For transforming the tip force vector F^t, involving moments, the transformation from F^t to f^i is given by:

$$f^t = [G2L]F^t, \tag{C.8}$$

where G2L is the transformation matrix between the FEM's global frame and element local frame. Also the Eq. (C.9) holds for tip forces involving moments:

$$f^i = f^B = f^t, \tag{C.9}$$

where F^t is the applied tip force vector in the FEM model's global frame, f^t is the applied tip force vector in the element local frame, f^B is the force vector at the element end B in element local frame and, f^i is the internal force resultant vector in the element local frame.

C.1.1.2 Load Cases Involving Tip Forces

For the load cases involving the tip forces, the transformation works a different way as the moments induced by the tip forces need to be accounted for as well. The resultant forces at the element end B would involve moments as a results of the applied forces which is given by:

$$f^B = r \times f^t, \tag{C.10}$$

where r is the position vector from the element end B to the point of applied tip force. Therefore, using vector f^t which is given by the Eq. (C.9), the vector f^B can be evaluated using the equation Eq. (C.10). Now, the vector f^i can be evaluated using the vector f^B:

$$f^i = \begin{Bmatrix} f^i_x \\ f^i_y \\ f^i_z \\ m^i_x \\ m^i_y \\ m^i_z \end{Bmatrix} = [T] f^B = \begin{bmatrix} 1 & 0 & 0 & 0 & 0 & 0 \\ 0 & 1 & 0 & 0 & 0 & 0 \\ 0 & 0 & 1 & 0 & 0 & 0 \\ 0 & 0 & 0 & 1 & 0 & 0 \\ 0 & 0 & -(l-x) & 0 & 1 & 0 \\ 0 & (l-x) & 0 & 0 & 0 & 1 \end{bmatrix}, \tag{C.11}$$

where l is the length of the element in consideration. The Eq. (C.11) is evaluated by knowing the fact that for any forces in the y and z direction, there would be induced internal moments which would be a function of the distance x along the length of the element in consideration.

C.1.2 Evaluation of the Local Element Stiffness Matrix

The evaluation of the element stiffness matrix k, follows the approach given by Malcolm [110]. It starts with first evaluating the 6×6 stiffness matrix K, which is still a local element stiffness

matrix but related the forces with the displacements and is given by:

$$f^B = K\Delta u, \tag{C.12}$$

where Δu is the displacement of the end B relative to the end A in the local element reference frame and is given by:

$$\Delta u = \begin{Bmatrix} u_x^B - u_x^A \\ u_y^B - u_y^A - l\theta_z^A \\ u_z^B - u_z^A + l\theta_y^A \\ \theta_x^B - \theta_x^A \\ \theta_y^B - \theta_y^A \\ \theta_z^B - \theta_z^A \end{Bmatrix} = k\epsilon. \tag{C.13}$$

Hence using Eq. (C.13), we can evaluate the matrix K. Malcolm [110] derives a relation between the matrix K and matrix k which is given by:

$$K^{-1}Q^{-1} = k^{-1}HQ^{-1} + Ek^{-1}. \tag{C.14}$$

Equation (C.14) is the Lyapunov's equation and can be solved in MATLAB for k^{-1}. Inverting the same would give us the k matrix. The final step is to reduce the 6×6 matrix into 4×4 as required by UM/NAST.

It is important to note that the matrices E, Q and H in Eq. (C.14) are all functions of the length of an element and are constant for a given element. The formulation in the paper [110] was given for a different local coordinate frame. Therefore, the equations have been re-derived to calculate the matrices E, Q and H for the local reference frame that is used in UM/NAST.

C.2 Derivation of the Local Element Stiffness Matrix

Element stiffness matrix k can be calculated by Eq. (C.14). Since, Eq. (C.14) involve constant matrices E, Q and H which are dependent on the type of the local reference frame that is used for an element, we need to derive the equation again as per the UM/NAST local coordinate system. To derive the same, we need to start with expressing the stiffness matrix k in terms of stiffness matrix K. For this the first step is to start with expressing the vector Δu in terms of strains, such that

strains can be related to the stiffness matrix k. Hence starting with Eq. (C.15), we have

$$\Delta u = \int_0^l \begin{Bmatrix} \frac{\partial u_x}{\partial x} \\ \frac{\partial u_y}{\partial x} \\ \frac{\partial u_z}{\partial x} \\ \frac{\partial \theta_x}{\partial x} \\ \frac{\partial \theta_y}{\partial x} \\ \frac{\partial \theta_z}{\partial x} \end{Bmatrix} \mathrm{d}x. \tag{C.15}$$

But using Eq. (C.27), we can write

$$\int_0^l \begin{Bmatrix} \frac{\partial u_x}{\partial x} \\ \frac{\partial u_y}{\partial x} \\ \frac{\partial u_z}{\partial x} \\ \frac{\partial \theta_x}{\partial x} \\ \frac{\partial \theta_y}{\partial x} \\ \frac{\partial \theta_z}{\partial x} \end{Bmatrix} \mathrm{d}x = \int_0^l \begin{Bmatrix} \epsilon_x \\ \gamma_y + \theta_z \\ \gamma_z - \theta_y \\ \kappa_x \\ \kappa_y \\ \kappa_z \end{Bmatrix} \mathrm{d}x. \tag{C.16}$$

Hence, using Eq. (C.15) and Eq. (C.16), we can write

$$\Delta u = \int_0^l \begin{Bmatrix} \epsilon_x \\ \gamma_y + \theta_z \\ \gamma_z - \theta_y \\ \kappa_x \\ \kappa_y \\ \kappa_z \end{Bmatrix} \mathrm{d}x = \int_0^l \begin{Bmatrix} \epsilon_x \\ \gamma_y \\ \gamma_z \\ \kappa_x \\ \kappa_y \\ \kappa_z \end{Bmatrix} \mathrm{d}x + \int_0^l \begin{Bmatrix} 0 \\ \theta_z \\ -\theta_y \\ 0 \\ 0 \\ 0 \end{Bmatrix} \mathrm{d}x. \tag{C.17}$$

Further, using Eq. (2.59) and Eq. (C.27), we have

$$f^i = k \begin{Bmatrix} \epsilon_x \\ \gamma_y \\ \gamma_z \\ \kappa_x \\ \kappa_y \\ \kappa_z \end{Bmatrix} \mathrm{d}x. \tag{C.18}$$

Inverting Eq. (C.18), we can substitute in the Eq. (C.17), to get

$$\Delta u = \int_0^l k^{-1} f^i \, \mathrm{d}x + \int_0^l \begin{Bmatrix} 0 \\ \theta_z \\ -\theta_y \\ 0 \\ 0 \\ 0 \end{Bmatrix} \mathrm{d}x. \tag{C.19}$$

Also, we can use Eq. (C.11), to substitute for f^i in the Eq. (C.19), to get

$$\Delta u = k^{-1} \int_0^l \begin{bmatrix} 1 & 0 & 0 & 0 & 0 & 0 \\ 0 & 1 & 0 & 0 & 0 & 0 \\ 0 & 0 & 1 & 0 & 0 & 0 \\ 0 & 0 & 0 & 1 & 0 & 0 \\ 0 & 0 & -(l-x) & 0 & 1 & 0 \\ 0 & (l-x) & 0 & 0 & 0 & 1 \end{bmatrix} f^B \, \mathrm{d}x + \int_0^l \begin{Bmatrix} 0 \\ \theta_z \\ -\theta_y \\ 0 \\ 0 \\ 0 \end{Bmatrix} \mathrm{d}x. \tag{C.20}$$

Next, using Eq (C.27), we can write

$$\begin{Bmatrix} 0 \\ -\theta_z \\ \theta_y \\ 0 \\ 0 \\ 0 \end{Bmatrix} = \int_0^x \begin{Bmatrix} 0 \\ -\kappa_z \\ \kappa_y \\ 0 \\ 0 \\ 0 \end{Bmatrix} \mathrm{d}x. \tag{C.21}$$

But we can write Eq. (C.21) in terms of strain as

$$\begin{Bmatrix} 0 \\ -\theta_z \\ \theta_y \\ 0 \\ 0 \\ 0 \end{Bmatrix} = \int_0^x \begin{Bmatrix} 0 \\ -\kappa_z \\ \kappa_y \\ 0 \\ 0 \\ 0 \end{Bmatrix} \mathrm{d}x = \int_0^x \begin{bmatrix} 0 & 0 & 0 & 0 & 0 & 0 \\ 0 & 0 & 0 & 0 & 0 & 1 \\ 0 & 0 & 0 & 0 & -1 & 0 \\ 0 & 0 & 0 & 0 & 0 & 0 \\ 0 & 0 & 0 & 0 & 0 & 0 \\ 0 & 0 & 0 & 0 & 0 & 0 \end{bmatrix} \epsilon \, \mathrm{d}x = \int_0^x \begin{Bmatrix} 0 \\ -\kappa_z \\ \kappa_y \\ 0 \\ 0 \\ 0 \end{Bmatrix} \mathrm{d}x = \int_0^x E\epsilon \, \mathrm{d}x. \tag{C.22}$$

Further, inverting Eq. (C.18), we have

$$\begin{Bmatrix} 0 \\ -\theta_z \\ \theta_y \\ 0 \\ 0 \\ 0 \end{Bmatrix} = \int_0^x Ek^{-1} f^i \, \mathrm{d}x. \tag{C.23}$$

Now, again using Eq. (C.11), we have

$$\begin{Bmatrix} 0 \\ -\theta_z \\ \theta_y \\ 0 \\ 0 \\ 0 \end{Bmatrix} = Ek^{-1} \int_0^x \begin{bmatrix} 1 & 0 & 0 & 0 & 0 & 0 \\ 0 & 1 & 0 & 0 & 0 & 0 \\ 0 & 0 & 1 & 0 & 0 & 0 \\ 0 & 0 & 0 & 1 & 0 & 0 \\ 0 & 0 & -(l-x) & 0 & 1 & 0 \\ 0 & (l-x) & 0 & 0 & 0 & 1 \end{bmatrix} f^B \, \mathrm{d}x. \tag{C.24}$$

On integrating the above, we have

$$\begin{Bmatrix} 0 \\ -\theta_z \\ \theta_y \\ 0 \\ 0 \\ 0 \end{Bmatrix} = Ek^{-1} \begin{bmatrix} x & 0 & 0 & 0 & 0 & 0 \\ 0 & x & 0 & 0 & 0 & 0 \\ 0 & 0 & x & 0 & 0 & 0 \\ 0 & 0 & 0 & x & 0 & 0 \\ 0 & 0 & -x(l-x/2) & 0 & x & 0 \\ 0 & x(l-x/2) & 0 & 0 & 0 & x \end{bmatrix} f^B = Ek^{-1} G_x f^B. \tag{C.25}$$

Now, we can substitute Eq. (C.25) in Eq. (C.20) to get

$$\Delta u = k^{-1} \int_0^l \begin{bmatrix} 1 & 0 & 0 & 0 & 0 & 0 \\ 0 & 1 & 0 & 0 & 0 & 0 \\ 0 & 0 & 1 & 0 & 0 & 0 \\ 0 & 0 & 0 & 1 & 0 & 0 \\ 0 & 0 & -(l-x) & 0 & 1 & 0 \\ 0 & (l-x) & 0 & 0 & 0 & 1 \end{bmatrix} f^B \, \mathrm{d}x + Ek^{-1} \int_0^l G_x f^B \, \mathrm{d}x. \tag{C.26}$$

Next, integrating Eq. (C.26), we have

$$\Delta u = k^{-1}\begin{bmatrix} l & 0 & 0 & 0 & 0 & 0 \\ 0 & l & 0 & 0 & 0 & 0 \\ 0 & 0 & l & 0 & 0 & 0 \\ 0 & 0 & 0 & l & 0 & 0 \\ 0 & 0 & -l^2/2 & 0 & l & 0 \\ 0 & l^2/2 & 0 & 0 & 0 & l \end{bmatrix} f^B + Ek^{-1}\begin{bmatrix} l^2/2 & 0 & 0 & 0 & 0 & 0 \\ 0 & l^2/2 & 0 & 0 & 0 & 0 \\ 0 & 0 & l^2/2 & 0 & 0 & 0 \\ 0 & 0 & 0 & l^2/2 & 0 & 0 \\ 0 & 0 & -l^3/3 & 0 & l^2/2 & 0 \\ 0 & l^3/3 & 0 & 0 & 0 & l^2/2 \end{bmatrix} f^B \tag{C.27}$$

or,

$$\Delta u = k^{-1}Hf^B + Ek^{-1}Qf^B. \tag{C.28}$$

But, using Eq. (C.12), we can write Eq. C.27 as

$$\Delta u = K^{-1}f^B = k^{-1}Hf^B + Ek^{-1}Qf^B, \tag{C.29}$$

which gives us on simplification

$$K^{-1} = k^{-1}H + Ek^{-1}Q. \tag{C.30}$$

Post multiplying by Q^{-1}, we finally get:

$$K^{-1}Q^{-1} = k^{-1}HQ^{-1+Ek^{-1}} \tag{C.31}$$

where,

$$E = \begin{bmatrix} 0 & 0 & 0 & 0 & 0 & 0 \\ 0 & 0 & 0 & 0 & 0 & 1 \\ 0 & 0 & 0 & 0 & -1 & 0 \\ 0 & 0 & 0 & 0 & 0 & 0 \\ 0 & 0 & 0 & 0 & 0 & 0 \\ 0 & 0 & 0 & 0 & 0 & 0 \end{bmatrix}, \tag{C.32}$$

$$H = \begin{bmatrix} l & 0 & 0 & 0 & 0 & 0 \\ 0 & l & 0 & 0 & 0 & 0 \\ 0 & 0 & l & 0 & 0 & 0 \\ 0 & 0 & 0 & l & 0 & 0 \\ 0 & 0 & -l^2/2 & 0 & l & 0 \\ 0 & l^2/2 & 0 & 0 & 0 & l \end{bmatrix} \tag{C.33}$$

and

$$Q = \begin{bmatrix} l^2/2 & 0 & 0 & 0 & 0 & 0 \\ 0 & l^2/2 & 0 & 0 & 0 & 0 \\ 0 & 0 & l^2/2 & 0 & 0 & 0 \\ 0 & 0 & 0 & l^2/2 & 0 & 0 \\ 0 & 0 & -l^3/3 & 0 & l^2/2 & 0 \\ 0 & l^3/3 & 0 & 0 & 0 & l^2/2 \end{bmatrix}. \tag{C.34}$$

BIBLIOGRAPHY

[1] Mosquera, P. D. B., Catalano, F. M., and Zingg, D. W., "Unconventional Aircraft for Civil Aviation: A Review of Concepts and Design Methodologies," *Progress in Aerospace Sciences*, Vol. 131, 2022, pp. 100813.

[2] BAE-Systems, "De Havilland DH106 Comet," *https://www.baesystems.com/en/heritage/de-havilland-comet*, BAE-Systems, July 2022.

[3] Airbus, "A380," *https://www.airbus.com/en/products-services/commercial-aircraft/a380*, Airbus, July 2022.

[4] Bradley, M. and Droney, C., "Subsonic Ultra Green Aircraft Research Phase II: N+4 Advanced Concept Development," Tech.rep. CR-2012-217556, NASA, 2013.

[5] Airbus, "ZEROe: Towards the World's First Zero-emission Commercial Aircraft," *https://www.airbus.com/en/innovation/zero-emission/hydrogen/zeroe*, Airbus, January 2022.

[6] FAA, "Aviation Climate Action Plan," *https://www.faa.gov/sites/faa.gov/files/2021-11/Aviation_Climate_Action_Plan.pdf*, FAA, November 2021.

[7] Cesnik, C. E. S., Palacios, R., and Reichenbach, E. Y., "Reexamined Structural Design Procedures for Very Flexible Aircraft," *Journal of Aircraft*, Vol. 51, No. 5, 2014, pp. 1580–1591.

[8] Dees, P., Good, M. S., Sakurai, S., Kordel, J., Fox, S. J., Lassen, M. A., Fox, R. B., Walker, S. P., and Santini, G. M., "Hinged Raked Wing Tip," *United States Patent US0099060*, 2013.

[9] Juttle, C. V. and Stanford, B. K., "Aeroelastic Tailoring of Transport Aircraft Wings: State-of-the-Art and Potential Enabling Technologies," Tech. Rep. TM-2014-218252, NASA, April 2014.

[10] Regan, C. D. and Juttle, C. V., "Survey of Applications of Active Control Technology for Gust Alleviation and New Challenges for Lighter-weight Aircraft," Tech. Rep. TM-2012-0013450, NASA, April 2012.

[11] Weisshaar, T. A. and Nam, C., "Aeroservoelastic Tailoring for Lateral Control Enhancement," *Journal of Guidance, Control, and Dynamics*, Vol. 13, No. 3, 1990, pp. 458–465.

[12] Lebofsky, S., Ting, E., Trinh, K. V., and Nguyen, N. T., "Optimization for Load Alleviation of Truss-Braced Wing Aircraft With Variable Camber Continuous Trailing Edge Flap," *AIAA Applied Aerodynamics Conference*, Dallas, TX, June 2015.

[13] Ting, E., Dao, T., and Nguyen, N. T., "Aerodynamic Load Analysis of a Variable Camber Continuous Trailing Edge Flap System on a Flexible Wing Aircraft," *AIAA/ASCE/AHS/ASC Structures, Structural Dynamics, and Materials Conference*, Kissimmee, FL, January 2015.

[14] Stanford, B. K., "Static and Dynamic Aeroelastic Tailoring with Variable-Camber Control," *Journal of Guidance, Control, and Dynamics*, Vol. 39, No. 11, 2016, pp. 2522–2534.

[15] Lee, S. J., Hashemi, K. E., Drew, M. C., Nguyen, N. T., and Kim, H. J., "Robust Gust Load Alleviation Control using Disturbance Observer for Generic Flexible Wing Aircraft in Cruising Condition," *Annual American Control Conference (ACC)*, Milwaukee, WI, June 2018.

[16] Nguyen, N. T., Hashemi, K. E., and Drew, M. C., "Multi-Objective Adaptive Control for Load Alleviation and Drag Minimization of Flexible Aircraft," *AIAA Guidance, Navigation, and Control Conference*, Kissimmee, FL, January 2018.

[17] Nguyen, N. T. and Hashemi, K. E., "Multi-Objective Flight Control for Ride Quality Improvement for Flexible Aircraft," *AIAA SciTech 2020 Forum*, Orlando, FL, January 2020.

[18] Drew, M. C., Hashemi, K. E., Cramer, N. B., Xiong, J., and Nguyen, N. T., "Multi-Objective Gust Load Alleviation Control Designs for an Aeroelastic Wind Tunnel Demonstration Wing," *AIAA SciTech 2020 Forum*, Orlando, FL, January 2020.

[19] Cramer, N. B. and Nguyen, N. T., "Development of an Aeroservoelastic Model for Gust Load Alleviation of the NASA Common Research Model Wind Tunnel Experiment," *AIAA SciTech 2020 Forum*, Orlando, FL, January 2020.

[20] Stanford, B. K., "Optimal Aircraft Control Surface Layouts for Maneuver and Gust Load Alleviation," *AIAA SciTech 2020 Forum*, Orlando, FL, January 2020.

[21] Breuker, R. D., Binder, S., and Wildschek, A., "Combined Active and Passive Loads Alleviation through Aeroelastic Tailoring and Control Surface/Control System Optimization," *AIAA Aerospace Sciences Meeting*, Kissimmee, FL, January 2018.

[22] Pusch, M., Knoblach, A., and Kier, T., "Integrated Optimization of Control Surface Layout for Gust Load Alleviation," *CEAS Aeronautical Journal*, 2019.

[23] Krupa, E., Cooper, J. E., Pirrera, A., and Nangia, R., "Improved Aerodynamic Performance Combining Control Surface Deflections and Aeroelastic Tailoring," *Applied Aerodynamics Conference, Royal Aeronautical Society*, Vol. 122, June 2016, pp. 1–33.

[24] Krupa, E., Cooper, J. E., Pirrera, A., and Nangia, R., "Improved Aerostructural Performance via Aeroservoelastic Tailoring of a Composite Wing," *The Aeronautical Journal*, Vol. 122, June 2018, pp. 1–33.

[25] Woods-Vedeler, J. A., Pototzky, A. S., and Hoadley, S. T., "Rolling Maneuver Load Alleviation Using Active Controls," *Journal of Aircraft*, Vol. 32, No. 1, 1995, pp. 68–76.

[26] Tang, D., Li, A., and Dowell, E. H., "Experimental and Theoretical Study on Rolling Effectiveness of Multiple Control Surfaces," *AIAA Journal*, Vol. 41, No. 2, 2003, pp. 160–167.

[27] Platanitis, G. and Strganac, T. W., "Suppression of Control Reversal Using Leading- and Trailing-Edge Control Surfaces," *Journal of Guidance, Control, and Dynamics*, Vol. 28, No. 3, 2005, pp. 452–460.

[28] Oremland, J., Suryakumar, V. S., Strganac, T. W., and Mangalam, A. S., "Flutter Suppression of an Aeroelastic Wing Using Aerodynamic Observables, Leading-Edge, and Trailing-Edge Control Surfaces," *AIAA Atmospheric Flight Mechanics Conference*, Denver, CO, June 2017.

[29] Klug, L., Radespiel, R., Ullah, J., Seel, F., Lutz, T., Wild, J., Heinrich, R., and Streit, T., "Actuator Concepts for Active Gust Alleviation on Transport Aircraft at Transonic Speeds," *AIAA SciTech 2020 Forum*, Orlando, FL, January 2020.

[30] Ullah, J., Lutz, T., Klug, L., Radespiel, R., and Wild, J., "Active Gust Load Alleviation by Combined Actuation of Trailing Edge and Leading Edge Flap at Transonic Speeds," *AIAA SciTech 2021 Forum*, Virtual Event, January 2021.

[31] Ullah, J., Kamoun, S., Müller, J., and Lutz, T., "Active Gust Load Alleviation by Means of Steady and Dynamic Trailing and Leading Edge Flap Deflections at Transonic Speeds," *AIAA SciTech 2022 Forum*, San Diego, CA and Online, January 2022.

[32] Bradley, M. K., Allen, T. J., and Droney, C. K., "Subsonic Ultra Green Aircraft Research Phase II - Volume I - Truss Braced Wing Design Exploration," NASA/CR–2015-218704, NASA, 2015.

[33] Mastracci, P., Saltari, F., Mastroddi, F., Wilson, T., and Castrichini, A., "Unsteady Aeroelastic Analysis of the Semi Aeroelastic Hinge Including Local Geometric Nonlinearities," *AIAA Journal*, Vol. 60, No. 5, 2022, pp. 3147–3165.

[34] Castrichini, A., Hodigere Siddaramaiah, V., Calderon, D. E., Cooper, J. E., Wilson, T., and Lemmens, Y., "Nonlinear Folding Wing Tips for Gust Loads Alleviation," *Journal of Aircraft*, Vol. 53, No. 5, 2016, pp. 1391–1399.

[35] Castrichini, A., Siddaramaiah, V. H., Calderon, D., Cooper, J. E., Wilson, T., and Lemmens, Y., "Preliminary Investigation of Use of Flexible Folding Wing Tips for Static and Dynamic Load Alleviation," *Aeronautical Journal*, Vol. 121, No. 1235, January 2017, pp. 73–94.

[36] Wilson, T., Castrichini, A., Azabal, A., Calderon, D., Cooper, J. E., Ajaj, R. M., and Herring, M., "Aeroelastic Behaviour of Hinged Wing Tips," *International Forum on Aeroelasticity and Structural Dynamics - IFASD*, Como, Italy, June 2017.

[37] Castrichini, A., Cooper, J. E., Wilson, T., Carrella, A., and Lemmens, Y., "Nonlinear Negative Stiffness Wingtip Spring Device for Gust Loads Alleviation," *Journal of Aircraft*, Vol. 54, November 2016.

[38] Wilson, T., Castrichini, A., Paterson, J., and Arribas Ardura, R., "Non-linear Aeroelastic Behavior of Hinged Wing Tips," *Aircraft Structural Design Conference*, Bristol, UK, October 2018.

[39] Castrichini, A., Wilson, T., and Cooper, J. E., "On the Dynamic Release of the Semi Aeroelastic Wing-Tip Hinge Device," *Aircraft Structural Design Conference*, Bristol, UK, October 2018.

[40] Wilson, T., Kirk, J., Hobday, J., and Castrichini, A., "Small Scale Flying Demonstration of Semi Aeroelastic Hinged Wing Tips," *International Forum on Aeroelasticity and Structural Dynamics - IFASD*, Savannah, GA, USA, June 2019.

[41] Healy, F., Cheung, R. C., Neofet, T., Lowenberg, M. H., Rezgui, D., Cooper, J. E., Castrichini, A., and Wilson, T., "Folding Wingtips for Improved Roll Performance," *AIAA SciTech 2021 Forum*, Virtual Event, January 2021.

[42] Wilson, T., Kirk, J., Hobday, J., and Castrichini, A., "Update on AlbatrossONE Semi Aeroelastic Hinge Small Scale Flying Demonstrator Project," *International Forum on Aeroelasticity and Structural Dynamics - IFASD*, Madrid, Spain, June 2022.

[43] Cheung, R., Wales, C., Rezgui, D., Cooper, J. E., and Wilson, T., "Modeling of Folding Wing-Tip Devices for Gust Loads Alleviation," *AIAA/ASCE/AHS/ASC Structures, Structural Dynamics, and Materials Conference*, Kissimmee, FL, January 2018.

[44] Cheung, R., Rezgui, D., Cooper, J. E., and Wilson, T., "Testing of a Hinged Wingtip Device for Gust Loads Alleviation," *Journal of Aircraft*, Vol. 55, 2018, pp. 1–18.

[45] Cheung, R., Rezgui, D., Cooper, J. E., and Wilson, T., "Testing of Folding Wing-Tip for Gust Load Alleviation in High Aspect Ratio Wing," *AIAA Scitech 2019 Forum*, San Diego, CA, January 2019.

[46] Cheung, R., Rezgui, D., Cooper, J. E., and Wilson, T., "Analyzing the Dynamic Behavior of a High Aspect Ratio Wing Incorporating a Folding Wingtip," *AIAA Scitech 2020 Forum*, Orlando, FL, January 2020.

[47] Gu, H., Healy, F., Rezgui, D., and Cooper, J. E., "Sizing of High Aspect Ratio Wings with Folding Wing Tips," *AIAA SciTech 2022 Forum*, San Diego, CA and Online, January 2022.

[48] Valente, C., Castrichini, A., Wilson, T., Landi, A., and Cooper, J. E., "High Fidelity CFD/CSM Analysis of a Folding Wing-Tip Device for Aircraft Loads Alleviation," *Aircraft Structural Design Conference*, Bristol, UK, October 2018.

[49] Delavenne, M., Barriety, B., Vetrano, F., Ferrand, V., and Salaun, M., "Parametric Analysis of an Active Winglet Concept for High Aspect Ratio Wing Using CFD/CSM Computations," *AIAA Aviation 2020 Forum*, Virtual Event, June 2020.

[50] Conti, C., Saltari, F., Mastroddi, F., Wilson, T., and Castrichini, A., "Quasi-Steady Aeroelastic Analysis of the Semi-Aeroelastic Hinge Including Geometric Nonlinearities," *Journal of Aircraft*, Vol. 58, 2021, pp. 1–11.

[51] Healy, F., Cheung, R. C., Rezgui, D., Cooper, J. E., Wilson, T., and Castrichini, A., "On the Nonlinear Geometric Behaviour of Flared Folding Wingtips," *AIAA SciTech 2022 Forum*, San Diego, CA and Online, January 2022.

[52] Bendiksen, O. O., "Transonic Limit Cycle Flutter of High-Aspect-Ratio Swept Wings," *Journal of Aircraft*, Vol. 45, No. 5, 2008, pp. 1522–1533.

[53] Anon, "Flight Test Guide for Certification of Transport Category Airplanes," Advisory Circular, Federal Aviation Administration, March 2011.

[54] Anon, "Easy Access Rules for Large Aeroplanes," Certification Specification, European Aviation Safety Agency, November 2018.

[55] Green, J. A., "Aeroelastic Tailoring of Aft-Swept High-Aspect-Ratio Composite Wings," *Journal of Aircraft*, Vol. 24, No. 11, 1987, pp. 812–819.

[56] Cook, R., Palacios, R., Goulart, P., and Roberts, I., "Robust Manoeuvring and Gust Alleviation of Very Flexible Aircraft using Novel Control Effectors," *International Forum on Aeroelasticity and Structural Dynamics - IFASD*, Paris, France, June 2011.

[57] Stanford, B. K., Wieseman, C. D., and Juttle, C. V., "Aeroelastic Tailoring of Transport Wings Including Transonic Flutter Constraints," *AIAA/ASCE/AHS/ASC Structures, Structural Dynamics, and Materials Conference*, Kissimmee, FL, January 2015.

[58] Stodieck, O., Cooper, J. E., Weaver, P. M., and Kealy, P., "Aeroelastic Tailoring of a Representative Wing Box Using Tow-Steered Composites," *AIAA Journal*, Vol. 55, No. 4, 2017, pp. 1425–1439.

[59] Natella, M., Wang, X., and Breuker, R. D., "The Effects of Aeroelastic Tailoring on Flight Dynamic Stability," *AIAA SciTech 2018 Forum*, Kissimmee, FL, January 2018.

[60] Liu, D., Wan, Z., and Yang, C., "The Influence of Spar Position on Aeroelastic Optimization of a Large Aircraft Wing with Different Materials," *53rd AIAA/ASME/ASCE/AHS/ASC Structures, Structural Dynamics and Materials Conference*, Hololulu, HI, April, 2012.

[61] Chen, P. C., Sarhaddi, D., Jha, R., Liu, D. D., Griffin, K., and Yurkovich, R., "Variable Stiffness Spar Approach for Aircraft Maneuver Enhancement Using ASTROS," *Journal of Aircraft*, Vol. 37, No. 5, 2000, pp. 865–871.

[62] Cesnik, C. E. S., Ortega-Morales, M., and Patil, M., "Active Aeroelastic Tailoring of High Aspect Ratio Composite Wings," *AIAA/ASME/ASCE/AHS/ASC Structures, Structural Dynamics, and Materials Conference*, Atlanta, GA, April 2000.

[63] Khot, N. S., Zweber, J. V., Veley, D. E., Oslash, H. Z., and Eastep, F. E., "Flexible Composite Wing with Internal Actuation for Roll Maneuver," *Journal of Aircraft*, Vol. 39, No. 5, 2002, pp. 521–527.

[64] Gomes, A. A. and Suleman, A., "Topology Optimization of a Reinforced Wing Box for Enhanced Roll Maneuvers," *AIAA Journal*, Vol. 46, No. 3, 2008, pp. 548–556.

[65] Kitson, R. C., Lupp, C., and Cesnik, C. E. S., "Modeling and Simulation of Flexible Jet Transport Aircraft with High-Aspect-Ratio Wings," *AIAA SciTech 2016 Forum*, San Diego, CA, January, 2016.

[66] Vassberg, J. C., DeHaan, M. A., Rivers, S. M., and Wahls, R. A., "Development of a Common Research Model for Applied CFD Validation Studies," *26th AIAA Applied Aerodynamics Conference*, Honolulu, HI, August, 2008.

[67] Brooks, T. R., Kenway, G. K. W., and Martins, J. R. R. A., "Benchmark Aerostructural Models for the Study of Transonic Aircraft Wings," *AIAA Journal*, Vol. 56, No. 7, 2018, pp. 2840–2855.

[68] Andersen, G., Forster, E., Kolonay, R., and Eastep, F., "Multiple Control Surface Utilization in Active Aeroelastic Wing Technology," *Journal of Aircraft*, Vol. 34, No. 4, 1997, pp. 552–557.

[69] Cook, R., Palacios, R., and Roberts, I., "Manoeuvre Efficiency of Unconventional Control Effectors on Very Flexible Aircraft," *RAeS Applied Aerodynamics Conference*, Bristol, UK, July 2010.

[70] Maraniello, S. and Palacios, R., "Optimal Rolling Maneuvers with Very Flexible Wings," *AIAA Journal*, Vol. 55, No. 9, 2017, pp. 2964–2979.

[71] Dowell, E. H., Bliss, D. B., and Clark, R. L., "Aeroelastic Wing with Leading- and Trailing-Edge Control Surfaces," *Journal of Aircraft*, Vol. 40, No. 3, 2003, pp. 559–565.

[72] Dussart, G., Yusuf, S., and Lone, M., "Effect of Wingtip Morphing on the Roll Mode of a Flexible Aircraft," *AIAA SciTech 2018 Forum*, Kissimmee, FL, 2018.

[73] Castrichini, A., Wilson, T., Saltari, F., Mastroddi, F., Viceconti, N., and Cooper, J. E., "Aeroelastics Flight Dynamics Coupling Effects of the Semi-Aeroelastic Hinge Device," *Journal of Aircraft*, Vol. 57, 2019, pp. 1–9.

[74] Blunt, W., Healy, F., Cheung, R. C., Lowenberg, M. H., and Cooper, J. E., "Trailing Edge Tabs on Folding Wingtips (FWTs) for Aircraft Roll Control," *AIAA SciTech 2022 Forum*, San Diego, CA and Online, January 2022.

[75] Stone, R. W., J., "Ride Quality Overview," *Symposium on Vehicle Ride Quality, NASA Langley Research Center*, 1972.

[76] Mckenzie, J. R. and Brumaghim, S. H., "Review of Ride Quality Technology Needs of Industry and User Groups," *The Ride Quality Symposium, NASA Langley Research Center*, 1975.

[77] Leatherwood, J. D., Dempsey, T. K., and Clevenson, S. A., "A Design Tool for Estimating Passenger Ride Discomfort Within Complex Ride Environments," *Human Factors*, Vol. 22, No. 3, 1980, pp. 291–312.

[78] Leatherwood, J. D. and Barker, L. M., "A User Oriented and Computerized Model for Estimating Vehicle Ride Quality," *NASA Technical Paper 2299*, 1984.

[79] König, R. and Hahn, K., "Load Alleviation and Ride Smoothing Investigations Using ATTAS." *17th Congress of the International Council of the Aeronautical Sciences*, 1991, pp. 1379–1393.

[80] Anon, "Mechanical Vibration and Shock–Evaluation of Human Exposure to Whole-Body Vibration—Part 1: General Requirements," Certification Specification, International Organization for Standardization, ISO STD 2631-1, Geneva, 1997.

[81] Anon, "Department of Defense Design Criteria Standard, Human Engineering, MIL-STD-1472G," Tech. rep., U.S. Dept. of Defense, 2012.

[82] Bizinos, N. and Redelinghuys, C., "Tentative Study of Passenger Comfort During Formation Flight Within Atmospheric Turbulence," *Journal of Aircraft*, Vol. 50, No. 3, 2013, pp. 886–900.

[83] Okolo, W., Dogan, A., and Blake, W., "Ride Quality Within Trail Aircraft In Formation Flight," *AIAA Atmospheric and Space Environments Conference*, Dallas, TX, June 2015.

[84] Wang, X., Kampen, E.-J. V., and Chu, Q. P., "Gust Load Alleviation and Ride Quality Improvement with Incremental Nonlinear Dynamic Inversion," *AIAA Atmospheric Flight Mechanics Conference*, Grapevine, TX, January 2017.

[85] Jacobson, I. and Richards, L., "Ride Quality Evaluation II: Modeling of Airline Passenger Comfort," *Ergonomics*, Vol. 19, 01 1976, pp. 1–10.

[86] Khalil, A., "Flight Dynamics, Handling and Ride Qualities of a Flexible Aircraft," *Conference: Deutscher Luft- und Raumfahrtkongress*, Munich, Germany, September 2017.

[87] Hanson, C. E., Andrade, S., and Pahle, J., "Experimental Measurements of Passenger Ride Quality During Aircraft Wake Surfing," *AIAA Atmospheric Flight Mechanics Conference*, Atlanta, GA, June 2018.

[88] Hartwell, B. and Nguyen, N. T., "Nonlinear 6-DoF Simulations of a Multi-Objective Optimal Flight Control System for Flexible Wing Aircraft," *AIAA SciTech 2021 Forum*, Virtual Event, January 2021.

[89] Krishnamurthy, V. and Handojo, V., "Structural Design Process and Subsequent Flight Mechanical Evaluation in Preliminary Aircraft Design: Demonstrated on Passenger Ride Comfort Assessment," *CEAS Aeronautical Journal*, Vol. 12, 2021, pp. 457–469.

[90] Riso, C., Sanghi, D., Cesnik, C. E. S., Vetrano, F., and Teufel, P., "Parametric Roll Maneuverability Analysis of a High-Aspect-Ratio-Wing Civil Transport Aircraft," *AIAA SciTech 2020 Forum*, Orlando, FL, January 2020.

[91] Skujins, T. and Cesnik, C. E. S., "Reduced-Order Modeling of Unsteady Aerodynamics Across Multiple Mach Regimes," *Journal of Aircraft*, Vol. 51, No. 6, 2014, pp. 1681–1704.

[92] Sanghi, D., Riso, C., Cesnik, C. E. S., and Vetrano, F., "Impact of Control-surface Flexibility on the Dynamic Response of Flexible Aircraft," *AIAA Scitech 2020 Forum*, Orlando, FL, January 2020.

[93] Sanghi, D., Riso, C., Cesnik, C. E. S., and Vetrano, F., "Conventional and Unconventional Control Effectors for Load Alleviation in High-Aspect-Ratio-Wing Aircraft," *AIAA SciTech 2022 Forum*, San Diego, CA and Online, January 2022.

[94] Sanghi, D., Riso, C., Cesnik, C. E. S., and Vetrano, F., "Analysis of Ride Qualities in Transonic High-Aspect-Ratio-Wing Aircraft," *International Forum on Aeroelasticity and Structural Dynamics - IFASD*, Madrid, Spain, June 2022.

[95] Sanghi, D., Riso, C., Cesnik, C. E. S., and Vetrano, F., "Influence of Aileron Placement on Roll Response of High-Aspect-Ratio-Wing aircraft," *AIAA Aviation 2020 Forum*, Virtual Event, June 2020.

[96] Su, W. and Cesnik, C. E. S., "Nonlinear Aeroelasticity of a Very Flexible Blended-Wing-Body Aircraft," *Journal of Aircraft*, Vol. 47, No. 5, 2010, pp. 1539–1553.

[97] Su, W. and Cesnik, C. E. S., "Strain-Based Geometrically Nonlinear Beam Formulation for Modeling Very Flexible Aircraft," *International Journal of Solids and Structures*, Vol. 48, No. 16-17, 2011, pp. 2349–2360.

[98] Peters, D. A., Hsieh, M. C. A., and Torrero, A., "A State-Space Airloads Theory for Flexible Airfoils," *Journal of the American Helicopter Society*, Vol. 52, No. 4, 2007, pp. 329–342.

[99] Shearer, C. M. and Cesnik, C. E. S., "Nonlinear Flight Dynamics of Very Flexible Aircraft," *Journal of Aircraft*, Vol. 44, No. 5, 2007, pp. 1528–1545.

[100] Puyou, G., *Multi-Objective Design of Piloting Laws for a Civil Transport Aircraft*, PhD Thesis, National School of Aeronautics and Space, Toulouse, France, 2005.

[101] Anon, "Measurement and Evaluation of Human Exposure to Whole-body Mechanical Vibration and Repeated Shock," Certification Specification, British Standards Institution, 1987.

[102] Riso, C., Pereira, M. F. V., Lustosa, L., and Cesnik, C. E. S., "Sensor Output Extraction Formulation and Implementation into UM/NAST," Tech. rep., Airbus-Michigan Center for Aero-Servo-Elasticity of Very Flexible Aircraft, CASE-VFA-2019-P4-D3, University of Michigan, Ann Arbor, Michigan, December 2019.

[103] Bleecke, H., "Personal Communication," Airbus Operations GmbH, June 2021.

[104] Brezillon, J., "Personal Communication," Airbus Operations S. A. S., June 2021.

[105] Jones, J. R. and Cesnik, C. E. S., "Nonlinear Aeroelastic Analysis of the X-56A Multi-Utility Aeroelastic Demonstrator," *AIAA SciTech 2016 Forum*, San Diego, CA, January, 2016.

[106] Riso, C. and Cesnik, C. E. S., "Preliminary Aerodynamic Reduced Order Model of the Baseline XRF1," Tech. rep., Airbus-Michigan Center for Aero-Servo-Elasticity of Very Flexible Aircraft, CASE-VFA-2018-P4-D2, University of Michigan, Ann Arbor, Michigan, July 2018 (updated April 2019).

[107] Theodorsen, T., "General Theory of Aerodynamic Instability and the Mechanism of Flutter," Tech. rep., NACA Report 496, 1935.

[108] Cheung, R. C. M., Rezgui, D., Cooper, J. E., and Wilson, T., "Testing of Folding Wingtip for Gust Load Alleviation of Flexible High-Aspect-Ratio Wing," *Journal of Aircraft*, Vol. 57, No. 5, 2020, pp. 876–888.

[109] Lophaven, S. N., Nielsen, H. B., and Sondergaard, J., "DACE Matlab Kriging Toolbox," Tech. rep., Informatics and Mathematical Modeling, Technical University of Denmark, Lyngby, Denmark, August 2002.

[110] Malcolm, D. J. and Laird, D. L., "Extraction of Equivalent Beam Properties from Blade Models," *Wind Energy*, Vol. 10, No. 2, 2007, pp. 135–157.